STARS, GAS, AND DUST AT HIGH RESOLUTION IN THE TRIANGULUM GALAXY

by

Thomas George Williams

A THESIS SUBMITTED TO CARDIFF UNIVERSITY
FOR THE DEGREE OF DOCTOR OF PHILOSOPHY

AUGUST 2019

To see a World in a Grain of Sand
And a Heaven in a Wild Flower
Hold Infinity in the palm of your hand
And Eternity in an hour

William Blake

ACKNOWLEDGEMENTS

When I got the email from Cardiff telling me I'd been accepted for a PhD position with Walter Gear and Matt Smith, I was told by the conductor that a rehearsal was not a suitable place for unimportant news, and it would have to wait until the pub later. What follows here then, I suppose, is three years of unimportant work (although the pub has remained an ever-present source of unimportant news).

In my time at Cardiff, I've gained a supervisor (Tim Davis), lost Walter to the Emerald Isle, and met a number of people who I consider as friends first, colleagues second. This includes the (frankly legion) PhD intake when I appeared along with the people who have joined or left in the meantime, the ever-helpful postdocs in the office, the regulars at coffee/cake/Flankard/Bandaoke, and the people I've had the chance to meet through collaborations both large and smaller. Of course, special thanks go to my supervisors, Walter and Matt, who have gently guided me along the way, and given me the opportunity to go to exotic places like Hawai'i (twice!) and Manchester. I would also like to thank my examiners, Haley Gomez and Amélie Saintonge for giving me a productive grilling in my viva, and Carole Tucker for chairing (and pointing out where the chocolate biscuits were). Finally, a huge thanks to my parents for their unwavering support in the face of extremely confusing questions like "what does Tom actually do?"

There are also a number of people I would like to thank in particular for the work contained within this thesis. In terms of people, for the chapter on the star formation law, I thank Stephen Eales and Jenifer Millard for valuable discussions, Sébastien Viaene for providing the extended MAGPHYS IR libraries, Elisabete da Cunha for MAGPHYS assistance. For the radiative transfer chapter, Peter Camps for valuable technical SKIRT advice, along with all of the participants at the SKIRT day in Ghent for comments, discussions, and jenever. I also thank all of the peer reviewers for their constructive comments which improved the manuscripts.

In terms of computational tools, this research has made use of MONTAGE (`http://montage.ipac.caltech.edu/`), which is funded by the National Science Foundation under Grant Number ACI-1440620, and was previously funded by the National Aeronautics and Space Administration's Earth Science Technology Office, Computation Technologies Project, under Cooperative Agreement Number NCC5-626 between NASA and the California Institute of Technology. This research has made use of Astropy (`http://www.astropy.org/`; Astropy Collaboration et al. 2013, 2018), NumPy (`http://www.numpy.org/`; van der Walt et al. 2011), SciPy (`http://www.scipy.org/`), MatPlotLib (`http://matplotlib.org/`; Hunter 2007), APLpy, (`https://aplpy.github.io/`; Robitaille & Bressert 2012). This research has made use of the NASA/IPAC Infrared Science Archive, which is operated by the Jet Propulsion Laboratory, California Institute of Technology, under contract with the National Aeronautics and Space Administration, as well as the NASA/IPAC Extragalactic Database (NED) which is operated by the Jet Propulsion Laboratory, California Institute of Technology, under contract with the National Aeronautics and Space Administration.

PUBLICATIONS

FIRST AUTHOR

Williams, T. G., Davis, T. A., et al., 2019, *A WISDOM View of the GMC Populations of Early-Type Galaxies.* In prep.

Williams, T. G., Baes, M., De Looze, I., et al., 2019, *High-resolution Radiative Transfer Modelling of M33.* MNRAS 487, 2753.

Williams, T. G., Gear, W. K., Smith, M. W. L., 2018, *A High-Resolution, Dust-Selected Molecular Cloud Catalogue of M33, the Triangulum Galaxy.* MNRAS 483, 5135.

Williams, T. G., Gear, W. K., Smith, M. W. L., 2018, *The Star Formation Law at GMC Scales in M33, the Triangulum Galaxy.* MNRAS 479, 297.

CO-AUTHOR

Li, Z., Li, Z., Smith, M. W. L., et al. 2019. *HASHTAG II. A Survey of CO(3–2) Emission from the Star Forming Disc of M31.* MNRAS submitted.

Gao, Y., Xiao T., Li C., et al., 2019. *Estimating the molecular gas mass of low-redshift galaxies from a combination of mid-infrared luminosity and optical properties.* ApJ submitted.

Dawson, J. M., Davis, T. A., Gomez, E. L., et al., 2019, *Using machine learning to study the kinematics of cold gas in galaxies.* MNRAS submitted.

North, E. V., Davis, T. A., Bureau, M., et al., 2019, *WISDOM project – V: Resolving molecular gas in Keplerian rotation around the super-massive black hole in NGC 0383.* MNRAS 490, 319.

Lamperti, I., Saintonge, A., De Looze, I., et al., 2019, *JINGLE V: Dust properties of nearby galaxies derived from hierarchical Bayesian SED fitting.* MNRAS 489, 4389.

Smith, M. W. L., Clark, C. J. R., De Looze, I., et al., 2019, *JINGLE, a JCMT legacy survey of dust and gas for galaxy evolution studies: II. SCUBA-2 850*μ*m data reduction and dust flux density catalogues.* MNRAS 486, 4166.

Pan, H-A., Lin, L., Hsieh, B-C., et al., 2018, *The Effect of Galaxy Interactions on Molecular Gas Properties.* ApJ 868, 132.

Saintonge, A., Wilson, C. D., Xiao, T., et al., 2018, *JINGLE, a JCMT Legacy Survey of Dust and Gas for Galaxy Evolution Studies - I. Survey Overview and First Results.* MNRAS 481, 3497.

ABSTRACT

This thesis investigates the interplay between dust, gas, and stars at high resolution in nearby Local Group galaxy M33.

Using panchromatic spectral energy distribution (SED) fitting along with ancillary gas tracer data, the star formation law is studied at scales of 100pc. A strong scale dependence is seen in the fitted power law index no matter which gas tracer is used, and whilst correlations between each tracer of gas and SFR remain strong, the correlation between SFR and molecular gas is strongest, perhaps indicating that the molecular gas is the more important driver of star formation.

A catalogue of Giant Molecular Clouds (GMCs) is extracted from sub-millimetre wavelength data. These clouds have a much lower gas-to-dust ratio (GDR) than found in the Milky Way. The mass function of these clouds follows a slope proportional to $M^{-2.84}$, implying that M33 is poorer at forming massive clouds than other nearby spirals. This study finds no absence of massive clouds at large galactocentric radius as in earlier CO studies, perhaps indicating a population of CO-dark gas dominated clouds at these larger distances. I also find that these clouds generally have masses several times larger than their virial mass, indicating that they are dominated by gravitational forces.

A high-resolution, radiative transfer model for M33 is constructed from inputted maps of stellar and dust geometries. This simple model well fits the observed SED from UV to sub-millimetre wavelengths. In terms of stellar attenuation by dust, a reasonably strong, broad UV bump is found, as well as significant systematic differences in the amount of dust attenuation when compared to standard SED modelling. There are discrepancies in the residuals of the spiral arms versus the diffuse interstellar medium (ISM), indicating a difference in properties between these two regimes. Dust heating is dominated by unevolved stellar populations at all wavelengths. The dust-energy balance is restored at spatial scales greater than around 1.5kpc.

CONTENTS

LIST OF TABLES

LIST OF FIGURES

CHAPTER 1

INTRODUCTION

In the beginning there was nothing,
To be honest, that suited me just fine.

JARVIS COCKER

Extragalactic objects have been known about since prehistory, with ancient Chilean petroglyphs depicting what appear to be the Magellanic Clouds. The earliest written observation of an extragalactic object was in AD964, when Persian astronomer al-Sufi in his "Book of Fixed Stars" (al-Sufi, 964) described the galaxy Andromeda (M31) as "A Little Cloud". In 1755, Immanuel Kant speculated that there may be "island universes," or galaxies outside the Milky Way (MW). The first catalogue of these objects, which clearly contrast with the point-like stars of our own Milky Way (MW) was by Messier (1781), who termed these objects "nebulæ". Observations were also carried out by William Herschel, who noted a number of these nebulæ (Herschel, 1785). Catalogues were later published by Herschel (1864) and Dreyer (1888), which expanded on the original Messier catalogue. However, despite these nearby objects being known about for more than a millennium, it was not until the early 1900s that Edwin Hubble proved that these objects were indeed outside of our own Milky Way. Using Cepheid variables, he calculated the distance to M31 and M33 (the Triangulum) to be around 285kpc (Hubble, 1925). This was far greater than any estimate of the size of the Milky Way, and so we finally had definitive proof that our Galaxy was not alone in the Universe.

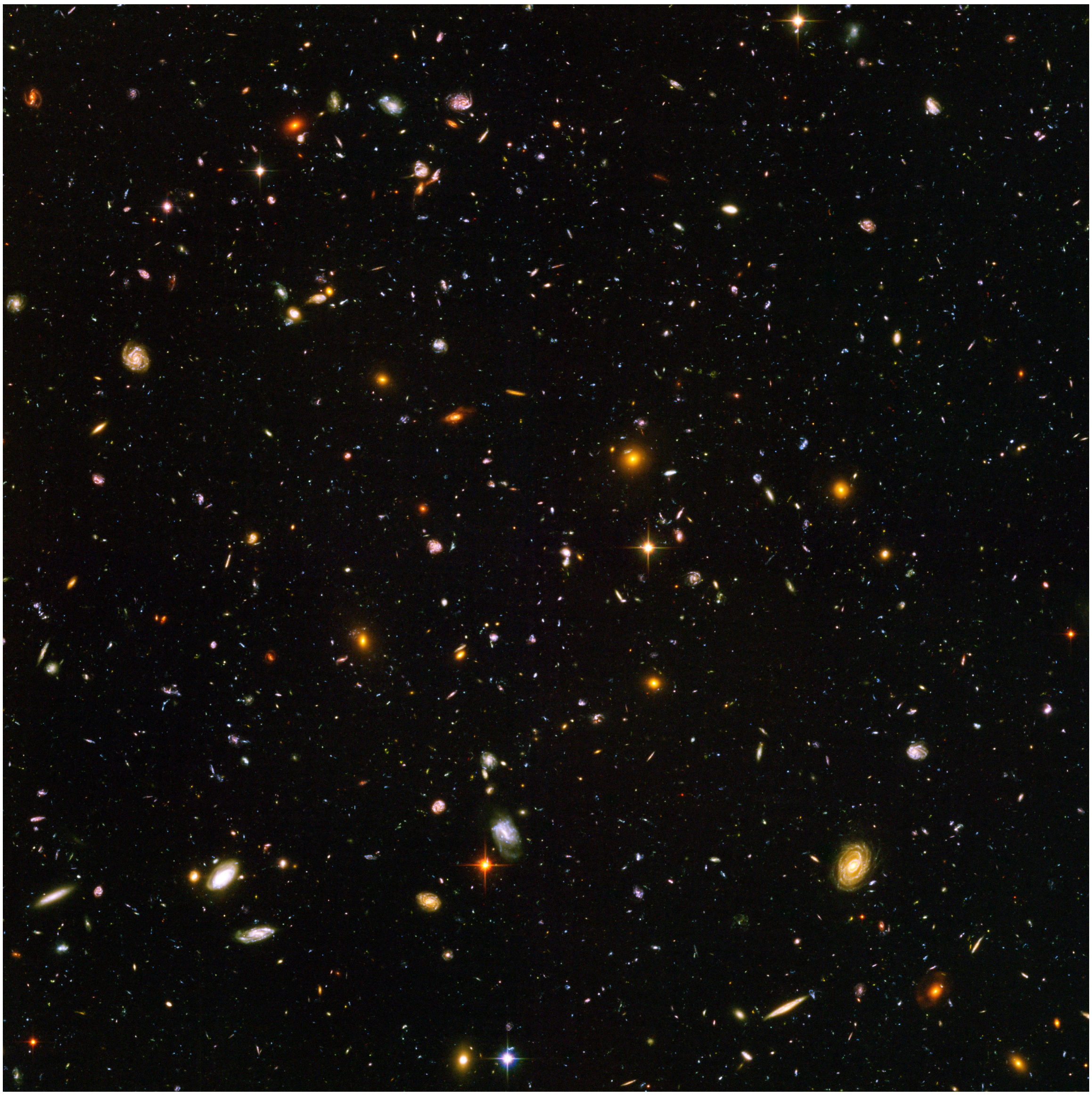

Figure 1.1: The Hubble Ultra-Deep Field. Image credit: NASA, ESA, and S. Beckwith (STScI) and the HUDF Team.

1.1 A SKY FULL OF STARS

Around a century after Hubble's distance measurements, we now know that these extragalactic objects not only exist, but are ubiquitous. Fig. 1.1 shows the Hubble Ultra-Deep Field (HUDF), a 2.4 arcmin^2 observation from within the Fornax constellation. Despite the field of view of this image being only around one tenth of the size of a full moon in terms of diameter, there are around 10,000 galaxies, looking back over almost all of cosmic time. It therefore appears that galaxies are located all over the Universe, both spatially and temporally. This image also highlights the diversity of the galaxy population – galaxies have a variety of colours and morphologies. In terms of colours, we find that (at least in the optical) there is a bimodality; galaxies that are not forming stars are red (as they are dominated by long-lived, cooler stars), and actively star-forming galaxies are blue (due to the presence of ongoing star formation and hot stars). A similar bimodality is seen in the morphology of these objects, with galaxies generally showing spiral arms if star-forming, or being relative featureless and smooth if not. Hubble (1926) divided these two broad categories of morphologies into late-type galaxies (the spirals) and early-type galaxies (ellipticals and lenticulars). Although Hubble did not think of this as an evolutionary sequence, one explanation for this bimodality is that late-type galaxies may evolve into early-type galaxies, either through some internal process such as active galactic nuclei (AGN) feedback (e.g. Dubois et al. 2013), or environmental process such as the high densities in cluster environments (e.g. Dressler 1980). Given the dearth of transitionary galaxies (the so-called green valley), it is implied that this star-formation quenching process must either be rapid, or that we are somehow systematically missing these green valley galaxies (Eales et al., 2018).

A natural question is to ask how these galaxies originally formed, and the currently accepted cosmological model for the cosmic history of galaxies is known as ΛCDM, with the Λ indicating the cosmological constant, which drives (and accelerates) the expansion of the Universe, and CDM the dominant material in the Universe – Cold Dark Matter. In this model, quantum fluctuations in the early Universe lead to overdensities, which are the seeds of structure formation. From this, small galaxies form, and merge over time to form the larger galaxies we see today – a process referred to as 'hierarchical assembly.' ΛCDM does have issues reconciling theory with observation, however. For example, quantum field theories predict a cosmological constant that is some 100 orders of magnitude larger than seen in reality (Adler et al., 1995). Another is that many massive galaxies appear to have been formed earlier in time than the hierarchical model would predict through mergers at later times (e.g. Kashlinsky & Jimenez, 1997). This problem is known as 'downsizing.' A review of many of the small-scale issues with ΛCDM is given in Del Popolo & Le Delliou (2017). Of course, these issues may not be due to a fundamental issue with ΛCDM, merely that we do not yet fully understand the smaller scale physics. Thus, it is critically important to study both the larger picture of galaxy evolution, as well as detailed analyses of how individual galaxies evolve.

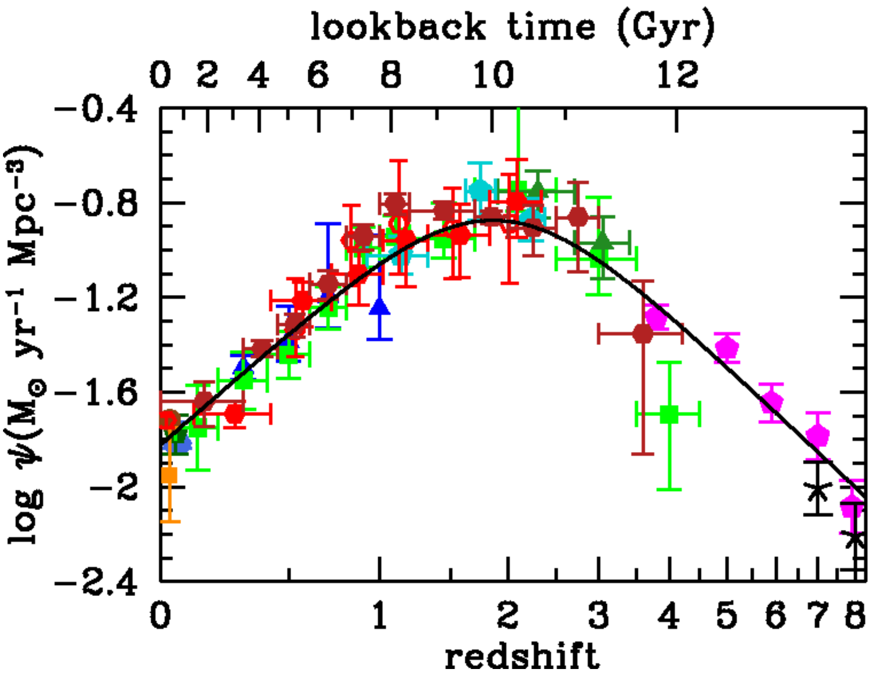

Figure 1.2: The star formation history of the Universe, from both FUV and IR SFR measurements (Madau & Dickinson, 2014).

1.1.1 STAR FORMATION

The star formation rate (SFR) of a galaxy is one of its most fundamental parameters. The rate at which gas is converted into stars has a direct influence on a galaxy's evolution, and also allows us to constrain theoretical models of star formation. Given that star formation produces the vast majority of the heavy elements in the Universe up to iron (although some elements such as Lithium and Beryllium are burned through almost instantly), and the death of massive stars produce the elements beyond that, understanding this also has ramifications outside of extragalactic astronomy. Similar, the star formation history (SFH) of a galaxy informs us how this varies over cosmic time, and thus lets us examine how this galaxy has evolved over that time. In terms of measuring the star formation history, there are two methods than can be employed. The first is directly measuring the SFH for single galaxies through spectroscopic fitting (e.g. Cid Fernandes et al. 2013; Tojeiro et al. 2011; Goddard et al. 2017), or photometric fitting (e.g. Williams et al. 2017; Cignoni et al. 2018). However, this fitting is subject to degeneracies, and therefore we may not converge to a unique solution in every case. An alternative is to look back in time, by observing the instantaneous SFR of galaxies at higher redshifts. Using many different galaxies at different stages of evolution, a history of the star formation in the Universe can be obtained. This is shown in Fig. 1.2, which is taken from Madau & Dickinson

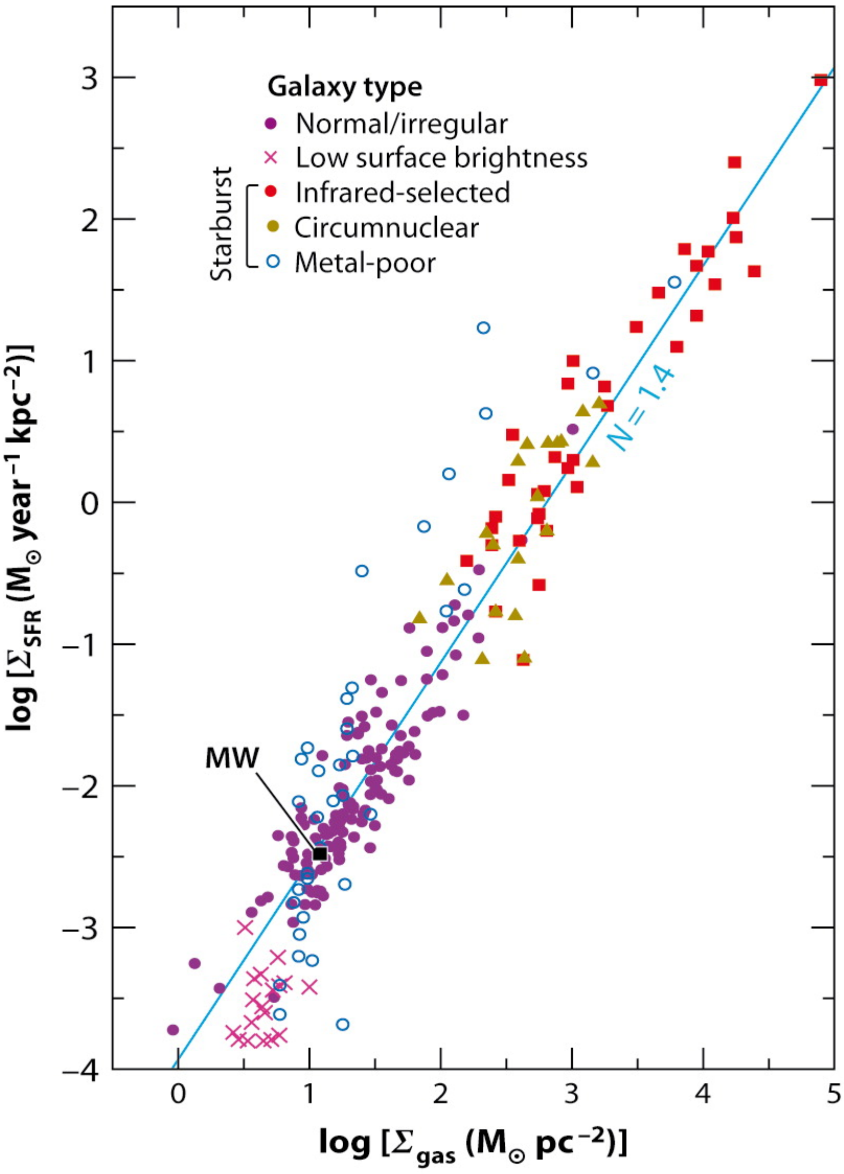

Figure 1.3: The integrated star-formation law for a number of different types of galaxy. The blue line indicates the canonical power-law index, $N = 1.4$. Figure from Kennicutt & Evans (2012).

(2014). A peak in star formation is seen at a redshift of ~2, with around an order of magnitude higher star formation than seen today.

Many extragalactic studies focus on the scales of galaxy-wide star formation, simply because of the resolution of available instruments. On these scales, galaxies follow a number of tight scaling relationships. Possibly the most famous of these is the "Kennicutt-Schmidt" law, so-named after the original work on the MW by Schmidt (1959) and the extension of this to extragalactic measurements by Kennicutt

(1998b). This is covered in much more detail in Chapter 2, but briefly this is an empirical relationship between the surface density of gas and the surface density of SFR in a galaxy (surface density due to the fact that in extragalactic measurements we must average along the line-of-sight; Fig. 1.3). A number of mechanisms have been proposed to explain this empirical relationship – one interpretation is that as gas collapses under its own gravity, a roughly constant fraction of the gas converts into stars (e.g. Elmegreen 1994; Krumholz et al. 2008). Another is that the SFR is set by the dense gas fraction, and so N is linear; in this case, a value of $N = 1.4$ is simply due to sampling galaxies with different dense gas fractions (Lada et al., 2012). However, the true nature of this "law" remains unknown.

1.2 THE INTERSTELLAR MEDIUM

The tight relationship seen in Fig. 1.3 implies that there is some fundamental underlying relationship between the SFR and the gas content of a galaxy. This gas is not seen in Fig. 1.1 – UV and optical light is dominated by stellar emission within a galaxy, but the material in-between stars (the interstellar medium, or ISM) plays a huge role in shaping galaxy evolution. The bulk of the ISM is composed of hydrogen, in a variety of states. The ISM is complex, and spans a wide range of temperatures and densities. Generally, these are broken up into three phases – firstly, the "hot" phase, consisting of ionized medium with densities less than 0.01 cm^{-3} and temperatures in excess of 10^5 K. Secondly, the "warm" phase, which consists of some neutral and some ionized medium (the WIM and WNM, respectively) – these have densities of $0.1 - 1$ cm^{-3} and temperatures of 1000s of K. Finally, the cold neutral medium (CNM) is the densest of these three phases, with densities above 10 cm^{-3} and temperatures less than 100K. It is in this dense, cold regime that star formation occurs, and so will be the focus of the following section. For details of the other two phases, Cox (2005) provides a overview of the three phases of the ISM.

Star-formation takes place within the CNM, in structures referred to as clouds (this is discussed in more detail in Chapter 3). These clouds are dominated by the molecular gas that is believed to be the basis of star-formation (André et al., 2010; Lada et al., 2010), and are surrounded by atomic gas (van Dishoeck & Black, 1988). Given sufficiently high ($\sim$pc) resolution observations, these clouds decompose yet again, revealing a rich structure of filaments and small cores, which are believed to be the sites of the formation of individual stars (André et al., 2010; Men'shchikov et al., 2010; Molinari et al., 2010). The structure of these clouds is complex, and thus the naming and identifying conventions surrounding them is similarly confusing, and oftentimes inconsistent. Generally, the boundary of a cloud is defined by some detection level against the background (e.g. Kirk et al. 2013), or by some level of extinction from the background stars (e.g. Lada et al. 2010). However, this detection criterion is essentially arbitrary. Given that many clouds may be co-spatial, the ability to detect and classify clouds is limited by spatial resolution, and in the case of spectral data, spectral resolution as well. Several clouds may also join together to form a "clump", which is theoretically gravitationally bound (Williams et al., 2000), but this is hard to confirm observationally, as proxies for gravitational boundedness for these intermediate structures are ill-defined.

1.2.1 GAS

Tracing the gas in clouds is vital for categorising the properties, and charting the evolution of these clouds. This task proves observationally complex, however, and so this section provides an overview of the commonly adopted methods for tracing the atomic and molecular gas in galaxies.

1.2.1.1 Atomic Gas

The cold atomic hydrogen in a galaxy can be traced directly, via the hyperfine transition which occurs at 21cm (in the rest frame). Given an HI intensity, I_{HI}, a surface density can be calculated as (Rohlfs & Wilson, 1996)

$$\Sigma_{\mathrm{HI}} = 1.8 \times 10^{18}\mathrm{cm}^{-2} \times I_{\mathrm{HI}}/(\mathrm{K\ km/s}). \tag{1.1}$$

It is important to note that the optical depth effects can be important in these HI observations. The transition reaches an optical depth of unity at a V-band extinction of $A_V = 0.24$ mag (Draine, 2011), and so accounting for this can be important in areas of higher extinction.

Given that observations of HI are at 21 cm, even the largest single-dish telescopes have resolutions of ∼arcminutes, and so these single-dish observations are generally limited to integrated measurements (aside from in the most nearby galaxies). One such large survey of galaxies is the Arecibo Legacy Fast ALFA Survey (ALFALFA; Giovanelli et al. 2005), which surveyed around 30,000 galaxies over 7000 deg^2

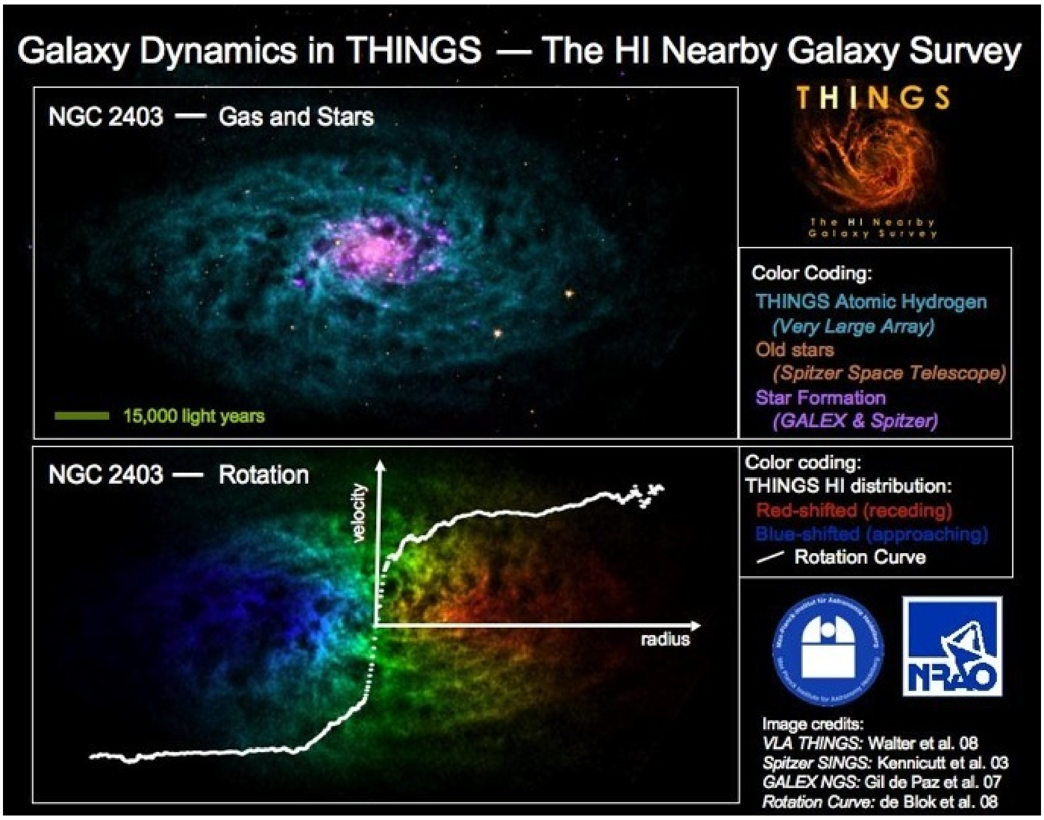

Figure 1.4: *Top:* A false-colour image showing the extend of the HI (light blue), the old stellar population (orange), and ongoing star-formation (purple) for NGC 2403. *Bottom:* the rotation curve of the HI – red indicates red-shifted gas, blue blue-shifted gas. Image credits are in the figure, which was obtained from `http://www.mpia.de/THINGS/Galaxy_Dynamics.html`.

of the sky. This data has been used to, for example statistically survey the star-formation efficiency of nearby galaxies, finding it to be reasonably constant from galaxy to galaxy (Schiminovich et al., 2010). Another example of the use of this data is to stack many spectra of similar galaxies to improve the signal-to-noise. Fabello et al. (2011) used this technique to study the effect of bulges on the HI content of a galaxy, finding that the bulge has little effect on the star-formation efficiency of a galaxy.

In order to resolve nearby galaxies, interferometric telescopes must be used at these long wavelengths. The Karl G. Jansky Very Large Array (VLA) is one of the most popular arrays for HI measurements, which in its most extended configurations can reach resolutions of <10 arcsecond. The HI Nearby Galaxy Survey (THINGS; Walter et al. 2008) is a high-resolution survey of 34 nearby galaxies, one of which can be seen in Fig. 1.4. These data have been used to study, e.g. the star-formation threshold density (Leroy et al., 2008), with very little atomic hydrogen exceeding a density of $\sim 10\,\mathrm{M_\odot\,pc^{-2}}$. Given that the HI typically extends much further than most of the other observable constituents of a galaxy, this data is also useful for modelling the rotation curves of these galaxies, and constraining the distribution of dark matter (de Blok et al., 2008).

1.2.1.2 Molecular Gas

H_2 forms the bulk of the molecular mass of a galaxy, but tracing the cold component of molecular hydrogen is essentially impossible observationally. This is due to two reasons – firstly, the hydrogen molecule is symmetric, and thus lacks a permanent dipole moment. Secondly, hydrogen is the smallest molecule, and thus requires high temperatures to excite. Given that the temperatures in these cold environments are less than 100K, this makes the spectrum of hydrogen a poor tracer of the cold regions of a galaxy. H_2 has rotation lines in the MIR at temperatures of $\sim$1000 K, which trace the surfaces of clouds and some small amount of the total molecular gas mass (1% to 30%, Roussel et al. 2007), but here continuum optical depth is an issue.

To trace the bulk of the cold molecular component, we generally turn to the rotational transitions of CO, as it is the next most abundant molecule in the ISM, much larger than H_2, and possesses a dipole moment. The quantised rotational energy is

$$\mathrm{E_{rot}} = \frac{J(J+1)\hbar^2}{2I}, \tag{1.2}$$

where J is an integer and I is the moment of inertia ($\sim 2 \times 10^{-46}\,\mathrm{kg\,m^2}$ for CO). The energy released when a molecule transitions from rotation J to $J-1$ is therefore

$$\Delta \mathrm{E}_{\mathrm{rot}} = [J(J+1) - J(J-1)]\frac{\hbar^2}{2I} = \frac{\hbar^2 J}{I}. \tag{1.3}$$

The frequency of an emitted photon in this transition is

$$\nu = \frac{\Delta \mathrm{E}_{\mathrm{rot}}}{h} = \frac{\hbar J}{2\pi I}, \tag{1.4}$$

which is ~115 GHz (~2.6 mm) for $J = 1-0$. The rotational lines of CO are relatively strong, and therefore inexpensive to observe (at least, in local galaxies). Assuming that CO and H_2 are well-mixed, an integrated CO intensity can therefore be transformed to an H_2 column density (or mass), via a "CO conversion factor," X_{CO} (for column density), or α_{CO} (for mass). These conversion factors are different for the various rotational transitions of CO, and the conversion factor can vary by orders of magnitude in different environments (Narayanan et al., 2012), so the true H_2 mass traced by this CO is uncertain. Sandstrom et al. (2013) found that for a sample of 26 nearby galaxies, the average α_{CO} was $3.1\mathrm{M}_\odot\mathrm{pc}^{-2}$, with variation both between and within galaxies. Importantly, α_{CO} appears to be correlated with metallicity – Schruba et al. (2012) find an increase of an order of magnitude in α_{CO} for low metallicity, dwarf galaxies.

With instruments such as Atacama Large Millimeter/submillimeter Array (ALMA), it is now becoming possible to perform surveys of nearby galaxies in CO at very high (arcsecond or less) resolution. One such effort is the recently completed Physics at High Angular resolution in Nearby GalaxieS (PHANGS) ALMA survey, which consists of 74 galaxies observed at arcsecond (~60-120 pc, depending on the distance to the galaxy) resolution, along with follow-up optical imaging from HST, and integral field spectroscopy from the Multi Unit Spectroscopic Explorer (MUSE) on the VLT, to trace ionized gas and stellar kinematics for a subset of those galaxies. Due to the cloud-scale nature of these observations, these data can be used to statistically study the molecular cloud properties for galaxies spanning a wide parameter space (Sun et al., 2018). Combining information about SFR, these data can also be used to study the scales at which star-formation relations break down, which gives us vital insights into the timescales of star formation, and the lifetimes of molecular clouds (e.g. Kreckel et al., 2018; Kruijssen et al., 2019). The mm-Wave Interferometric Survey of Dark Object Masses (WISDOM) team have also surveyed a number of nearby galaxies at sub-arcsecond resolution (e.g. Davis et al., 2017; Onishi et al., 2017; Davis et al., 2018; Smith et al., 2019), originally with the intention of measuring black hole masses but these data can also be used to study the molecular gas in a wide range of galaxy types, including ETGs, LTGs, and dwarfs. These investigations are currently ongoing (Liu et al., in prep.; Williams et al., in prep.). Given the small field of view of ALMA, surveys of this nature are extremely time-consuming, and so for a very large sample of galaxies it is necessary to use integrated galaxy measurements.

The CO Legacy Data base for the GASS survey (xCOLD GASS) (Saintonge et al., 2011, 2017) was a large program on the IRAM 30 m telescope, surveying the integrated molecular gas content of ∼500 nearby galaxies, probing the entire star-formation main sequence. Using this, it is possible to probe the molecular gas depletion timescale of galaxies (Tacconi et al., 2018), which gives insights into how quickly galaxies turn their gas into stars, and how it varies as a function of galaxy property. This work found the depletion timescale to vary systematically across the galaxy population, as a function of both redshift and the distance from the star formation main sequence. It is also possible to use this data along with other datasets to calibrate the CO conversion factor for a number of galaxies (Accurso et al., 2017), finding that the primary driver in the variation of α_{CO} galaxy-to-galaxy is the metallicity.

Whether the CO is, in fact, a good tracer of H_2 is a matter of debate. For instance, CO is easily photo-dissociated, and thus requires shielding to be present in galaxies. This is a problem in low-metallicity environments, where this shielding is not so readily available and so a sharp upturn in X_{CO} is seen (Bolatto et al., 2013, their Sect. 6). CO is also essentially almost always optically thick in observations – Kennicutt & Evans (2012) describe it as “akin to using the presence of a brick wall to estimate the depth of the building behind it.”However, although the CO is optically thick, by assuming the Larson (1981) relations hold in a cloud, and some average mass for each cloud, the CO intensity can be converted into an H_2 mass (see Bolatto et al., 2013, their Section 2). ^{13}CO and C^{18}O suffer less from optical depth issues, but these lines are weaker. The different rotational transitions of CO also trace different aspects of the molecular gas, with higher rotational transitions tracing denser, warmer gas. Thus, the low rotational transitions of CO do not only trace the dense molecular gas present in a galaxy. Due to the low excitation density of low-J CO lines, they also trace the bulk, diffuse molecular gas. To trace more exclusively dense molecular gas, we turn to lines from, e.g., HCN and HNC. Given that work has shown it may be this dense gas that truly is the fundamental unit of star-formation (e.g. Gao & Solomon, 2004a,b; André et al., 2010; Lada et al., 2010), the fact that we may be missing it with our measurements is alarming. However, if clouds have

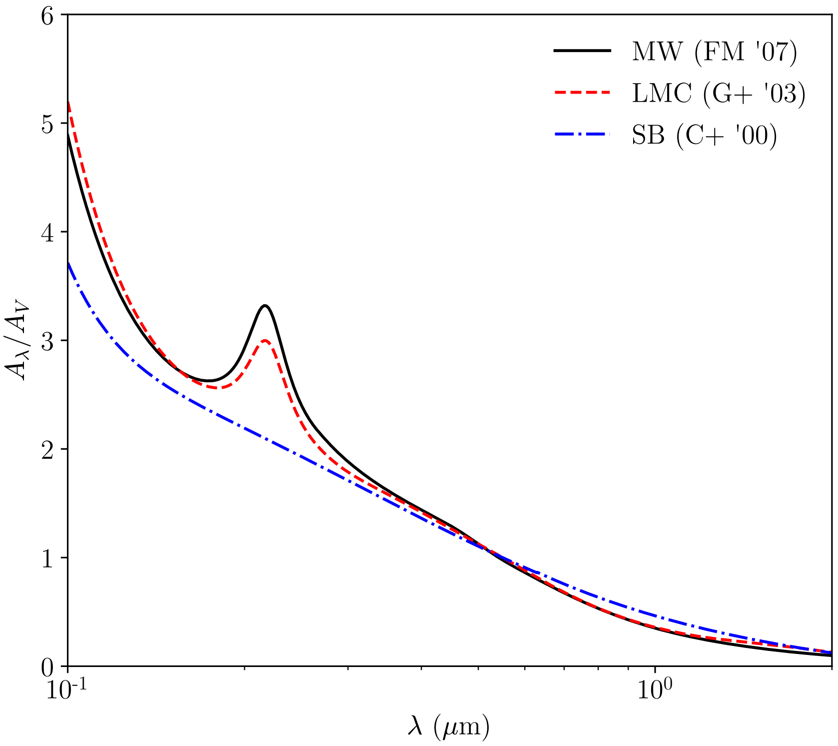

Figure 1.5: A selection of literature extinction curves. The black solid line is from the MW (Fitzpatrick & Massa, 2007), the red dashed line the average of the LMC (Gordon et al., 2003), and the blue dot-dashed line the starburst relationship of Calzetti et al. (2000).

similar density distribution functions, then the dense gas fraction is a constant – this would mean that CO would be just as good a tracer of the dense gas as, e.g. HCN. By correlating optical depth and total gas column density, Planck Collaboration et al. (2011) find a linear correlation at both low and high gas column density. However, at intermediate column densities the optical depth is in excess of this correlation. They have attributed this to a "CO-dark" gas phase, which may contribute ∼50% of the total molecular content, so a significant fraction of molecular gas may be missed by CO observations. Given this, it is important to develop independent measures of the gas content of a galaxy, both to calibrate the severity of these issues and as a vital sanity check to our measurements.

1.2.2 DUST

Typically, 1% by mass of the ISM is solid, and this is referred to as dust (formed of mainly carbonaceous and silicate grains). These solid particles range in size from 0.3nm to 0.3μm, and given that this dust seems to be well mixed with the gas (Knapp et al., 1973), this means that the dust can be used as an independent measure of the total gas column density (e.g. Hildebrand, 1983; Magdis et al., 2012; Eales et al., 2012). However, the calibration of the conversion factor between the dust and gas mass seems to vary dependent on the regional properties. A value for the gas-to-dust ratio (GDR) of 100 is appropriate for the MW (Bohlin et al., 1978). However, in low metallicity environments where dust grains may be destroyed as they are less well shielded from the harsh interstellar radiation field (ISRF), the GDR rises drastically, up to values of 500 (Rémy-Ruyer et al., 2014). This quantity can be simultaneously calibrated with $X_{\rm CO}$, given simultaneous HI, CO and dust measurements of an object. The work of Sandstrom et al. (2013) performed this for a sample of 26 nearby galaxies, finding an average GDR of 72.

In terms of optical astronomy, dust is generally considered to be a nuisance, getting in the way of measuring the intrinsic flux at shorter wavelengths. Dust absorbs, processes and re-emits around 30% of the stellar luminosity (e.g. Popescu & Tuffs, 2002; Viaene et al., 2016). The effect of this dust attenuation is dependent on the properties of the dust grains, as well as their geometrical distribution. Therefore, a two-pronged approach can be taken to studying this attenuation. If we have sufficiently high-resolution optical observations, by comparing the spectra of stars that are close to each other, where one is affected by dust attenuation and the other is attenuation free, a map of the amount of attenuation can be built up (Dalcanton et al., 2015; Gordon et al., 2016). At the other end of the wavelength range, by modelling the dust we can immediately get a handle on the dust grain properties, and therefore estimate how much attenuation we would expect in optical wavebands (Li & Draine, 2001; Jones et al., 2013; Whitworth et al., 2019). These approaches are independent, but highly complementary.

A selection of extinction curves for various galaxies are shown in Fig. 1.5, and show the variety from galaxy to galaxy. Generally, there are two main features to consider in the extinction curve – the first is an NUV 'bump' at 2170Å, which is generally attributed to absorption from graphite (Stecher & Donn, 1965), but could also be due to other small carbon grains such as amorphous carbon nano-particles (Jones, 2012; Galliano et al., 2018). The strength of this bump is variable, and appears to be mainly absent in starburst galaxies (Calzetti et al., 2000). There is then also an underlying polynomial, which can vary significantly in different environments (see, e.g. Salim et al. 2018). Due to the diversity in these curves, despite our best efforts the flux at these shorter wavelengths may still be significantly under- or over-estimated.

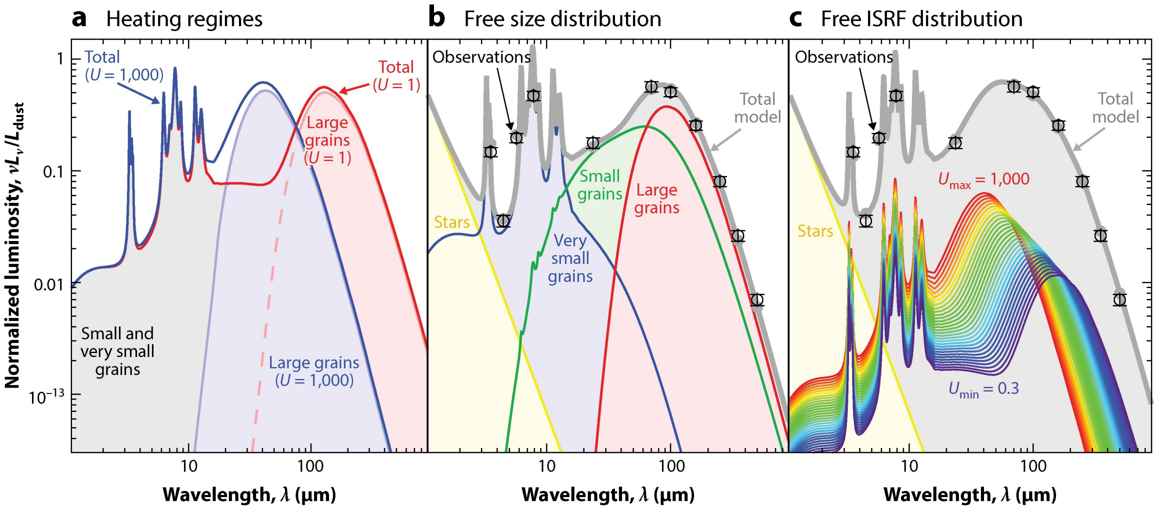

Figure 1.6: Options for dust SED modelling, using the THEMIS model (Jones et al., 2013). *Left:* varying heating regimes (i.e. cold and warm dust). In this case, the dust grain composition is kept constant, and is illuminated by ISRF intensities, U, of 1 (red line) and 1000 (blue line). *Middle:* varying mass fractions. In this case, U is kept constant (at 8), and mass fractions are allowed to vary: very small carbonaceous dust grains ($0.35 \leq r < 1.5\,$nm; blue), small carbonaceous grains ($1.5 \leq r < 20\,$nm; green), and large grains, which consist of both carbon and silicates ($0.02 \leq r < 0.3\,\mu$m; red). *Right:* Fitting using a parameterised ISRF distribution, such that $\mathrm{dM}_{\mathrm{dust}} \propto U^{-\alpha}$, such as in Dale et al. (2001). Figure from Galliano et al. (2018).

The observed emission from dust is complex, and strongly dependent both on the assumed geometry and mixing of the stars and dust, as well as the composition of the dust itself. In the MIR regime are features that are generally attributed to polycyclic aromatic hydrocarbons (PAHs, Leger & Puget, 1984; Allamandola et al., 1985). However, more recent work (Jones et al., 2013) has shown that some missing PAH features could be explained by partially hydrogenated amorphous hydrocarbons. These emission lines were first detected in Galactic nebulae by Gillett et al. (1973), but are present in many extragalactic objects (e.g. Galliano et al., 2008). However, the intensity of these emission lines varies drastically from galaxy to galaxy. For instance, it appears that the presence of an AGN can destroy the grains that emit these features (Smith et al., 2007), and metallicity has a large impact on PAH feature strength (O'Halloran et al., 2006), which they attribute to destruction via enhanced supernova activity.

Along with these emission features, the dust is also characterised by an underlying continuum, arising from the various components that it is comprised of. This continuum is generally modelled as a series of modified blackbodies. This combined model can then be scaled accordingly to matched observed flux measurements. Generally, the dust model is fixed to one- or two-components (corresponding to variations in the ISRF strength, or equivalently dust temperature), a series of modified blackbodies (e.g. da Cunha et al., 2008), more complex parameterised ISRF distributions (e.g. Dale et al., 2001), or intrinsically to the dust, by varying the dust grain properties (e.g. Chastenet et al., 2017).

The most simple model used for dust is that of a single-temperature modified blackbody. To derive this, we start from the general form of the radiative transfer equation (e.g. Chandrasekhar, 1960):

$$\boldsymbol{n} \cdot \nabla I_\nu\left(\boldsymbol{x}, \boldsymbol{n}\right) = -\kappa_\nu\left(\boldsymbol{x}\right)\rho(\boldsymbol{x}) I_\nu\left(\boldsymbol{x}, \boldsymbol{n}\right) + j_\nu\left(\boldsymbol{x}, \boldsymbol{n}\right), \tag{1.5}$$

where $I_\nu\left(\boldsymbol{x}, \boldsymbol{n}\right)$ is the specific intensity at location $\boldsymbol{x}$ in space, and $\boldsymbol{n}$ is the unit vector indicating the propagation direction of the radiation. $\kappa_\nu\left(\boldsymbol{x}\right)$ is the mass extinction coefficient, $\rho(\boldsymbol{x})$ the mass density and $j_\nu\left(\boldsymbol{x}, \boldsymbol{n}\right)$ indicates an emission coefficient (the new luminosity injected at $\boldsymbol{x}$ in direction $\boldsymbol{n}$). This equation can be simplified substantially – firstly by using the distance s along a path defined by $\boldsymbol{x}$ and $\boldsymbol{n}$, and secondly by defining an opacity, $\alpha_\nu(s) = \kappa_\nu(s)\rho(s)$. Given this, equation 1.5 becomes

$$\frac{\mathrm{d}I_\nu}{\mathrm{d}s}(s) = -\alpha_\nu(s) I_\nu(s) + j_\nu(s). \tag{1.6}$$

It is also useful to define an optical depth, τ_ν which is simply the integral of the opacity along a path, i.e. $\mathrm{d}\tau_\nu = \alpha_\nu(s)\mathrm{d}s$. We can also define a source term, $J_\nu(s) = j_\nu(s)/\alpha_\nu(s)$. Equation 1.6 then can be expressed

$$\frac{\mathrm{d}I_\nu}{\mathrm{d}\tau_\nu}(s) = -I_\nu(s) + J_\nu(s). \tag{1.7}$$

This equation has the general solution

$$I_\nu = I_\nu(0)\mathrm{e}^{-\tau_\nu} + \int_0^{\tau_\nu} \mathrm{e}^{-(\tau_\nu - \tau_\nu')} J_\nu(\tau_\nu')\mathrm{d}\tau_\nu'. \tag{1.8}$$

If we assume that J_ν has no dependence on the optical depth, then

$$I_\nu = J_\nu + \mathrm{e}^{-\tau_\nu}\left(I_\nu(0) - J_\nu\right). \tag{1.9}$$

The source function for a dust at temperature T is a blackbody $[B_\nu(T)]$, and with the condition that for $T = 0$, $I_\nu = 0$, then

$$I_\nu = \left(1 - e^{-\tau_\nu}\right) B_\nu(\mathrm{T}). \tag{1.10}$$

For the assumption that the dust is optically thin (an acceptable assumption at long wavelengths, Draine 2006; Casey 2012), $\tau_\nu \ll 1$ and so Equation 1.10 can be simplified to

$$I_\nu = \tau_\nu B_\nu(\mathrm{T}). \tag{1.11}$$

The optical depth can be given in terms of the dust grain cross-section (σ), absorption efficiency (Q_{abs}) and dust column density (n_{dust}):

$$\tau_\nu = \sigma Q_{\mathrm{abs}} n_{\mathrm{dust}}, \tag{1.12}$$

and so the dust luminosity can be calculated, by taking into account the cross sectional area (A_{dust}) and integrating over the solid angle:

$$L_\nu = 4\pi A_{\mathrm{dust}} \sigma Q_{\mathrm{abs}} n_{\mathrm{dust}} B_\nu(\mathrm{T}). \tag{1.13}$$

This can be trivially converted to an observable flux using the area of the sphere between the object and the observer. Using the Mie (1908) solution of Maxwell's equations, $Q_{\mathrm{abs}} \propto \nu^\beta$, and so the optical depth can be expressed as

$$\tau_\nu = \left(\frac{\nu}{\nu_0}\right)^\beta. \tag{1.14}$$

ν_0 here is the reference frequency where $\tau_\nu = 1$, and β modifies the blackbody to make the long wavelength Rayleigh-Jeans tail either steeper (higher β) or shallower (lower β). Rather than optical depth, extragalactic astronomers typically use a dust mass absorption coefficient:

$$\kappa_\nu = \kappa_0 \left(\frac{\nu}{\nu_0}\right)^\beta, \tag{1.15}$$

where κ_0 is the dust mass absorption coefficient at reference frequency ν_0, and so at long wavelengths the cold dust continuum emission can be well modelled as $S_\nu \propto \kappa_\nu B_\nu(\mathrm{T})$.

Much like α_{CO}, the value of κ_0 is uncertain and can vary by orders of magnitude depending on the dust composition assumed (see Clark et al., 2019, their Fig. 1). However, with the assumption that the amount of dust per metals in a galaxy is constant, κ_0 can be calculated within galaxies (James et al., 2002). This has now been performed for a number of galaxies on an integrated scale (Clark et al., 2016), and more recently on a resolved level (Clark et al., 2019). This latest work has shown both significant variation in κ_0 between galaxies, and also within a galaxy itself. Given that the uncertainty in κ_0 is similar to that of $\alpha_{\rm CO}$, it is clear that these quantities should be cross-calibrated simultaneously.

There are a multitude of options for fitting the dust continuum, and the complexity of the models should be driven by the breadth of data available, as well as the intended science to be probed. A variety of dust Spectral Energy Distributions (SEDs) are shown in Fig. 1.6. For instance, most of the dust mass is concentrated in the coldest components, so neglecting shorter wavelengths may be acceptable if this is the desired parameter. To simplify the number of parameters, generally PAH models are based on a fixed template (e.g. da Cunha et al., 2008), and then scaled accordingly, but these could also be set to vary if the study is investigating these small, stochastically heated dust grains. Ultimately, the number of free parameters is far greater than the number of available datapoints so some assumptions must be made – instruments such as the James Webb Space Telescope (JWST) will be able to probe NIR and MIR wavelengths, and the Space Infrared Telescope for Cosmology and Astrophysics (SPICA), or Origins Space Telescope (OST) will bolster the FIR wavelengths (if selected to fly by ESA/NASA). Whilst dust models are already reasonably complex, the complexity will only grow in the next decade with new facilities coming online.

Given that dust preferentially absorbs and re-emits UV light, it seems natural that the dust can be used as an SFR tracer. Monochromatic calibrations exist at these IR/sub-mm wavelengths (e.g. Rieke et al., 2009; Calzetti et al., 2010), as well as for the total infrared (TIR) luminosity (e.g. Hao et al., 2011; Murphy et al., 2011). Like all SFR tracers, however, using the dust continuum comes with caveats. Firstly, any starlight not absorbed by the dust will cause an underestimate of the true SFR (e.g. Hirashita et al., 2001). Given that we can observe galaxies in the optical, the assumption that all young stellar emission is absorbed by dust is clearly untrue. Secondly (and acting in the opposite direction), a significant amount of dust heating can come from more evolved stellar populations (e.g. Cortese et al., 2008; Bendo et al., 2015). In this case, the TIR luminosity will overestimate the true SFR. It seems that on integrated galaxy scales, these two effects tend to cancel each other out (at least in spiral galaxies), but in resolved observations these are important assumptions to consider.

The *Herschel* Space Observatory (Pilbratt et al., 2010) has been instrumental in transforming our view of dust in galaxies. Given that the instruments on-board primarily traced the cold dust content of a galaxy, galaxies that are much brighter in these wavebands are much easier to detect with *Herschel*. Thus, this instrument is extremely sensitive to Luminous Infrared Galaxies (LIRGs), which tend to be galaxies undergoing violent physical processes, such as AGN internally, or merger activities externally. These galaxies are also much more prevalent at high redshift, and so a survey like the *Herschel* ATLAS (Eales et al., 2010) covering some 500 deg^2 offers us a look at the dusty, high-redshift Universe.

DustPedia (Davies et al., 2017) is a database of ∼850 nearby galaxies covered by *Herschel*, but also with a rich ancillary dataset. The goals of this project include providing data for multi-wavelength SED fitting, which Nersesian et al. (2019) have used to study the fraction of dust heated by young stellar populations (to determine the applicability of infrared light as an SFR tracer). They found that much of the dust in spirals is heated by young stars, but the precise fraction is strongly dependent on morphology and specific star formation rate (SFR per unit stellar mass). The dust heating in elliptical galaxies, however, is generally dominated by the ambient stellar radiation field. This data is also being used to produce radiative transfer models for some of these galaxies (Nersesian et al., in prep.; Verstocken et al., in prep; Viaene et al., in prep.) to give further insights on the dust heating and dust geometry of a variety of galaxies.

1.3 RESOLVED OBSERVATIONS OF NEARBY GALAXIES

Extragalactic observations are inevitably hindered by the resolution of instruments combined with the large distances galaxies outside our MW are away from us. Historically, the studies of star-formation and the ISM have been limited mainly to integrated measurements of entire galaxies. Although this has brought us useful scaling relationships such as the Kennicutt-Schmidt law (see Chapter 2 for more details), these observations capture the variation inter-galactically, but not intra-galactically. As such, these integrated measurements are simply an average of the rich variation of the properties of an entire galaxy, and so the relationships seen on galaxy-wide scales may not hold into resolved measurements (e.g. Kruijssen & Longmore, 2014). This gives us an insight into the physics driving the “laws” we see on integrated galaxy scales.

Many galaxies exhibit a wide range of properties within them, so resolved observations also allow us to probe a wide range of fundamental parameters of galaxies, such as metallicity or SFR. They also allow us to localise the effects of processes happening within the galaxy, such as intense star formation within HII regions, the effects of supermassive black holes in the centre of a galaxy, and radio jets flowing out of a galaxy. High resolution studies also allow us to degrade this resolution, to study the effects of the measured spatial scale on any such process. Resolved measurements of galaxies also may give more accurate estimates of galaxy parameters. By smoothing to coarser resolutions, we average out the small-scale variation between regions, which can lead to underestimates of, e.g. dust masses (e.g. Smith et al., 2012; Tabatabaei et al., 2014; Chastenet et al., 2017; Utomo et al., 2019).

It is useful, then, to perform resolved studies of galaxies, and, given the resolution limits of telescopes, the best laboratories for us to do this is with the galaxies most nearby to us. The most nearby galaxies to us are the Large and Small Magellanic Clouds (the LMC and SMC), which are low metallicity, irregular dwarf galaxies, located at distances of 50 kpc for the LMC (Pietrzynski et al., 2019), and 62 kpc for the SMC (Graczyk et al., 2014). The three nearest massive spirals are the MW (which we reside in), M31 (at a distance of 780 kpc, McConnachie et al. 2005), both of which are reasonably evolved, solar metallicity spirals, and finally M33.

1.3.1 M33

The work in this thesis focuses on the nearby spiral galaxy M33, or the Triangulum galaxy (Fig. 1.7). This galaxy is the third largest spiral on the sky to us (behind M31 and our own MW) and is a distance of 840 kpc away (Madore & Freedman, 1991). It has a relatively low inclination of 56° (Regan & Vogel, 1994), which means that studies suffer less from deprojection degeneracies when compared to the 77° inclination of M31 (McConnachie et al., 2005). Compared to M31 and the MW, M33 is a smaller galaxy, with an optical extent of ∼7.4 kpc (Paturel et al., 2003). However, despite this, it has a higher SFR than M31 ($0.2-0.45\,\mathrm{M_\odot\,yr^{-1}}$, Verley et al. 2009), and is actively star-forming across its disc. As M33 has around ten times less gas than M31 ($\sim 5\times10^{8}\,\mathrm{M_\odot}$ versus $\sim 5\times10^{9}\,\mathrm{M_\odot}$), this means that it has a much higher star formation efficiency, and a correspondingly lower gas depletion timescale $1.6-3.2\times10^{8}\,\mathrm{yr}$ (Gardan et al., 2007), which is shorter than other local spirals ($1-3\,\mathrm{Gyr}$ Kennicutt 1998b; Murgia et al. 2002; Wong & Blitz 2002).

M33 has also a roughly half-solar metallicity ($12+\log(\mathrm{O/H})=8.36$), with

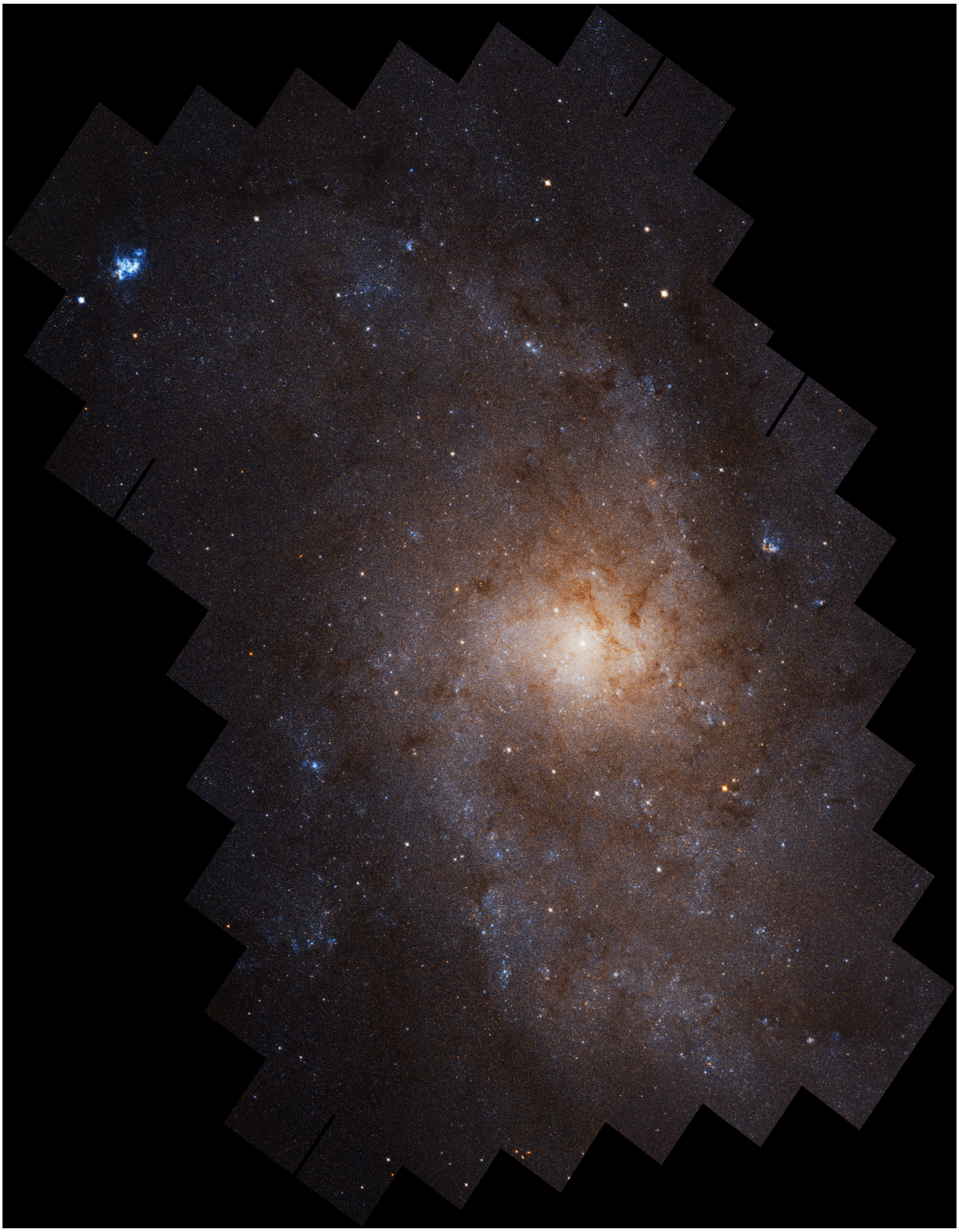

Figure 1.7: M33 as seen by the Hubble Space Telescope. Image credit: NASA, ESA, and J. Dalcanton (University of Washington)

little metallicity variation seen radially (Rosolowsky & Simon, 2008). This makes it more analogous to higher redshift (or younger) galaxies, and is also a "metallicity bridge" between the local spirals and the Large and Small Magellanic clouds; the MW has a metallicity of $12 + \log(\mathrm{O/H}) = 8.76$ (Nieva & Przybilla, 2012), M31 has $12 + \log(\mathrm{O/H})$ of $8.71 - 8.91$ (Zurita & Bresolin, 2012). The LMC and SMC have $12 + \log(\mathrm{O/H})$ of 8.49 and 8.09, respectively (Russell & Dopita, 1992). Unlike the LMC and SMC, M33 is relatively undisturbed – its rotation appears to be stable (Kam et al., 2015), and the disc is unperturbed, despite a potential tidal encounter with M31 (McConnachie et al., 2010; Wolfe et al., 2013), as these two galaxies are ~800 kpc away from each other.

M33 has also been observed to have strikingly different dust properties than M31 and the MW. Many works have found it has a "sub-mm excess," where the observed sub-mm flux is higher than dust models would predict (Hermelo et al., 2016; Relaño et al., 2018). This may be due to systematic errors in photometry – Kirkpatrick et al. (2013) find that using improved photometry on the same sample of galaxies with previously detected sub-millimetre excess alleviates some of this excess. However, this has been observed in many low-metallicity galaxies (e.g. Galametz et al., 2011), and the true nature of this excess emission remains a mystery.

Because of M33's proximity and its unique properties in the Local Group, high resolution observations are available across many wavelengths from a variety of observatories. This makes it an ideal target for multi-wavelength or panchromatic studies, which are the focus of this thesis.

1.3.2 High-Resolution Modelling

One of the most useful tools for studying a number of intrinsic properties of the galaxy is to model a Spectral Energy Distribution (SED), using data that captures both the starlight and dust continuum emission of a galaxy (this is the focus of Chapter 2). Fitting an SED can help constrain a number of properties (e.g. SFR, star formation history, metallicity, AGN fraction, stellar mass, dust mass), but given the large parameter space to explore (for which priors are generally not well known), this task is computationally expensive. A solution to this is to use a library of models, and tools exist that do this as efficiently as possible (e.g. Silva et al., 1998; da Cunha et al., 2008; Noll et al., 2009). These tools, however, are designed to fit the integrated SED of a galaxy, and so assume a dust energy balance – i.e. that all of the starlight absorbed by the dust in a galaxy is re-emitted, which is a reasonable assumption at integrated scales, but is not formally true at high resolution (Boquien et al., 2015; Smith & Hayward, 2018). Despite this, however, it is possible to modify

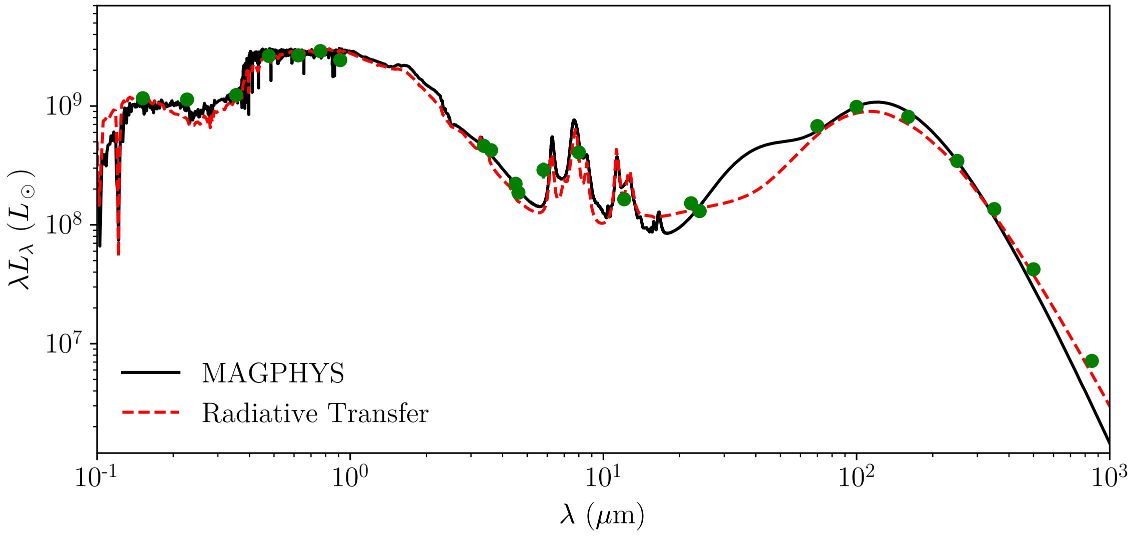

Figure 1.8: A comparison of traditional SED fitting using MAGPHYS (solid black line) to SKIRT radiative transfer (red dashed line) for the measured fluxes of M33. The small error bars here are dominated by the calibration uncertainty (see Table 2.1), and do not include any additional error added in quadrature during the fitting process.

these codes for use on high-resolution observations (e.g. Viaene et al., 2014). In this case, we break up the galaxy into a number of pixels for which we have broadband photometric observations in each pixel, and model each as a separate galaxy (for the purposes of the code). Thus, parameter maps can be built up from the output. Given the computationally expensive nature of fitting one SED, the prospect of fitting ∼10s of thousands of pixels represents a huge computational investment, and has only become possible recently with high-performance computing, along with heavy parallelisation. For meaningful fits, the data must also be degraded to the poorest resolution considered in the study. Some techniques (e.g. Juvela & Montillaud, 2013; Marsh et al., 2017) overcome this limitation, but generally we throw away a great deal of information in these kinds of studies.

Traditional SED fitting tools make a number of assumptions to simplify calculations, and one of these is how the dust and starlight is mixed. The two simplest cases are for when the dust is in front of the stars (i.e. a foreground screen), or when the dust is homogeneously mixed with the stars. These two different geometries predict very different amounts of attenuation (see Calzetti, 2001). The geometry can have a huge impact on the observed SED of a galaxy, but traditional SED modelling neglects the effects of geometry. For this, we must turn to 3D radiative transfer modelling, which take into account the 3D nature of the galaxy, and do not assume a per-pixel dust energy balance. A comparison of the integrated SEDs for M33 calculated from

MAGPHYS (an SED fitting code; da Cunha et al., 2008) and SKIRT (radiative transfer software; Baes et al., 2003) are shown in Fig. 1.8, and the differences between these two techniques are explored in more detail in Chapter 4. However, this radiative transfer is even more computationally expensive than traditional SED modelling, and tend to use highly optimized Monte Carlo techniques for efficiency, as well as adaptive grids, as the radiative transfer calculations are non-local and non-linear. Even with these optimizations, high-resolution radiative transfer simulations can take hundreds, or thousands of CPU hours, and so are only feasible on large, high-performance computing systems.

1.4 THESIS OUTLINE

This thesis presents three studies of the nearby spiral galaxy M33. I have brought together archival observations across 4 orders of magnitude in wavelength, as well as new sub-mm data from SCUBA-2 to study some resolved properties of this galaxy. This thesis is presented as follows:

- Chapter 2 presents a resolved study of the star-formation law, and how this varies with the resolution of the observations
- Chapter 3 presents a dust-selected molecular cloud catalogue of M33, characterising the dust properties of these clouds and linking to earlier CO and HI studies
- Chapter 4 presents the results of a panchromatic radiative transfer model of M33, investigating the origins of dust heating in this galaxy
- Finally, Chapter 5 summarises the main results of this thesis, as well as ongoing and potential future investigations.

Much of this work has been published in refereed journals – see Williams et al. (2018), Williams et al. (2019a), and Williams et al. (2019b).

CHAPTER 2

THE STAR FORMATION LAW IN M33

One thing I've learned. You can know anything. It's all there.
You just have to find it.

NEIL GAIMAN

This chapter presents an investigation of the star formation, or Kennicutt-Schmidt law, and its variation with the spatial resolution measured. This work is published in Williams et al. (2018).

2.1 INTRODUCTION

An understanding of the processes that govern star-formation within a galaxy is vital to understanding how galaxies form and evolve. Historically, studying these relationships has been limited to the scale of entire galaxies, although this has led to important relations, such as the star-formation law. This law relates the star-formation rate (SFR) of a galaxy to its gas content, describing how efficiently gas is transformed into stars, and thus constraining theoretical models of star-formation. Schmidt (1959) originally suggested a power-law scaling relation between the volume density of SFR to a volume density of gas, i.e.

$$\rho_{\rm SFR} \propto \rho_{\rm gas}^{n}, \tag{2.1}$$

and this original work by Schmidt (1959) observed a power-law index of $n = 2$ for the Milky Way (MW). The first extragalactic measurements of this star-formation law were that of Sanduleak (1969) and Hartwick (1971), who found a value of n to be 1.84 ± 0.14 in the SMC and 3.5 ± 0.12 in M31, respectively. However, since most observations of extragalactic objects can only average a surface density along a line-of-sight, more recent studies use a surface, rather than a volume density, i.e.

$$\Sigma_{\rm SFR} = A\Sigma_{\rm gas}^{N}, \tag{2.2}$$

where $\Sigma_{\rm SFR}$ and $\Sigma_{\rm gas}$ are the surface densities of SFR and gas, respectively. The current form of this law was studied for a series of ∼100 galaxies in the seminal work of Kennicutt (1998a), which found a very tight scaling relation, with $N \sim 1.4$; this "Kennicutt-Schmidt" or KS law appears to have a similar N (the so-called Schmidt, or KS index), over a wide range of redshift and environments (see, e.g. Kennicutt & Evans 2012 and references therein). Although this is, necessarily, an oversimplification of a series of complex processes, this indicates that the gas content of a galaxy is a major driver of star-formation, and star-formation is more efficient at higher gas densities. However, these lower resolution studies were unable to determine whether the molecular or total gas content of a galaxy is more strongly correlated with star-formation (e.g. Wong & Blitz 2002). It is also unclear from these works whether star-formation is governed by local processes within star-forming clouds (e.g. Krumholz & McKee 2005), or global processes such as cloud-cloud interactions (e.g. Wyse 1986).

One physical interpretation of this empirically derived law is that roughly constant fractions of the total gas present in molecular clouds convert into stars on their free-fall time (Elmegreen, 1994; Krumholz & Thompson, 2007). This interpretation produces a Schmidt index of 1.5. Another is that the SFR is dictated by the amount of dense molecular gas, with the star-formation law being linear given a constant dense gas fraction. In this case, the traditional superlinear star-formation law is simply an artifact of the variations in this dense gas fraction between the star-forming disc galaxies and starburst galaxies used in studies (Lada et al., 2012). For a series of nearby spiral galaxies, Bigiel et al. (2008) found $N \sim 1$ to be a suitable index at sub-kpc scales when considering H_2, traced by the ^{12}CO(J=1-0) line – this would indicate that the molecular gas is simply counting uniform populations of Giant Molecular Clouds (GMCs).

Dense (with number densities, $n > 10^4 \text{cm}^{-3}$) molecular gas is also a promising tracer of star-formation, as stars are believed to condense out of the dense gas in

GMCs (André et al., 2010; Lada et al., 2010). If this is the case, then we would expect the dense gas mass and SFR to be strongly and linearly correlated. A number of works comparing the far infrared (FIR) luminosity and proxies for this dense gas, such as HCN or HCO$^+$ have found this to be the case (e.g. Gao & Solomon 2004a,b; García-Burillo et al. 2012). These relationships appear to hold down to ∼kpc regions (Bigiel et al., 2015; Usero et al., 2015), and large programs are looking to extend these samples (Gao et al., 2017).

With the advent of higher resolution, multi-wavelength surveys of nearby galaxies, our understanding of this star-formation law has improved dramatically. It is now possible to resolve the star-formation law in a number of nearby galaxies; it has been suggested that the KS law would appear to break down on scales similar to that of a GMC (∼10-100pc; e.g. Onodera et al. 2010; Boquien et al. 2015; Khoperskov & Vasiliev 2017). For apertures targeted on CO and Hα peaks in M33, Schruba et al. (2010) find a breakdown at the star-formation law at scales of 300pc, although with increasing aperture size the correlation is restored, which they argue indicates variations between the evolutionary states of GMCs in a galaxy. We can also express the star-formation law in terms of various phases of the gas. Bigiel et al. (2008) claim that the molecular, rather than total gas better correlates with SFR. Work by Ford et al. (2013) suggests that a superlinear N is suitable for the total gas content of M31, whilst a sublinear star-formation law is applicable when considering only molecular gas. Finally, searches for systematic variation within galaxies has been carried out – Leroy et al. (2008) have found a radial dependence in N, with decreasing star-formation efficiency at larger galactocentric radius for a series of 23 nearby galaxies.

M33 is the third massive disc galaxy of our Local Group (behind the MW and M31), and is an excellent laboratory for high-resolution extragalactic studies. M33 is a late-type spiral galaxy located at a distance of 840kpc (Madore & Freedman, 1991), and is more face-on than M31 with a moderate inclination of 56° (Regan & Vogel, 1994). With a large optical extent (R_{25}) of 30.8 arcmin (∼7.4kpc, Paturel et al. 2003), M33 is ideally suited for detailed study. Despite being smaller and less massive than the MW, it has a much higher gas fraction (∼20% versus ∼10%, Tavakoli, 2012; Licquia & Newman, 2015; Roman-Duval et al., 2016), and is actively star-forming throughout its disc (Heyer et al., 2004). It has a high star-formation efficiency (Gardan et al., 2007), with a molecular gas depletion timescale of $1.6 - 3.2 \times 10^8\,$yr, shorter than other local spiral galaxies ($1 - 3\,$Gyr, Kennicutt 1998b; Murgia et al. 2002; Wong & Blitz 2002). It also has a roughly half-solar metallicity

($12 + \log(\mathrm{O/H}) = 8.36 \pm 0.04$, Rosolowsky & Simon 2008), with a shallow metallicity gradient, making it more analogous to younger or higher redshift galaxies than the MW or M31. Recent work has suggested that following a tidal encounter with M31 (McConnachie et al., 2010; Wolfe et al., 2013), the stripped gas now returning to the disc of M33 is fuelling star-formation (Putman et al., 2009). Despite this, the disc of M33 is relatively unperturbed. This is in contrast to the Magellanic Clouds, which are highly disturbed, irregular dwarf galaxies. It is, therefore, particularly noteworthy to study the interplay between the gas and star-formation of M33.

The choice of SFR tracer is critical, as they are sensitive to different timescales and stellar populations. For instance, Verley et al. (2007) found a SFR of $0.2\,\mathrm{M}_\odot/\mathrm{yr}$ in M33 when considering IR data from *Spitzer*, whilst Hα and UV gives a much higher SFR of $0.45 \pm 0.10\,\mathrm{M}_\odot/\mathrm{yr}$ (Verley et al., 2009). Similarly, the adopted tracer of gas and fitting method can have a large impact on the calculated N. For M33, Heyer et al. (2004) find a molecular Schmidt index, N of 1.36 ± 0.08, but Verley et al. (2010) find a range of indices ($1.0 < N < 2.6$), depending on the gas tracer and fitting method employed.

A fundamental assumption of the method used to trace SFR is that the emission arises either directly from young stars, or from their heating of the ISM. UV emission directly traces the unobscured star-formation from these young stars, and hence is a good tracer of this recent star-formation. However, UV is particularly sensitive to dust attenuation, and so in this work I combine this with 24μm emission to account for re-emission of this dust-absorbed light.

Another estimate of SFR is the total infrared (TIR) luminosity. This prescription assumes that the dust is heated entirely by young stars. This measure of SFR, however, will miss the starlight that is not absorbed by the dust (e.g. Hirashita et al. 2001), and therefore underestimate the SFR. Older stellar populations will also contribute to the heating of this dust, potentially causing an overestimate of the SFR (e.g. Cortese et al. 2008).

Finally, I use a third measure of the SFR – the spectral energy distribution (SED) fitting tool Multi-wavelength Analysis of Galaxy Physical Properties (MAGPHYS, da Cunha et al. 2008). This tool fits an SED from a library of models to a series of provided fluxes, and outputs the physical parameters of the fitted model. MAGPHYS allows for a bursty star-formation history, and variations in SFR down to 1Myr. This is particularly important at sub-kpc scales, where the assumption of stationary star-formation (i.e. that the star-formation rate is continuous over the timescales the tracer is sensitive to) may be inappropriate (Relaño & Kennicutt, 2009). It also includes an energy balance between the stellar and dust components of the SED, accounts for the filter response of a particular instrument, and performs a thorough Bayesian error analysis.

The gas present in the ISM of a galaxy is dominated by hydrogen, both in its atomic (HI) and molecular (H_2) phases. Whilst the HI can be measured directly, via the 21cm line, H_2 cannot be traced directly as it is has a low mass, and lacks a dipole moment. Hence, the next most abundant molecule, CO, is commonly used as a proxy, and is traced via its rotational transitions – in the case of this work, the CO(J=2-1) line.

Alternatively, the gas content of a galaxy can, theoretically, be traced by the cold dust continuum (e.g. Hildebrand 1983; Eales et al. 2012; Magdis et al. 2012). However, the resolution of these dust maps have usually been limited by the resolution of the *Herschel* (Pilbratt et al., 2010) Space Observatory. This is particularly true of objects with large angular extents, as ground-based instruments such as SCUBA-2 are poor at recovering large-scale structure due to atmospheric effects. I, along with Matthew Smith have developed a technique to combine higher resolution SCUBA-2 data with the larger spatial frequency data of other instruments (Williams et al. 2019a, i.e. Chapter 3; Smith et al. in prep), and I present an initial combination of those data for the first time in this work. Using this, we can sample the dust continuum from 100-850μm at a spatial scale of 100pc, a factor of ~1.4 better than previous panchromatic galaxy studies (Viaene et al., 2014). This allows us to probe the relationships between star-formation and constituents of the ISM at the scales of individual star-forming regions.

In this chapter, I present an overview of the data used to calculate the SFR, as well as the data processing techniques required to carry out a pixel-by-pixel study of the star-formation law (Section 2.2) as well as my methods of calculating SFR at these small scales, and comparisons between them (Section 2.3). I present an overview of our various methods of tracing the gas within M33 (Section 2.4). I then use this data to study the star-formation law (Section 2.5), before the discussion and main conclusions (Section 2.6).

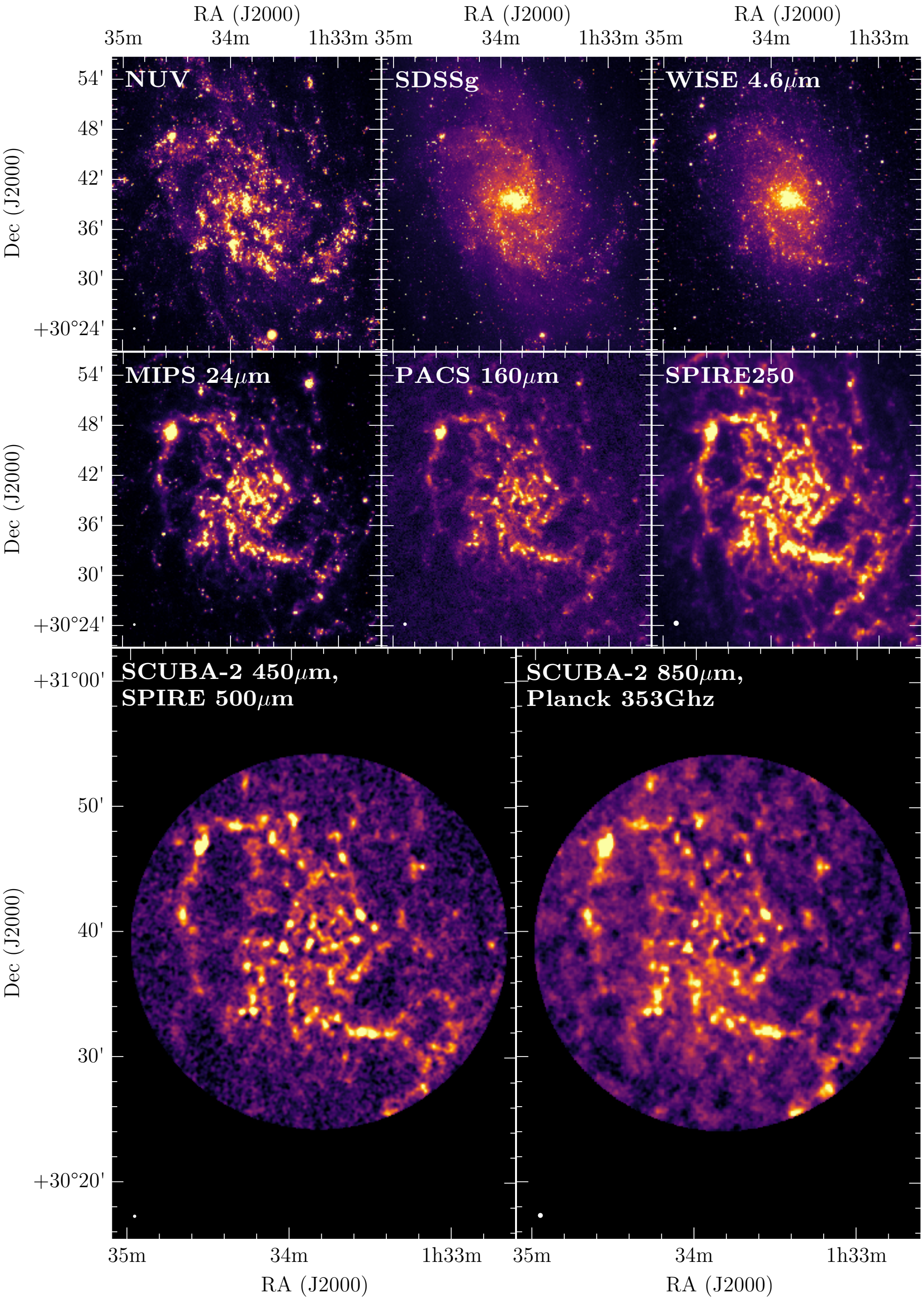

Figure 2.1: Examples of the data used to calculate SFR in this work. From top left: GALEX NUV (Lee et al., 2011) map, SDSS g band mosaic, WISE 4.6μm mosaic, MIPS 24μm (Dale et al., 2009) map, PACS 160μm and SPIRE 250μm (Kramer et al., 2010) data, and SCUBA-2 data – 450μm combined with SPIRE 500μm , and 850μm combined with Planck 353GHz data. The SCUBA-2 maps have both been convolved with a 6 arcsec Gaussian and cropped to circles of 15 arcmin radius, to aid visualisation. The beam for each frame is shown as a solid circle in the bottom left – in many cases, the beam is negligible compared to the image size.

2.2 DATA

In this section, I present an overview of the datasets used in order to probe the star-formation in M33. Particularly for MAGPHYS, it is important to sample the entire galaxy SED from UV to sub-millimetre (sub-mm), so as to provide meaningful constraints on its output parameters. Examples of the data used in this work are shown in Fig 2.1.

2.2.1 SUBMILLIMETRE AND IR DATA

Sub-mm data of M33 at 450 and 850μm was obtained with SCUBA-2 (Holland et al., 2013) on the James Clerk Maxwell Telescope (JCMT) between 2017-10-17 and 2017-11-21 under Program ID M17BP003. These 30 arcmin PONG maps were taken in band 1 weather (with 225 GHz opacity, $\tau_{225} < 0.05$). This data has a resolution of 8 arcsec at 450μm, and 14 arcsec at 850μm. I have also included earlier, public data taken between 2012-07-01 and 2012-07-12 under Program ID M12AC16, taken in marginal band 2/band 3 weather ($0.06 < \tau_{225} < 0.12$) and acquired from the CADC archive[1]. The final maps have an RMS noise level of 33mJy/beam (450μm) and 4mJy/beam (850μm). Due to variations in the sky over small scales at sub-mm wavelengths, the SCUBA-2 data reduction process applies a harsh filter to remove the sky. This means that SCUBA-2 is generally unreliable at recovering large-scale structure. To mitigate for this I have combined the high spatial frequencies of these data with low spatial frequencies from other telescopes, so as to increase the resolution without losing large-scale structure. For the 450μm data, I set a maximum filter scale of 120 arcsec in the data reduction pipeline. The large scale structure is recovered using data from the *Herschel* Spectral and Photometric Imaging Receiver (SPIRE, Griffin et al. 2010) instrument, at 500μm, adjusting the flux accordingly (multiplying the flux by a factor of 1.524, which assumes a fixed dust emissivity index, β, of 2). The combination of these maps was performed using the FEATHER task in the Common Astronomy Software Applications (CASA) package[2]. The SCUBA-2 850μm map was treated in much the same way, but instead using 353GHz Planck data, and using a maximum filter scale of 320 arcsec. The maps cover an area larger than 30 arcmin, but the radial dependence on the noise was found to cause artifacts in the feathering process. Hence, for these maps I only use the central 30 arcmin.

---

[1] `http://www.cadc-ccda.hia-iha.nrc-cnrc.gc.ca/en/`

[2] `https://casa.nrao.edu/`

Complementing this sub-mm data, I made use of the other two SPIRE bands, at 250 and 350μm, with a resolution of 18 and 25 arcsec respectively. This SPIRE dataset was obtained as part of the *Herschel* M33 extended survey (HerM33es, Kramer et al. 2010) open time key project. This project mapped the entirety of M33 with SPIRE, covering a total area of the sky of approximately 70arcmin × 70arcmin. This data was obtained from the Herschel Science Archive[3], utilising the Standard Product Generation (SPG) software v14.1.0. These maps have been calibrated for extended sources, and I include the small beam correction recommended in the SPIRE handbook[4]. The RMS noise levels of this SPIRE data are 14.1, 9.2, and 8mJy/beam at 250, 350 and 500μm, respectively.

The HerM33es project also mapped this same 70arcmin × 70arcmin at 100 and 160μm with the Photoconductor Array Camera and Spectrometer (PACS, Poglitsch et al. 2010). This data has a resolution of 7.7 and 12 arcsec respectively, with an RMS noise level of 2.6mJy pixel^{-1} (100μm) and 6.9 mJy pixel^{-1} (160μm). This data was processed using the SPG software v14.2.0, using the JSCANAM map-maker. Again, these maps are calibrated for extended sources.

My first source of near infrared (NIR) data is from the Wide-field Infrared Survey Explorer (WISE[5], Wright et al. 2010). These images have wavelengths of 3.4, 4.6, 12 and 22μm with FWHM of 6.1, 6.4, 6.5 and 12 arcsec respectively. I used MONTAGE[6] to mosaic together various frames from the AllWISE data release, incorporating both the WISE cryogenic and NEOWISE (Mainzer et al., 2011) post-cryogenic surveys. MONTAGE also matches background levels between each frame, so that overlaps between frames match as closely as possible. However, this is not a background subtraction, so to adequately model the sky, I created a 3deg^2 mosaic of M33 in each band, to ensure I had a sufficiently large amount of sky to model.

Additional IR data was obtained by the *Spitzer* Infrared Array Camera (IRAC, Fazio et al. 2004), as part of the Local Volume Legacy (LVL, Dale et al. 2009) Survey[7]. I used data from IRAC taken at 3.6, 4.5, 5.8 and 8μm. The resolution of these data are $\sim$ 2arcsec, and cover approximately 90arcmin × 60arcmin. Along with IRAC data, I also made use of the Multiband Imaging Photometer for *Spitzer* (MIPS, Rieke et al. 2004) data, taken again as part of the LVL. This data covers approximately 130arcmin × 80arcmin, and is at 24 and 70μm, with a resolution of 6 and 18 arcsec

---

[3] `http://archives.esac.esa.int/hsa/whsa`

[4] `http://herschel.esac.esa.int/Docs/SPIRE/spire_handbook.pdf`

[5] `http://irsa.ipac.caltech.edu/Missions/wise.html`

[6] `http://montage.ipac.caltech.edu`

[7] `http://irsa.ipac.caltech.edu/data/SPITZER/LVL/`

respectively. The overlap between several *Spitzer* and WISE bands improves sampling of the mid-infrared (MIR) SED, reducing the dependence of the fit on a single point.

2.2.2 UV AND OPTICAL DATA

The UV data used in this work comes from the *Galaxy Evolution Explorer* (GALEX, Martin et al. 2005), obtained by Thilker et al. (2005). Data was obtained for both the FUV (1516Å) and NUV (2267Å), covering a circular area of radius ∼36 arcmin. The angular resolution of this data is 4.2 arcsec and 5.3 arcsec for the FUV and NUV, respectively, and with ∼3ks exposures, typical 1σ RMS flux sensitivities are ∼28 AB mag arcsec^{-2}.

The optical data used in this study comes from the Sloan Digital Sky Survey (SDSS[8], York et al. 2000). Using only primary frames from the SDSS DR13 (Alam et al., 2015), a mosaic of 3deg^2 was created, allowing enough sky to accurately model the background. The SDSS data was mosaicked together using MONTAGE for all five bands – u (3543Å), g (4770Å), r (6231Å), i (7625Å), and z (9134Å).

2.2.3 DATA PREPARATION

Incorporating data from a variety of sources requires careful consideration so that meaningful comparisons can be drawn on a pixel-by-pixel basis. Hence, it was necessary to process the dataset, so as to make it homogeneous, and I give a description of that process here.

2.2.3.1 Background Subtraction

For each frame, I performed a background subtraction. Depending on the background, I employed a variety of methods to achieve this. Before this background subtraction process, I also converted all of the data into units of Jy/px, if it was required.

GALEX: The average background for the GALEX frame was found to be 0, with no clear gradient, so no background subtraction was applied.

SDSS: Due to the mosaicking process, the SDSS frames had a varying non-zero background. In order to remove this background, M33 was masked (using an ellipse

---

[8] `https://dr13.sdss.org/home`

of 80arcmin × 60arcmin) before fitting and subtracting a 2-dimensional polynomial. This reduced the background variation in the image to the order of a few percent, consistent with, e.g., Corbelli et al. (2014).

***Spitzer*, WISE, *Herschel*:** For the *Spitzer*, WISE and *Herschel* frames, the background was constant throughout the image, so in these frames a median background was subtracted using a 3σ clipped median after masking all sources with a signal-to-noise (S/N) > 2.

SCUBA-2: The SCUBA-2 data reduction process performs an iterative sky modelling and subtraction procedure (Chapin et al., 2013), so no further sky subtraction was performed.

Following background subtraction, I apply a Galactic extinction correction for frames with central wavelengths shorter than 4.6μm (the WISE-2 band). We use the method prescribed by Schlafly & Finkbeiner (2011) for the central position of M33, provided by the IRSA DUST[9] service. Due to the large angular extent of M33, the extinction correction can vary by a significant amount (14% in the FUV and NUV frames, for example). I included this variation in our uncertainty treatment (Section 2.2.4).

2.2.3.2 Star Masking

It was also necessary to mask any flux contamination from foreground stars, both around and in the line-of-sight of M33. I masked stars using a comparison of the UV fluxes, as described by Leroy et al. (2008). Using SExtractor (Bertin & Arnouts, 1996), I found the positions of all 5σ detections in the NUV. An optimal aperture size was then calculated for each of these detections using a similar method to Viaene et al. (2014), by calculating a radius for each detection where the flux at that radius dropped below two times the local background level. These apertures were then placed in the FUV maps and the flux within each calculated. Leroy et al. (2008) found that foreground stars have an NUV-to-FUV flux ratio of $\gtrsim 15 \pm 5$. Upon visual inspection, I found that a ratio 15 was insufficient to mask all foreground stars, and so opted instead for a value of 10. These stars were subsquently masked in all frames up to $\sim 20\mu$m, after which the foreground star emission was no longer an issue. Of the $\sim$6000 sources detected with SExtractor, around 200 were masked.

---

[9] `http://irsa.ipac.caltech.edu/applications/DUST/`

2.2.3.3 Convolution and Regridding

In order to make comparisons on a pixel-by-pixel basis, it was necessary to match the data to a common resolution and pixel scale. In order to do this, I made use of the convolution kernels[10] provided by Aniano et al. (2011) in order to achieve a common resolution. In this case, I match everything to the PSF of the SPIRE 350μm data, which has a FWHM of 25 arcsec. I regridded all of the data to a common pixel scale of 25 arcsec (corresponding to a spatial scale of 100pc), which ensured that I could safely assume each pixel to be statistically independent. For an ellipse of 60arcmin × 70arcmin, this corresponded to 19004 pixels.

2.2.4 UNCERTAINTIES

Table 2.1: Calibration uncertainty for each pixel.

Telescope	Calibration Uncertainty	Reference
GALEX FUV	5%	1
GALEX NUV	3%	1
SDSS u	2%	2
SDSS g,r,i,z	1%	2
IRAC-1	10%	3
IRAC-2	10%	3
IRAC-3	15%	3
IRAC-4	15%	3
MIPS 24μm	4%	4
MIPS 70μm	5%	5
WISE W1	2.4%	6
WISE W2	2.8%	6
WISE W3	4.5%	6
WISE W4	5.7%	6
PACS	5%	7
SPIRE	5.5%	8
SCUBA-2 450μm	12%	9
SCUBA-2 850μm	8%	9
Planck 353GHz	3%	10

References: 1) Morrissey et al. (2007); 2) Padmanabhan et al. (2008); 3) Dale et al. (2009); 4) Engelbracht et al. (2007); 5) Gordon et al. (2007); 6) Jarrett et al. (2011) 7) PACS Handbook[11]; 8) SPIRE Handbook; 9) Dempsey et al. (2013); 10) Planck Collaboration et al. (2014b)

---

[10] `http://www.astro.princeton.edu/~ganiano/Kernels.html`

[11] `http://herschel.esac.esa.int/Docs/PACS/pdf/pacs_om.pdf`

There were a number of uncertainties to take into account for each pixel. In areas of high S/N, the calibration error (σ_{cal}) of the instrument dominates. I considered these calibration errors, which are summarised in Table 2.1. In the case of the SCUBA-2 maps combined with other, lower resolution maps, I take the calibration error as the sum of the two relevant uncertainties in quadrature. I also included uncertainties from the varying Galactic extinction correction (σ_{ext}) due to the large angular extent of M33. The GALEX data is most affected by this, with a scatter of 14%. I also considered the background variation (σ_{bg}) in each frame. For this, I took the standard deviation of the background, having masked any sources greater than 2σ. In the case of the SDSS frames, this error also incorporated any remaining large-scale residuals due to the mosaicking process. Finally, for the GALEX and SDSS frames an uncertainty arose from the small numbers of photons incident at these wavelengths (σ_{poiss}). These errors are Poissonian. To estimate these errors, the flux was converted back into a count number and the square root of this count converted into a flux to give an error. The total uncertainty for each pixel was given by

$$\sigma_{\text{total}} = \sqrt{\sigma_{\text{cal}}^2 + \sigma_{\text{bg}}^2 + \sigma_{\text{ext}}^2 + \sigma_{\text{poiss}}^2} \tag{2.3}$$

2.3 CALCULATING SFR

Different tracers of SFR are subject to different systematic effects, such as dust attenuation and the impact of older stellar populations. To ensure that our pixel-by-pixel SFR measurements are robust, I have compared three different SFR calibrations.

2.3.1 TOTAL INFRARED LUMINOSITY

I first calculated the SFR from the integrated TIR luminosity. TIR luminosity effectively captures the bolometric luminosity of the dust-obscured stellar population, and so traces the starlight absorbed by the dust in a galaxy. Two important assumptions for TIR luminosity tracing the total SFR of a galaxy are that all of the emission from the young stellar population is absorbed by dust, and that the dust heating is exclusively from these young stars. Both of these assumptions are oversimplifications for galaxies (see, e.g. Hirashita et al. 2001; Cortese et al. 2008), and whilst on the scale of integrated galaxies appear to balance each other out (e.g. Kewley et al. 2002), on a pixel-by-pixel basis these assumptions may not hold true. However, the

TIR SFR is a useful diagnostic, and informs us both about the stellar population of a galaxy, as well as its dust content. In this work, I have used the calibration given by Kennicutt & Evans (2012), using values from Hao et al. (2011) and Murphy et al. (2011), integrating the greybody fit from 3-1100μm:

$$\log_{10}(\mathrm{SFR}_{\mathrm{TIR}}) = \log_{10}(L_{\mathrm{TIR}}) - 43.41, \tag{2.4}$$

where L_{TIR} is in ergs s^{-1}. This assumes the default IMF of Starburst99 (Leitherer et al., 1999), the broken Kroupa (2001) power law with a maximum mass of 120 M$_\odot$, and a time-scale of ~100 Myr. Including an error of 30% to estimate an uncertainty in the IMF and amount of dust attenuation, I found a TIR SFR of 0.17 ± 0.06 M$_\odot$/yr.

2.3.2 FUV+24μM

The TIR SFR misses the unattenuated component of the SFR, which can vary dramatically in different environments. Particularly significantly for M33, the unattenuated component can be a major proportion of the total SFR in low metallicity environments (e.g. Hirashita et al. 2001). One effective method of overcoming this is to combine IR measurements tracing obscured star-formation with UV emission that measures the unattenuated star-formation. In this work, I have elected to combine the GALEX FUV and MIPS 24μm data. FUV emission traces unobscured star formation over a timescale of ~10-100 Myr (e.g. Kennicutt 1998a; Calzetti et al. 2005), whilst the 24μm emission traces emission from small dust grains heated by starlight over a timescale of ~10 Myr (e.g. Calzetti et al. 2005, 2007), although this wavelength can also have a non-negligible contribution from evolved stellar populations or AGN (Calzetti et al., 2010). I use the SFR density prescription of Leroy et al. (2008):

$$\Sigma_{\mathrm{SFR}} = 8.1 \times 10^{-2} I_{\mathrm{FUV}} + 3.2^{+1.2}_{-0.7} \times 10^{-3} I_{24} \tag{2.5}$$

where Σ_{SFR} is in units of M$_\odot$ kpc^{-2} yr^{-1}, I_{FUV} and I_{24} are intensities in units of MJy/sr. Again, this assumes the default Starburst99 settings, and is sensitive over a timescale of ~20 Myr. Some of the emission at these wavelengths may be due to an older stellar population (e.g. Kennicutt et al. 2009), indicated by a correlation between these bands and the 3.6μm data. To correct for this, I remove this contribution using

$$I_{\mathrm{FUV,\,corr}} = I_{\mathrm{FUV}} - \alpha_{\mathrm{FUV}} I_{3.6}, \tag{2.6}$$

$$I_{24,\,\mathrm{corr}} = I_{24} - \alpha_{24} I_{3.6}, \tag{2.7}$$

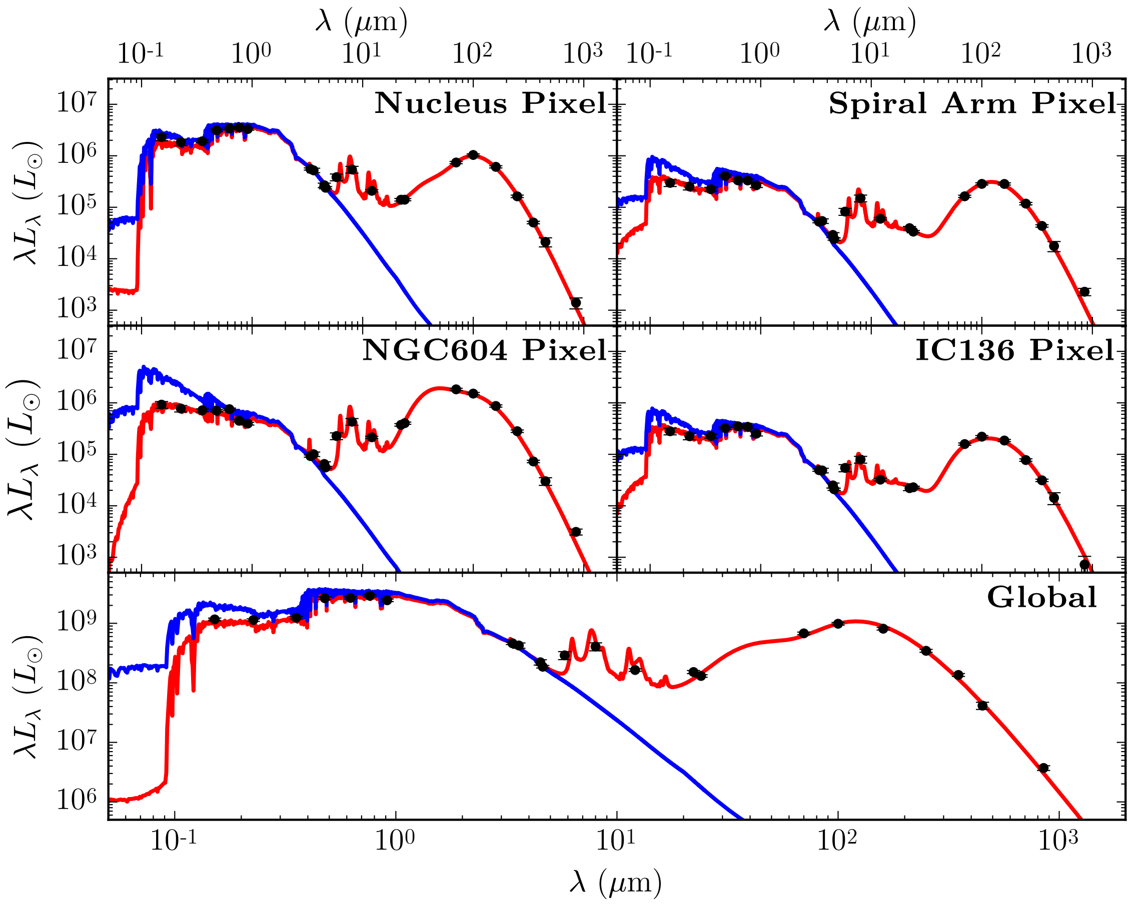

Figure 2.2: Example MAGPHYS SEDs for single pixels. The blue line represents the unattenuated SED, the red line the best fit to the data (i.e. the dust attenuated SED). From left to right, there is a pixel from within the nucleus (R $<$ 0.5kpc) of M33 ($\chi^2_\nu = 1.247$), a pixel from the northern spiral arm ($\chi^2_\nu = 2.007$), a pixel from within NGC604 (an HII region; $\chi^2_\nu = 3.554$) and a pixel from within IC136 (a stellar association; $\chi^2_\nu = 1.789$). The lowermost panel shows the global SED of M33 ($\chi^2_\nu = 2.328$).

where $\alpha_{\rm FUV} = 3 \times 10^{-3}$ and $\alpha_{24} = 0.1$ (Leroy et al., 2008). This correction has the effect of reducing the total SFR by 0.01M$_\odot$/yr. Using this method, I find a total SFR of $0.25^{+0.10}_{-0.07}$ M$_\odot$/yr, somewhat higher, but still consistent with the TIR SFR.

2.3.3 MAGPHYS

Finally, I calculate the SFR using MAGPHYS. MAGPHYS fits an SED from a large library of optical and IR models with known, physically motivated input parameters. It finds the best fit to the data in each case, and outputs the physical parameters of these fits, as well as modelling uncertainties upon them. For the optical models, MAGPHYS assumes a Chabrier (2003) initial mass function (IMF), which it evolves using the Bruzual & Charlot (2003) stellar population synthesis (SPS) model, and has a star-formation history (SFH) resolution of 1 Myr. Dust obscuration is calculated using the model of Charlot & Fall (2000). The total MAGPHYS SFR as calculated from the integrated flux across the galaxy is $0.33^{+0.05}_{-0.06} M_\odot$/yr. These uncertainties only take into account uncertainties on the flux, so are likely an underestimate of the true error. This value for SFR is consistent with work by Verley et al. (2009), but higher than both the total SFR calculated using FUV+24μm and from TIR luminosity. The MAGPHYS SFR averaged over 100 Myr is $\sim$0.12 $M_\odot$/yr, similar to the TIR SFR. However, whilst MAGPHYS has a parameter space suitable for integrated galaxies, a single pixel in M33 is far outside this space in terms of flux. I artificially increased each flux by a factor of 10^4 to put it within MAGPHYS parameter space. Most quantities from MAGPHYS tend to be ratios and so are not affected by this scaling – the four that scale with flux do so linearly, and are the SFR, dust mass ($\mathrm{M_{dust}}$), stellar mass ($\mathrm{M_{star}}$) and dust luminosity (L_{dust}).

One important feature of MAGPHYS is that it enforces an energy balance, where all attenuated light is re-emitted by the dust. Whilst this may hold true for a whole galaxy, the light from neighbouring regions may have an impact on the pixel in question in these sub-kpc regions. If this is the case, there may be an offset between the values calculated on a per-pixel basis, and those on a global scale. To test this, I also calculated the SFR from the sum of the individual pixels, giving us a value of $0.33 \pm 0.10\,\mathrm{M_\odot}$/yr. This indicates that MAGPHYS is suitable for pixel-by-pixel fitting, despite its original intent for galaxy-scale SED fits.

A benefit of using MAGPHYS is that the entire range of data can be used, regardless of the errors on each individual point. The fitted parameters can then be filtered a posteriori, based on how well constrained they are. MAGPHYS gives a probability distribution function (PDF) for each parameter, and the width of this PDF indicates how well constrained each parameter is. MAGPHYS provides in its outputs the 2.5th, 16th, 50th, 84th, and 97.5th percentiles for each parameter, I calculated a relative uncertainty for each pixel – any pixels which did not satisfy

$$0.5 \times \frac{p_{86} - p_{16}}{p_{50}} < 0.32 \tag{2.8}$$

where p_x is the xth percentile, were removed. This method of pixel filtering has previously been employed by Viaene et al. (2014), who found it a sufficient cut to remove any broad or bimodal (i.e. poorly constrained) PDFs. I have used this method

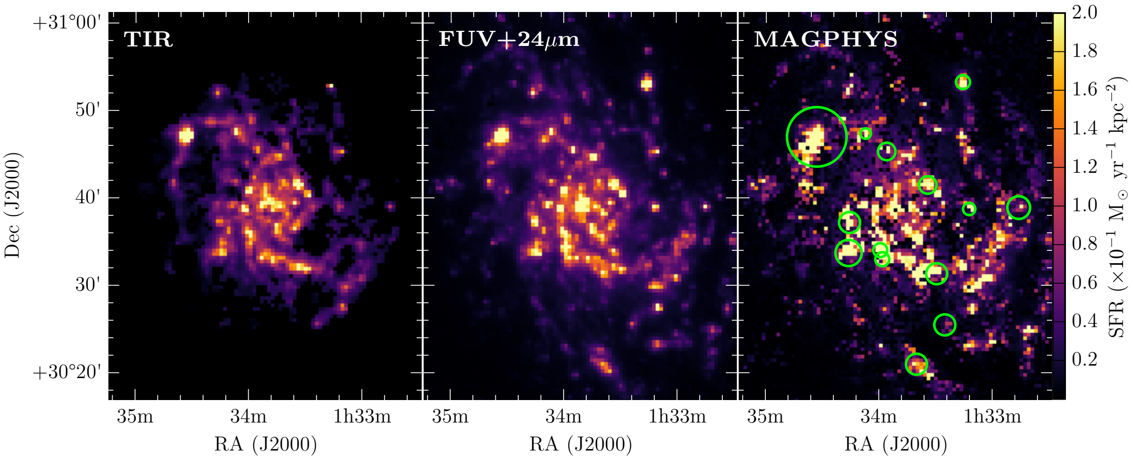

Figure 2.3: From left to right, SFR density maps from TIR luminosity found by integrating modified blackbody fits from 3-1100μm, SFR from a combination of FUV+24μm data, and median-likelihood estimates of SFR from MAGPHYS. Particularly bright pixels in the MAGPHYS map are due to recent starbursts, producing an SFR ~10 times higher than the average pixel value, and tend to be associated with HII regions and stellar clusters (a selection of which are shown as green circles). All maps have pixel sizes of 25 arcsec.

Table 2.2: Comparisons between the three SFR tracers. For the TIR and FUV+24μm maps, only pixels with S/N>5σ have been considered. In the case of MAGPHYS, the well-constrained pixels are used (see text). Given are the RMS scatter of the points (σ) and the median offset from the 1-1 relation [Δlog (SFR)].

	$\mathrm{SFR}_{\mathrm{FUV+24}\mu\mathrm{m}}$		$\mathrm{SFR}_{\mathrm{TIR}}$	
	σ	$\Delta\log(\mathrm{SFR})$	σ	$\Delta\log(\mathrm{SFR})$
$\mathrm{SFR}_{\mathrm{TIR}}$	0.16	-0.05	-	-
$\mathrm{SFR}_{\mathrm{MAGPHYS}}$	0.25	0.04	0.34	0.08

of filtering pixels in the proceeding analysis, rather than a more traditional S/N cut on the map, leaving us with 6,574 pixels (~35%). In this work, rather than using the SFR for the best fit model, we used the median-likelihood estimate given by the PDF. On the filtered pixels, however, the median offset is consistent with zero, with a median absolute deviation of <0.01 dex. I also find that a small number of these fits (~2%) are in areas of the parameter space with very few models, and so the error on this SFR will be zero. These pixels are masked in later fitting, so will not affect results. Some example SEDs, as well as the global SED can be seen in Fig. 2.2.

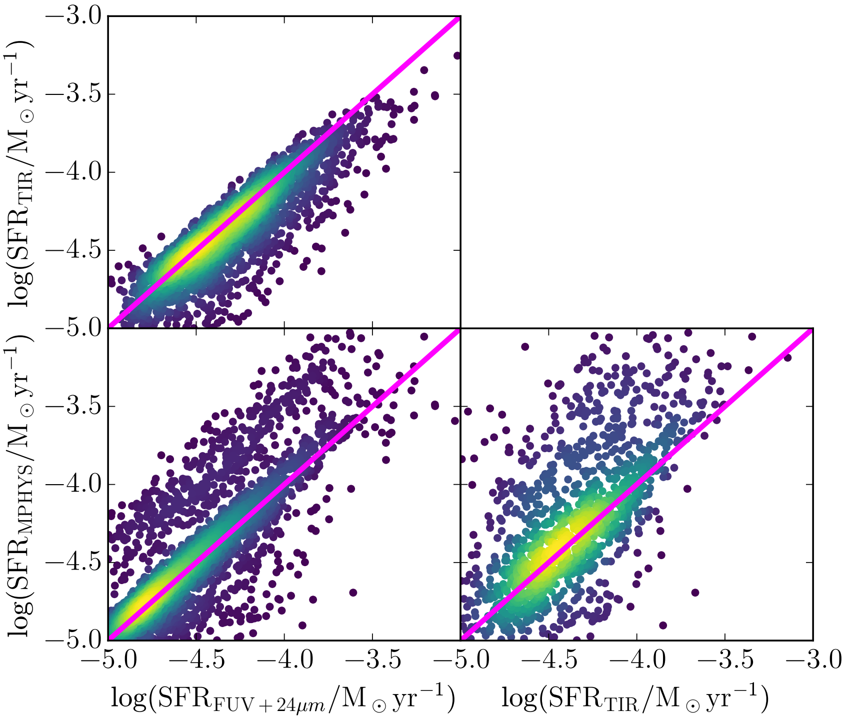

Figure 2.4: Comparisons for single pixel fits between *left,top*: SFR as calculated by the TIR luminosity and by FUV+24μm data. *Left, bottom*: SFR as outputted from MAGPHYS and as calculated by a combination of FUV and 24μm data. *Right, bottom*: SFR parameter from MAGPHYS and calculated from the TIR luminosity. The one-to-one relation is shown as a fuchsia line. Blue points indicate a lower point density, yellow a higher point density.

2.3.4 SFR COMPARISONS

I find that the lowest SFR calculated is from the TIR luminosity, at $0.17 \pm 0.06\,\mathrm{M_\odot/yr}$. Including the unattenuated component of the starlight increases the SFR to $0.25^{+0.10}_{-0.07}\,\mathrm{M_\odot/yr}$ using FUV+24μm , and even higher from MAGPHYS ($0.33^{+0.05}_{-0.06}\,\mathrm{M_\odot/yr}$). This lack of dust attenuation is highlighted in Fig. 2.2 – the stellar component dominates over the dust, as highlighted by the small offset between the unattenuated and attenuated lines, especially within the nucleus. That this unattenuated component accounts for ~50% of the SFR highlights the importance of the inclusion of the unattenuated component, particularly in low-metallicity or dust-poor galaxies.

As well as a global SFR, I have also calculated the SFR on a per-pixel basis, and these maps can be seen in Fig. 2.3, with a comparison of these three tracers of SFR in Fig 2.4. In the cases of the TIR and FUV+24μm SFR map, I compare only the pixels with $\mathrm{S/N} > 5\sigma$. The three broadly agree – the RMS scatter (σ) and median offset from the 1-1 relation [$\Delta\log(\mathrm{SFR})$] is summarised in Table 2.2. However, there is a population of pixels with higher SFRs given by MAGPHYS than the other two tracers, and this is reflected in a much higher scatter. In the cases where the MAGPHYS SFR is significantly higher, this is due to MAGPHYS injecting a recent starburst. Both the SFR from TIR luminosity and FUV+24μm assume stationary star-formation over the timescales that they trace. Taking instead the MAGPHYS SFR averaged over 100 Myr, the SFR tends to lower in these regions, and improve the agreement between the three tracers. This would indicate that MAGPHYS is indeed sensitive to these shorter star-formation timescales. At sub-kpc resolutions, star-formation may vary over timescales of a few Myr (Boselli et al., 2009). I find that these areas of bursty star-formation tend to be associated with HII regions and stellar associations (a sample of which are shown in the rightmost panel of Fig 2.3). As the spectra of HII regions strongly resemble those of starburst galaxies (e.g. Ho et al. 1997), it is not surprising that MAGPHYS has treated them as such. Additionally, UV and FUV spectroscopy has shown that at least 2 populations of stars exist within the nucleus of M33, and that star-formation occurred within the nucleus ~40Myr ago (Long et al., 2002), so this injected starburst within the nucleus of M33 is plausible. Overall, these tracers of SFR show very similar characteristics on a pixel-by-pixel level, but as MAGPHYS uses all available data, provides an energy balance, and can take into account recent bursts of star-formation, I elect to use this tracer going forwards.

2.4 GAS

2.4.1 ATOMIC GAS

For studying the atomic hydrogen, archival VLA[12] B, C, and D array data for the 21cm line was reduced by Gratier et al. (2010). The data used was an integrated intensity map in units of K km/s, with a spatial resolution of 12 arcsec (~50pc at the distance of M33). The original data cube has a spectral resolution of 1.27 km/s. This data can be seen in the left panel of Fig 2.5. From the HI 21cm line a density could be immediately calculated, using the equation presented in Rohlfs & Wilson (1996):

$$\Sigma_{\mathrm{HI}} = 1.8 \times 10^{18} \mathrm{cm}^{-2} / (\mathrm{K\ km/s}). \tag{2.9}$$

The mass of atomic gas as traced by HI is found to be $5 \times 10^8\ \mathrm{M}_\odot$, including a factor of 1.36 for He.

---

[12] `https://science.nrao.edu/facilities/vla/archive/index`

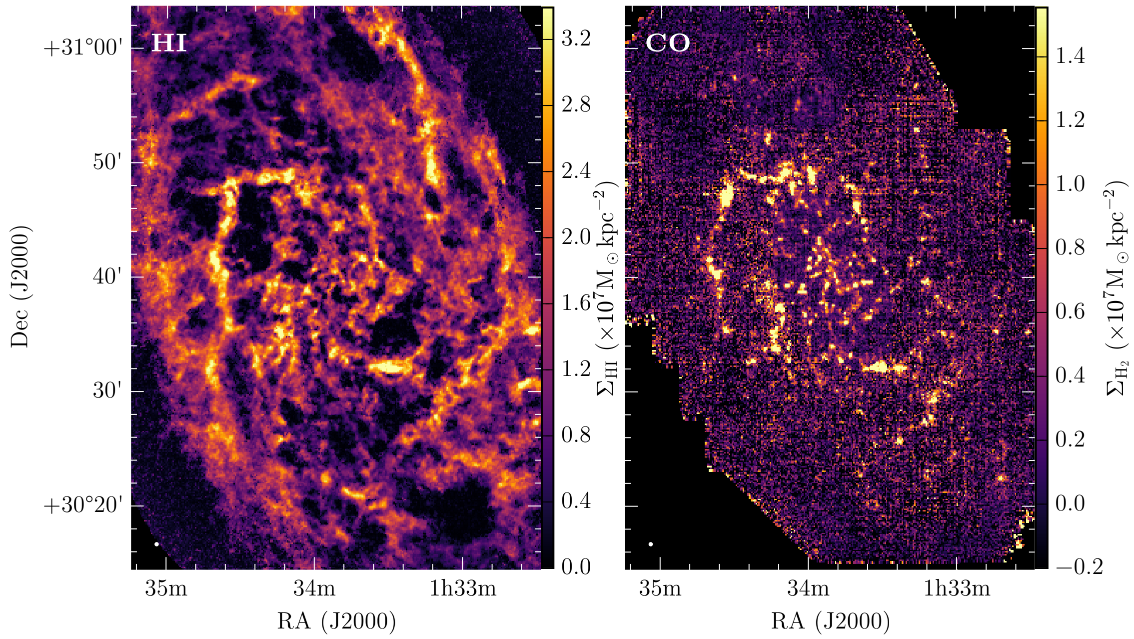

Figure 2.5: *Left*: Atomic gas mass surface density calculated from integrated HI emission (Gratier et al., 2010). *Right*: Molecular gas mass surface density calculated from integrated CO(J=2-1) emission (Gratier et al., 2010; Druard et al., 2014). The beam is indicated as a white circle in the lower left.

2.4.2 MOLECULAR GAS

CO is traced using the CO(J=2-1) rotational line data taken as part of IRAM's M33 Survey Large Program[13] (Gratier et al., 2010; Druard et al., 2014), which traces the molecular gas out to a radius of 7kpc using IRAM's Heterodyne arRAy (HERA, Schuster et al. 2004) instrument. This data has an angular resolution of 12 arcsec and a spectral resolution of 2.6km/s. The integrated intensity map can be seen in the right panel of Fig 2.5. I use this to trace molecular hydrogen within M33, rather that the earlier CO(J=1-0) map (Rosolowsky et al., 2007), as this map only traces the CO out to a radius of 5.5kpc, and is less sensitive (σ_{RMS}=60 mK for the (1-0) map, versus σ_{RMS}=20 mK for the (2-1) data).

A conversion factor must be used to convert the CO intensity to a number density of H_2 (X_{CO}), and this value is uncertain. Historically, a value of approximately $2 \times 10^{20}\,\mathrm{cm}^{-2}$ (Solomon et al., 1987; Strong & Mattox, 1996; Smith et al., 2012) has commonly been used for the CO(J=1-0) line, as calculated for the Milky Way, but a more comprehensive study by Sandstrom et al. (2013) found an average value of $1.42 \times 10^{20}\,\mathrm{cm}^{-2}$ for a sample of 26 nearby galaxies. This conversion depends on a

---

[13] `http://www.iram.fr/ILPA/LP006/`

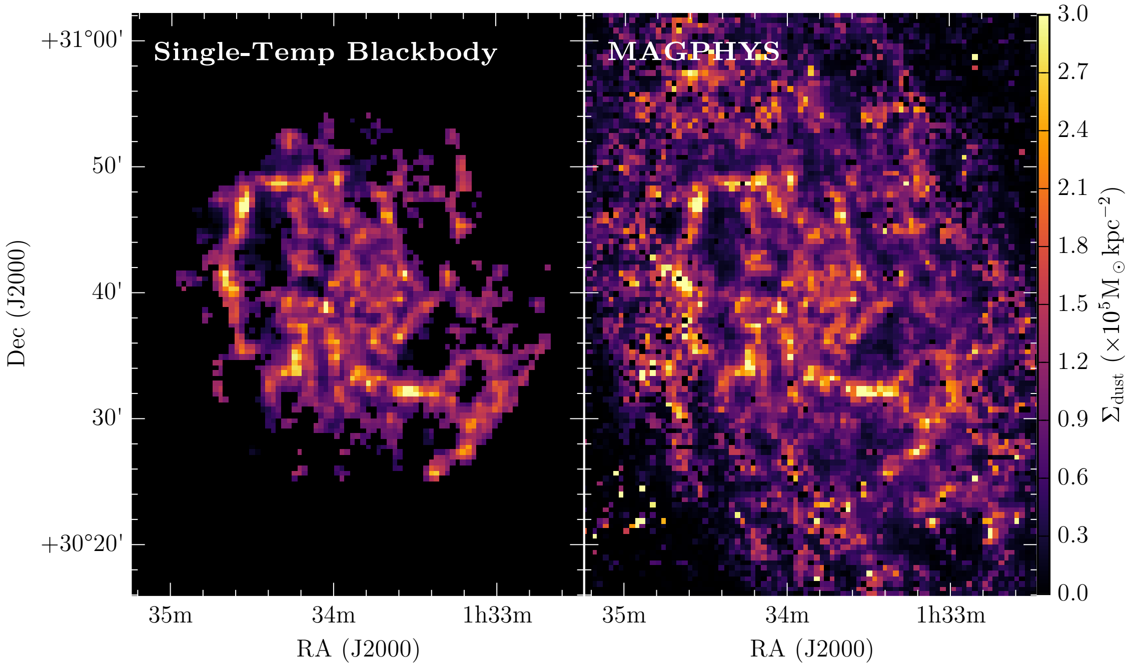

Figure 2.6: *Left*: Dust mass surface density from one-temperature greybody fit. *Right*: Dust mass surface density from MAGPHYS.

variety of factors, including the metallicity of the galaxy in question, and can vary across a galaxy. Narayanan et al. (2012) has shown that depending on the choice of $X_{\rm CO}$, the Schmidt index can vary by ±0.2 and so the accurate treatment of this conversion factor is imperative. In this case, I used the values calculated by Braine et al. (2010) for M33. This work found two distinct populations: one within the central 2kpc of the galaxy ($X_{\rm CO} = 1.54 \times 10^{20}\,{\rm cm}^{-2}$) and one outside this radius ($X_{\rm CO} = 2.87 \times 10^{20}\,{\rm cm}^{-2}$). These values are for the CO(J=1-0) line, so I turn these into conversion factors for the J=2-1 line using the commonly employed ratio of CO $\left(\frac{2-1}{1-0}\right) = 0.7$ (e.g. Eckart et al. 1990; Bigiel et al. 2008). Including a factor of 1.36 for He, the total molecular gas mass was calculated to be $4.5 \times 10^7\,{\rm M}_\odot$, an order of magnitude lower than the HI mass.

2.4.3 Gas traced by dust

I also traced the gas via the dust in a galaxy, and to that end have created two dust maps. The first was a simple one-temperature modified blackbody (MBB), with a variable β, which takes the form

$$S_\nu = \frac{\kappa_\nu M_{\rm dust} B(\nu, T_{\rm dust})}{D^2}, \tag{2.10}$$

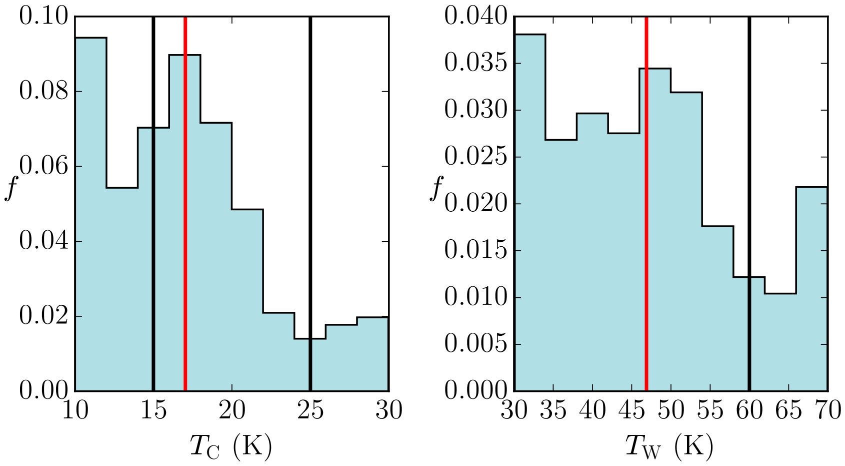

Figure 2.7: Distribution of cold and warm dust temperatures from all fitted MAGPHYS pixels. The red line shows the average value of the sample, the black lines the bounds of the standard MAGPHYS parameter space.

where S_ν is the flux at frequency ν, κ_ν is dust absorption coefficient at frequency ν, $M_{\rm dust}$ is the dust mass, $B(\nu, T_{\rm dust})$ is the Planck function at frequency ν and dust temperature $T_{\rm dust}$, and D is the distance to the source. I assumed $\kappa_{850} = 0.077{\rm cm}^2{\rm g}^{-1}$ (Dunne et al., 2000). Recent work by Clark et al. (2016) would suggest using a value of $\kappa_{500} = 0.051^{+0.070}_{-0.026}{\rm m}^2{\rm kg}^{-1}$ instead, but I use this older value for consistency with MAGPHYS. I fit the MBB from 100-850μm, using the 70μm point as an upper limit to prevent fitting to warmer dust components (Smith et al., 2010). The dust mass and β were allowed to vary freely, and the dust temperature was allowed to vary between 0-200K. For all pixels with a S/N > 2.5 in at least 5 of the *Herschel*/SCUBA-2 bands, a fit is performed independently on each pixel, giving me 2320 pixels with at least 1 degree of freedom, corresponding to a total area of 23.2kpc^2. The data has filter corrections suitable for extended sources applied, although no colour corrections were accounted for. Errors were accounted for via MCMC uncertainty estimation using EMCEE[14]. I used 100 walkers, each taking 300 steps, and the second half of these steps are used for error estimation to make sure the walkers have 'burnt-in'. In each case, I take the error value to be the 16th and 84th percentiles of the samples in the marginalised distributions, and the 50th percentile as the value for the quantity in question. This MCMC estimation does not take into account correlated SPIRE uncertainties, but the effects of this are expected to be minor. This dust map can be seen in the left panel of Fig 2.6.

The second dust map was provided as an output by MAGPHYS. The MAGPHYS

---

[14] `http://dan.iel.fm/emcee/current/`

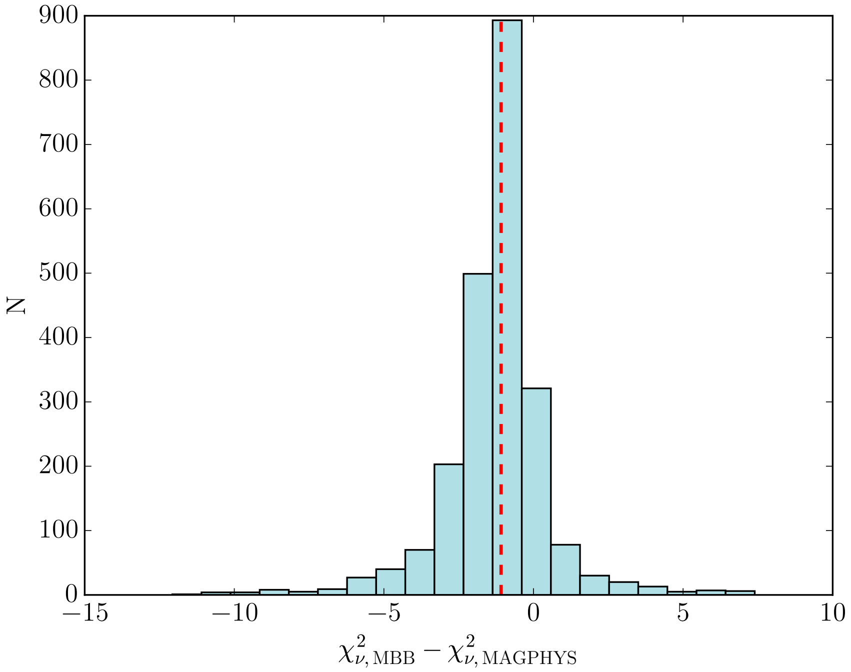

Figure 2.8: Comparison of reduced χ^2 between MBB and MAGPHYS fits for individual pixels. The red dashed line indicates the median of the distribution (-1.08).

dust models incorporate polycyclic aromatic hydrocarbons (PAHs), which are based on observations of M17, and these features of the SED dominate at MIR wavelengths. MAGPHYS also includes hot dust, which it models with a series of greybodies with temperatures of 850, 250, and 130K. The warm dust is modelled with a modified blackbody with an emissivity index β of 1.5, and can vary between 30-60K. The cold dust is modelled in much the same way, but with $\beta = 2$, and can vary between 15-25K. These values of β are selected to match the assumed MAGPHYS dust properties, and are discussed in more detail in Dale & Helou (2002). This map can be seen in the right panel of Fig 2.6.

Although these dust parameters are not unreasonable for an entire galaxy, at these sub-kpc scales some pixels may not fall within the standard MAGPHYS parameter space. I used an extended library of dust models (Viaene et al., 2014) that increase the parameter space of the cold dust temperature from $10\mathrm{K} < T_\mathrm{C} < 30\mathrm{K}$, and the warm dust temperature to $30\mathrm{K} < T_\mathrm{W} < 70\mathrm{K}$. As with the SFR map, I performed filtering to remove any pixels for which the cold or warm dust temperatures were poorly constrained. The distributions of the cold and warm dust for these filtered pixels (i.e. those that satisfy Equation 2.8) can be seen in Fig 2.7 – with an average relative uncertainty on the cold dust temperatures of 4% and on the warm dust of 10%, ~51% of pixels are estimated to have cold dust temperatures outside of the standard

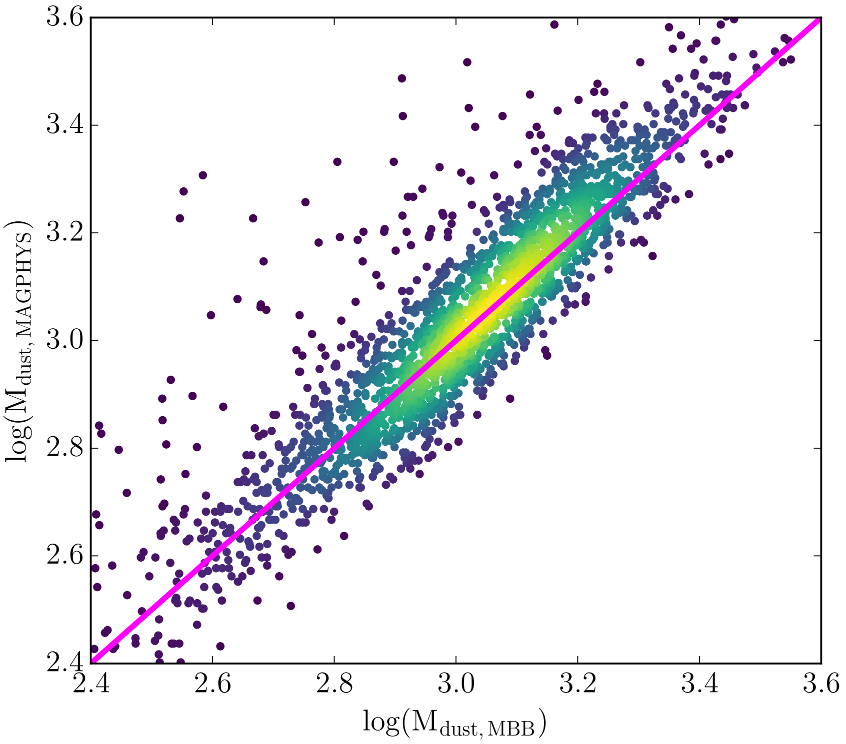

Figure 2.9: Comparison between the dust masses from MAGPHYS and MBB fitting. The one-to-one relation is shown as a fuchsia line. Blue points indicate a lower point density, yellow a higher point density.

MAGPHYS priors, with ~32% of pixels estimate to have warm dust temperatures outside of the standard range. It appears there may be a dust population with T < 10K, although this is most likely due to MAGPHYS using a fixed β of 2 – Xilouris et al. (2012) find that with a fixed β of 1.5, the minimum dust temperature is 11K. This could also be due to the sub-mm excess in M33 (Hermelo et al., 2016) causing MAGPHYS to fit colder dust components. However, performing the fits without the 850μm data (where this submillimetre excess is most apparent) produced very little change in the cold dust temperatures output by MAGPHYS. It also appears from the right panel of Fig 2.7 that a significant number of pixels are hitting the lower bound of the priors for warm dust temperature. This would indicate that these pixels are well fitted by a single-temperature blackbody fit, but as MAGPHYS enforces two temperatures to be fitted, this effect is unavoidable. This is not a concern, as the warm dust fit is unconstrained from 24 to 70μm, and the majority of the dust mass is in the cold component. For both the MBB and MAGPHYS fits, I calculate the reduced χ^2 in a consistent way from the observed and model fluxes. A comparison of the reduced χ^2 of the MBB and MAGPHYS fits (Fig 2.8) finds a median offset of -1.08, indicating that on average, the MAGPHYS fits tend to be slightly worse.

A comparison of these two dust maps is shown in Fig 2.9. The two methods yield very similar results, and a very tight relationship with an RMS scatter of 0.10 (23% of the points lie outside the 1σ scatter). There is a median offset of 0.02, indicating that the MAGPHYS calculated dust masses tend to be slightly higher. Whilst some of the points where the MAGPHYS dust masses are higher tend to be associated with colder dust, many are associated with a 'warmer' cold dust component. The differences in dust mass are not unexpected, as the MBB has been fitted with a variable β. Many of the fitted β values are less than 2 (the value MAGPHYS uses for its cold dust temperature), which will result in the MBB fitting higher dust temperatures, and thus lower dust masses. MAGPHYS takes into account a variety of dust compositions and temperatures, but this more sophisticated modelling does not greatly affect the calculated dust masses. As there is only a slight deviation from the one-to-one relation, this indicates that the MAGPHYS warm dust temperatures often running up against the lower bounds of the parameter space is not having a significant impact on the calculated dust masses.

The total gas mass can be calculated from dust masses (assuming that the gas and dust are well mixed) using a dust to gas ratio (DGR). Sandstrom et al. (2013) find that the DGR is well correlated with metallicity, with a relationship given by

$$\log(\mathrm{DGR}) = 0.55[12 + \log(\mathrm{O/H})] - 6.50. \tag{2.11}$$

I combined this with work from Rosolowsky & Simon (2008), who find the metallicity gradient within M33 to take the form

$$12 + \log(\mathrm{O/H}) = -0.027R + 8.36 \tag{2.12}$$

where R is in kpc. Combining these two, the radial variation in DGR is

$$\log(\mathrm{DGR}) = -0.015R - 1.902. \tag{2.13}$$

I note this gives similar results for the gas-to-dust ratio as the MW (~100, Spitzer 1978), rather than the much higher results of 200-400 found in M33 by Gratier et al. (2017) within a radius of 7 kpc. I find total dust masses of $2.6 \times 10^6\,\mathrm{M}_\odot$ (MBB fits), and $3.8 \times 10^6\,\mathrm{M}_\odot$ (MAGPHYS), and by applying this radial DGR, gas masses of $2.25\times10^8\,\mathrm{M}_\odot$ (MBB fits) and $9.75\times10^8\,\mathrm{M}_\odot$ (MAGPHYS), similar to the total gas mass inferred from HI+CO ($5.45 \times 10^8\,\mathrm{M}_\odot$).

Table 2.3: Spearman's rank ($\rho_{\rm sp}$) and Pearson correlation coefficient ($\rho_{\rm pears}$) for the various gas maps derived in this work and the MAGPHYS SFR (Fig. 2.3) at scales of 200 pc. All correlations have $p < 0.025$.

	HI	H_2	Total gas	Total gas (M_d; MBB)	Total gas (M_d; MAGPHYS)
$\rho_{\rm sp}$	0.35	0.57	0.42	0.44	0.51
$\rho_{\rm pears}$	0.29	0.55	0.37	0.41	0.51

2.4.4 WHICH GAS TRACER BEST CORRELATES WITH SFR?

To find out which of these gas maps best traced the SFR, I performed a series of Spearman's rank and Pearson correlation coefficient tests between these gas maps and the MAGPHYS calculated SFR. I also included a total gas map, combining the HI and CO(J=2-1) data. If the star-formation law breaks down at scales of ∼100pc, I would expect only a weak correlation here, so I regridded this data to 50 arcsec pixels (corresponding to 200pc), to mitigate against this effect.

The correlations between the MAGPHYS SFR and the various gas maps can be seen in Table 2.3. I find that the correlations between gas and SFR are weaker than those found when comparing integrated galaxies (which typically have $\rho_{\rm sp}$ ∼0.8). This indicates much more scatter on these sub-kpc regions. Of the line-based gas tracers, I find that molecular gas has the strongest correlation – this is not surprising, as work by, e.g., Bigiel et al. (2008) has also shown that molecular gas correlates better with SFR than the atomic gas, or the sum of the two.

Of the total gas traced by dust, I find that the MAGPHYS dust fits correlate better than the modified blackbody dust map. This is probably due to MAGPHYS more effectively tracing the total dust continuum, whereas the blackbody is only fitting to the cold dust. It is important to note that there may be degeneracies present between the SFR as calculated from MAGPHYS along with the dust mass. However, the SFR is calculated from the stellar models, and the dust mass from the dust models, and so these two parameters are calculated relatively independently. I elect to perform our analysis on the molecular gas, the total gas, and the total gas traced by dust from MAGPHYS fitting going forward.

2.5 THE STAR-FORMATION LAW

In this section, I investigate the star-formation law within M33 at high resolution. I start by comparing the average SFR and gas density to that of other galaxies in previous studies, before performing pixel-by-pixel fits within the galaxy. At high resolution, I also look at the radial variation in the Schmidt index. I have also investigated the effect of the spatial resolution used in the calculation of the KS index, as well as depletion timescale. Finally, I look at the relationship between SFR and dense gas at high resolution in M33.

2.5.1 GLOBAL FITS

Fig 2.10 shows the mean surface density of SFR and gas for M33 compared with various other galaxies. The mean values here have been calculated from any pixels in the relevant gas map that match up with a pixel from the filtered MAGPHYS SFR map. Given that the pixel sum and value from the global fit are consistent within errors (Sect. 2.3.3), I do not believe this will bias the results in any significant way. In the case of the molecular gas, the surface density of SFR is about an order of magnitude higher than expected from this relationship. It is, however, consistent in terms of its molecular gas surface density with work by Ford et al. (2013) on M31, with this higher $\Sigma_{\rm SFR}$ due to its higher star-formation rate and smaller size. Given the relatively low contribution of the molecular gas to the total gas budget, it is not surprising that this value lies away from the relationship, which has been calculated for the total gas content. The total gas, and gas from dust values lie on the trend. This is unsurprising, as literature values compare SFR surface density with total, rather than molecular gas. Globally, these values are similar to other galaxies, with a somewhat higher star-formation efficiency than M31. Overall, I find that the total surface density of gas and SFR is consistent with previous studies – hence, M33 is a typical galaxy in terms of these parameters.

2.5.2 PIXEL-BY-PIXEL FITTING

I also investigated the star-formation law on a pixel-by-pixel basis in M33. For this, I used all pixels in the corresponding gas maps that have a "constrained" (as defined by Equation 2.8) SFR. In this sense, I have effectively performed a S/N cut on the SFR map. This SFR cut biases the data somewhat, although I find that repeating the fits with the unfiltered data produces results consistent within the error bars. With pixel sizes of 100pc×100pc, I converted the SFR and gas maps into units of surface density. These points can be seen for the three gas tracers in the top row of Fig 2.11. At spatial scales of 100pc, although I see significant scatter in the points,

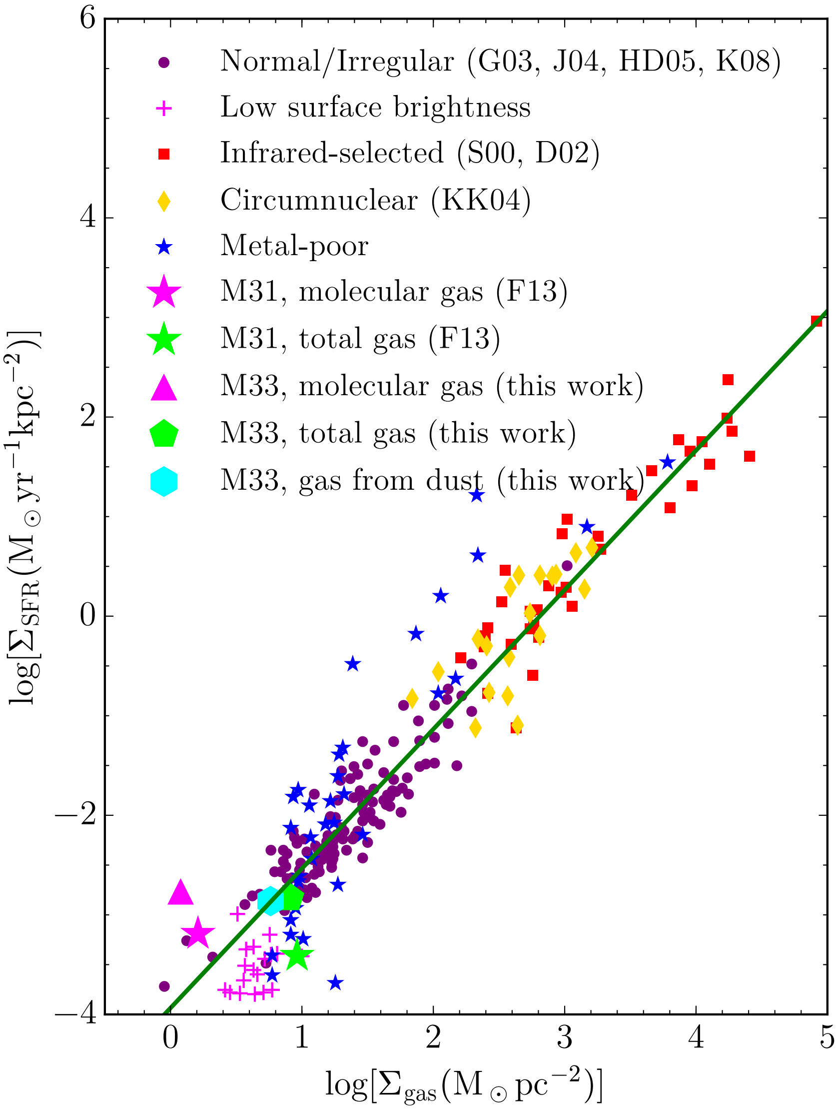

Figure 2.10: Surface density of SFR against surface density of gas for a variety of galaxies. Purple circles indicate the normal and irregular galaxies of Gavazzi et al. (2003), James et al. (2004), Hameed & Devereux (2005), and Kennicutt et al. (2008). Fuchsia pluses show the subset of these galaxies classified as low-surface brightness. The red squares are infrared-selected starburst galaxies of Scoville et al. (2000) and Dopita et al. (2002), with circumnuclear starburst galaxies from Kormendy & Kennicutt (2004) shown as yellow diamonds. The subset of all of these galaxies with metal abundances, $Z < 0.3Z_{\odot}$ are shown as blue stars. The values for molecular and total gas for M31 (Ford et al., 2013) are shown as purple and light green stars, respectively. The purple triangle, light green pentagon and light blue hexagon show the values calculated in this work from the molecular gas, total gas, and gas from dust respectively. Also shown is a green line with slope, $N = 1.4$.

I find correlations between the gas and SFR surface densities ($\rho_{\rm sp}$ = [0.54,0.42,0.37] for molecular gas, total gas and gas from dust respectively). This is in stark contrast

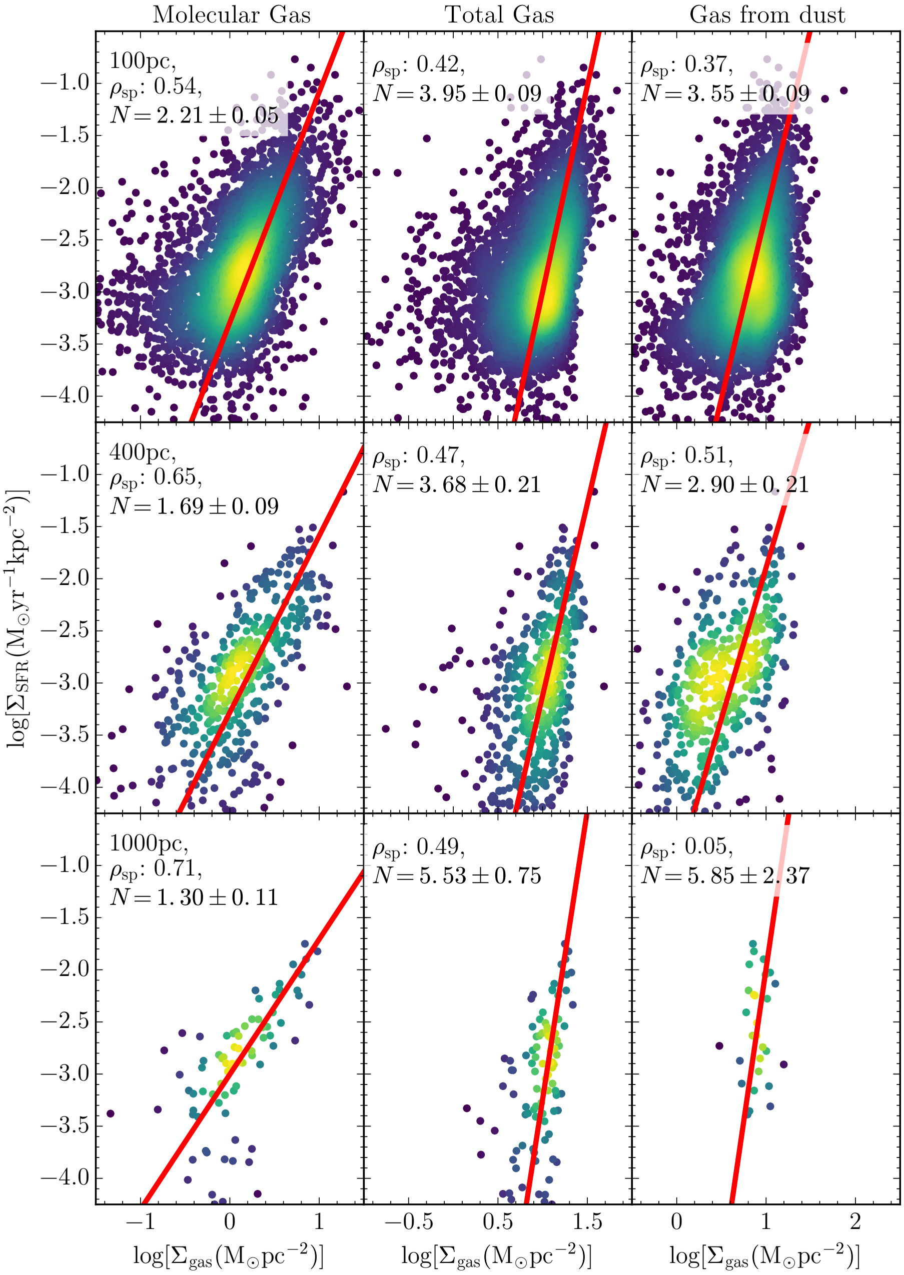

Figure 2.11: *Left column:* SFR surface density against molecular gas surface density. *Middle column:* SFR surface density against total gas surface density. *Right column:* SFR surface density against gas surface density, as traced by dust. The points are coloured by point density, from blue (low density) to yellow (high density). The red line indicates the best fit in each case.

to, e.g., Onodera et al. (2010); Schruba et al. (2010), who find very little correlation between these quantities at comparable spatial scales. I attribute this to the methods these works have employed to calculate the SFR in these sub-kpc regions. These works calculated SFR using methods that assume constant star-formation over the last 100Myr, which the magphys fits and work by Relaño & Kennicutt (2009) show is likely inappropriate over these sub-kpc regions. This can affect the calculated SFR by an order of magnitude (Fig. 2.4). I find that using other SFR measures results in much more scatter at the highest resolutions, similar to that shown in Onodera et al. (2010).

Another difference in my method is the choice of molecular gas tracer. Whilst Onodera et al. (2010) and Schruba et al. (2010) opt to use the J=1-0 line to trace the molecular gas, I make use of observations of the J=2-1 line. Higher rotational transitions of CO trace warmer, denser, molecular gas, which may be more closely associated with star-formation. Work has shown that higher rotational transitions are more strongly correlated with SFR (e.g. Komugi et al. 2007; Bayet et al. 2009), and so this stronger correlation would be expected.

To calculate a Schmidt index, I use orthogonal distance regression (ODR), to account for errors in both $\Sigma_{\rm SFR}$ and $\Sigma_{\rm gas}$. The error in $\Sigma_{\rm SFR}$ comes from the magphys modelling uncertainties, and the errors in gas surface density are derived from the RMS noise of the particular map (ignoring any calibration error, as this will simply cause an offset to all points and not affect the slope). I have not considered an uncertainty factor in the conversion of CO to molecular gas mass. Given that I have used conversion factors calculated specifically for M33, I would expect this conversion to be fairly robust, but there is scatter from the relationship (see Fig. 5 of Braine et al. 2010). Thus, the uncertainty in $\Sigma_{\rm gas}$ will be somewhat underestimated, but quantifying the level of this is beyond the scope of this work. In the case of the magphys dust map, I use the relative error calculated from the percentiles of the PDF. I perform this fit in linear space, as these error bars will be asymmetrical in log space. I fit this line to the entire data set, and these fits can be seen in Fig. 2.11. With the large range of S/N values of our $\Sigma_{\rm SFR}$ and $\Sigma_{\rm gas}$, particularly the large number of low S/N points, it is necessary to account for uncertainties in both variables when performing the model fitting. The method of fitting can have a significant impact on the measured power law slope (e.g. Shetty et al., 2013). Given I do not use a strict S/N cut on the data, and account for errors in both of the variables, this is a much more rigorous (and robust) measurement of N than linear regression including only errors on one axis. The effects of assuming a constant fractional uncertainty for all the data points rather than our measured uncertainty estimates is discussed in Appendix A.

At the highest resolutions, I find three very different indices to the classic $N = 1.4$. Even in the case of molecular gas where I see the strongest correlations, the

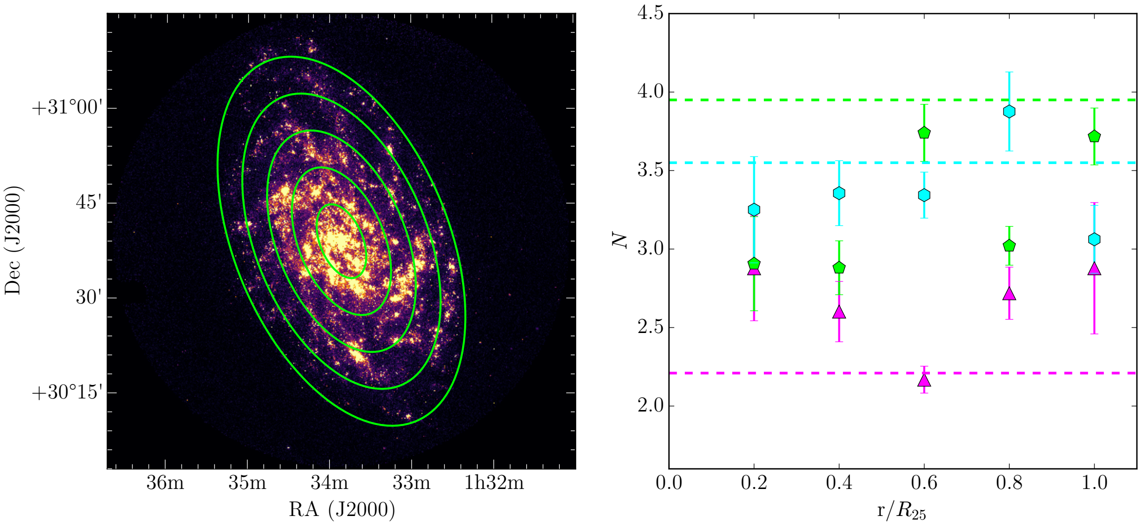

Figure 2.12: Schmidt index with galactocentric radius within M33. Purple triangles indicate values calculated using the molecular gas, light green pentagons from the total gas, and light blue hexagons from the gas traced by dust. Also shown are dashed lines indicating the average value of N fitted to all pixels.

Schmidt index is higher than expected from Kennicutt (1998a). To my knowledge, these values are higher than others previously reported. It also appears that the dust traces the total, rather than molecular gas. This is expected from previous work linking dust to the total gas content of a galaxy (e.g. Hildebrand, 1983; Eales et al., 2012; Magdis et al., 2012). In the case of the total gas tracers, this high index could be due to "HI saturation" at atomic gas column densities of around 10 $\mathrm{M_\odot pc^{-2}}$ (Leroy et al., 2008). This was also noted in M31 by Ford et al. (2013). The high indices with molecular gas are more difficult to reconcile. Shetty et al. (2014) find evidence that the Kennicutt-Schmidt law varies from galaxy-to-galaxy, although their fits are primarily sublinear. Simulational work by Schaye & Dalla Vecchia (2008) finds that increasingly high N become difficult to reproduce in simulations. An alternative is that the much harsher radiation field at higher SFR surface densities preferentially photo-dissociates the CO (e.g. Glover & Clark, 2012). This would lead to a systematic underestimate of the molecular gas surface density that increases with increasing Σ_{SFR}, and would lead to a higher N than expected. However, with strong correlations remaining between Σ_{SFR} and the molecular gas, I argue that the star-formation law holds at these small scales.

Table 2.4: Schmidt index for the molecular gas, total gas, and gas from dust, for a variety of pixel scales. Asterisks indicate correlations with $p > 0.025$.

	Molecular gas		Total gas		Gas from dust	
Scale (pc)	N	$\rho_{\rm sp}$	N	$\rho_{\rm sp}$	N	$\rho_{\rm sp}$
100	2.21 ± 0.05	0.54	3.95 ± 0.09	0.42	3.55 ± 0.09	0.37
200	1.90 ± 0.06	0.57	1.93 ± 0.12	0.42	3.13 ± 0.09	0.51
400	1.69 ± 0.09	0.65	3.68 ± 0.21	0.47	2.90 ± 0.21	0.51
600	1.51 ± 0.09	0.70	3.90 ± 0.29	0.52	2.78 ± 0.26	0.57
1000	1.30 ± 0.11	0.71	5.53 ± 0.75	0.49	5.85 ± 2.37	0.05*
2000	1.07 ± 0.16	0.87	5.20 ± 1.33	0.50	0.07 ± 0.36	0.14*

2.5.3 A SEARCH FOR A RADIAL VARIATION IN N

Work such as Leroy et al. (2008) and Ford et al. (2013) have shown that a radial variation can be seen in the Schmidt index in some galaxies. To investigate this at high resolution in M33, I have taken the pixels inside five annuli of constant galactocentric radius from the centre of M33 to $1.2R_{25}$. The results of this can be seen in Fig. 2.12. I see little radial variation in N for all three tracers of gas, indicating that the star-formation efficiency is reasonably constant across the disc of M33. The exception to this is at around $r/R_{25} = 0.6$. This is the radial bin that contains NGC 604, which is extremely molecular gas rich (Gratier et al., 2012). Given the high molecular gas surface densities in this annulus, this means a significantly lower N in this radial bin. These results for all three gas tracers appear very different to those of Leroy et al. (2008) for spiral galaxies in general and Ford et al. (2013) for M31 in particular. I find that the calculated value of N is reasonably consistent with each tracer of gas for these radial bins, with a peak in the outer spiral arms for the total gas, and the gas from dust.

2.5.4 VARIATION WITH PIXEL SCALE

Although I find correlations at scales of 100pc, these are not as strong as those found by, e.g., Schruba et al. (2010) in M33 ($\rho_{\rm sp}$ ~0.8 at 1200pc resolution). I expect this correlation to increase, and scatter between points to decrease with increasing pixel scale – at this point, we probe an average over GMCs in various evolutionary states at larger spatial scales, and it is this that is believed to drive the KS relation (Onodera et al., 2010). In order to test this increase in correlation, I regridded our data to a number of pixel scales (50 arcsec to 500 arcsec, 200pc to 2kpc). For the gas maps, I performed this using MONTAGE's mProject routine, and for any quantities derived from MAGPHYS I ran the fits on the regridded data. I then performed a fit to each pixel scale, using the same method as detailed in Section 2.5.2. A selection of these fits can be seen in the lower panels of Fig 2.11, and the calculated values of N, along with Spearman's rank correlations can be seen in Table 2.4.

Between pixel scales and gas tracers, I see variation in the Schmidt index. With molecular gas, this decreases with increasing pixel scale before becoming approximately linear at a scale of ~2kpc. This value is consistent with the index found by Bigiel et al. (2008) when considering molecular gas, and indicates that at kpc resolutions, these GMC populations appear much more uniform, and we are simply counting the numbers of them. I also find that, in general, N increases with increasing pixel scale for the total gas. There is, however, significant scatter in my calculated N with pixel scale with gas from dust, and at large pixel scales the correlation between this tracer of gas and SFR is no longer statistically significant. For my more conventional gas tracers, I find an increasing correlation between the surface density of gas and SFR with increasing pixel scale, with decreasing scatter from the relationship. This would indicate that the star-formation law seen at integrated galaxy scales is driven by an average of GMCs at various evolutionary states in a galaxy.

I also investigate the scale dependence on the gas depletion timescale – this can be seen in Fig. 2.13. I calculate the depletion timescale in the same manner as Schruba et al. (2010), where $\tau_{\rm dep} = \Sigma_{\rm gas}/\Sigma_{\rm SFR}$. I quote the 1σ errors based on the percentiles of the depletion timescale distribution. Unlike Schruba et al. (2010), I find no significant variation in the gas depletion timescale with resolution, for any of my three gas tracers. This would appear to be due to their targeted selection of only the brightest regions of CO and Hα which they restricted themselves to in order to only study the regions of strongest star-formation or gas quantity – when taking into account the entire ensemble of regions within M33, these resolution effects are no longer significant.

It is also important to note that these results cover a much smaller dynamic range than Fig. 2.10, and so the correlations would naturally be weaker. I took a subset of the data in Fig. 2.10 over the ~2 orders of magnitude that the data covers. I found that the average Spearman correlation coefficient is ~0.84 for these data, still stronger than we find for M33 at any spatial scale. To recover the correlation seen comparing galaxy to galaxy, it seems necessary to take into account the entire ensemble of GMCs within that particular galaxy.

I find that these data also do not reproduce the correlations seen by Schruba

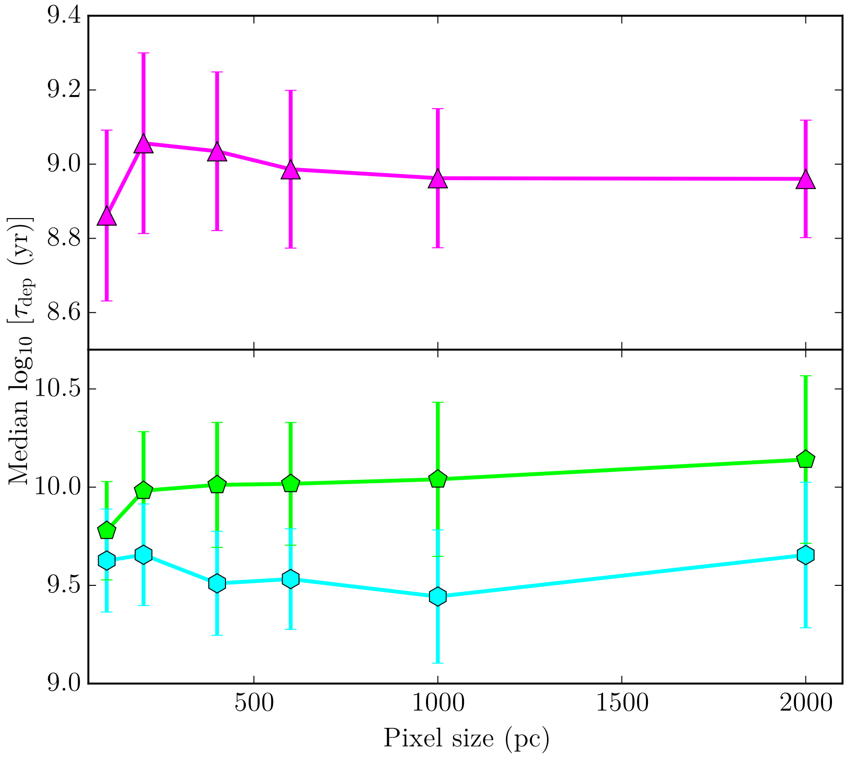

Figure 2.13: Depletion timescales for the three gas tracers with pixel size. Purple triangles indicate the molecular gas, green pentagons the total gas, and light blue hexagons the gas traced by dust.

et al. (2010), who find a correlation coefficient of ∼0.8 at scales of ∼1kpc. However, their work used targeted apertures on CO and Hα peaks, biasing their results towards areas of high star-formation and S/N, where this star-formation law holds more strongly. When I place apertures centered on peaks of gas or SFR, rather than pixel-by-pixel comparisons, I find a stronger correlation ($\rho_{\rm sp}$ = 0.82 for apertures of 1200pc diameter), comparable with that of Schruba et al. (2010). My work blindly includes all areas within a galaxy, so I avoid the very high S/N requirements of Schruba et al. (2010). Thus, this is the cause of these slightly weaker correlations.

2.5.5 SFR and Dense Gas

I have investigated the relationship between dense gas and SFR, to see if this relationships show a similar scale dependence to the star-formation law. I have used HCN(J=1-0) emission to trace the dense molecular gas. These nine pointings are targeted on GMCs within M33. Most of these dense gas pointings come from Buchbender et al. (2013), with some complementary measurements from Rosolowsky et al. (2011);

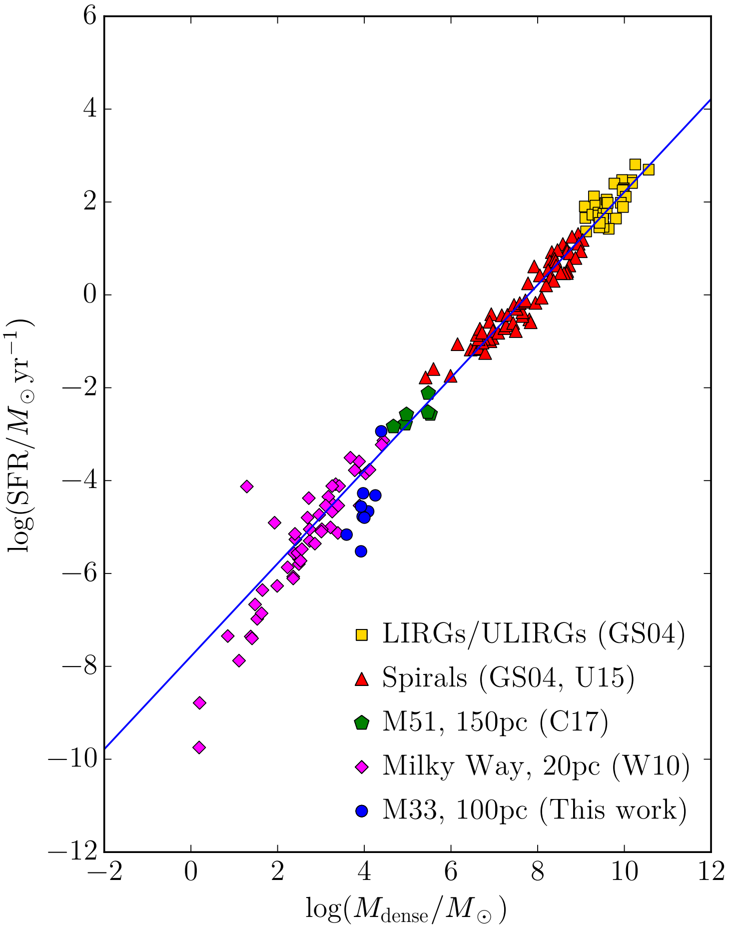

Figure 2.14: Relationship between SFR and dense gas mass across a range of environments and scales. Yellow squares indicate values for the LIRGs and ULIRGs of Gao & Solomon (2004b), red triangles spiral galaxies from the surveys of Gao & Solomon (2004b) and Usero et al. (2015). Green pentagons are sub-kpc measurements taken in M51 by Chen et al. (2017), purple diamonds are from the MW pointings of Wu et al. (2010). Blue circles indicate values for this work – SFR values have been calculated using MAGPHYS, and dense gas pointings come from a variety of sources, described in the main text. In every case, the dense gas mass has been calculated using HCN(J=1-0), and for pointings that are resolved, the approximate spatial scale is given in the legend. For clarity, the errorbars have been omitted from this plot, but they are on the order of 20%. As the literature values as presented in terms of dense gas mass rather than surface density, they are presented as such here. The blue line indicates a linear fit to the data.

Braine et al. (2017). All of these pointings were from the IRAM 30m telescope, with a beam size of 28 arcsec, comparable to our pixel size. To convert the HCN luminosity to a mass of dense H$_2$, I used a conversion factor, $\alpha_{\rm HCN} = 10\,{\rm M}_\odot\,({\rm K\,km\,s^{-1}})^{-1}$ (Gao & Solomon, 2004a). The results of this can be seen in Fig 2.14 – a strong correlation is seen between the dense gas mass and SFR ($\rho_{\rm sp} = 0.68$, $p = 0.04$), although this may be simply due to the targeted nature of these pointings. Additionally, these points lie approximately on the extrapolation of the linear fit seen for integrated galaxies, indicating that this dense gas relation holds down to these 100pc scales. Possibly the reason these points are somewhat below the line is due to the low metallicity of M33, since due to their sensitivity to photodissociation, dense gas tracers are very strongly dependent on metallicity (Rosolowsky et al., 2011). Nevertheless, these results indicate that the dense molecular gas correlates more strongly than the regular molecular gas with SFR at these sub-kpc scales.

2.6 DISCUSSION AND CONCLUSIONS

In this chapter, I have presented a high-resolution study of the star-formation law in M33 on spatial scales of $\sim$ 100pc. By assembling GALEX UV, SDSS, WISE, *Spitzer*, *Herschel*, Planck, and new SCUBA-2 observations I have measured the SFR using the panchromatic SED fitting tool MAGPHYS. I have compared this SFR with that calculated both by the TIR luminosity and FUV+24μm data. I find that much of the starlight in M33 is unattenuated by dust, leading to an underestimate of the total SFR from the TIR luminosity. MAGPHYS models many of the HII regions of M33 as starburst-like, and thus produces pixels with much higher SFR than even the FUV+24μm calculated SFR. Since MAGPHYS uses all available data and allows variations in SFR to much shorter timescales than the TIR and FUV+24μm prescriptions, I have used this in my analysis.

I have combined the SFR calculated from these SED fits with gas maps created from HI and CO(J=2-1) data. I have also constructed dust mass maps of M33 using both a MBB fitting code and MAGPHYS, and compared the two. I find that these two maps agree very closely, with the MAGPHYS masses tending to be slightly higher – not unexpected with a variable β and a single temperature in the case of the MBB fitting. It is important to note that when fitting a two-temperature MBB to M33, Tabatabaei et al. (2014) find that a fixed β of 1.5 for the cold dust component was a better fit than the 2 the MAGPHYS uses, but the effect of this is minor. Using the DGR calculated from the metallicity gradient, I turn these dust maps into total gas mass maps. I use maps of the molecular gas, total gas (CO + HI) and total gas from dust to probe the star-formation law at scales of 100pc.

I find that M33 is not an unusual galaxy in terms of its overall gas and SFR surface density, and whilst correlations remain down to scales of 100pc, the measured

Schmidt index shows a strong scale dependence. This indicates that the GMCs within M33 are at a variety of evolutionary states, and so the star-formation law is very different at GMC, rather than galaxy scales. I also find that at these scales, molecular gas better traces SFR. The gas depletion timescale, however, shows no such scale dependence. I find that N is reasonably invariant with galactocentric radius, with a peak in N for total gas and gas from dust in the outer spiral arms. If I consider the dense gas mass of a galaxy, a tight, linear relationship is found, perhaps indicating that dense molecular gas is the fundamental building block of star-formation.

Using a wide range of high-resolution data, and leveraging the close proximity of M33, I have been able to probe the light at GMC scales in this galaxy across some four orders of magnitude in wavelength. From this broad range of coverage, a large range of galaxy parameters can be calculated, and various laws probed down to the small-scale. It would appear that, at the scales of GMCs, the star-formation law does hold, although the Schmidt index is very different at these scales. I also find a quasi-universal star-formation law with dense molecular gas.

CHAPTER 3

A DUST-SELECTED GMC CATALOGUE OF M33

OK, one last time. These are small
...but the ones out there are far away.

FATHER TED

This chapter uses new, high-resolution SCUBA-2 observations of M33 to perform a dust-selected molecular cloud catalogue of M33. This work is published in Williams et al. (2019a).

3.1 INTRODUCTION

The study of star-formation and the study of molecular clouds are inexorably linked. As stars are believed to form from the dense molecular gas in these clouds (André et al., 2010; Lada et al., 2010), our understanding of star-formation is ultimately limited by our ability to resolve ensembles of these star-forming regions. Within our own galaxy, we are faced with the challenges of distance ambiguity – to overcome this, we can turn to high-resolution mapping of galaxies for studies of large numbers of these molecular clouds.

One option for locating these molecular clouds is to trace the molecular hydrogen that they contain. However, due to the size and symmetry of the H_2 molecule, it is impossible to trace the cold component associated with star formation directly and so a proxy must be employed. Generally, the rotational transitions of CO (the next most common molecule) are favoured, as they are believed to trace the cold molecular gas that resides within these clouds. Resolving these molecular clouds poses a great challenge – with the average Milky Way (MW) GMC size being ∼40 pc (Solomon et al., 1979), and ∼30 pc in the LMC (Hughes et al., 2010), we are limited to studies in our local Universe (e.g. Israel et al. 1993; Rosolowsky 2007; Hughes et al. 2010). Recently, with the advent of the Atacama Large Millimetre/submillimetre Array (ALMA), these studies can be extended beyond our Local Group of galaxies (e.g. Sun et al. 2018; Liu et al. in prep.).

Alternatively, an independent method to probe the properties of GMCs uses the cold dust continuum emission of a galaxy. It has long been established that there is a link between the dust content of a galaxy and its molecular gas (e.g. Hildebrand 1983; Magdis et al. 2012; Eales et al. 2012). Thus, the dust continuum allows us an alternative method to CO measurements to probe the properties of GMCs. However, due to the limited resolution of these instruments and the sizes of clouds this method of probing GMCs is only suitable for some of our most nearby galaxies. Using, for example, the *Herschel* Space Observatory (Pilbratt et al., 2010), we can resolve an average-sized molecular cloud up to a distance of around 200kpc at 500μm wavelengths. Using *Herschel* observations of Andromeda (M31), Kirk et al. (2013) extracted a GMC catalogue from the cold dust continuum, finding the cloud properties to be consistent with clouds in the Milky Way. With the Submillimetre Common-User Bolometer Array 2 (SCUBA-2; Holland et al. 2013) on the James Clerk Maxwell Telescope (JCMT), we can resolve these objects up to 600 kpc away (850μm), or 1.2 Mpc (450μm). However, with ground-based sub-mm observatories we must overcome noise from the sky varying over small scales at the sub-mm wavelengths we probe – a harsh sky subtraction process must be performed, which has the drawback of also filtering out large-scale structure in these galaxies. Using a Fourier combination technique, we can use space-based observatories operating at similar wavelengths to add this large-scale structure back in to this data, allowing us to retain both the large-scale structure and the much finer structure these ground-based observatories offer.

M33 provides an excellent laboratory for resolved molecular cloud studies. Located at a distance of 840 kpc (Madore & Freedman, 1991), it is the third massive spiral galaxy of our Local Group, behind our own Milky Way (MW), and M31. Unlike M31, however, M33 is more face-on, with an inclination of 56° (Regan & Vogel, 1994), and so suffers less from projection effects. It is also actively star-forming across its disk (Heyer et al., 2004), and is host to a large number of GMCs. Previous studies of M33 have identified GMCs using line data from ^{12}CO(J=1–0), such as Wilson & Scoville (1990), surveying the inner 2 kpc of M33 at 7 arcsec resolution, finding 38 GMCs. All-disk surveys of M33 have suffered from poorer resolution than this, such as Engargiola et al. (2003), using the J=1–0 line, and Gratier et al. (2012), using the J=2–1 line, finding 148 and 337 GMCs across the disk of M33, respectively. Both of these surveys have resolutions of $\sim$50 pc, and so many of the GMCs are only marginally resolved.

In this chapter, I take an alternative approach to map the GMC content of M33. By combining far-infrared and sub-millimetre data, I probe the properties of GMCs via the cold dust continuum emission of M33. The layout of this chapter is as follows: I first present an overview of the data used in our study (Sec. 3.2), and my method of source extraction (Sec. 3.3). I then move on to measure the properties of these GMCs (Sec. 3.4) and a comparison to earlier CO surveys (Sec. 3.5). Finally, I summarise my main results (Sec. 3.6).

3.2 DATA

3.2.1 FAR INFRARED/SUB-MILLIMETRE

My first source of FIR/sub-mm data comes from the *Herschel* Space Observatory. I make use of observations taken as part of the *Herschel* M33 extended survey (HerM33es, Kramer et al. 2010), which mapped a 70 arcmin^2 region around M33. Data at 100 and 160μm was taken with the Photoconductor Array Camera and Spectrometer (PACS, Poglitsch et al. 2010), with beam sizes of 7.7 arcsec and 12 arcsec, respectively. The details of this data reduction are presented in Boquien et al. (2011) and Boquien et al. (2015). This data has a Root Mean Squared (RMS) noise level of 2.6 mJy pixel^{-1} (100μm) and 6.9 mJy pixel^{-1} (160μm).

HerM33es simultaneously used the Spectral and Photometric Imaging Receiver (SPIRE, Griffin et al. 2010) aboard *Herschel*, which mapped M33 at 250μm, 350μm, and 500μm with a resolution of 18 arcsec, 25 arcsec, and 36 arcsec, respectively. This data covers the same region as the PACS maps, to an RMS noise level of 14.1, 9.2, and 8 mJy beam^{-1} at 250, 350 and 500μm, respectively.

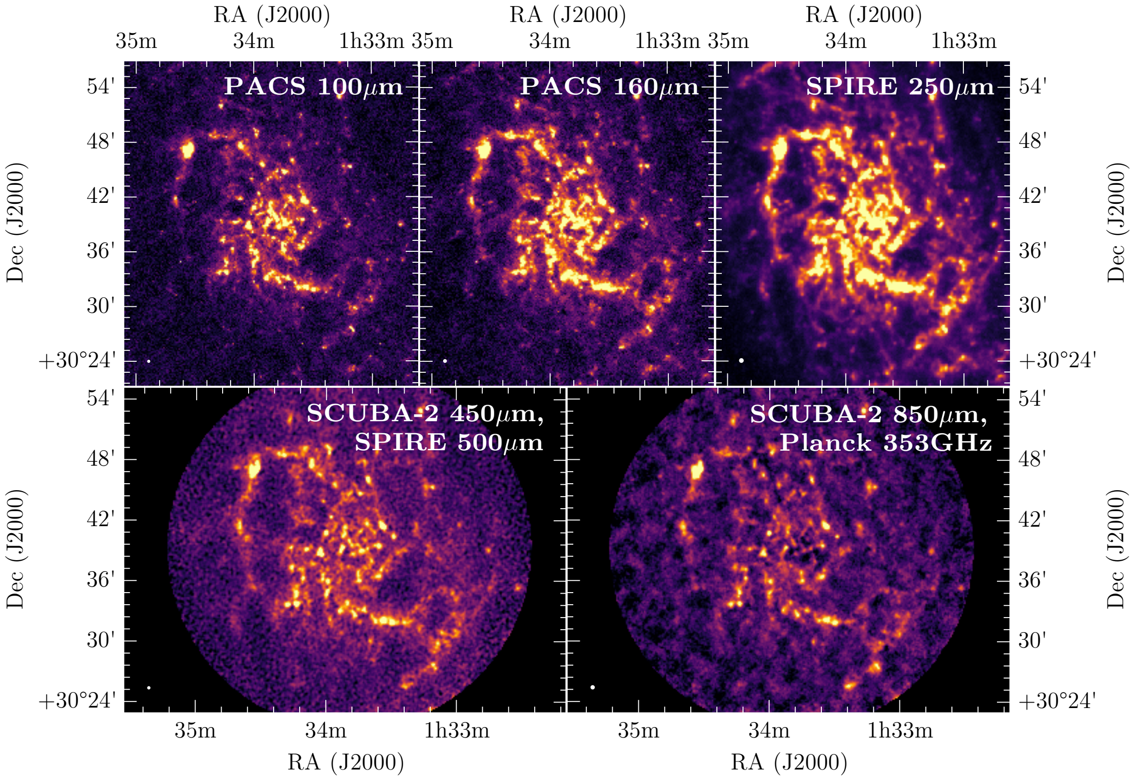

Figure 3.1: Data used for calculating the dust properties of GMCs in M33. From the top left, PACS 100μm and 160μm data, SPIRE 250μm map, and SCUBA-2 data at 450μm (combined with the SPIRE 500μm map) and 850μm (combined with Planck 353GHz data). To aid with visualisation for the SCUBA-2 maps, we have trimmed to a radius of 15 arcmin and smoothed slightly with a Gaussian kernel. In each case, the beam is indicated as a white circle in the lower left.

Archival SCUBA-2 observations of M33 at 450 and 850μm were taken between 2012-07-01 and 2012-07-12, consisting of ~7 hours of PONG1800 (which maps a roughly circular, 30 arcmin field) observations of M33, and ~4 hours of smaller, CV DAISY (constant velocity, small field-of-view) observations. For more details of these SCUBA-2 observing modes, I refer readers to the JCMT observing mode webpage[1]. These observations were taken in mostly Band 2/Band 3 weather (225 GHz opacity, $0.04 \leq \tau_{225} \leq 0.12$). Due to my adopted reduction parameters (see the details on flagslow in Section 3.2.1.1), I cannot use these DAISY maps in my reduction, and so for my purposes, this archival data reaches an RMS noise level of ~6 mJy beam^{-1} at 850μm, and ~85 mJy beam^{-1} at 450μm (with pixel sizes of 4 arcsec and 2 arcsec respectively). As I am particularly interested in the resolution the 450μm data provides, I found that this RMS noise was inadequate and so between 2017-10-17 and

---

[1] `https://www.eaobservatory.org/jcmt/instrumentation/continuum/scuba-2/observing-modes/`

2017-11-21, under Program ID M17BP003 (PI Walter K. Gear), we obtained a further 12 hours of PONG1800 observations of M33, in good Band 1 weather ($\tau_{225} < 0.05$). In the following sections, I describe the data reduction process, which allowed me to create 450μm and 850μm maps of M33 with RMS noise levels of ∼35 mJy beam^{-1} and ∼4 mJy beam^{-1}, respectively. An initial reduction of the data was first presented in (Williams et al., 2018) (Chapter 2), but in this chapter I detail this new reduction. I have performed a much more detailed reduction in this chapter as the fitted SEDs rely on far fewer points than in the previous Chapter. This means it is important to make sure the noise in the data is minimised as much as possible, which my reduction here allows for. The entire dataset used to measure the dust continuum of our GMCs can be seen in Fig. 3.1.

The resolution of this SCUBA-2 data is 7.9 arcsec at 450μm and 13 arcsec at 850μm (Dempsey et al., 2013), corresponding to 32 pc and 52 pc at the distance of M33. However, due to atmospheric variations, extended large-scale structure is filtered out in the reduction process. In order to restore this, I make use of complementary *Herschel* 500μm data for the 450μm data and Planck 353GHz data for the 850μm map. A similar technique has previously been employed with Atacama Pathfinder Experiment Telescope (APEX) Large APEX BOlometer CAmera (LABOCA) data (Csengeri et al., 2016) to recover large-scale, extended structure in the Galactic plane, but I have tailored this technique to SCUBA-2 data.

3.2.1.1 SCUBA-2 Data Reduction and Calibration

The SCUBA-2 data reduction pipeline, MAKEMAP, is described in detail in Chapin et al. (2013), and I refer readers to this work for a full description. I used a modified version of this algorithm, called SKYLOOP, which performs a single MAKEMAP iteration each time, including data from all individual observations simultaneously. This helps to constrain the map, and reduce spurious extended emission, which is particularly important for SCUBA-2 observations of local, extended galaxies.

MAKEMAP is invoked with a file containing the parameters for the map maker. I have attempted to recover some large-scale structure in the SCUBA-2 maps, and so have based our reduction strategy on that of the JCMT Plane Survey (JPS, Eden et al. 2017). My most important, non-default parameters are summarised in Table 3.1 – for a more detailed description of these parameters, I refer the reader to the SCUBA-2 Data Reduction Cookbook[2].

---

[2] `http://starlink.eao.hawaii.edu/docs/sc21.htx/sc21.html`

Table 3.1: SCUBA-2 data reduction parameters for both the main data reduction, and the data calibration.

Parameter	Value	Description
		Data reduction
maptol	0.005	Defines when the map has ‘converged’.
com.perarray	0	Calculate a single common-mode signal for all subarrays.
flt.filt_edge_largescale	120 (450μm), 320 (850μm)	Specifies the largest scale structure to be recoverable in the reduction.
ast.zero_mask	1	Use external astronomical signal mask, based on the *Herschel* 500μm image.
ast,flt,com.zero_freeze	0	Calculate these masks every iteration.
com.sig_limit	5	Remove high-frequency ‘blobs’ from the map.
flt.filt_order	4	Reduce ringing around bright sources.
flt.ring_box1	0.5	Reduce ringing around bright sources.
flagslow	300	Flag data where sources are obscured by 1/f noise.
		Calibration
ast.zero_mask	0	Do not use an external mask.
ast,flt.zero_circle	0.033	Use a circular mask of 120 arcsec radius.
ast.mapspike	10	Ensure very bright pixels are included in the final map.
dcthresh	10000	Ensure very bright pixels are included in the final map.

MAKEMAP produces an output file in units of picowatts (pW), so it is necessary to apply a flux conversion factor (FCF) to the data, to convert it into units of Jy beam^{-1}. The standard FCFs have been calculated to be 491 Jy beam^{-1} pW^{-1} at 450μm, and 537 Jy beam^{-1} pW^{-1} at 850μm (Dempsey et al., 2013), but can vary during the night due to effects such as variations in seeing. Particularly for observations near the start of the night, dish cooling can have a major impact on the measured FCF. It is also important to note that the standard FCFs are calculated using a standard configuration file tailored for bright, compact sources, and the configuration parameters can also have an effect. I therefore calibrated the data using FCFs calculated from standard calibrators taken on the same night as the observations. These calibration observations are taken from Mars, Uranus, CRL618, CRL2688, or HL Tau. For observations of M33 between calibrator observations, I take a linear interpolation between the nearest calibrator FCF before and after. In the case that I did not have a calibrator observed either before or after, I took the FCF of the nearest calibrator. I reduced these calibrator observations using the same configuration file as my M33 reduction, with some small modifications (see Table 3.1). Along with these, I also removed the flagslow parameter, as since these calibration observations are DAISYs, rather than the larger PONGs, the telescope was moving slowly enough that all data were flagged.

Using this reduction method, I find an average FCF of 522±51 Jy beam^{-1} pW^{-1} at 450μm (6% higher than the standard FCF), and 518±44 Jy beam^{-1} pW^{-1} at 850μm (4% lower than the standard FCF). The scatter in FCF is similar to the 10% at 450μm found by (Dempsey et al., 2013), but higher than the standard 5% scatter at 850μm. Having calculated an FCF for each observation, I then multiplied the raw data by the ratio of the calculated to the standard FCF. After then reducing the data using SKYLOOP, I multiplied the final map by the standard FCF value. I found that calibrating the data in this way led to an increase in flux of ~3% in the 450μm map, and a negligible change in the 850μm map compared to simply using the standard FCF on the final map. I also found a decrease in noise of ~3% in the 450μm map, and ~15% in the 850μm map.

3.2.1.2 Combination with *Herschel* and Planck Data

As previously mentioned, the SCUBA-2 data reduction process necessarily removes extended structures in the map. However, using a method similar to interferometric 'feathering', we can restore this extended structure. Previous work has shown that this technique can work to combine Planck and LABOCA data (Csengeri et al., 2016), but I have tailored this code for SCUBA-2.

First, the units of the two input maps are converted to Jy beam^{-1}, if necessary. If a SCUBA-2 map is provided in units of pW, the standard FCF is applied. Generally, SPIRE 500μm maps are in units of MJy sr^{-1}, so I convert to Jy beam^{-1} using a beam size of 1665 arcsec^2 (As reported in the SPIRE Handbook[3]). The Planck maps (which are publicly available in HEALPIX format[4]) are provided in units of $\mathrm{K_{CMB}}$ temperature units, so I convert to Jy beam^{-1} using a conversion factor of 287.45 MJy sr^{-1} $\mathrm{K_{CMB}^{-1}}$ (Planck Collaboration et al., 2014a), and beam FWHM of 5.19 arcmin and 4.52 arcmin (Planck Collaboration et al., 2013). I also subtract the contribution of the Cosmic Microwave Background (CMB) from this data following Planck Collaboration et al. (2015), as the CMB varies over scales similar to the extent of M33. I then reproject these maps to the image size and pixel scale of the SCUBA-2 data using Python's REPROJECT package.

There are two corrections that must also be applied to the data, to account for the difference in central wavelengths, and colour corrections due to differences in spectral response. In the case of combining SCUBA-2 850μm and Planck 353GHz, the central wavelength correction is negligible. For the *Herschel* data, I perform a central frequency correction, assuming a modified blackbody (MBB), so

$$F(\beta, T) = \left(\frac{500\mu\mathrm{m}}{450\mu\mathrm{m}}\right)^{3+\beta} \times \frac{\exp\left(\frac{\mathrm{hc}}{500\mu\mathrm{m}\times\mathrm{kT}}\right)}{\exp\left(\frac{\mathrm{hc}}{450\mu\mathrm{m}\times\mathrm{kT}}\right)} \tag{3.1}$$

where β is the dust emissivity index (if not specified, defaults to 2) and T is the dust temperature (with a default value of 20K).

The colour correction to the Planck data is calculated using

$$C_{\mathrm{Planck}} = \frac{\int R(\nu)(\nu/353)^{-1}\mathrm{d}\nu}{\int R(\nu)(\nu/353)^{\alpha}\mathrm{d}\nu} \tag{3.2}$$

where $R(\nu)$ is the Planck 353GHz passband. α is the index of the source spectrum. In the Rayleigh-Jeans spectral regime, $\alpha = 2 + \beta$, which gives a default correction factor of 0.854. In the case of the *Herschel* data, I use a factor 1.0049, the colour correction given in Table 5.2 of the SPIRE Handbook for extended sources.

---

[3] `http://herschel.esac.esa.int/Docs/SPIRE/html/spire_om.html`

[4] `https://irsa.ipac.caltech.edu/data/Planck/release_2/all-sky-maps/`

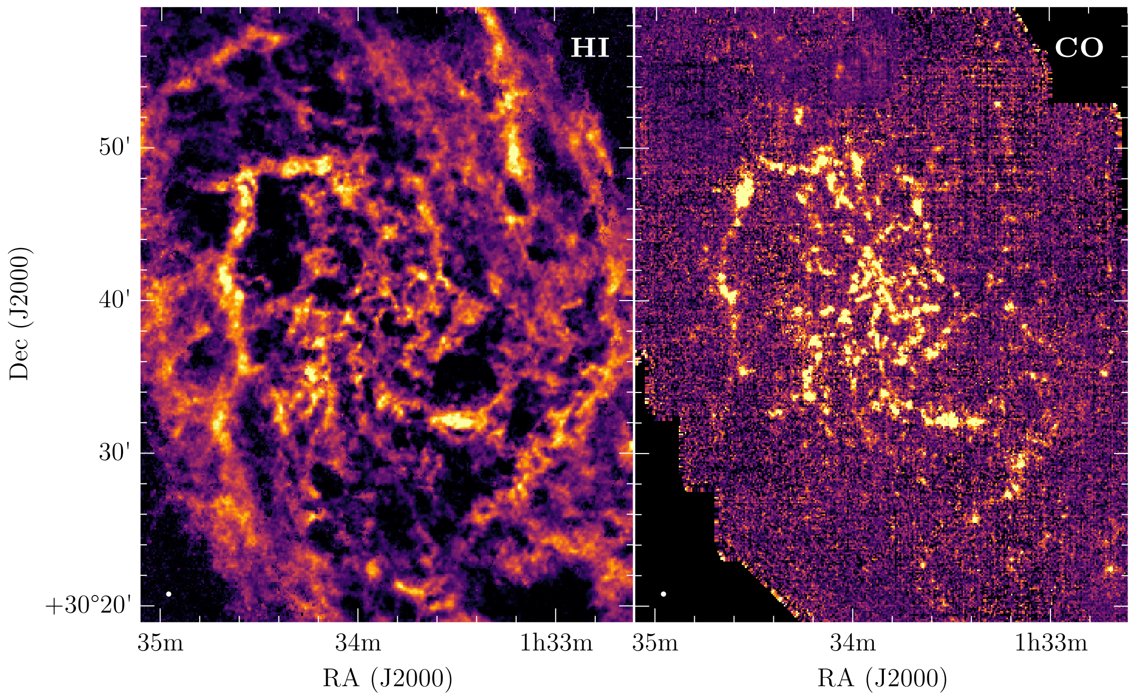

Figure 3.2: *Left:* 21cm HI data and *right:* CO(J=2-1) used in this study. The synthesised beam is indicated as a white circle in the lower left in each case.

I perform a background subtraction on the Planck and SPIRE 500μm data, using a 3σ clipped median. As the SCUBA-2 reduction pipeline models and subtracts the sky, I perform no further sky subtraction on the SCUBA-2 data. My code applies a Gaussian filter when combining the data, specified by an inputted FWHM. In my case, I set the FWHM to 36 arcsec for the 450μm data, and 8 arcmin for the 850μm data. If this value is too small, negative bowling will be present around bright sources, and conversely, if set too high the fine detail desired is lost. These values are set by the lower resolution instrument. The 450μm data can be safely filtered much more harshly without losing extended structure. I perform Fast Fourier Transforms (FFTs) on the data and the filter to transform them into the uv plane, and create parity between the Jy/beam units by multiplying by the volume ratio of the high- and low-resolution beams. The filter is normalised such that its amplitude at the centre of the uv plane is 1.

The FFT of the low-resolution data is then filtered by multiplying by the FFT of the filter, added to the FFT of the high-resolution data and transformed back into the image plane. There is an inherent uncertainty due to errors in β and T, but in practice these are negligible. The total flux density should be determined by the low-resolution map, and I find that the flux density of the low-resolution data alone and the combined data are consistent to well within the calibration uncertainty of the SCUBA-2 data.

I homogenised this dataset to a common resolution (that of the SPIRE 250μm image) and pixel scale. I convolved the data using the method of Aniano et al. (2011), and regrid to pixel sizes of 6 arcsec, to ensure that my maps are Nyquist sampled. This regridding is performed using Python's REPROJECT routine, which also astrometrically aligns each image.

3.2.2 GAS DATA

I also make use of atomic and molecular gas data in this study. HI is traced via the 21cm line from archival VLA[5] B, C, and D array data (reduced by Gratier et al. 2010). The CO(J=2-1) data used in this investigation was taken as part of IRAM's M33 Survey Large Program[6] (Gratier et al., 2010; Druard et al., 2014), which traces the molecular gas out to a radius of 7 kpc using IRAM's Heterodyne arRAy (HERA, Schuster et al. 2004) instrument. This data has an angular resolution of 12 arcsec and a spectral resolution of 2.6 km s^{-1}. These maps can be seen in Fig. 3.2.

3.3 GMC CATALOGUE

3.3.1 IDENTIFYING GMCS

Disentangling sources from regions of complex emission is a non-trivial task, and several source extraction methods have been developed to achieve this goal (see Men'shchikov et al. 2012 for descriptions of a number of source extraction algorithms). Initial testing using the algorithms CLUMPFIND (Williams et al., 1994) and FELLWALKER (Berry 2015, an algorithm developed to deal with some issues in CLUMPFIND) revealed shortcomings in these more traditional methods – given that much of the emission at these wavelengths is diffuse, the entire galaxy becomes segmented into unreasonably large "sources". I also attempted source extraction using SEXTRACTOR (Bertin & Arnouts, 1996), which can deblend overlapping sources, but this source extraction software only produces an ellipse, and so fails to take into account the irregular nature of many of the structures I am attempting to recover. The structure

---

[5] `https://science.nrao.edu/facilities/vla/archive/index`

[6] `http://www.iram.fr/ILPA/LP006/`

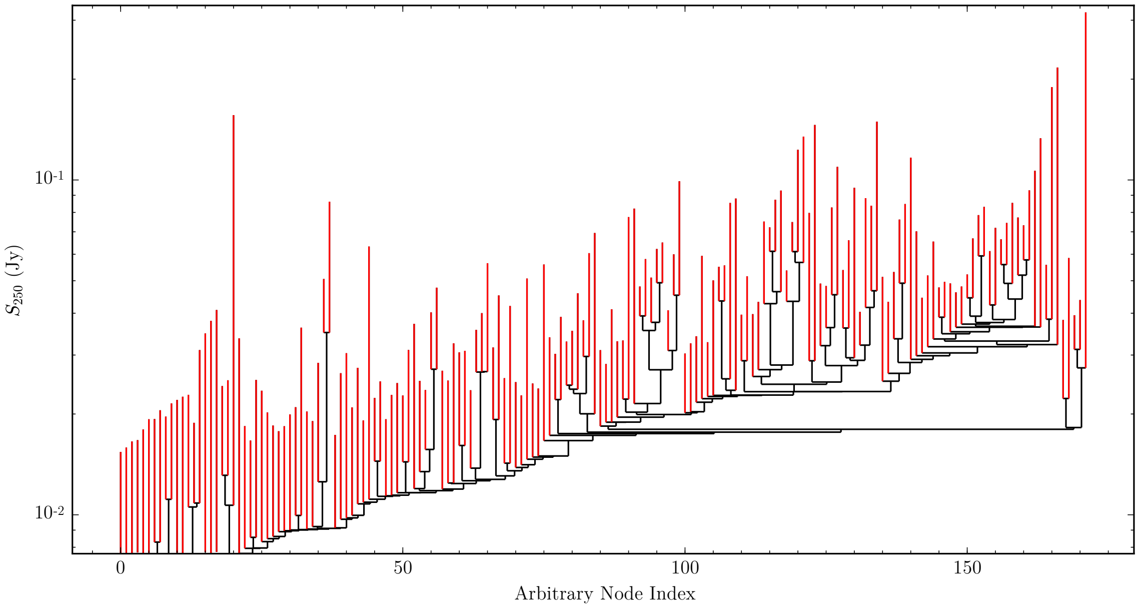

Figure 3.3: Dendrogram showing SPIRE 250μm flux in M33. The top of each vertical line indicates a leaf node (highlighted in red), which I assume to be the GMCs.

of a galaxy is hierarchical and interconnected, and so computing a dendrogram of this structure is one way of identifying sources within the galaxy (Rosolowsky et al., 2008); dendrograms also have the additional benefit of extracting nested structure, which is vital in this study. In this work, I use the ASTRODENDRO dendrogram package[7]. I refer the readers to the documentation on the ASTRODENDRO website for a more thorough description of the algorithm, but briefly a tree is constructed by arranging the pixels in order of flux. The first structure is centred on the brightest pixel, then the next brightest pixel is checked to see whether it should be considered a new structure or merged into another. The code moves down in flux until neighbouring regions touch, and if the difference between the maxima is significant, these 'leaf' structures are merged into a 'branch'. The code works down to a minimum value and the structure is complete – a series of leaves connected to branches, with a 'trunk' at the bottom of each structure. These leaves are analagous to traditional sources, and it is these that I consider as the molecular clouds. For a visual comparison of these various algorithms on this data, see Appendix B. I also note that this data does not include kinematic information. This may lead to unrelated, but co-spatial along the line-of-sight, clouds becoming associated to one source when integrating along that line-of-sight. This is highlighted in Sect. 3.5.

As I wish to compute dust properties, I require sufficient data across the dust

---

[7] `http://www.dendrograms.org`

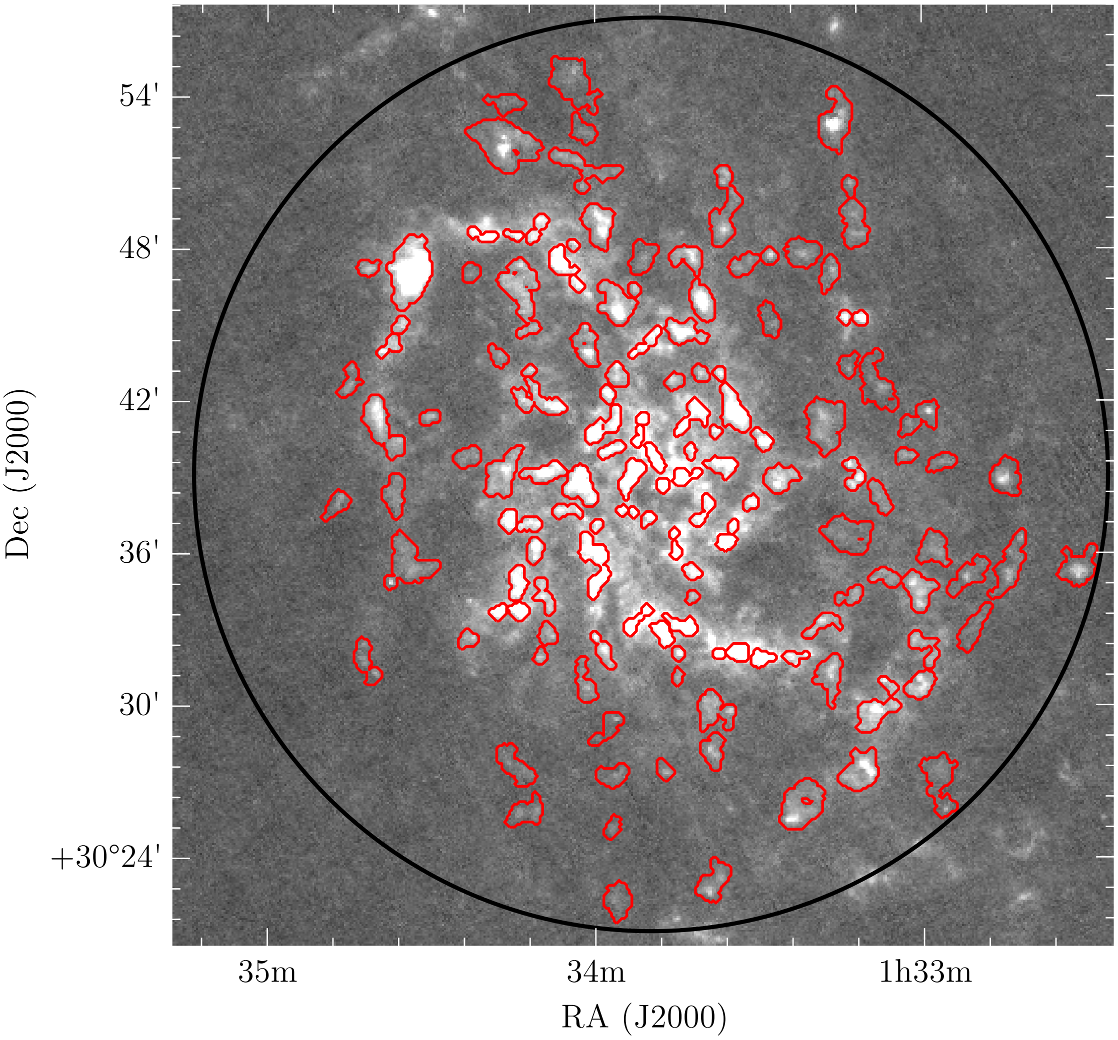

Figure 3.4: GMC contours (red) found using ASTRODENDRO overlaid on the PACS160 μm map. The black circle indicates the extent of our search radius, 18 arcmin.

continuum peak, and into longer wavelengths where the bulk of the mass is contained. I therefore choose five wavebands across this peak, as a balance between spectral coverage and spatial resolution. These are the PACS 100 and 160μm data, the SPIRE 250μm data and the SCUBA-2 450 and 850μm maps. I compute my dendrogram on the SPIRE 250μm data, as I found that after regridding and smoothing to the resolution and pixel scale of our lowest resolution data (the 250μm; a pixel scale of 8″), that this map had the highest S/N. I select only regions with flux greater than 3σ in each pixel, and regions must have a difference of greater than 3σ to be considered significant and separate. This extraction criteria is selected to be as analogous as possible to Kirk et al. (2015), in order to make my results immediately comparable to this earlier work. I also impose conditions that the region must be bigger than

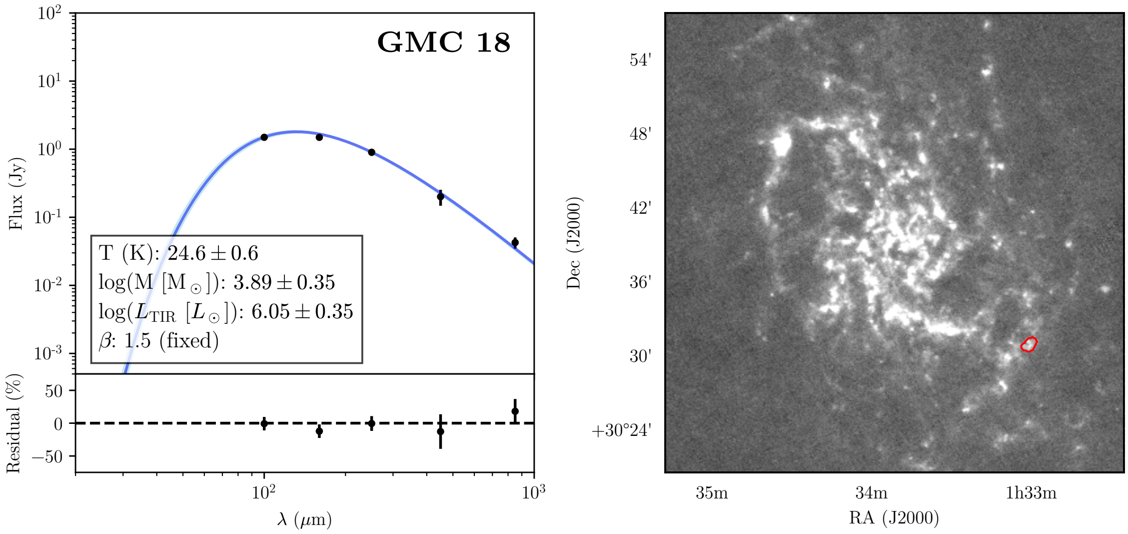

Figure 3.5: An example SED, from GMC ID 18. The left panel shows the fit, along with various parameters. The 1σ error is shown as the shaded region (not including error in κ_{500}). The right shows the contour of this cloud overlaid on the PACS 160μm map.

the SPIRE 250μm beam, and that none of these regions can touch the edge of the data. I find 165 leaves (i.e. no resolved substructure) in this dendrogram, which I assume to be GMCs. Given the sizes of these clouds (see Sect. 3.4.1), many of these "GMCs" are likely associations of several smaller clouds. The dendrogram for M33 can be seen in Fig. 3.3, and the positions of these clouds in Fig. 3.4. The majority of our analysis was performed on these clouds, although I also highlight the effect of performing this extraction on the SCUBA-2 450μm map (our highest resolution data) in the size distribution (Sect. 3.4.1).

3.3.2 FLUX EXTRACTION AND SED FITTING

Various parameters of these leaf nodes can be seen in Table C.1. For each node, I list the mean position of the structure, and the deprojected distance from the centre of M33 (01h33m50.9s, +30°39′37″; Plucinsky et al. 2008). I also calculate a FWHM of the cloud, based on its intensity-weighted second moment.

I have also computed fluxes in the PACS and SCUBA-2 bands for each of these clouds. ASTRODENDRO outputs a mask for each node, and I measured the flux within each mask in each waveband for all of the nodes. I estimated a local background from the median of the isocontour surrounding the mask, which I subtracted from the pixels before summation. This should effectively subtract any diffuse emission. An estimate of the local RMS error is given by the standard deviation of the pixels in this isocontour. The fluxes are also listed in Table C.1 – for fluxes less than 3σ, I list the flux as an upper limit. The error listed in this table reflects only the RMS error; I have not included any calibration error in this value.

For the clouds with fluxes $>3\sigma$ in 3 or more bands (in this case, every cloud), I fit a single modified blackbody (MBB) of the form

$$S_\nu = \frac{\kappa_\nu \mathrm{M_{dust}} B(\nu, T_{\mathrm{dust}})}{D^2}, \tag{3.3}$$

where S_ν is the flux at frequency ν, κ_ν is dust absorption coefficient at frequency ν, i.e.

$$\kappa_\nu = \kappa_{\nu_0} \left(\frac{\nu}{\nu_0}\right)^\beta, \tag{3.4}$$

$\mathrm{M_{dust}}$ is the dust mass, $B(\nu, T_{\mathrm{dust}})$ is the Planck function at frequency ν and dust temperature T_{dust}, and D is the distance to the source. I normalise κ_ν using the value calculated by Clark et al. (2016), $\kappa_{500} = 0.051^{+0.070}_{-0.026}\,\mathrm{m^2\,kg^{-1}}$. I note that this only holds true for the optically thin case, but as the theoretically expected value for when the optical depth becomes unity is 100μm (Draine, 2006), and experimentally only affects points shorter than 50μm (Casey, 2012), this is a reasonable assumption for my fits. To minimise the number of free parameters in this fit, I assumed a fixed β of 1.5, which Tabatabaei et al. (2014) find to be a good fit to M33 using both one- and two-temperature MBB fitting. I include correlated uncertainties in the PACS and SPIRE bands (as the SCUBA-2 450μm data includes the SPIRE 500μm map). This is implemented by employing the full covariance matrix. I performed my fitting within an MCMC framework using EMCEE[8], and I quote the errors as the 84th percentile minus the 50th percentile, as I find that the errors are symmetric. My initial guess for dust mass and temperature were set from a simple least-squares fit. I allowed the dust temperature to freely vary from 0 to 200K, and the dust mass from 0 to 10^{13} $\mathrm{M_\odot}$. An example SED fit is shown in Fig. 3.5. I also calculated the total infrared (TIR) luminosity of this cloud by integrating the MBB from 3-1100μm. I find that these clouds contribute around 50% of the total dust luminosity of M33, despite only occupying around 20% of the area. This indicates that these clouds are, in general, compact and bright in their dust emission. All of my derived SED parameters are given in Table D.1. The dominant error in the dust mass and luminosity is error in κ_{500} ($\sim$0.32 dex). As this is a systematic error I do not include this in Table D.1. I

---

[8] `http://dfm.io/emcee/current/`

do, however, include this uncertainty in my analysis. I expect the dust mass to be relatively invariant to changes in β (e.g. Smith et al., 2012), and so I believe that imposing that this parameter be fixed will not change the results significantly.

I also include a measurement of the CO(J=2–1) luminosity (in K km s^{-1}) in Table D.1. Finally, I calculated HI surface densities (in M$_\odot$ pc^{-2}) of each of my sources. A surface density is calculated, assuming (Rohlfs & Wilson, 1996)

$$\Sigma_{\mathrm{HI}} = 1.8 \times 10^{18}\,\mathrm{cm}^{-2}/(\mathrm{K\ km\ s}^{-1}). \tag{3.5}$$

With this gas data, I performed the same procedure as for the FIR/sub-mm flux extraction – convolution and regridding to the same pixel scale, as well as local background subtraction. Similarly to the FIR/sub-mm fluxes, I list upper limits for intensities less than 3σ.

3.4 CLOUD PROPERTIES

3.4.1 SIZE DISTRIBUTION

For each source, I take the ellipse enclosing the cloud as computed by ASTRODENDRO from the half-width at half maximum (HWHM) of the second moments. I calculate a FWHM for each cloud from the average of these HWHM. The size distribution of the clouds can be seen as a Kernel Density Estimator (KDE) plot in Fig. 3.6. The median size of these clouds is 105 pc, close to the FWHM of the SPIRE 250μm beam, and so may initially be assumed to be complexes of smaller clouds. However, when performing the same extraction on our higher-resolution SCUBA-2 450μm and 850μm data, which has a minimum FWHM of 28 and 56 pc as defined in our extraction criteria, very similar trends are seen (Fig. 3.6). This would indicate that these objects are either (a) genuinely more extended than seen in the MW or (b) complexes of many very small clouds, rather than several larger clouds. Roman-Duval et al. (2010) find cloud sizes of 0.2 to 35pc, with a mean size of ∼8pc. More recently, Miville-Deschênes et al. (2017) find MW cloud sizes up to ∼ 500pc, with a mean size of ∼30pc. Given these results from the MW, this would indicate these sources are likely complexes of smaller clouds. Additionally, comparisons to CO surveys (see Sect. 3.5) show that scenario (b) is more likely the case.

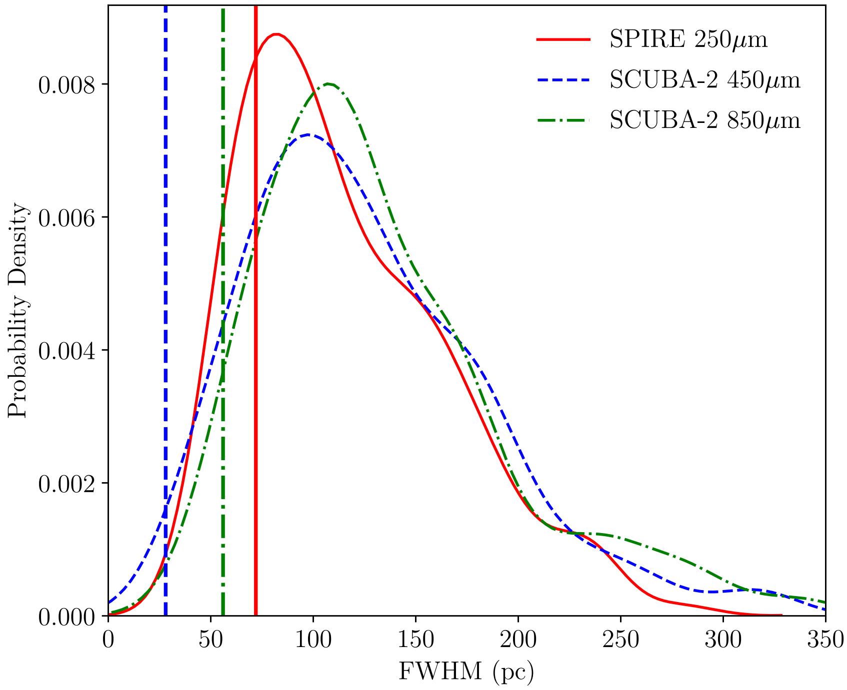

Figure 3.6: Kernel Density Estimator plot for size distribution of GMCs in M33. The red solid indicates the distribution of the SPIRE 250μm sources, the blue dashed line the SCUBA-2 450μm sources, the green dot-dashed line the SCUBA-2 850μm. The equivalently coloured vertical line shows the beam size for the particular instrument (which I enforce the clouds to be larger than).

3.4.2 DUST TEMPERATURES

One of the fitted parameters in the MBB is the dust temperature, and the distribution of this is shown in Fig 3.7. I find that the clouds have a median temperature of 23 ± 4K, somewhat warmer than found for clouds in M31, which have a dust temperature of 18 ± 2K (Kirk et al., 2015). I find that applying my fitting procedure to the cloud fluxes of Kirk et al. (2015) produces similar dust masses and temperatures (within errors), and so this variation in dust temperature is not due to differences in MBB fitting. I instead attribute this to the fact that M33 is much more actively star-forming than M31 (Heyer et al., 2004), and thus this dust is more strongly irradiated by these young stars. The distributions of cloud FWHMs (Fig. 3.6) and dust temperature (Fig. 3.7) look somewhat similar. However, a calculation of the Kendall rank correlation coefficient (Kendall, 1938), where $\tau = +1$ indicates a perfect correlation, and $\tau = -1$ a perfect anti-correlation gives a weak anti-correlation of -0.17. A two-sample Kolmogorov-Smirnov test gives a p-value $\ll$1%, indicating that these two distributions are significantly different.

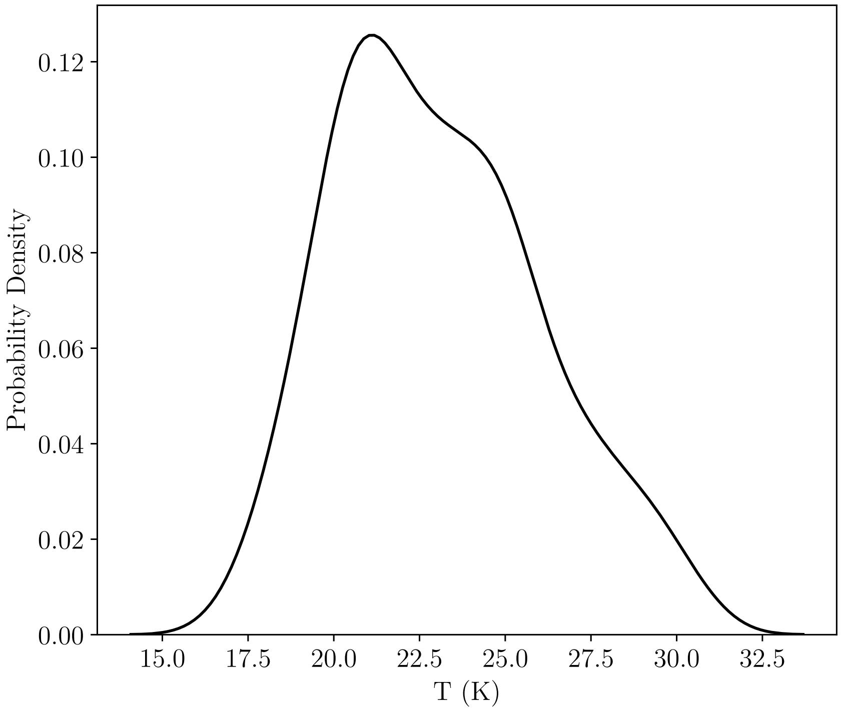

Figure 3.7: Kernel Density Estimator plot for temperature distribution of GMCs in M33.

3.4.3 CLOUD MASSES

3.4.3.1 Calculating Masses

I simultaneously calculate a gas-to-dust ratio (GDR) and CO conversion factor ($\alpha_{\rm CO}$) in a fashion similar to that of Sandstrom et al. (2013). A dust mass surface density can be converted to a total gas mass surface density via

$$\mathrm{GDR} \times \Sigma_{\rm Dust} = \Sigma_{\rm HI} + \alpha_{\rm CO} \times I_{\rm CO}. \tag{3.6}$$

Here, surface densities are in $\mathrm{M_\odot\,pc^{-2}}$, $\alpha_{\rm CO}$ is in $\mathrm{M_\odot\,pc^{-2}\,(K\,km\,s^{-1})^{-1}}$, and $I_{\rm CO}$ is in $\mathrm{K\,km\,s^{-1}}$. Sandstrom et al. (2013) find the best fit of these two unknown parameters simultaneously by minimising the scatter in the log of the dust to gas ratio (DGR), and we perform this fitting using an MCMC analysis, accounting for errors in the dust mass surface density, HI surface density and CO intensity.

I performed this fitting by grouping the clouds into bins of increasing galactocentric radius. Sandstrom et al. (2013) find that $\alpha_{\rm CO}$ and the GDR are reasonably invariant with galactocentric radius within a galaxy, so these quantities should be

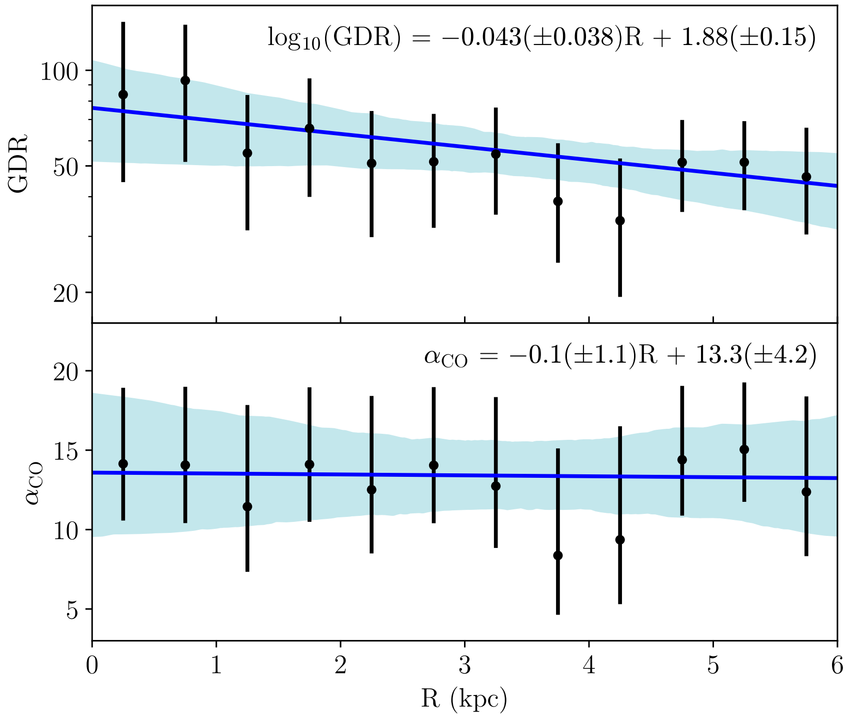

Figure 3.8: *Top:* radial variation in the GDR of M33. The blue line shows the median fit to the data, the blue shaded region the 1σ errors on this fit. *Bottom:* radial variation in $\alpha_{\rm CO}$. The line and shaded region have the same meanings as the top panel.

constant within each annulus. I split the clouds into radial bins of 0.5 kpc and simultaneously fit $\alpha_{\rm CO}$ and GDR. The results of this can be seen in Fig. 3.8, and the slope for the GDR is given by

$$\log_{10}(\mathrm{GDR}) = -0.043(\pm 0.038)\,\mathrm{R[kpc]} + 1.88(\pm 0.15). \tag{3.7}$$

My maximum GDR is somewhat lower than seen in nearby galaxies (Sandstrom et al., 2013), with a value of around 90. However, variation in κ_ν can easily lead to huge variations in dust mass. Given that the adopted κ_ν is on the low end of literature values (Clark et al., 2016), this is not unexpected. However, I note that whilst the adopted κ_ν of Clark et al. (2016) is lower than many other literature estimates, it is still compatible with the κ_ν of Draine & Li (2007), which Sandstrom et al. (2013) use in their work. Thus, this low value for the GDR cannot simply be attributed to my choice of κ_ν. Using this calculated GDR, I transformed the dust mass into a total gas mass using Equation 3.7 and then calculated a total cloud mass (the sum of the dust and gas mass). The mass distribution can be seen in the left panel of Fig. 3.9.

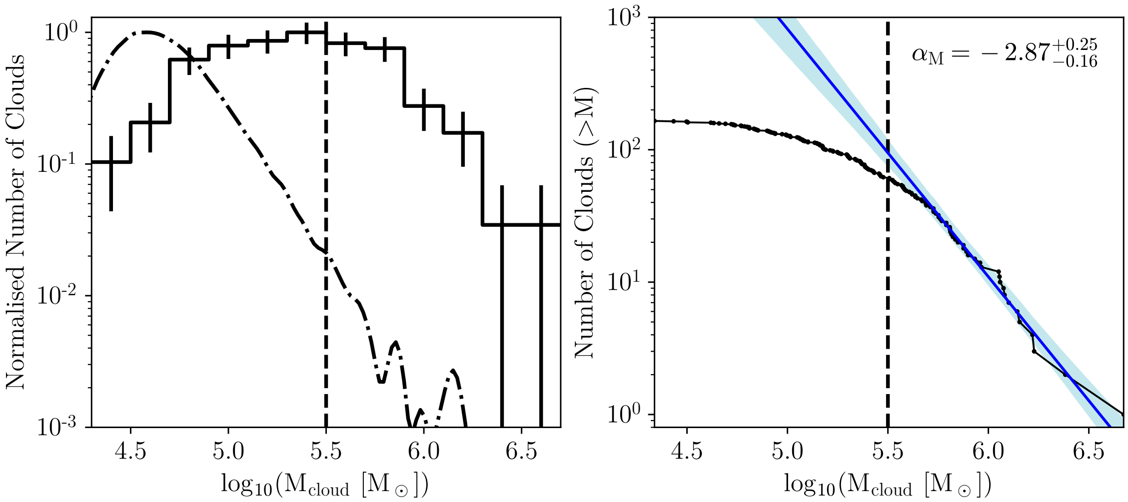

Figure 3.9: *Left:* Cloud mass distribution for clouds in M33. The dot-dash line shows the point source sensitivity. The vertical dashed line shows the 95% completeness limit. Both of these distributions are normalised such that the peak is unity. *Right:* Cumulative cloud mass distribution for clouds in M33. The vertical dashed line again represents the 95% completeness limit, above which we fit the power-law relationship. The blue line shows the power-law fit to the data points above $10^{5.5}M_\odot$. 1σ errorbars on this power-law fit are shown as the blue shaded region.

I also calculated α_{CO} simultaneously radially, and we show this in the bottom panel of Fig. 3.8. This is a CO conversion factor for the J=1–0 line, assuming CO(2–1)/CO(1–0) = 0.7 (Sandstrom et al., 2013). There is little radial variation, unlike the GDR, but the value of α_{CO} is much higher than seen in other, nearby galaxies ($3.1\,M_\odot\,pc^{-2}$ with a standard deviation of 0.3 dex, Sandstrom et al., 2013). Even given variation in κ_ν that could decrease these values by a factor ~2, this would indicate a CO conversion factor, α_{CO}, that is around a factor of 3 higher than seen in other, nearby galaxies. This is likely due to the subsolar metallicity of M33, with CO molecules becoming more easily dissociated by UV radiation at low metallicity (Glover & Clark, 2016). Based on their simulations, the CO conversion factor is expected to be around twice that of the MW ($4.4\,M_\odot\,pc^{-2}$, Solomon et al., 1987) . Given the errors on the α_{CO} I measure for M33, this would make this α_{CO} consistent with these simulations. Work by Roman-Duval et al. (2014) finds a similar α_{CO} in the LMC, which has similar metallicity to M33.

I estimated the point source mass sensitivity by taking a limiting flux of 68.9mJy (a 3σ point source as defined by the dendrogram extraction criteria), and sampled the GDR and dust temperature from distributions given by the distributions of our clouds (T = 23 ± 4K, log(GDR) = 1.74 ± 0.09). Bootstrapping this 10,000 times, we find a point-source sensitivity of $4.63^{+0.28}_{-0.22}\ \log_{10}(\mathrm{M}_\odot)$. This is shown in Fig. 3.9, and cannot fully account for the deviation from a power-law at the low-end of the mass distribution.

I next estimated the completeness by injecting point sources of given cloud mass into a fake map with the same noise properties as the SPIRE 250μm data, and a background similar to that of M33. I sample the dust temperature and GDR as with the point source sensitivity, and inject 100 sources of each mass into this map. I performed the same extraction criteria as I did with the real data and calculated the completeness for each mass. I find that I am 95% complete above a mass of $10^{5.5}$ $\mathrm{M}_\odot$. This means that the observed downturn is simply due to incompleteness, and is *not* a genuine turnover. However, I must stress that this is only an approximation of the true completeness limit. I have here assumed only point sources present in a constant background, but given that these sources are extended, and embedded in a complex background, the true completeness limit will be a function of mass, radius, cloud shape and position within the map. Accounting for this complex completeness is beyond the scope of this work.

3.4.3.2 Power-Law Fitting

I fit a power-law of the form $N(\mathrm{M}) \propto \mathrm{M}^{\alpha_\mathrm{M}}$ to the high-end of the mass distribution. However, in a standard distribution the fit can become biased by small number statistics at high-mass (Maschberger & Kroupa, 2009), and so it is more reliable to fit to the cumulative mass distribution (shown in the right panel of Fig. 3.9). In this case, the power-law takes the form $N(>\mathrm{M}) \propto \mathrm{M}^{\alpha_\mathrm{M}-1}$. To avoid incompleteness, I fit only to values with a cloud mass greater than $10^{5.5}\mathrm{M}_\odot$. I find a value of α_M of $-2.83^{+0.24}_{-0.15}$, steeper than the value of $\alpha_\mathrm{M} = -2.0 \pm 0.1$ found previously in M33 by Gratier et al. (2012) using CO(J=2–1), and -2.6 ± 0.3 from the CO(J=1–0) work of Engargiola et al. (2003). Work by Bigiel et al. (2010) based on CARMA CO(J=1-0) observations of eight GMCs has hinted at a steeper slope in the outskirts of M33, and our calculated slope appears to confirm this. I also find that this value is steeper than molecular clouds in the MW, which has an exponent of around -1.5 (e.g. Sanders et al. 1985; Solomon et al. 1979). The slope is also steeper than that found in M31 (-2.34 ± 0.21, Kirk et al. 2015, -2.55 ± 0.2, Blitz et al. 2007). The steepness of this slope appears to indicate that M33 is more dominated by smaller clouds than in, e.g., the MW. Given that Gratier et al. (2012) use the CO luminosity as a proxy for molecular hydrogen, whilst the dust content should be an independent tracer of total

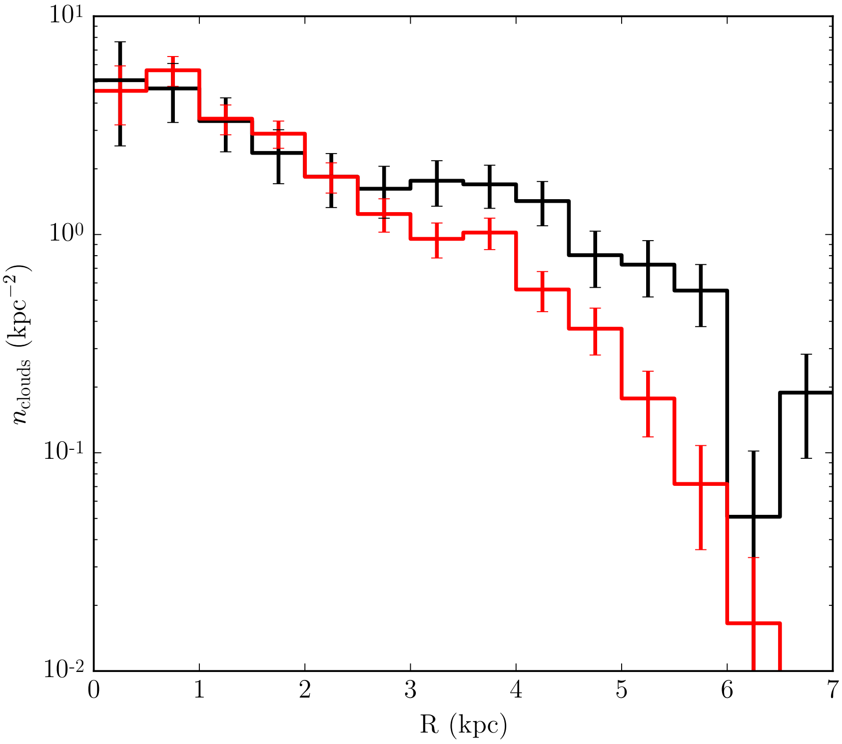

Figure 3.10: Number density of GMCs with galactocentric radius. The black line indicates the clouds in my study, the red from the work of Gratier et al. (2012). The curves are normalised to the level of the dust-selected number density of clouds at the 2-2.5 kpc bin.

gas content, we can rule out this steep slope being due to a lower CO intensity per H_2. It would appear that M33 is intrinsically poorer at cloud assembly than other local spirals.

The efficiency of cloud assembly has been linked to a variety of processes. The amplitude of the spiral density wave can have an effect on the GMC population (e.g. Shu et al. 1972). However, given that recent modelling work has shown that the spiral arms of M33 are most likely driven by gravitational instabilities (Dobbs et al., 2018), it seems unlikely that the density wave is the primary factor affecting the GMC population. The interstellar pressure of gas (Elmegreen & Parravano, 1994; Blitz & Rosolowsky, 2006) may also be a factor. However, work has shown that there is higher interstellar pressure in M33 than in the MW (Kasparova & Zasov, 2008), so given this hypothesis we would expect more massive clouds. We can therefore rule out the interstellar pressure as the main driver of this inefficient cloud formation. Alternatively, metallicity can play a role in the conversion of H I to H_2 (Krumholz et al., 2008). Given the subsolar metallicity of M33, we would expect this conversion to be less efficient, and therefore cloud formation similarly inefficient. Finally, it is believed that H_2 can form from merging HI clouds (e.g. Heitsch et al. 2005), so we may expect from larger HI velocity dispersions, more massive clouds may form. The average HI velocity dispersion in M33 is of the order $13\,\mathrm{km\,s^{-1}}$, with little radial variation (Corbelli et al., 2018), whilst the outer MW shows much more turbulent HI gas, with velocity dispersions of $74\,\mathrm{km\,s^{-1}}$ (Kalberla & Dedes, 2008). My results are unable to distinguish which of these two mechanisms are the main driving force behind this inefficient cloud formation, but it is clear that the cloud mass distribution is significantly different in M33 than the other massive spirals in our Local Group. Perhaps this is due to the higher radiation pressure from elevated star formation in M33 breaking these larger clouds up more readily than we see in other galaxies. The exact cause of this is currently unclear, but high-resolution surveys of many galaxies with a wide range of properties will be able to explain the diversity in cloud populations seen even between the galaxies of our Local Group. This result also highlights the importance of multiple independent tracers of the cloud population – using CO alone gives significantly different exponents, even for different rotational transitions of the CO line.

3.4.4 RADIAL VARIATION IN CLOUD PROPERTIES

I also investigated any radial variation in the cloud properties. Fig. 3.10 shows the number density (the number of clouds per annular area) of these clouds with galactocentric radius. I see that up to a radius of 2.5 kpc, the cloud distribution and the GMC distribution of Gratier et al. (2012) agree very well – however, after ∼3 kpc, the distribution of GMCs from Gratier et al. (2012) is systematically lower. I believe that this is due to the fact that the data used in this study covers a wider area than the CO map on which they perform their extraction. As they perform this analysis on an incomplete map of M33 (only the area covered by the *Herschel* PACS and Heterodyne Instrument for the Far Infrared [HIFI] spectrometers, see Fig. 1 of Gratier et al. 2010 for the area covered), they do not map the entire disk of M33. I would suggest my distribution is therefore less biased, and gives a more representative view of the GMC number density. Along with a peak in the distribution at the centre of the galaxy, there is a step in this distribution from around 2 kpc to 4 kpc radius, which corresponds to the positions of the spiral arms in M33. However, the spiral arms are less pronounced in this distribution than M31 (Kirk et al., 2015), where the positions of the spiral arms have clear peaks, and the SFR in the rest of M31 is very low.

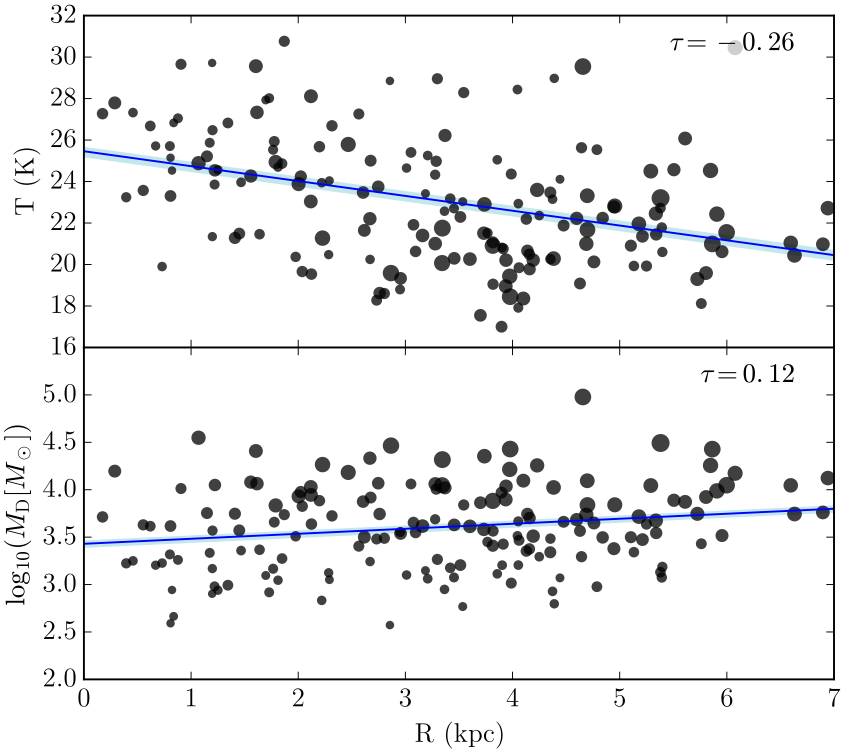

Figure 3.11: Radial variation in fitted dust temperature and dust mass. Point size is based on the FWHM of the cloud. In each case, the Kendall rank correlation coefficient (τ) is given in the top right. For clarity, errors are not shown but are on the order of 5% for dust temperature and 10% for dust mass. All values and errors are given in Table D.1.

I also investigated the radial variation in our two fitted MBB properties – dust temperature and dust mass (Fig. 3.11). The fitting is performed using EMCEE, and accounts for errors in the y-axis values. In both cases, we see that the radial correlations are weak – in the case of dust temperature, weakly negative (i.e. dust temperatures are lower at higher galactocentric radii), and weakly positive in the case of dust mass. I find a dust temperature gradient $-0.71 \pm 0.01\,\mathrm{K\,kpc^{-1}}$, and a dust mass gradient of $0.053 \pm 0.001\,\mathrm{dex\,kpc^{-1}}$. The decrease in dust temperature is naturally explained by a general decrease in the strength of the interstellar radiation field (ISRF) at increasing galactocentric radius (Rice et al., 1990). This gradient is also similar to that seen by Tabatabaei et al. (2014), when considering the global properties of M33. The invariance in dust mass is likely due to a balance of generally more compact but brighter clouds in the centre of the galaxy, whereas in the outskirts we tend to find somewhat more diffuse (but extended) sources.

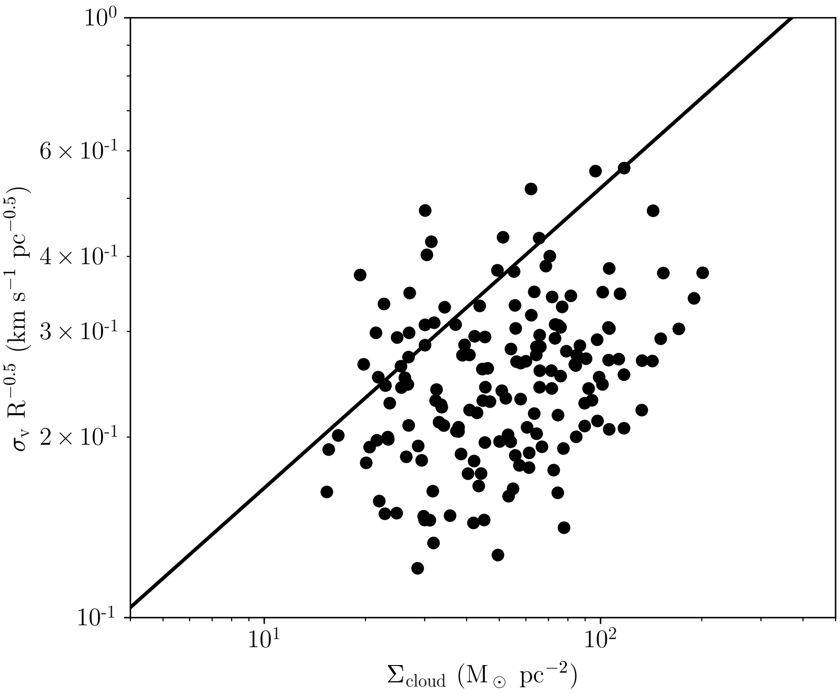

Figure 3.12: The ratio of velocity dispersion to the square root of the cloud radius as a function of the cloud surface density (black points). The black line shows the expected value for virialised clouds.

3.5 COMPARISON TO CO

Using kinematic CO data, I can relate the properties of these clouds to the observed scaling relations of Larson (1981). This can be neatly represented in the plane of the cloud surface density ($\Sigma_{\rm cloud}$) with the ratio of the velocity dispersion ($\sigma_{\rm v}$) to the square root of the cloud radius (R), as demonstrated in Heyer et al. (2009). If these clouds are ideally virialised (Larson's second law), and the velocity dispersion is related to the cloud's radius as $\sigma_{\rm v} \propto R^{1/2}$ (Larson's first law), then it can be shown

$$\sigma_{\rm v} = \left(\frac{\pi G}{5}\right)^{1/2} \Sigma^{1/2} R^{1/2}. \tag{3.8}$$

Larson's third law states that $\Sigma_{\rm cloud}$ is approximately equal for any cloud, so we would expect little dynamic range in this quantity. We calculate the velocity dispersion from the CO data cube of Gratier et al. (2012), following the "equivalent width" as defined in Heyer et al. (2001):

$$\sigma_{\rm v} = \frac{I_{\rm CO}}{\sqrt{2\pi} T_{\rm peak}}, \tag{3.9}$$

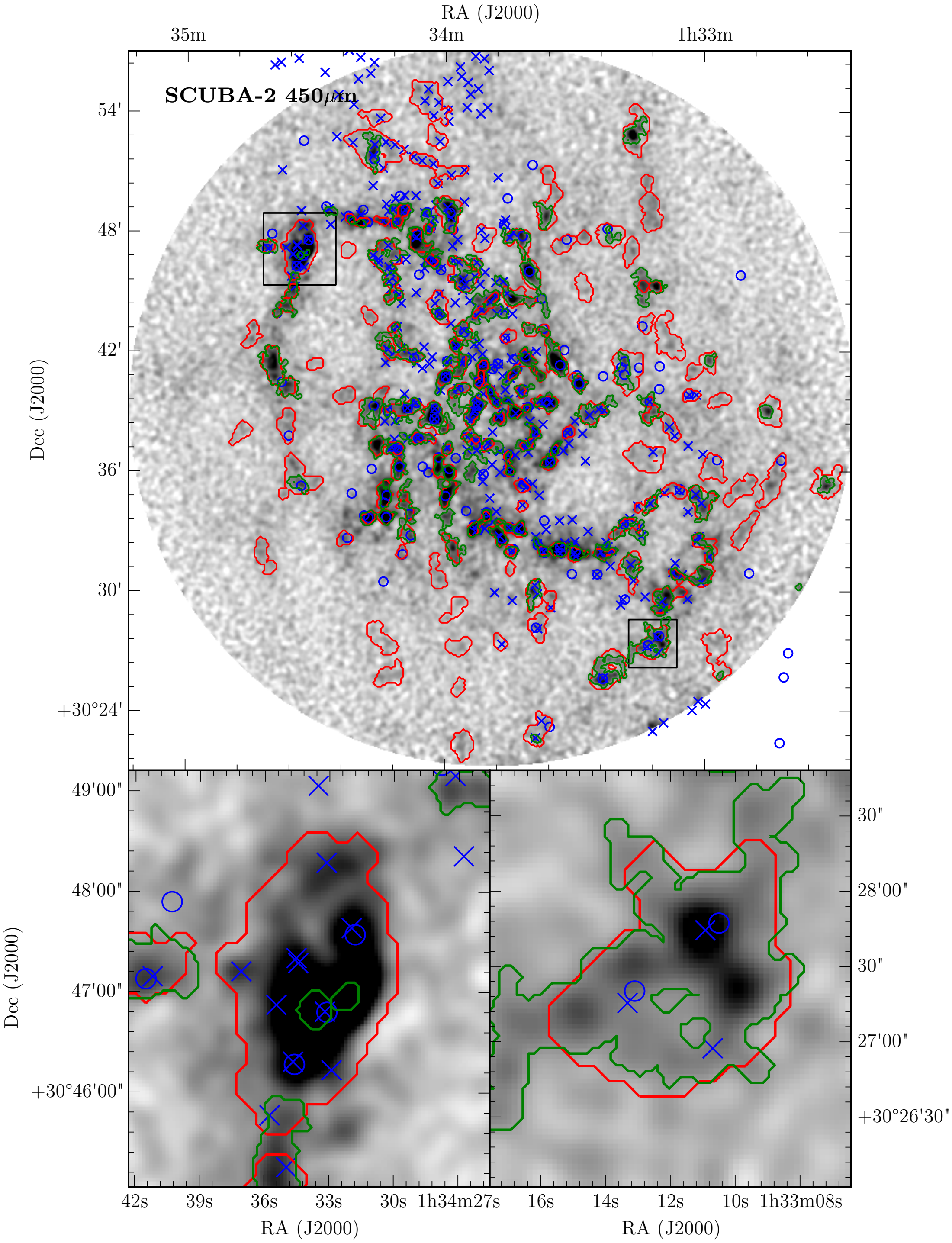

Figure 3.13: *Top:* Comparison to earlier GMC studies of M33, overlaid on the slightly smoothed SCUBA-2 450μm data. The red contours are our clouds defined from the SPIRE 250μm source extraction, the green contours the SCUBA-2 450μm source extraction, the blue crosses the GMCs of Gratier et al. (2012) from CO(J=2-1), and the blue circles the GMCs from CO(J=1-0) of Engargiola et al. (2003). *Lower left:* Zoom-in of top-left rectangle (NGC 604). *Lower right:* Zoom-in of lower-right rectangle. The symbols used are the same as in the top panel.

with $I_{\rm CO}$ the integrated CO in each leaf contour, and $T_{\rm peak}$ the peak line intensity. This relationship is shown in Fig. 3.12. We find that there is a weak correlation ($\tau = 0.21$) between $\sigma_{\rm v}/R^{0.5}$ and $\Sigma_{\rm cloud}$ for our clouds. This is somewhat weaker than that found by Heyer et al. (2009) for a selection of clouds in the MW, but still showing a dependence of $\sigma_{\rm v}/R^{0.5}$ on the gas surface density. Given the proximity of these clouds to the line of virial equilibrium (the median deviation below this line is a factor of 1.5), I conclude that these clouds are likely ideally virialised.

Finally, I make comparison to the locations of GMCs identified with earlier CO studies. Fig. 3.13 shows the positions of our clouds against those of Gratier et al. (2010) and Engargiola et al. (2003). These earlier studies have somewhat better resolution than I have achieved in this investiation (18 arcsec versus 12 arcsec), but clearly the cloud distribution is broadly similar, indicating that these particularly dusty regions are indeed associated with GMCs. However, what often appears to be a single region, even in the 450μm data, is identified as several clouds in the CO data. Fig. 3.13 shows that at the 450μm resolution, larger sources are beginning to break up into smaller clouds, but this is not statistically significant enough for the extraction criteria to define them as separate leaves. Some of these sources may also be co-spatial along the line-of-sight of the galaxy, but given no kinematic information I cannot separate these as in the CO surveys. There are also a significant number of clouds for each study that do not have a counterpart in any other. This, again, highlights that the choice of gas tracer has an impact on the clouds detected, and that multiple tracers should be employed.

One notable difference between my detected sources and earlier CO surveys is that the works of Engargiola et al. (2003) and Gratier et al. (2012) find a dearth of massive clouds beyond a galactocentric radius of 4kpc. However, I find a nearly flat distribution of dust mass with galactocentric radius. Given that I find my clouds to be co-spatial to these earlier works in the inner region of M33, I would expect these earlier surveys to detect these clouds. I do not believe this is a selection effect due to noise in these CO maps. Gratier et al. (2012) map an area significantly beyond 4kpc, with similar noise as in the centre of the map (see Fig. 3 of Gratier et al. 2010). Engargiola et al. (2003) estimate their map to be complete out to 5.2kpc and more than 50% complete up to 8kpc, so this variation cannot simply be attributed to completeness. Results from *Planck* (Planck Collaboration et al., 2011) have shown a significant reservoir of molecular hydrogen that is not traced by CO. Gratier et al. (2017) find that this “CO-dark” gas forms around 50% of the total molecular hydrogen mass of M33. The amount of CO dark gas is also expected to increase at lower metallicity (such as in the outskirts of M33), where the CO is more susceptible to photo-dissociation. Given that the dust continuum is not subject to these same caveats, the dust may offer a more representative view of the cloud population than CO surveys in these lower-metallicity environments. However, it is important to note that particularly at very low metallicities, the dust properties of these galaxies may be significantly different to that of the MW (e.g. Chastenet et al., 2017), and taking into account these differences are vital for properly measuring the dust mass.

3.6 CONCLUSIONS

In this chapter, I have combined archival *Herschel* FIR and sub-mm data with deep SCUBA-2 observations to probe the properties of GMCs using their dust content. Using wavelengths from 100 to 850μm, I have probed the cold dust continuum emission of these sources. I performed source extraction using dendrograms, which found a total of 165 GMCs with sizes (FWHM) of 46-280 pc, and a median size of 105 pc. By fitting a one-temperature MBB, I have calculated the dust mass and temperature for these 165 sources, and compared this to archival CO and HI data. Using a method similar to that of Sandstrom et al. (2013), I find a weak radial variation in the GDR of these sources, and use this GDR to calculate a total cloud mass.

These cloud masses span the range of $10^4 - 10^7 \mathrm{M}_\odot$, and the mass function can be fit with a power law slope proportional to $\mathrm{M}^{-2.84}$, steeper than seen in previous CO studies of M33 and the MW. Whilst I can rule out pressure as the major driver of this inefficient cloud assembly, I am unable to distinguish whether metallicity or turbulent HI velocities contribute more to this inefficiency. The dust temperatures of these clouds range from 17-32 K, and dust masses from 10^2-$10^5\,\mathrm{M}_\odot$. In terms of these clouds' dust properties, I find only weak radial trends with dust mass and dust temperature.

A comparison to CO data shows an α_{CO} factor several times higher than found in nearby galaxies. I attribute this to the subsolar metallicity of M33, where CO is likely a less suitable tracer of molecular hydrogen. The much higher α_{CO} found in this work is consistent with numerical simulations of subsolar metallicity galaxies (Glover & Clark, 2016). Alternatively, α_{CO} may indeed be close to the values calculated by Sandstrom et al. (2013), and this much higher value simply reflecting a genuine variation in κ_d – Clark et al. (2019) has recently reported both inter- and intra-galaxy variation in this coefficient, and this may be the case here. However, since the quantities are degenerate it is impossible to say which is the case from this study. I have examined these clouds in the framework of Larson's scaling relations, and I find a dependence of $\sigma_{\rm v}/R^{0.5}$ with the gas surface density, much like that of Heyer et al. (2009). It would also appear that my clouds are ideally virialised (to within a median factor of 1.5). Finally, a comparison with earlier CO studies shows that the GMCs I am detecting and those found using CO data are generally co-spatial, but due to the limited resolution of the SPIRE 250μm data that we convolve and regrid to, the crowded complexes of clouds seen in this CO data are generally confused into one large cloud in my source extraction. I also find clouds beyond 4kpc in galactocentric radius, unlike earlier CO surveys. This may be due to the CO being a poorer tracer of molecular hydrogen at these larger distances (and lower metallicities), and these clouds being dominated by CO-dark gas.

CHAPTER 4

RADIATIVE TRANSFER MODELLING OF M33

There is no spoon.

NEO

This chapter builds a simple radiative transfer model of M33, to provide insights into the 3D geometry of the galaxy, as well as local dust heating mechanisms. This work is published in Williams et al. (2019b).

4.1 INTRODUCTION

Despite only contributing around 1% of the mass of the interstellar medium (ISM) of a galaxy, dust absorbs, scatters, and reprocesses around 30% of the starlight in star-forming galaxies (e.g. Popescu & Tuffs, 2002; Viaene et al., 2016). An understanding of the processes governing the interactions of stars and dust is, therefore, essential to understanding how galaxies evolve, their dust properties, and extracting important intrinsic parameters such as the star formation rate (SFR) and initial mass function (IMF). The starlight absorbed in UV and optical is re-emitted by the dust at far-infrared (FIR) and sub-mm wavelengths. Assuming only absorption of light from younger stars, the total infrared (TIR) luminosity can therefore be used as a proxy for star-formation (see, e.g. Murphy et al., 2011). Alternatively, by understanding the (wavelength-dependent) amount of dust attenuation, wavebands that suffer from attenuation can be corrected using some combination of dust measurements (e.g. Leroy et al., 2008; Hao et al., 2011), or by assuming some dust model (e.g. Charlot & Fall, 2000).

One method of modelling the light from a galaxy is by fitting an SED across these wavelengths, often using a large library of models, and several tools are available for this purpose (e.g. da Cunha et al., 2008; Noll et al., 2009; Chevallard & Charlot, 2016; Boquien et al., 2019). However, these tools assume a local dust-energy balance (i.e. that the dust emission per unit area comes from light originating from stars in that same area), which may be unsuitable for modelling sub-kpc regions (Boquien et al., 2015; Smith & Hayward, 2018). These tools also neglect the 3D geometry of a galaxy, and do not consider the propagation vectors of photons through this medium. For a complete study of the interactions of the dust and stellar components of a galaxy, 3D radiative transfer (RT) models are required, which take into account this 3D geometry and are not beholden to a per-pixel local dust-energy balance. There are a number of codes available for this purpose (see Steinacker et al. 2013 for a review of these, as well as an overview of the RT mathematics). Due to the complexity of the RT calculations, and the fact that these calculations are both non-linear and non-local, most of these codes make use of Monte Carlo (MC) or ray-tracing techniques. Unlike traditional SED fitting, RT is computationally very expensive, and thus faces its own series of challenges, such as loss of information due to projection effects, and the difficulty of applying traditional solution algorithms to these problems.

Previous work in this area has tended to focus on “simpler”, better-behaved galaxies such as edge-on (or nearly edge-on) spirals (e.g. Misiriotis et al., 2001; Bianchi, 2008; Baes et al., 2010; De Looze et al., 2012b,a; De Geyter et al., 2014, 2015; Mosenkov et al., 2016, 2018). Galaxies at lower inclinations have also been modelled, including the spiral galaxy M51 (De Looze et al., 2014) and very nearby galaxy M31 (Viaene et al., 2017b), finding significant variations in dust heating by old and young stellar populations; these works also find that the relative contributions to dust heating are both wavelength- and position-dependent. A large step in increasing the complexity of these simulations was employed by De Looze et al. (2014), using observed images to describe the distribution of stars and dust. A framework for modelling face-on galaxies is currently in development by Verstocken et al. (in prep.), which will be applied to a number of the DustPedia (Davies et al., 2017) galaxies. Different approaches to RT modelling of galaxies have also been employed – in particular, taking an axisymmetric approach, Popescu et al. (2017) have produced an

RT model for the Milky Way (MW).

In this chapter, I perform a high-resolution RT simulation of the third massive spiral galaxy in our Local Group, M33 (the Triangulum Galaxy). Being the third largest spiral on the sky, smaller only than our own MW and M31, and with a close proximity of 840kpc (Madore & Freedman, 1991), it is an excellent target of choice for high-resolution observations. M33 has been mapped across many wavelengths with a variety of observatories. Due to the wealth of high-resolution data, this galaxy is therefore naturally suited for detailed RT simulations. M33 has a roughly half-solar metallicity ($12 + \log(\mathrm{O/H}) = 8.36 \pm 0.04$, Rosolowsky & Simon 2008), and a shallow metallicity gradient. This lower metallicity makes M33 a very different environment to M31 and the MW, more analogous to younger, higher redshift galaxies. As the RT model is 3D, the data is necessarily deprojected, and a third dimension modelled, but with a moderate inclination of 56° (Regan & Vogel, 1994), the deprojection degeneracies are not as pronounced as in M31. M33 has significant star-formation across its disc (Heyer et al., 2004), with SFRs between $0.2\,\mathrm{M}_\odot\,\mathrm{yr}^{-1}$ and $0.45\,\mathrm{M}_\odot\,\mathrm{yr}^{-1}$, depending on the SFR tracer used (Verley et al., 2007; Williams et al., 2018). Given its relatively small size ($R_{25} = 30.8\,\mathrm{arcmin}$, $\sim$7.4 kpc, Paturel et al. 2003), this means that M33 has a much higher star formation efficiency than other Local Group galaxies (with a gas depletion timescale of 1.6-3.2$\times10^8$ yr; Gardan et al. 2007). Because of this active star formation, we may expect a higher contribution to the overall dust heating by younger stellar populations, but it is important not to neglect the effect of dust heating by older stellar populations.

Earlier RT studies of M33 have focussed on the nucleus (Gordon et al., 1999), and in modelling the global SED (Hermelo et al., 2016). Gordon et al. (1999) modelled only the ultraviolet to near-infrared (UV-NIR) SED of this nucleus, finding evidence of strong dust attenuation. Hermelo et al. (2016) applied the RT model of Popescu et al. (2011) which uses a series of axisymmetric models to describe the various geometries of the galaxy, and produced a global SED from UV-sub-mm wavelengths. The goal of this study was to investigate the "sub-mm excess", which appears to be present in many low-metallicity environments (e.g. Bot et al., 2010; Galametz et al., 2011; Kirkpatrick et al., 2013; Rémy-Ruyer et al., 2013). The main conclusion of this work was that likely, the sub-mm excess could be accounted for by modifying the dust grain composition. This work seeks to build on these previous works, studying the attenuation of M33 on a global level with a richer data-set than Gordon et al. (1999), as well as to modify the dust grain properties in the input model to better fit the data, and to use input geometries based on observables to produce a resolved study of many of these properties.

The layout of this chapter is as follows: I present an overview of the dataset we use in this work (Sect. 4.2), before an overview of the setup of the RT model (Sect. 4.3). I then fit this model to the observed SED of M33 (Sect. 4.4), before investigating some of the global and resolved properties of M33 (Sect. 4.5). Finally, I summarise my main conclusions in Sect. 4.6.

4.2 DATA

The data used in this work is largely the same as in Chapter 2 (Williams et al. 2018), and I refer the reader to that chapter for a more detailed description. A brief description is given here. Both FUV and NUV data was obtained (Thilker et al., 2005) by the Galaxy Evolution Explorer (GALEX; Martin et al. 2005). In the optical, Sloan Digital Sky Survey (SDSS; York et al. 2000) data was mosaicked together using primary frames from the SDSS DR13 (Alam et al., 2015), using MONTAGE[1]. A 3 square degree mosaic was created for all of the u, g, r, i, and z bands, to allow me to accurately model background variations. I also make use of Hα data (Hoopes & Walterbos, 2000), which was not included in the previous work of Williams et al. (2018) (Chapter 2). This map has a pixel size of around 2 arcsec, and covers a total field-of-view of 1.75 deg^2. This map has also been continuum-subtracted. Corrections for contamination from [N II] emission have not been carried out, although it is estimated that a maximum of 5% of the flux could result from [N II] emission in any region of the galaxy (Hoopes & Walterbos, 2000).

For near- and mid-infrared, I make use of *Spitzer* and Wide-field Infrared Survey Explorer (WISE; Wright et al. 2010) data. The former of these was taken as part of the Local Volume Legacy (LVL, Dale et al. 2009) survey, with Infrared Array Camera (IRAC, Fazio et al., 2004) data at 3.6, 4.5, 5.8 and 8 μm and Multiband Imaging Photometer (MIPS, Rieke et al., 2004) data at 24 and 70 μm. The latter covers a similar wavelength range to the former, with data at 3.4, 4.6, 12, and 22 μm, and has been mosaicked together from the ALLWISE data release, which includes both the WISE cryogenic and NEOWISE (Mainzer et al., 2011) post-cryogenic phase.

Far-infrared and sub-mm data was obtained from the *Herschel* space observatory (Pilbratt et al., 2010) and the Submillimetre Common-User Bolometer Array 2 (SCUBA-2, Holland et al., 2013) on the James Clerk Maxwell Telescope

---

[1] `http://montage.ipac.caltech.edu`

(JCMT). As part of the HerM33es (Kramer et al., 2010) open time key project, M33 was mapped by both the Photodetector Array Camera and Spectrometer (PACS, Poglitsch et al., 2010) at 100 and 160 μm, and the Spectral and Photometric Imaging REceiver (SPIRE, Griffin et al., 2010) at 250, 350, and 500 μm. The SCUBA-2 data is at 450 and 850 μm, and I use the technique presented in Smith et al. (in prep.), to maintain the high resolution offered by SCUBA-2, but add back in the large-scale structure that is lost in the data reduction process. Details of this SCUBA-2 data reduction are given in (Williams et al., 2019a, Chapter 3). I note that this SCUBA-2 data does not cover the entirety of M33, so for global flux values I use the SPIRE 500 μm and Planck 850 μm fluxes. In total, the dataset covers almost 4 orders of magnitude in wavelength, from 1516 Å to 850 μm.

For each of these images, I have performed a number of steps to make this diverse dataset homogeneous. For frames in which foreground star emission is present, I masked this using UV colours (Leroy et al., 2008). I performed a Galactic extinction correction using the prescription of Schlafly & Finkbeiner (2011), using extinction values calculated for the central position of M33, although I note that due to M33's large angular extent, this correction varies across the face of the disc, which is taken into account in the treatment of the uncertainties. However, for the GALEX bands, which are most affected by this variation in extinction correction, the difference in flux is maximally ∼3%, which is negligible when combined with the other errors considered (see Williams et al., 2018, for more details on this error analysis). I then convolved all of the data to our worst working resolution, the SPIRE 350 μm beam (which has a FWHM of 25 arcsec, corresponding to 100 pc at the distance of M33). This data is then regridded to pixels of 25 arcsec, so that they can be considered statistically independent.

With this dataset homogenized, I performed pixel-by-pixel SED fitting for the ∼19000 pixels within a radius of 60 arcmin × 70 arcmin, using the SED fitting tool MAGPHYS (da Cunha et al., 2008), and I refer readers to this work for details on the MAGPHYS model details. This allowed me to calculate a number of intrinsic quantities of the galaxy, and provides both an attenuated and unattenuated SED for each pixel, with the attenuation following the model of Charlot & Fall (2000). This modelling technique has previously been employed by Viaene et al. (2017b) for their modelling of M31, and means that I can make immediate comparison with this earlier work. I also note that Viaene et al. (2014) and Williams et al. (2018) find that MAGPHYS produces similar results to more conventional measures of, e.g., dust mass and SFR with observational data at resolutions of 130 and 100 pc, respectively. Smith

& Hayward (2018) find statistically acceptable fits to many key galaxy properties, when compared to simulated data at resolutions of 200 pc to 25 kpc.

Table 4.1: Overview of parameters in the model. Although most parameters are fixed, for free parameters I indicate the parameter search range and the wavelength these luminosities are normalised at. All luminosities are given in $L_\odot$ at the normalisation wavelength. The dust mass is given in $\mathrm{M}_\odot$. The error in each parameter is calculated by sampling the likelihood distributions, and is quoted as half the bin width if the sampled error is smaller than a single bin.

Component	Parameter	Value	Best Fit Luminosity/Mass ($L_\odot/\mathrm{M}_\odot$)
Old Stellar Disc	2D Geometry	IRAC 3.6 μm	$(2.8^{+1}_{-0.5}) \times 10^8$
	Total Luminosity	$0.4 - 4 \times 10^8$ (3.6 μm)	
	Vertical Scale Height	200 pc	
Non-Ionizing Stellar Disc	2D Geometry	GALEX FUV[1]	$(1.7 \pm 0.5) \times 10^9$
	Total Luminosity	$0.8 - 5 \times 10^9$ (0.15 μm)	
	Vertical Scale Height	100pc	
Ionizing Stars	2D Geometry	Hα + 24 μm[2]	$(3.3 \pm 1.5) \times 10^7$
	Total Luminosity	$0.3 - 3.3 \times 10^7$ (0.66 μm)	
	Vertical Scale Height	50 pc	
Dust	2D Geometry	MAGPHYS Dust Mass Map[3]	$(3.6 \pm 0.6) \times 10^6$
	Total Dust Mass	$2.5 - 7 \times 10^6$ $\mathrm{M}_\odot$	
	Vertical Scale Height	100 pc	

[1] Corrected for attenuation and diffuse emission. [2] Corrected for diffuse stellar emission. [3] Obtained from pixel-by-pixel MAGPHYS fitting.

4.3 THE 3D MODEL

For the radiative transfer simulations, I make use of SKIRT[2] (Baes et al., 2003; Camps & Baes, 2015), a publicly available, Monte Carlo RT code. This code was originally developed to investigate the effects of dust extinction on the photometry and kinematics of galaxies, but has developed to accurately model the absorption, scattering and emission of starlight by dust. It has also been tested against the major benchmarks published that the code is applicable to (e.g Camps et al., 2015). SKIRT can accept an arbitrary number of components to model, where each of these components are defined by a 3D geometry, an intrinsic spectrum, and a normalisation of this spectrum (either at a given wavelength, or a bolometric luminosity. This code allows for panchromatic RT simulations, using a wide variety of geometry models and optional modifiers for these geometries (Baes & Camps, 2015). It also provides a number of options for efficient dust grids (Saftly et al., 2014), for which I use a binary tree adaptive grid method. This means that I can effectively increase the resolution in dense regions (such as spiral arms), while minimising the computational cost of this increased resolution. The code can also model stochastically heated dust grains (Camps et al., 2015). It is also provided with parallelisation, to allow these computationally expensive simulations to run efficiently (Verstocken et al., 2017). Finally, it allows for the input of a 2D FITS image as a geometry, which was first employed by De Looze et al. (2014) in the grand-design spiral galaxy M51, and which I use to define the various geometries in this work. SKIRT deprojects and derotates this image given an inclination and position angle, and assumes that the distribution of pixel values in this input image corresponds to the density in a linear way. It then scales this map to a total density provided when setting up the geometry, and conserves total flux during deprojection. This 2D model is then given extra dimensionality by assuming an exponential profile with a provided vertical scale height (which will vary for each input geometry).

To make my notation consistent throughout this work, but comparable to earlier studies, I refer to flux densities using the symbol S, and luminosities as L. Fractions of these quantities will be referred to with the symbol $\mathcal{F}$.

---

[2] `skirt.ugent.be`

4.3.1 Model Components

A typical galaxy model setup for RT simulations composes of a bulge and thick disc containing old stars, with a thin star-forming disc containing dust and young stars (e.g. Xilouris et al., 1999; Popescu et al., 2000). I use this model with one alteration – M33 does not appear to have a bulge, at least in the traditional sense (Bothun, 1992). This claim is somewhat controversial, but for the purposes of this work I treat M33 as bulge-less. This means that I assume all of the old stars reside within the same exponential disc, rather than a population at the centre extending much further above the plane of the galaxy. I use three stellar components in the model: the first represents the old stellar populations (stars of ages around ∼8 Gyr; Sect. 4.3.1.1). The second stellar component consists of the young stars that are UV bright but dissociated from their birth clouds, and have ages around 100 Myr (Sect. 4.3.1.2). The final stellar component are the young stars still present in their birth clouds, and producing hard, ionizing radiation (Sect. 4.3.1.3). I refer to the combination of these young non-ionizing and ionizing stellar populations as “young” throughout this work. I also provide a map of the dust mass surface density, which traces the dust distribution within the galaxy (Sect. 4.3.1.4). The details of this modelling approach are based on Verstocken et al. (in prep.).

For each component, I specify an input geometry, a particular SED type and a luminosity normalisation. Along with this, I provide an input FITS image, where we have truncated the disc to $1.2\,R_{25}$ and set to 0 any pixels that correspond to those that have signal-to-noise $(S/N) < 5$ in the SPIRE 350 μm map (the map that defines our working resolution). This is to match the modelling approach of Verstocken et al. (in prep.), and removes ∼50% of pixels. This truncation removes an estimated 15% of the flux, and will remove some diffuse component of the flux. For each stellar component, I specify a metallicity of $12 + \log(O/H) = 8.36$, corresponding to the central metallicity of M33 (Rosolowsky et al., 2008). Whether M33 has a radial gradient in its metallicity is a topic of contention. Whilst Rosolowsky et al. (2008) find a slight radial gradient, Bresolin (2011) find no such significant gradient. In either case, the practical effect this would have on the form of the SED is minor. Finally, in all cases for the geometries I assume a position angle of 22.5° (de Vaucouleurs, 1959) and an inclination of 56° (Regan & Vogel, 1994). A summary of the major parameters of the model are given in Table 4.1.

4.3.1.1 Old Stellar Disc

The geometry of the old stellar component is set by the IRAC 3.6 μm image, which is generally considered to be a pure tracer of stellar mass (e.g. Zhu et al., 2010). In my initial testing, I found significant contribution from the young stellar populations at this wavelength, and so using the MAGPHYS star formation history (SFH) I make a first-order correction to separate out the contribution of these younger populations from the total luminosity. I note that as I leave the luminosity of each stellar component as a free parameter, this is only needed for a first guess. There may also be a contribution at this wavelength from hot dust heated by the young stars, but leaving the stellar luminosities as free parameters in our fitting will effectively account for this. Also, in practice the contribution from young populations is likely position-dependent, but given the coarse nature of the MAGPHYS SFH, performing robust corrections of this nature is beyond the scope of this work. I normalise the luminosity of the old stellar disc at 3.6 μm.

For a panchromatic simulation, I require an emitted luminosity at each wavelength for each component. This is done by taking a template SED, and matching the observed emission to this. In the case of this old stellar population, I make use of the Bruzual & Charlot (2003) simple stellar populations (SSPs), at an age of 8 Gyr, which I assume is the average age of these older stars. Finally, to make this geometry 3D, I assume an exponential profile for the disc, characterised by a vertical scale height. Generally, the scale height of the old stellar populations is taken to be 1/8.86 the scale length (De Geyter et al., 2013). In M33 this scale length is 1.82 ± 0.02 kpc (Kam et al., 2015), giving a scale height of $\sim$200 pc. In initial testing, I found the adopted scale height has a negligible impact on the global SED (which I fit to, see also Fig. A.1 of De Looze et al., 2014). Small variation of the ages of the SSP have a similarly small impact on the SED, and thus constraining the ages of these populations is beyond the capabilities of the simulation.

4.3.1.2 Non-Ionizing Stellar Disc

The first of the young stellar populations are the stars of age $\sim$100 Myr, which are UV bright but unable to ionize hydrogen. These stars are only attenuated by dust in the diffuse ISM, and so suffer much less from dust attenuation than those stars in the birth clouds. I used as the initial input geometry the GALEX FUV image, which traces unobscured star formation over the last 10-100 Myr (Meurer et al., 1999). I calculated an unattenuated flux for each pixel by convolving the unattenuated MAGPHYS SED with the GALEX FUV filter response, which effectively corrects for the effects of dust attenuation.

Although the FUV is dominated by these young stars, there can also be a significant amount of UV flux from more diffuse, older, stellar populations, which I correct for using the prescription of Leroy et al. (2008):

$$S_{\mathrm{FUV,\ young}} = S_{\mathrm{FUV,\ unatten}} - \alpha_{\mathrm{FUV}} S_{3.6}, \tag{4.1}$$

where $\alpha_{\mathrm{FUV}} = 3 \times 10^{-3}$, and S_x is in Jy. Given that Leroy et al. (2008) do not correct the 3.6 μm flux for young stars when calculating this factor, I use the uncorrected 3.6 μm flux. As these young stars are expected to reside within a thinner disc than the old stars, I adopt a scale height of 100 pc, half that of the old stellar component, and normalise the extinction-corrected luminosity at the FUV wavelength.

4.3.1.3 Ionizing Stars

The final stellar component consists of very young (< 10 Myr) stars that are still embedded in their birth clouds and produce hard, ionizing radiation. This radiation is difficult to trace directly, but can be inferred from Hα emission, and dust grains heated to high temperatures. To create a map of the ionizing radiation, I used a continuum-subtracted Hα map, and combined this with a map of the hot dust. The hot dust is traced via the 24μm emission, which, much like the FUV map, I corrected for a diffuse stellar component:

$$S_{24,\ \mathrm{ion}} = S_{24} - \alpha_{24} S_{3.6}. \tag{4.2}$$

These fluxes are again in Jy, and α_{24} was determined by Leroy et al. (2008) to be 0.1. This factor was calculated from a sample of nearby galaxies, but appears to be robust throughout the sample (see the discussion in their appendix D.2.4), and thus should be applicable to M33. The input geometry for the ionizing map is then

$$S_{\mathrm{H}\alpha,\mathrm{ion}} = S_{\mathrm{H}\alpha} + 0.031 S_{24,\ \mathrm{ion}}, \tag{4.3}$$

where fluxes are in ergs/s (Calzetti et al., 2007).

The SED I used for this input geometry was the MAPPINGS III (Groves et al., 2008) nebular modelling code, and I refer readers to that work for definitions of the various parameters of the model. Generally, I adopt the same parameters for this SED as De Looze et al. (2014), with a compactness of $\log C = 5.5$, and a surrounding ISM pressure of $1 \times 10^{12}\,\mathrm{K\ m^{-3}}$. However, I choose a slightly lower cloud covering factor of 0.1, half that of De Looze et al. (2014), which I found in initial testing to be a slightly better fit to the data. A lower covering factor leads to slightly colder dust, and a higher fraction of UV flux escaping, which is likely the case in low-metallicity environments. I normalise this luminosity at the wavelength of Hα. I expect the ionizing component to be in a thinner disc than the older stars, and so I used a vertical scale height of 50 pc, half that of the 100 Myr stars, and similar to the scale height of the UV discs (Combes et al., 2012).

4.3.1.4 Dust System

I created a map of the dust mass as the input component for the dust geometry. For this, I made use of pixel-by-pixel MAGPHYS fits. The dust model is more thoroughly described in da Cunha et al. (2008), but as a brief overview, MAGPHYS models Polycyclic Aromatic Hydrocarbons (PAHs) using a fixed template based on M17, which dominate at MIR wavelengths. The hot dust is modelled as a series of modified blackbodies with temperatures of 850, 250 and 130 K. I use a MAGPHYS library with extended priors (Viaene et al., 2014), meaning that the warm dust is modelled as a modified blackbodies (MBBs) with a fixed β of 1.5, and can vary from 30 to 70 K. The cold dust has a fixed β of 2 and can vary from 10 to 30 K. I use a vertical scale height of 100 pc, the same as the young, non-ionizing stellar population, and similar to the 100 μm scale height found by (Combes et al., 2012). This is also consistent with model predictions of edge-on galaxies (e.g. Xilouris et al., 1999; Bianchi, 2008; De Geyter et al., 2013).

This model implicitly assumes a per-pixel local dust-energy balance. As I discuss in Sect. 4.5.5, this is not an acceptable assumption at scales <1500 pc. However, as shown in (Williams et al., 2018, Chapter 2), there is a very tight relationship between the dust masses obtained from MAGPHYS, and from a single-temperature MBB, with a median offset of 0.02 dex and an RMS scatter of 0.10 dex for the same data (Fig. 2.9). This map is chosen because it provides a wider areal coverage of dust masses than the MBB fits. As an additional check, I also performed this comparison on a pixel-by-pixel dust map fitted using my modified THEMIS fitting routine (Appendix E), and find a similar relationship. Thus, this choice of dust map will have a negligible impact on the simulation.

I use the THEMIS dust model (Jones et al., 2013) to describe the dust in M33. This model consists of small and large amorphous hydrocarbons (sCM20 and lCM20), along with silicates (aSilM5, Köhler et al., 2014) to model the diffuse ISM of the MW. This model is primarily laboratory-based, and can naturally explain most of the features of the dust SED in the MW. However, in initial testing I found that the default THEMIS parameterisation was insufficient to fit the dust SED of M33, particularly at sub-mm wavelengths, where M33 is known to have a sub-mm excess (Hermelo et al., 2016; Relaño et al., 2018). I therefore modified THEMIS from its default parameters, which is described in more detail in Appendix E. The main results of this modification are to use a dust mix with fewer very small carbon grains, which might be expected in a low-metallicity environment where the dust grains have less shielding from the interstellar radiation field (ISRF). The fit also modifies the silicate-to-carbon ratio. In the MW, this is ∼10 but I find a mass ratio of ∼0.3, very similar to the ratios found in the LMC and SMC by Chastenet et al. (2017). This would imply that either silicate grains are readily destroyed, or do not form in great numbers. This is unlikely, and so more likely is that the silicate grains are not emissive enough in the current THEMIS model, as inferred from more recent laboratory studies (Anthony Jones, priv. comm.). Given more emissive silicate grains, a smaller mass of carbon grains would be required to explain the flatter sub-mm slope, and this ratio would be closer to that of the MW. It is, therefore, not necessarily a much higher mass of carbon grains that are required, but simply a higher mass of more emissive dust grains. The ratio of small-to-large grains is very similar to the MW, however (0.4 in the MW, 0.3 in our fitting). As shown in Fig. E.1, the parameters of the THEMIS dust model can be adjusted to fit well in the sub-mm range. The results of this fitting confirm the hypothesis of Hermelo et al. (2016), who in modelling the SED from UV to mm wavelengths, suggest different physical grain properties as the most plausible explanation for the observed sub-mm excess in M33. I use these recalculated abundances and size distributions in the SKIRT model, but within the RT simulation keep this dust mix constant throughout the entire galaxy.

4.4 MODEL FITTING

To find the best fit model, I ran a series of simulations with a variety of luminosities exploring the parameter space around our initial guesses (see Table 4.1). As these simulations are computationally expensive, and I can only explore the parameter space using a grid method, we fix all of the parameters apart from the various

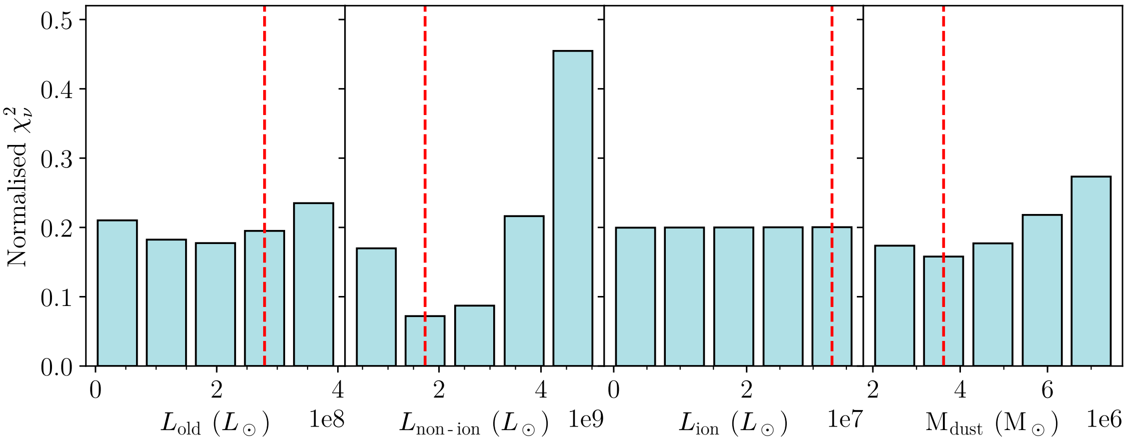

Figure 4.1: Normalised χ^2_ν distributions of the four free parameters in the model. From left to right, these are the old stellar luminosity, the non-ionizing young stars, the ionizing stars and the dust mass. The distribution is normalised such that the total sum of the bars is equal to one, so that the four distributions are at approximately the same scale. The dashed red line shows the best fit parameter used in the high-resolution simulation.

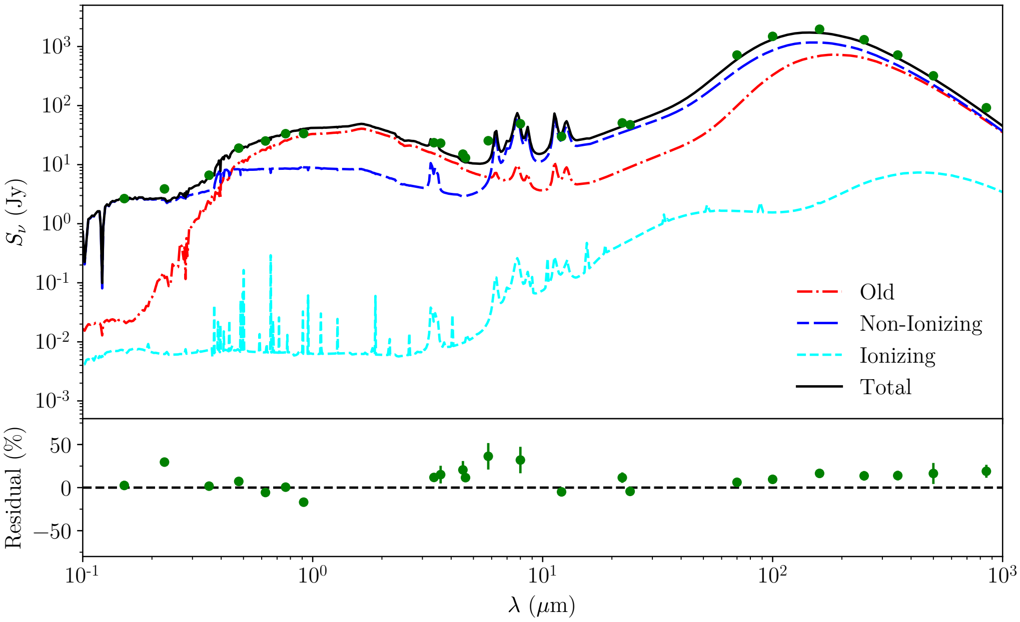

Figure 4.2: *Top:* High-resolution, best-fit RT simulation for M33. The red dot-dash line indicates the contribution from old stellar populations, the short-dash long-dash blue line young non-ionizing stars, light blue dashed line the ionizing population and the solid black line the total. Since the simulation considers the dust heating from the three stellar components simultaneously, this black line is not simply the sum of the three component lines. In this sense, the component decomposition should be taken as indicative only. Given the log-scale of the y-axis, the errorbars are generally smaller than the points, and better seen in the residuals below. *Bottom:* residuals for this fit.

normalisations. For each of these parameters, I use 5 equally spaced values between our minima and maxima, for a total of 625 simulations.

I ran the simulations using a wavelength grid of 90 points, spaced for effective convolution with various filters and weighted depending on the importance of photons in that particular energy regime (Verstocken et al., in prep). I also use a small number of photons (10^6), to reduce the computational time for each model. Our dust grid is a binary tree dust grid (see Saftly et al. 2014 for more details on this grid method), and cells are no longer split when their mass fraction is less than 10^{-5}. This means that cells are not equal in size, with smaller cells in areas of higher density. In total, each of these "low-resolution" simulations takes around 3 CPU hours, and contain around 150,000 dust cells. To determine the best fit model, I defined six wavelength regimes – UV (GALEX), optical (SDSS), NIR ($3.4 - 4.6\,\mu$m), MIR ($5.8 - 24\,\mu$m), FIR ($70 - 250\,\mu$m), and submm ($250 - 850\,\mu$m). I calculated the reduced chi-squared, χ^2_ν, for each of these wavelength regimes, as there are an uneven number of points in each wavelength range. The best fit is then the minimum of the sum of each of the χ^2_ν values, including an extra 10% error in each of the points to account for uncertainties in the modelling, which is often used in other studies (e.g. Noll et al., 2009). Table 4.1 gives the best fit values for each free parameter. The likelihood of each model is given by $\mathcal{L} \propto \exp^{-\chi^2_\nu/2}$, and I sample from this distribution, quoting our errors as the 16th and 84th percentiles. When this error is smaller than the width of the bin, I instead quote the error as half the bin width. I find that given the low luminosity of the ionizing stars, I cannot well constrain this parameter, and it has a flat χ^2_ν distribution across the parameter range, but the other parameters are reasonably well constrained (see Table 4.1). The normalised χ^2_ν distributions of these free parameters are shown in Fig. 4.1.

Having found a best-fit model, I then re-simulated this model using a higher resolution wavelength grid with 553 points, and 2×10^7 photons to produce images with more reliable filter convolution and higher S/N. The cell maximum mass fraction is decreased by a factor of 10, to 10^{-6}, which leads to around 1 million dust cells. These cell sizes vary from $37\,\mathrm{pc}^3$ to $1500\,\mathrm{pc}^3$, with an average size of $51\,\mathrm{pc}^3$. With a maximum optical depth in a cell of 0.47, and an average V-band optical depth of 0.01, I can be confident that this grid is well sampled, even in regions of high optical depth. I also break the simulation up into its various stellar components to see the relative contribution from each across our wavelength range. I use an instrument referred to as a FullInstrument in skirt, which separates the total recorded flux, at every pixel and at every wavelength, in contributions due to direct stellar flux, scattered stellar flux, direct dust flux, and scattered dust flux, i.e.

$$S_\lambda^{\rm tot} = S_\lambda^{\star,\rm dir} + S_\lambda^{\star,\rm sca} + S_\lambda^{\rm dust,dir} + S_\lambda^{\rm dust,sca}. \tag{4.4}$$

This instrument also calculates $S_\lambda^{\rm tra}$, i.e. the flux that would be obtained if the galaxy were completely dust-free. These simulations take around 600 CPU hours each.

4.5 RESULTS AND DISCUSSION

4.5.1 GLOBAL SED

The high-resolution, best-fit SED can be seen in Fig. 4.2. I also repeated the simulation for each stellar component individually, to illustrate the contribution from each of these components. As discussed in Sect. 4.5.4, this decomposition will not take into account the fact that the dust is simultaneously heated by each component. Thus, the sum of these lines will not be equal to the overall SED. I calculated the residuals by convolving the overall SED with the respective filter response for each waveband to produce a model flux, and then

$$\text{residual} = \frac{\text{observation} - \text{model}}{\text{observation}}. \tag{4.5}$$

In this sense, a negative residual means the model overestimates the observed data, and vice-versa. In the UV, the emission is dominated by light from the young stellar populations. In the optical and NIR, the emission is dominated by the old stellar populations. The dust emission is, in general, dominated by heating from the young stars, but is formed of a complex interplay of heating from the stellar components – a warmer component from heating due to the young stellar populations and a colder component from heating due to the older stars. The dust heating from the ionizing stars forms two distinct bumps, one from warmer dust heated from within the molecular clouds, and a cooler component from the emission of the more diffuse dust in the ISM surrounding these birth clouds.

I find a median absolute deviation (MAD) across all wavebands of 12%. I find that the NUV point is underestimated in the model (with a residual value of 30%). The RT model underestimating the NUV point is common across similar studies (see, e.g. De Looze et al., 2014; Mosenkov et al., 2016; Viaene et al., 2017b), and is likely caused by a UV attenuation bump that is too strong (see Sect. 4.5.3).

Table 4.2: SFRs for M33, calculated using a variety of SFR tracers. In each case, I give the model SFR ($\mathrm{SFR_{model}}$), the SFR as calculated from the data ($\mathrm{SFR_{obs}}$) and references for the SFR prescription used. SFRs are in $\mathrm{M_\odot\,yr^{-1}}$.

Band(s)	$\mathrm{SFR_{model}}$	$\mathrm{SFR_{obs}}$	Reference
24 μm	0.11	0.10 ± 0.01	a
70 μm	0.14	0.15 ± 0.02	b
FUV+24 μm	$0.23^{+0.04}_{-0.02}$	$0.25^{+0.10}_{-0.07}$	c
TIR	0.23	0.17 ± 0.06^1	d, e

(a) Rieke et al. (2009), (b) Calzetti et al. (2010), (c) Leroy et al. (2008), (d) Hao et al. (2011), (e) Murphy et al. (2011). ^{1}Including an error of 30% to estimate uncertainty in IMF, dust attenuation; single temperature modified blackbody.

I also find that many of the MIR points are underestimated. The MIR points are dominated by aromatic features, and so producing an adequate fit in this wavelength range is strongly dependent on the properties of the small carbon grains. Increasing the weighting to these points can produce a better fit at these wavelength ranges, but a much poorer fit to the UV/optical points. Given the complex nature of this wavelength range, and the particular interest in the local dust-energy balance of M33, this fit is preferable. Finally, the longer wavelengths are underestimated, potentially indicating a dust mass that is too low, or an incorrect dust emissivity. However, an increase in dust mass leads to increased dust attenuation and a poorer fit to the short wavelength points. Considering the uncertainty on the power-law slope for the small carbon grains (4.26±0.13), and the fact that this has a large effect on the dust emissivity, the emissivity could well be underestimated. Given the fact the UV/optical and FIR/sub-mm points are given equal weight, this is the preferable fit. Due to recent work on the sub-mm excess (Hermelo et al., 2016; Relaño et al., 2018), I explore the 450 and 850μm wavelengths in more detail in Sect. 4.5.2.1.

I calculated the SFR that this model produces using a variety of single- and multi-band SFR tracers (24 μm, 70 μm, a combination of FUV+24 μm, and TIR luminosity), and compared these to the values calculated from the data. The results of this can be seen in Table 4.2. There is a good correspondence between the modelled and observed SFRs in M33. The TIR SFRs marginally agree within error, but I note a difference in the way these are calculated – for SKIRT, I integrate the emission from 3-1100 micron to calculate a TIR flux. In the case of the observed data, I fit a single-temperature modified blackbody (MBB) to the cold dust continuum emission, which will have negligible contributions at shorter wavelengths. As the longer wavelength regime is more affected by dust heating from older stellar populations, with a higher fraction of dust heating at shorter wavelengths from the young stellar populations (see Sect. 4.5.4), our model TIR luminosity is likely more representative of the TIR luminosity. I also highlight the importance of including the unattenuated starlight here – compared to the monochromatic $24\,\mu$m and $70\,\mu$m calculated SFR, the FUV+$24\,\mu$m SFR is nearly a factor of 2 higher. This is also true for our observed SFRs. The calculated SFR is consistently lower (by a factor of 2-3) than those calculated by Verley et al. (2009). The reason for this is twofold – firstly, they use SFR prescriptions similar to that of Kennicutt (1998a). I use updated SFR measurements that are generally around a factor of two lower (see Kennicutt & Evans 2012, their Table 1). Secondly, in truncating and masking the disc, I remove a significant amount of flux in the outer disc. The values given in Table 4.2, therefore, should be treated as a consistency check between pixels considered in the simulation and observations, and not as a measure of the true SFR of M33.

Alternatively, the SFR can also be calculated directly from the SED templates inputted into SKIRT for the young stellar populations, as these are scaled from a known normalisation factor. For the non-ionizing stars (i.e. the SFR over 100 Myr), this gives a value of 0.15 $\mathrm{M_\odot\,yr^{-1}}$, similar to the single-band SFR prescriptions in Table 4.2. For the ionizing stars (the SFR over the last 10 Myr), this produces an SFR of 0.58 $\mathrm{M_\odot\,yr^{-1}}$, but given that the ionizing stellar luminosity is not well constrained, this is unlikely to be a good measure of the true SFR.

From this model, I can calculate the fraction of the stellar radiation absorbed by dust, $\mathcal{F}_{\mathrm{abs}}$, which is given by

$$\mathcal{F}_{\mathrm{abs}} = \frac{L_{\mathrm{dust}}}{L_{\mathrm{dust}} + L_{\mathrm{stars}}}. \tag{4.6}$$

For the DustPedia galaxies, Bianchi et al. (2018) find this value to be 19% on average (25% if only considering late-type galaxies). For M33, I find this value to be 21%, in agreement with the findings of this earlier study.

I find a dust mass of $(3.6 \pm 0.6) \times 10^6\,\mathrm{M_\odot}$. This is very comparable to Williams et al. (2018) (Chapter 2), with a dust mass calculated from MAGPHYS of $4 \times 10^6\,\mathrm{M_\odot}$, for a similarly good fit to this wavelength regime (see Fig. E.1 and Fig. 2 of Williams et al. 2018). However, Hermelo et al. (2016) find a significantly higher dust mass, of around $1.7 \times 10^7\,\mathrm{M_\odot}$ (albeit with a large uncertainty). As discussed in their work, this leads to a much lower gas-to-dust ratio (GDR) than expected in this low-metallicity environment, and so this dust mass estimate is likely too high, potentially due to grain properties or the dust attenuation assumed in their models. Assuming that the

GDR scales with metallicity as Z^{-1} (e.g. Draine et al., 2007; Leroy et al., 2011), we would expect a value of the GDR between 200-450 (Hermelo et al., 2016). Using a total gas mass of $1.7 \times 10^9\,\mathrm{M}_\odot$ (Gratier et al., 2010; Druard et al., 2014), I get a GDR of 470, significantly higher than the value of 101^{+135}_{-80} reported by Hermelo et al. (2016), but in agreement with the radial profiles of Relaño et al. (2018, their Fig. 10).

4.5.2 A Resolved Comparison of M33

skirt also produces a data cube which provides a 2D view of the galaxy at each wavelength in the wavelength grid. This means that I can compare the model on resolved scales at any given wavelength. To this end, I produced residual images at a number of wavelengths. I note that due to images going through rotation and projection within the skirt routine, comparing these images directly may be an unfair comparison. This is discussed in more detail in Appendix F, but the effect of this on a moderately inclined galaxy like M33 is minor, and so I opted to compare directly to the original images. Given the resolution of our input geometries, I first spectrally convolve these datacubes with the relevant filter response, before spatially convolving with the point-spread function (PSF) of that waveband and regridding to pixels of 25 arcsec (using montage) to make these images comparable. I also mask any pixels not considered in our simulation.

I find that across the 23 wavebands that form the high-resolution dataset for our simulation, I have a MAD of 33%, higher than the deviation seen in our global fluxes. Plots of the residuals at five wavelengths (FUV, SDSSg band, 3.6μm, 100 μm, and 250 μm) are shown in Fig. 4.3. In general, the residuals are centred around 0 and most of the values lie within ±50% of the observed values. I see strong structure in many of our residuals, with the model often overestimating in the spiral arms and underestimating in the more diffuse ISM. In the regimes where we are observing mainly starlight, this is likely due to the temporal and spatial resolution. Whilst I assume 3 discrete, average ages, the actual star-formation history is much more complex, with stars of similar ages clumping together (e.g. Lewis et al., 2015), and these variations are on scales smaller than we are able to model in the simulation. At the wavelengths where dust emission dominates, these spatial variations might indicate a variation in dust grain properties. Previous work has shown that there can be significant variation in the dust properties across a galaxy (e.g. Smith et al. 2012 in M31, Tabatabaei et al. 2014 in M33). Relaño et al. (2018) also suggest regional variations in dust properties to better explain the sub-mm excess. This

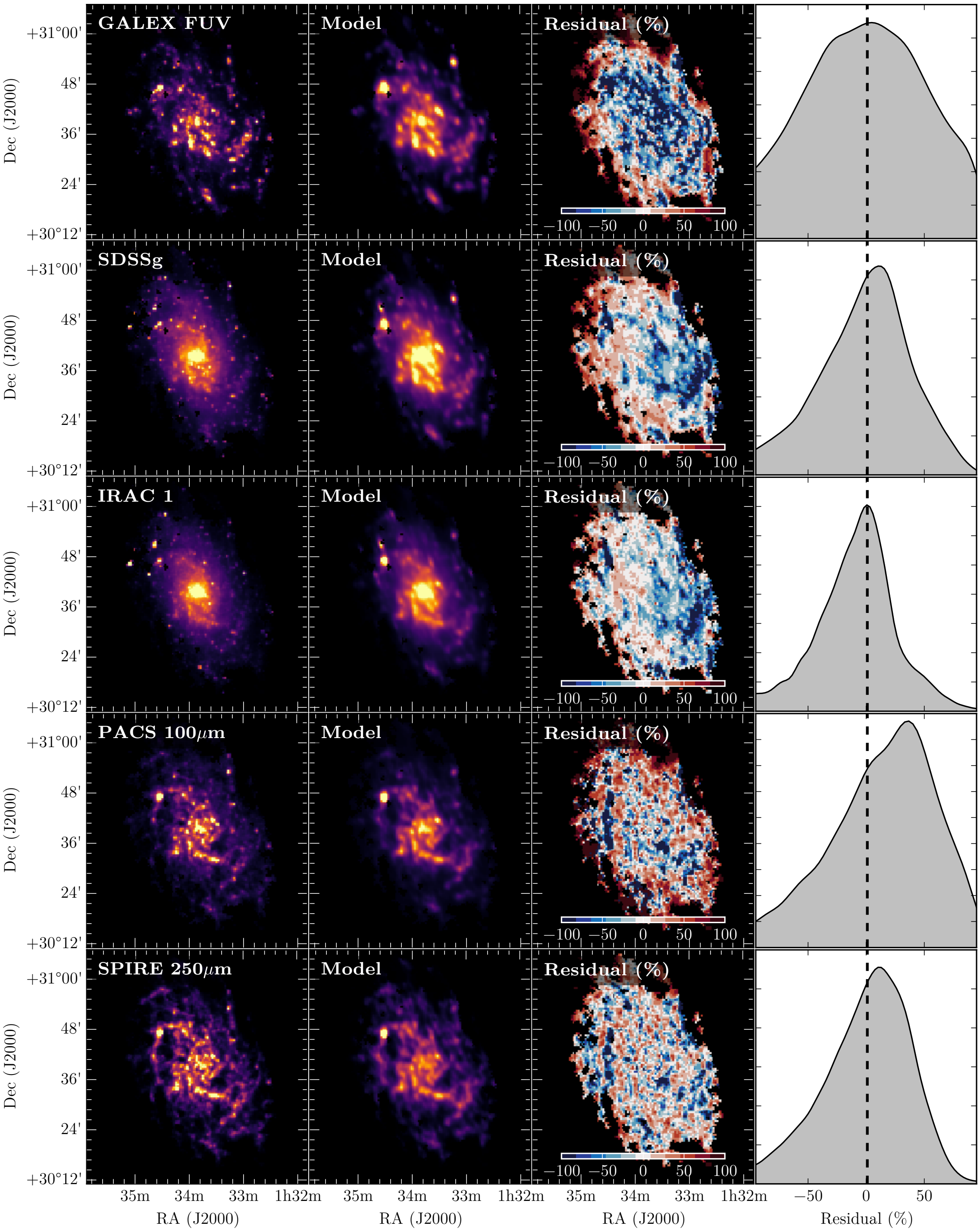

Figure 4.3: Residual plots of *first row:* GALEX FUV, *second row:* SDSS g-band, *third row:* IRAC 3.6μm, *fourth row:* PACS 100μm, *fifth row:* SPIRE 250μm wavebands. In each case, I show *first column:* the observed image, *second column:* the model image from our RT simulation, *third column:* the residuals, and *fourth column:* a KDE plot of these residuals.

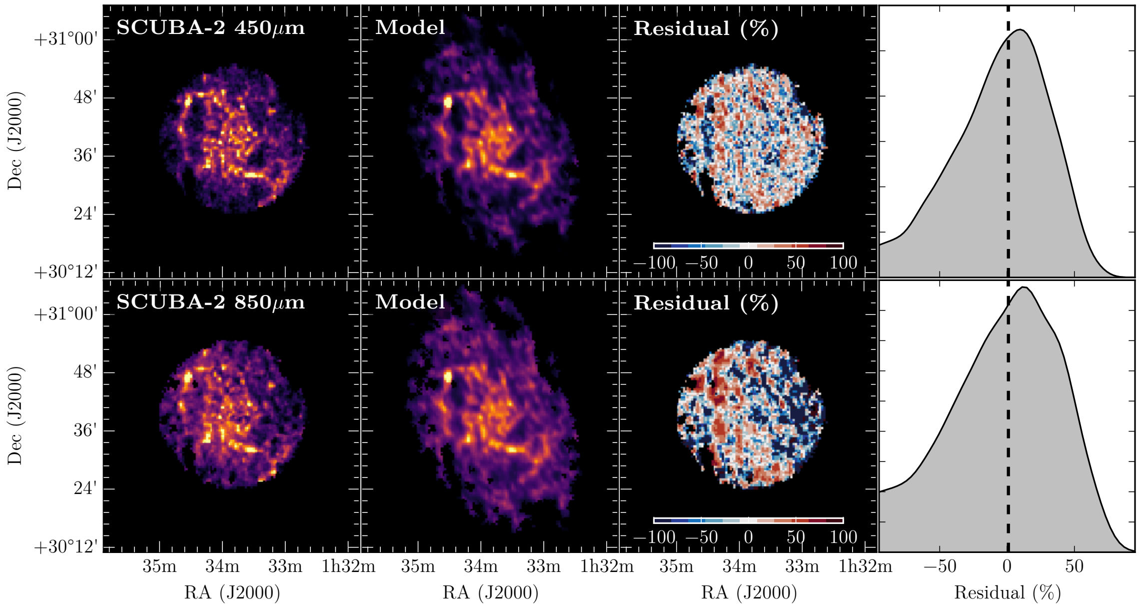

Figure 4.4: Residual plots of *top:* SCUBA-2 450μm and, *bottom:* SCUBA-2 850μm wavebands. I show *first column:* the observed image, *second column:* the model image from our RT simulation, *third column:* the residuals, and *fourth column:* a KDE plot of these residuals.

work, however, has assumed an average dust grain property and mix throughout the whole of M33. I do not believe the features present in the residuals are an artefact of the use of MAGPHYS, as these features are also present in the study of De Looze et al. (2014), where the geometries are defined in a completely independent way to this analysis. There is also noise inherent both in the observations and the simulation, which makes a resolved comparison difficult. However, despite the simplicity of the model, the simulations well resemble the observations.

4.5.2.1 The sub-mm excess

Given the sub-mm excess present in M33 (e.g. Hermelo et al., 2016; Relaño et al., 2018, i.e. that the observed fluxes are higher than the model), I have also produced residuals for the model at 450μm, and 850μm wavelengths. These are compared to our SCUBA-2 images, and can be seen in Fig. 4.4. Unlike Hermelo et al. (2016), I find no significant sub-mm excess in our model (any higher than the excess we have at all long-wavelength points), and I also find no clear radial dependence on our residuals (consistent with those seen in any other wavelength regime), unlike that of Relaño et al. (2018). However, I note that in the earlier THEMIS fitting I modify the dust grain properties *specifically* to fit the sub-mm excess by removing many of the small

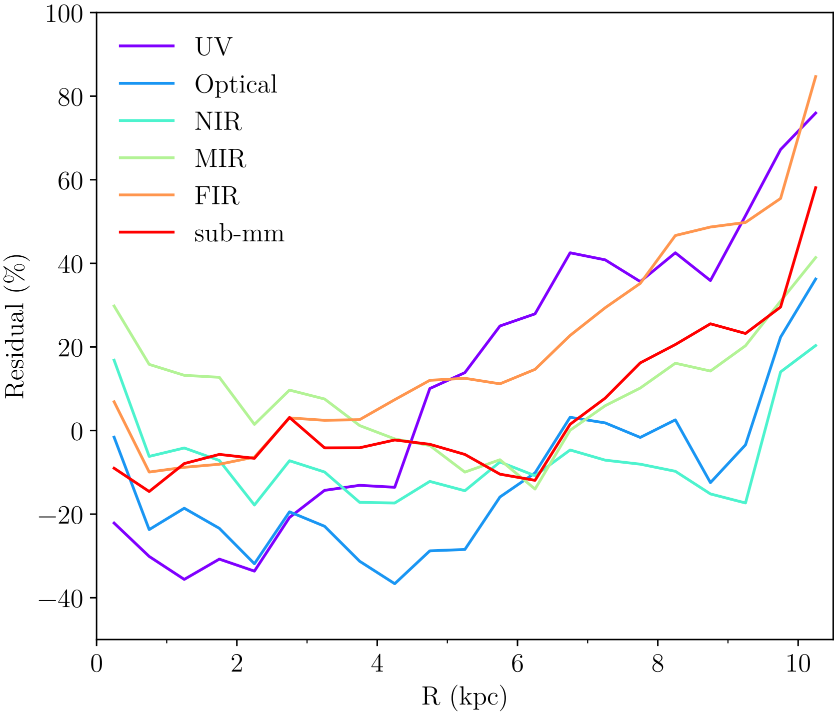

Figure 4.5: Median residual with galactocentric radius. Each differently coloured line indicates a wavelength regime as defined in Sect. 4.4.

carbon grains, and so the fact that I do not see this excess is not surprising.

4.5.2.2 Radial variation of the residuals

M33 has been shown to have a warped disc, both in the optical (e.g. Sandage & Humphreys, 1980), and in its Hi 21cm line (e.g. Corbelli & Schneider, 1997). If the inclination and position angle assumed in the deprojection of the model inputs has some radial variation, I would expect that to be seen as some radial dependence in the residuals. To quantify this, I calculate the median residual for each wavelength regime as defined in Sect. 4.4 for bins of 0.5 kpc width in deprojected galactocentric radius (assuming a position angle of 22.5°, and inclination of 56°). The results of this are shown in Fig. 4.5. Given the north/south asymmetry seen in the residuals, I do not believe this is a physical effect. I see that in general, the model tends to underestimate at low galactocentric radius, and increasingly overestimate with increasing galactocentric radius. Given that the trends seen are broadly similar between each wavelength regime, I therefore conclude that M33 is similarly warped across all wavelengths considered in this study. As SKIRT uses an exponential geometry when inputting an image, accounting for this warp is beyond the scope of this work.

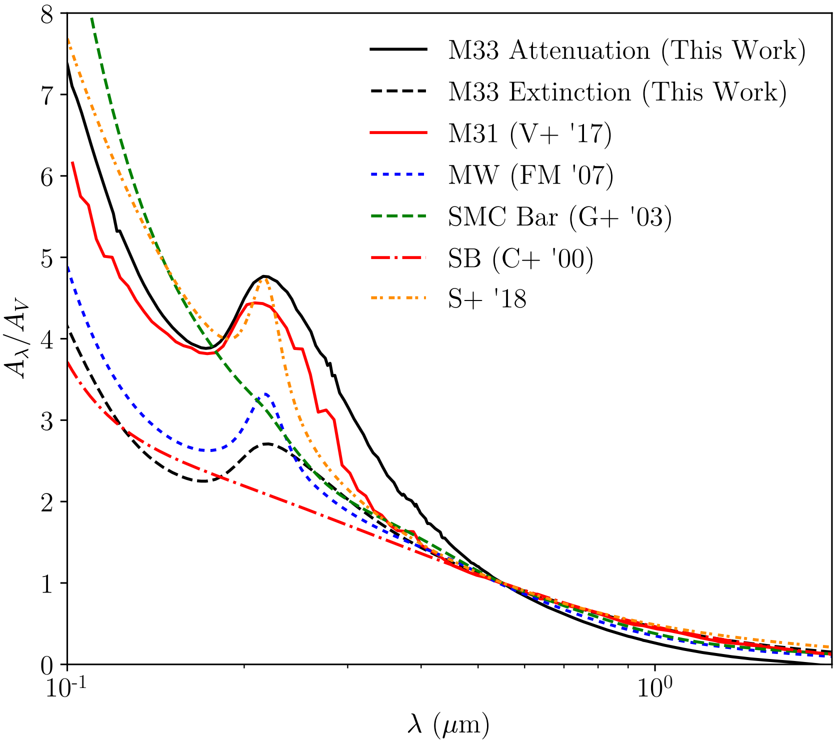

Figure 4.6: Dust attenuation for the RT model (solid black line) and underlying extinction curve (dashed black line), compared to extinction curves for the M31 (solid red line, Viaene et al. 2017b, V+ '17), the MW (short-dashed blue line; Fitzpatrick & Massa 2007, FM '07), the SMC bar region (long-dashed green line; Gordon et al. 2003, G+ '03), the Calzetti et al. (2000, C+ '00) law for starburst galaxies (dot-dash red line), and the derived attenuation curve of Salim et al. (2018, S+ '18) for the stellar mass of M33 (short dash-dot orange line). All of these curves are normalised at V-band.

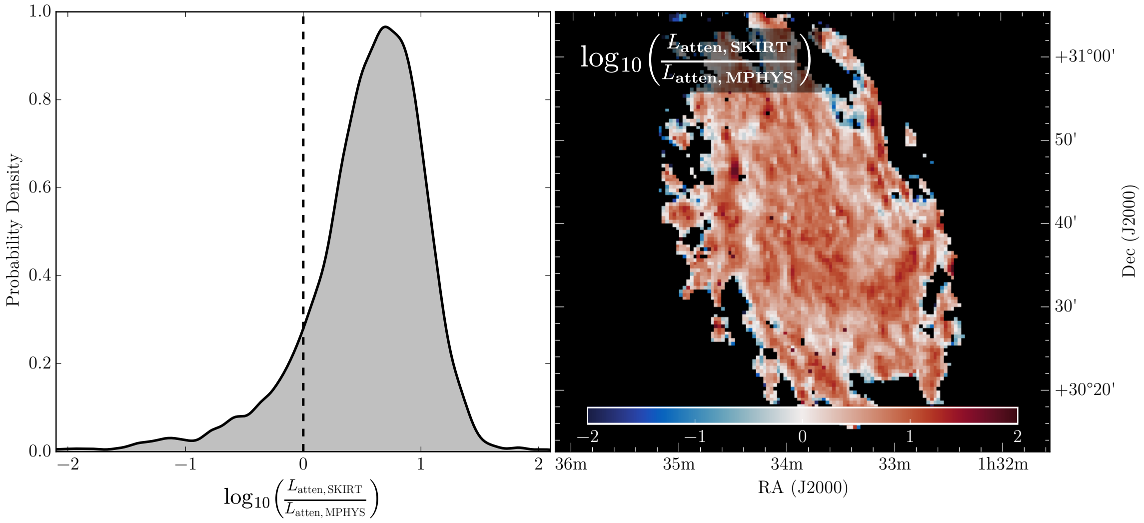

Figure 4.7: Comparison of SKIRT and MAGPHYS attenuated luminosities. *Left:* KDE plot of the ratio of the SKIRT attenuated luminosity to that of MAGPHYS. The black dashed line indicates where these two values are equal. *Right:* this same ratio, but instead plotted positionally.

4.5.3 Dust Attenuation

4.5.3.1 Global Attenuation

By using the FullInstrument instrument class type in SKIRT, a view of the system with no dust attenuation is produced as a result of the simulation. From this, the dust attenuation can be directly calculated at each wavelength, as

$$A_\lambda = 2.5\log_{10}\left(\frac{S_\lambda^{\rm unatten}}{S_\lambda^{\rm atten}}\right), \tag{4.7}$$

where $S_\lambda^{\rm unatten}$ and $S_\lambda^{\rm atten}$ are the total unattenuated and attenuated fluxes from the simulation at a given wavelength, respectively. One important caveat for the attenuation is that the MAPPINGS III SED used to describe the ionizing stellar disc (Sec. 4.3.1.3 and Groves et al. 2008) does not truly provide a transparent view of the system with no dust, as the dust is built-in to this SED type. I make an estimate of the effect this will have on the flux by comparing a “transparent” MAPPINGS SED (i.e., a covering factor of 0) with the SED produced by our adopted covering factor of 0.1. This makes an average difference of 10% to the fluxes, which given the much lower luminosity of the ionizing stellar populations will make a negligible difference to the results. Along with calculating an attenuation curve, I also extract the intrinsic dust extinction curve, to see the effects of geometry and scattering on this attenuation curve. The results of this are shown in Fig. 4.6, and are compared to several literature extinction curves.

Visually, the underlying extinction curve lies somewhere between the MW (Fitzpatrick & Massa, 2007) and starburst galaxies (Calzetti et al., 2000). I find a reasonably strong UV bump, which is broader than that of the MW. This is due to the adopted dust grain properties in the THEMIS model, which are discussed in more detail in Jones et al. (2013). This figure also highlights the effect of the treatment of geometry and dust scattering in shaping the difference between attenuation and extinction curves. These properties have previously been shown to have an important role in shaping attenuation curves (e.g. Granato et al., 2000; Witt & Gordon, 2000; Baes & Dejonghe, 2001; Panuzzo et al., 2007; Viaene et al., 2017a). The M33 dust attenuation curve appears much more similar to the SMC bar region of Gordon et al. (2003), albeit with a strong UV bump. This is somewhat counter-intuitive, as our fitting technique alters the size distribution of the very small carbon grains, which are responsible for this bump. However, the larger of these small grains ($1\,\mathrm{nm} < r < 20\,\mathrm{nm}$) also contribute to this bump (Jones et al., 2013, their Table 1), so removing the smallest grains will not necessarily eliminate this UV bump. The attenuation curve is also very similar to the attenuation curve calculated by Viaene et al. (2016) for M31, derived in a similar way. This is somewhat surprising, given the very different intrinsic properties and geometry between M31 and M33. Given the stellar mass of M33 (3-6$\times10^9$ $\mathrm{M}_\odot$, Corbelli 2003), the average dust attenuation curve for this stellar mass from the work of Salim et al. (2018) is very similar to that obtained in our simulations, although my calculated UV bump is wider. An analysis of the nuclear region of M33 (Gordon et al., 1999) finds evidence of strong attenuation, along with a strong 2175Å bump. My RT simulation shows that this may be the case across the whole of M33. However, I note that as the NUV flux is underestimated in our simulation by ∼30%, the strength of this NUV bump may be overestimated.

4.5.3.2 Comparison to SED Modelling

I can also compare, positionally, the amount of dust attenuation in our RT simulation to more traditional SED fitting. For this comparison, I take the pixel-by-pixel MAGPHYS fitting from (Williams et al., 2018, Chapter 2). MAGPHYS uses the dust attenuation model of Charlot & Fall (2000), and I refer readers to that work for details of the model. Essentially, this model assumes two populations of stars – one in their birth clouds, and others that have drifted away from these birth clouds. The light from both of these populations is subject to attenuation from dust in the ISM, and the stars in their birth clouds are additionally attenuated by the dusty clouds they reside within. This attenuation has a power-law type dependence on the wavelength, and the V-band optical depth is one of the parameters MAGPHYS fits, as well as the fraction of attenuation by dust in the ISM compared to birth clouds. The Charlot & Fall (2000) model, or variations of it, are typically used in panchromatic SED fitting tools. As MAGPHYS employs a dust-energy balance, the modelled dust luminosity is by definition the attenuated luminosity. For SKIRT, in terms of its FULLINSTRUMENT output, the attenuated luminosity is

$$L^{\mathrm{atten}} = 4\pi\, D^2 \int \left(S_\lambda^{\mathrm{tra}} - S_\lambda^{\star,\mathrm{dir}} - S_\lambda^{\star,\mathrm{sca}} \right) d\lambda \tag{4.8}$$

Given that this does not include the flux directly from the dust, this is not simply the transparent flux minus the total flux in the simulation. I calculate the ratio of the SKIRT to MAGPHYS attenuated luminosities, and show this in Fig. 4.7. I find a median offset of 0.56 dex for the SKIRT luminosity compared to the MAGPHYS attenuated luminosity, and a clear positional dependence in this offset, with much higher values for SKIRT in the spiral arms, and regions of more intense star formation, as compared to MAGPHYS. The reason for this may be two-fold – firstly, the pixel-by-pixel MAGPHYS fitting uses pixels of 100 pc^2, where the local dust-energy balance may not hold (i.e. the amount of dust luminosity and attenuated luminosity may not be the same). With simulations of a galaxy, Smith & Hayward (2018) find acceptable fits to the V-band attenuation on scales of 0.2-25 kpc in ∼99% of pixels modelled with MAGPHYS, so this is unlikely to explain the large discrepancy between these two attenuated luminosities. Secondly, the geometry can play an important role in affecting dust attenuation – given the positional dependence on the discrepancies between MAGPHYS and SKIRT, this is more likely to be the case.

4.5.3.3 Face-On Optical Depth

The optical depth of a galaxy is an important parameter to measure, as it quantifies the amount of stellar light that can be viewed directly without being obscured by dust. The question of whether galaxies are optically thin when viewed face-on is an outstanding problem, with some studies claiming the disc is nearly transparent (e.g. Xilouris et al., 1999), and some claiming that galaxies tend to be optically thick (e.g. Trewhella et al., 1997). Several works have attempted to answer this question through RT modelling of edge-on galaxies (De Geyter et al., 2014; Mosenkov et al., 2018, e.g.),

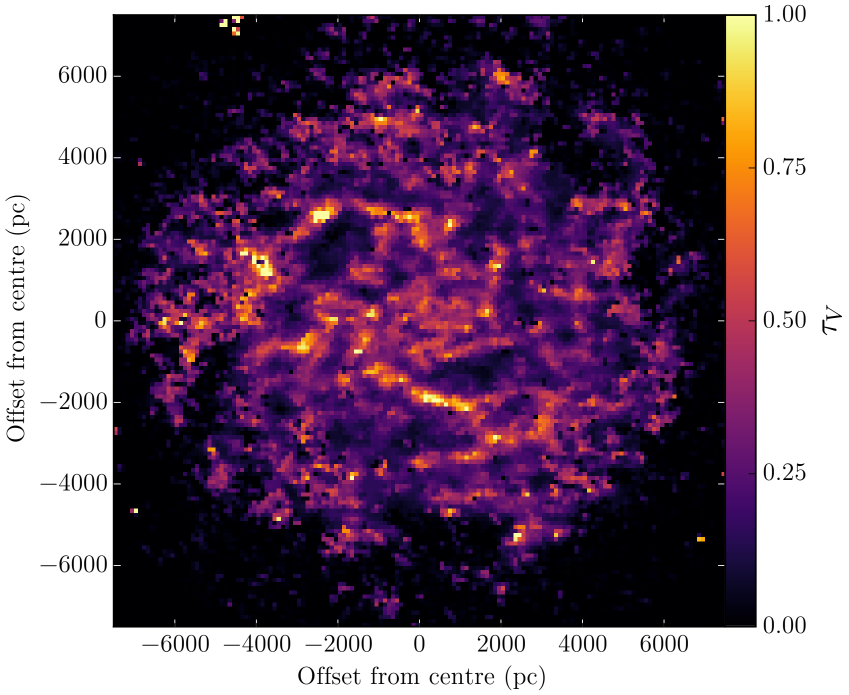

Figure 4.8: Face-on optical depth, τ_{V}, in V-band, derived from the RT simulation.

but given degeneracies between the dust scale-length and the face-on optical depth, a reliable estimate of τ_V has been difficult to ascertain.

The optical depth is simply given by the dust column density integrated along the path length of a photon, and multiplied by the extinction coefficient, i.e.:

$$\tau_V = \kappa_V \int_0^\infty \rho_{\mathrm{d}}(s)\, ds, \tag{4.9}$$

where κ_V for our dust mixture is calculated in the simulation to be $4625\,\mathrm{m}^2\,\mathrm{kg}^{-1}$. Taking a deprojected column density map, this can then be trivially converted into a map of the optical depth, and I show this in Fig. 4.8. This map shows that the optical depth is highest in the spiral arms, and peaks in areas of active star formation. This peak can reach values > 1, and thus these regions are optically thick. However, across the spiral arms the average optical depth is ~0.3, in the interarm regions are ~0.1, and the average V-band optical depth across the whole galaxy is ~0.2. There is a gentle radial decline with galactocentric radius, from ~0.5 in the centre to ~0.2 at a radius of 5 kpc. This agrees with Verley et al. (2009), who calculate A_V radially from FUV and TIR luminosities, using the prescription of Calzetti (2001). They find a decrease in A_V with increasing galactocentric radius. I therefore conclude that at scales of 100pc, M33 is generally optically thin across its disc.

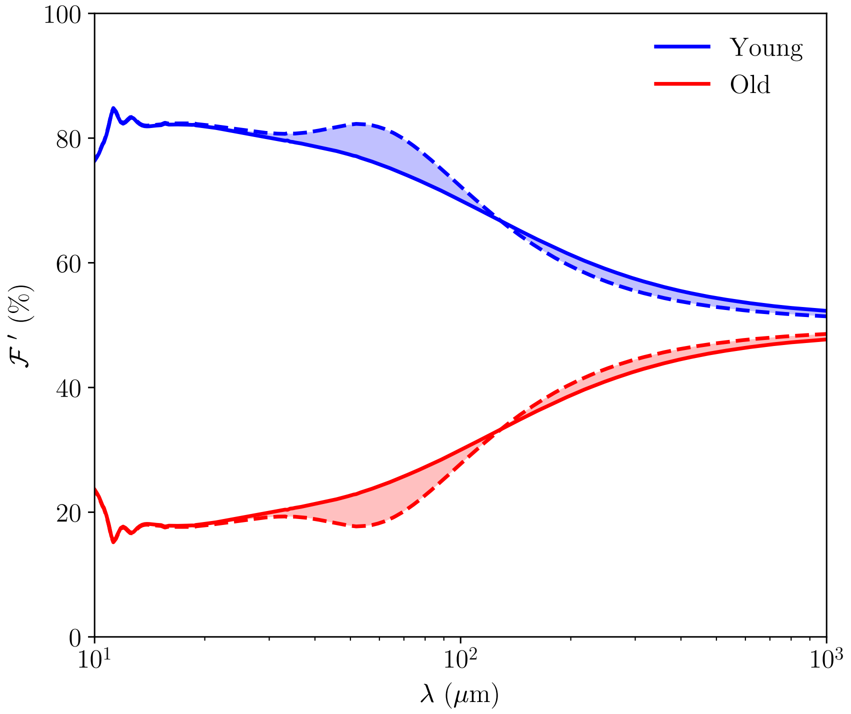

Figure 4.9: Dust heating fraction with wavelength from the young (blue) and old (red) stellar populations. In each case, the solid line corresponds to Eqs. 4.10 and 4.11, and the dashed line to Eqs. 4.12 and 4.13.

4.5.4 DUST HEATING MECHANISMS

From the SKIRT model, I can calculate the fraction of dust heating that comes from the young versus the old stars ($\mathcal{F}_{\rm young}$ and $\mathcal{F}_{\rm old}$, respectively), as simply the ratio of the total dust luminosity from the young stars divided by the total dust luminosity of the simulation. I find $\mathcal{F}_{\rm young}$ to be 72%, similar to the 63% found by De Looze et al. (2014) for M51, but significantly higher than the 9% found by Viaene et al. (2017b) for M31. Globally, the dust heating of M33 is driven mainly by the young stellar populations.

I next turn to the contributions to the dust heating by the various stellar populations on a resolved level. Whilst $\mathcal{F}_{\rm young} + \mathcal{F}_{\rm old} = 1$ on a global SED scale, due to the intertwined nature of the radiation fields and the non-locality in wavelength of the dust heating, separating these quantities can only be approximated. I used the approximation of De Looze et al. (2014), where

$$\mathcal{F}'_{\lambda,{\rm young}} = \frac{1}{2}\frac{S_{\lambda,{\rm young}} + (S_{\lambda,{\rm total}} - S_{\lambda,{\rm old}})}{S_{\lambda,{\rm total}}}, \tag{4.10}$$

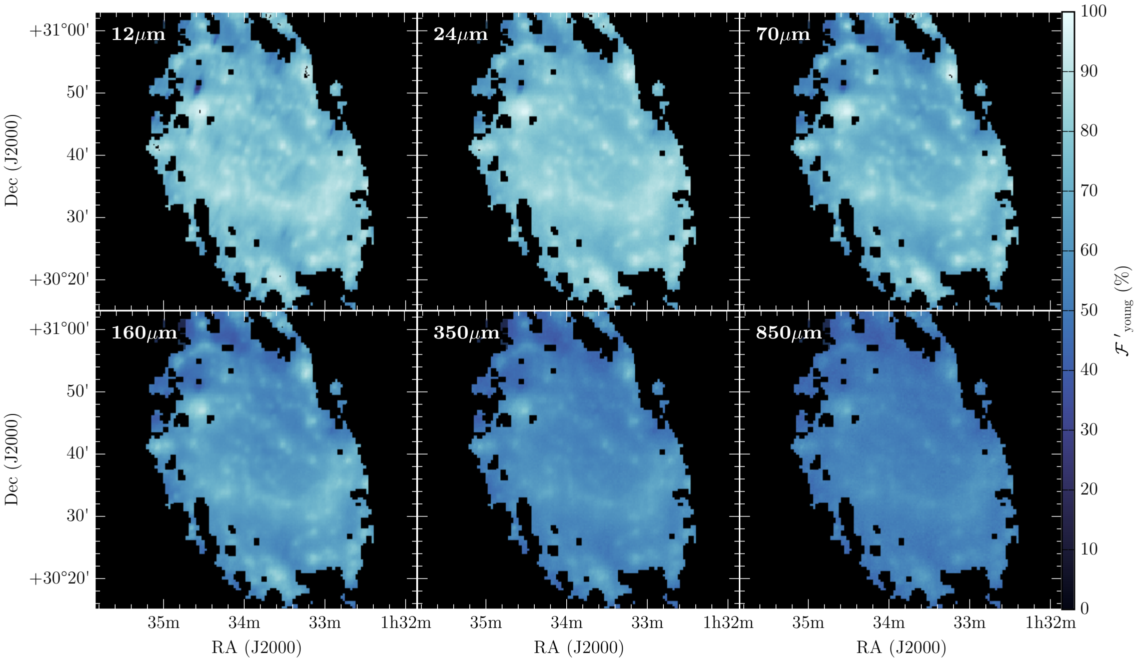

Figure 4.10: Dust heating fraction by young stellar populations ($F'_{\lambda,\rm young}$) for a selection of wavebands. From left to right, *top row:* WISE 12 μm, MIPS 24 μm, and MIPS 70 μm. *Bottom row:* PACS 160 μm, SPIRE 250 μm, and SCUBA-2 850 μm.

and

$$\mathcal{F}'_{\lambda,\rm old} = \frac{1}{2}\frac{S_{\lambda,\rm old} + (S_{\lambda,\rm total} - S_{\lambda,\rm young})}{S_{\lambda,\rm total}}. \tag{4.11}$$

Due to the non-local nature of the dust heating, $S_{\lambda,\rm total}$ is not simply $S_{\lambda,\rm old} + S_{\lambda,\rm young}$. I also included the naïve case where I do not include this non-locality, i.e.

$$\mathcal{F}_{\lambda,\rm young} = \frac{S_{\lambda,\rm young}}{S_{\lambda,\rm young} + S_{\lambda,\rm old}}, \tag{4.12}$$

and

$$\mathcal{F}_{\lambda,\rm old} = \frac{S_{\lambda,\rm old}}{S_{\lambda,\rm young} + S_{\lambda,\rm old}}. \tag{4.13}$$

The results of this are shown in Fig. 4.9. At wavelengths shorter than $\sim 2 \times 10^2 \mu$m, the dust heating is driven mainly by the young stellar populations, with a decreasing contribution towards longer wavelengths. At around $\sim 2 \times 10^2 \mu$m, the contributions from the old and young stars become comparable. It appears that contributions to the dust heating from the old stellar populations peak at colder dust temperatures, as they are heating the colder, more diffuse dust in the ISM (e.g. Bianchi, 2008; Natale et al., 2015; Bendo et al., 2015).

It is also possible to investigate the fractional contribution to the dust heating

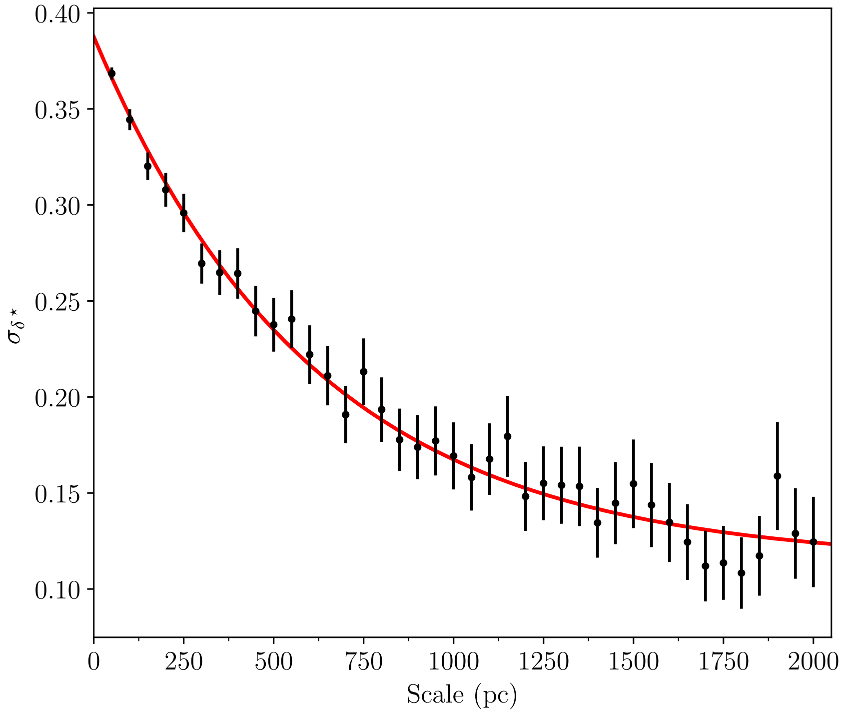

Figure 4.11: $\sigma_{\delta^\star}$ for a variety of spatial scales. Errors are plotted assuming normal errors. The values flatten at a scale of around 1500pc, indicating this is the scale at which the local dust-energy balance holds true. The red line shows a fitted exponential, intended to guide the eye.

from the young stellar populations on a resolved basis. Using Eq. 4.10, I calculate $F'_{\lambda,\mathrm{young}}$ across a number of wavebands, and the results of this can be seen in Fig. 4.10. It can be seen that at shorter wavelengths, there is a higher contribution to the dust heating from the young stellar populations in the spiral arms of M33, but this discrepancy decreases with increasing wavelength, to an almost uniform distribution at 850μm. This is similar to that observed by Viaene et al. (2017b), where the rings of M31 are clearly visible at shorter wavelengths.

4.5.5 LOCAL DUST-ENERGY BALANCE

The scales at which the local dust-energy balance holds is vital for diagnosing the suitability of resolved measurements. In suitably small regions where more dust is heated by starlight originating from stars in neighbouring pixels than in the pixel being considered, traditional SED fitting tools may not recover a reliable value. I investigated the spatial scale at which the local dust-energy balance in the RT simulation becomes an acceptable assumption. This also gives an estimate of the average distance a photon travels within a galaxy. To this end, I define a "stellar luminosity excess,"

$$\delta^{\star} = \frac{L^{\text{atten}} - L^{\text{dust}}}{L^{\text{atten}}}, \tag{4.14}$$

where L^{atten} is the total stellar luminosity attenuated (Eq. 4.8), and L^{dust} is the luminosity emitted by the dust. In terms of the SKIRT FullInstrument output, this is

$$L^{\text{dust}} = 4\pi\, D^2 \int \left(S_{\lambda}^{\text{dust,dir}} - S_{\lambda}^{\text{dust,sca}} \right) d\lambda \tag{4.15}$$

the integral of the direct flux from the dust. A value of 0 for $\delta^{\star}$ means the local dust-energy balance holds in that particular pixel, and increasingly positive (negative) values indicate more (less) flux attenuated than emitted by the dust in that pixel. Globally, the dust-energy balance should hold and therefore the mean of this distribution should be 0. I calculate this parameter for every 3D pixel in our data cube, and calculate the spread in these pixels, $\sigma_{\delta^{\star}}$, as the 84th percentile minus the 16th percentile. At the scale where the local dust-energy balance is a suitable assumption, $\sigma_{\delta^{\star}}$ should ideally be equal to 0. However, due to deviations between the model and observations, along with noise in the RT simulation, this is unlikely to be the case, so the point at which increasing the spatial scale causes no significant decrease in $\sigma_{\delta^{\star}}$ is the point at which I assume the local dust-energy balance takes hold. To calculate these parameters for a variety of spatial scales, I regrid the simulation output to a number of scales, rather than re-run the simulation many times. The results of this procedure for a variety of spatial scales is shown in Fig. 4.11. From this, we can see that the local dust-energy balance is a suitable assumption at scales greater than ∼1500 pc. This is in agreement with simulations, which show that the local dust-energy balance holds true at scales greater than around 1 kpc (Smith & Hayward, 2018), as well as observational comparisons of SFR tracers (Boquien et al., 2015).

4.6 CONCLUSIONS

In this chapter, I have presented a high-resolution (100 pc) RT simulation of nearby spiral galaxy M33. The simulation is self-consistent, includes the absorption and scattering effects of dust, and is performed in 3D. The inputs for this simulation are based on images produced from a multi-wavelength dataset, in order to describe the young and older stellar populations in the galaxy. I also include a dust system, with the geometry informed by pixel-by-pixel SED fitting, and the dust properties from a global fit.

I find that I can well reproduce the SED of M33 to within a median deviation of 12%. This SED is dominated across almost all wavelengths by the young stellar populations (direct emission at shorter wavelengths, and dust heating at longer wavelengths), and in the optical is characterised by strong dust attenuation, with a very strong and broad UV bump. I find that I can well reproduce the SFRs given by the observed data, as well as the total dust mass. However, I find discrepancies at a resolved level, with many wavebands showing strong features in the residuals. I argue that these are due to limitations in my simple model of this galaxy – the stellar and dust properties are not homogeneous across the disc of M33, and appear to be strikingly different in the spiral arms versus the diffuse ISM, and not due to our choices of input geometries. I am able to fit the sub-mm excess detected in previous works with a modified THEMIS dust model, showing that the excess is related to a difference in the grain properties of the dust, as suggested by Hermelo et al. (2016).

At a resolution of 100 pc, the galaxy is mostly transparent in the V-band, except in areas of high star-formation. This means that it should be possible to reliably calculate the stellar properties in galaxies at least to these scales. I also find that the dust is heated almost solely by the young stellar populations, and so the TIR luminosity should be a reasonable tracer for star formation in this galaxy.

Finally, I estimate that the local dust-energy balance does not hold below scales of around 1500pc. This means that tools that employ this balance (e.g. MAGPHYS, CIGALE) are likely to be unsuitable at these high resolutions. However, despite the local dust-energy balance not being valid at scales below 1.5 kpc, the difference between the attenuated luminosity and dust luminosity is maximally around 40%. This means that these tools are likely still able to reliably recover parameters at these high resolutions.

Despite the simple nature of this RT model, I find that we can broadly reproduce the characteristics of M33. Even given its simplicity, this type of RT modelling allows insights into the sub-kpc properties of galaxies that traditional SED fitting does not, and allows us to probe the complex interplay of starlight and dust in galaxies self-consistently at these small spatial scales.

CHAPTER 5

CONCLUSIONS AND FUTURE WORK

> *If I had a world of my own, everything would be nonsense.*
> *Nothing would be what it is, because everything would be what it isn't.*
>
> LEWIS CARROLL

The goal of this thesis was to investigate the complex interplay between gas, stars, and dust on the scale of individual star-forming regions in the Local Group spiral M33. For this, I have made use of the wealth of multi-wavelength public data that exists for this galaxy, and complemented it with new, high-resolution sub-millimetre data. Over the course of this thesis, I have made use of a number of public tools to model this data (MAGPHYS, SKIRT), as well as developed a number of SED fitting tools to characterise the dust properties of regions using a number of different models. I have also helped to develop the tool that allows for extended structure to be added back in to ground-based sub-millimetre observations.

5.1 KEY RESULTS

The main results of this thesis are as follows:

- By increasing the standard parameter range of MAGPHYS with lower dust temperatures, I have been able to use this tool to model 100 pc^2 regions of a galaxy. Due to its ability to model a star-formation history with more variation than traditional SFR tracers, I find that it models HII regions as very similar to starburst galaxies.

- The SFR density correlates strongest with molecular gas, rather than atomic gas, or the total gas (both traced by dust and HI/CO), although the correlations seen are weaker at 100 pc scales than at ∼kpc scales.
- The slope of the Kennicutt-Schmidt law is measured is strongly dependent on the spatial scale at which the measurements are carried out. At high resolution, I resolve regions at a variety of evolutionary states, and it is the variation between these that drives the slope of this power-law relationship.
- I have identified GMCs in M33 using a dendrogram technique, finding 165 GMCs. They have cloud masses of 10^4-$10^7\,M_\odot$, and have a lower GDR (and higher α_{CO}) than found in the MW.
- The mass function of these clouds is proportional to $M^{-2.84}$, steeper than many studies of clouds in nearby galaxies. This indicates that M33 is poorer at forming massive clouds than other nearby spirals.
- Whilst many of these clouds are co-spatial with earlier CO surveys, many clouds are detected at large galactocentric radii (with no equivalent CO detection). Given the sensitivity of these earlier surveys, this cannot be simply attributed to lower sensitivity at these higher galactocentric radii. This may be an indication that these clouds are dominated by CO-dark hydrogen.
- Using a state-of-the-art radiative transfer model consisting of three distinct populations of stars, and a dust geometry, I can well reproduce the observed SED of M33 (to within a median absolute deviation of 12%). To do this, the dust mixture needed to be modified to have fewer very small carbon grains, and a lower silicate-to-carbon ratio as compared to the MW. This indicates that the sub-mm excess reported by Hermelo et al. (2016) and Relaño et al. (2018) in M33 can be explained as a modified dust mixture.
- The amount of attenuation required in this RT model is significantly different to that obtained from standard SED modelling. There is a strong UV bump, and much stronger attenuation than seen in many other local galaxies.
- On a resolved level, there are discrepancies between the model and the observations in the spiral arms versus the diffuse ISM, with the model tending to over-predict the flux in the spiral arms, and under-predict in the more diffuse inter-arm regions. This indicates there may be a difference in stellar and/or

dust properties in these two regimes.

- The dust emission is dominated by heating due to young stellar populations at all wavelengths (~80% at 10 μm to ~50% at 1 mm). This would indicate the TIR luminosity should well trace the SFR in M33.
- The local dust-energy balance (the average distance a photon travels before being absorbed and processed by dust) is approximately 1.5 kpc. This in agreement with earlier simulational work (Smith & Hayward, 2018).

5.1.1 M33 – An Unusual Galaxy?

The work contained in this thesis shows that in many senses, M33 stands apart from the other spiral galaxies of the Local Group. This appears to be the case when looking at the resolved Kennicutt-Schmidt law (Chapter 2), with much higher Schmidt indices seen than in the MW (e.g. Lada et al., 2012), where the classic $N = 1.4$ seems to be appropriate, and M31 (Ford et al., 2013), which argues for a sub-linear Kennicutt-Schmidt law with molecular gas. In this work, I have attributed this to both the source of data, and the analysis techniques. Firstly, by modelling an SFH for each region with MAGPHYS, I can more effectively extract the SFR from regions that appear more like starburst regions. Secondly, I consider significantly lower S/N than earlier studies, performing a robust fitting accounting for errors in the surface densities of both SFR and gas. This also explains why I see significantly stronger correlations at similar spatial scales to earlier studies of M33 (e.g. Schruba et al., 2010; Onodera et al., 2010). Whether this difference in the Schmidt indices in M33 can be attributed to the higher ISRF strengths at higher SFR surface densities preferentially dissociating CO (Glover & Clark, 2012), or due to a real increase in star formation efficiency at high gas surface densities (which would be difficult to reconcile is current models of star formation, Schaye & Dalla Vecchia, 2008), clearly the conditions under which star formation is taking place in M33 is significantly different to both M33 and M31. Finally, the fact that we observe a scale dependence in the measured Kennicutt-Schmidt index indicates that we should be cautious when comparing resolved studies at different spatial resolutions. As observations average over a number of star forming regions in a variety of evolutionary states, we see variation in the Schmidt index measured. This scale dependence can be used to probe, e.g. the lifetime of molecular clouds and the timescales of star-formation (e.g. Kruijssen & Longmore, 2014).

Taking an alternative approach to creating a GMC catalogue using the dust continuum rather than CO (Chapter 3) also reveals that M33 has different cloud properties than our other nearby spirals. By extracting sources using dendrograms and calculating their dust properties (specifically the dust mass), I have studied the GDR and α_{CO} in these clouds, using a method similar to that of Sandstrom et al. (2013). I find that α_{CO} is significantly higher than found in other nearby spiral galaxies, but is consistent with numerical simulations of subsolar metallicity galaxies (Glover & Clark, 2016), and work in the LMC (Roman-Duval et al., 2014), which has a similar half-solar metallicity to M33. This reflects either a difference in the amount of CO that traces molecular hydrogen in this galaxy, or alternatively variation in the coefficient used to turn a dust continuum flux to a dust mass, which has been shown to vary galaxy-to-galaxy (Clark et al., 2016). Given the degenerate nature of these quantities, it is impossible in this study to say which may be the dominant factor.

The mass function of these clouds is also different to those seen in M31 and the MW. With a power law slope of $\alpha_{\mathrm{M}} = -2.83^{+0.24}_{-0.15}$, this is significantly steeper than these other local spirals (e.g. Sanders et al., 1985; Solomon et al., 1979; Blitz et al., 2007; Kirk et al., 2015). It is also steeper than previous studies of M33 (Gratier et al., 2012; Engargiola et al., 2003), which may be due to the dust's ability to probe clouds at higher galactocentric radii, where hints of a steeper cloud mass function have previously been noted (Bigiel et al., 2010). M33 appears to be dominated primarily by small clouds, although like in M31 and the MW these clouds are approximately virialised. What drives the inefficiency of cloud assembly in M33 is unknown, although large, resolved studies of CO and HI in a number of galaxies (such as PHANGS and its HI extension) may help to shed light on this.

Finally, in comparing the GMCs that I extract from the dust continuum with the earlier CO(2–1) and CO(1–0) surveys, I see strong differences. Particularly, at large galactocentric radii where very few CO detections are observed, there are many more sources detected in the dust continuum. This may indicate that these clouds are dominated by molecular gas that is not traced by CO. In this case, we may be systematically missing a significant fraction of the molecular gas if we just use CO. I have not attempted to quantify the amount of CO-dark gas in these clouds in this work, but tracing the amount is one of the science goals of HASHTAG, for M31. These results highlight, however, that it is critically important to have multiple, independent measures of quantities that must be traced indirectly.

In the last study of this thesis (Chapter 4), I have constructed a radiative transfer model for M33, to study the sources of dust heating and the scale of the dust-energy balance in a self-consistent way that takes into account the geometry of the galaxy. I find that whilst the THEMIS dust model has been constructed to well match the dust emission of the MW, it fares much more poorly in M33, which has a sub-mm excess (e.g. Hermelo et al., 2016; Relaño et al., 2018). I find that to fit this sub-mm excess requires a dust mixture more similar to the Magellanic clouds (Chastenet et al., 2017), with fewer of the smallest carbon grains, and a significantly lower silicate-to-carbon ratio than seen in the MW. Combining this with physically motivated maps of the young and older stellar populations, I can well recreate the global SED with a MAD of 12%, and study its global properties. Interestingly, despite the very different geometries and dust composition of M33, its attenuation curve appears very similar to that of M31 (Viaene et al., 2017a). Work by Salim et al. (2018) has shown the primary driver in shaping the dust attenuation curve is the optical depth rather than properties such as metallicity, so in this sense M33 appears similar to M31.

I have also used this model to study the resolved properties of M33. Due to the model having a fixed dust grain composition and stellar properties, the model tends to overestimate the flux in the spiral arms, and underestimate in the more diffuse ISM. I have attributed this to a variation in the properties of the stellar and dust components in these regimes. Unlike M31, the dust heating is dominated by the young stellar populations much like in M51 (De Looze et al., 2014), which is not surprising due to the higher star formation efficiency of M33.

Finally, I have attempted to quantify the scale of which the local dust-energy balance is an acceptable assumption. This energy balance appears to take hold at scales greater than 1.5 kpc, although even at 100 pc scales the difference between the flux attenuated and emitted is maximally ∼40%. This result would, initially, seem to contradict the pixel-by-pixel fitting I have performed using MAGPHYS, a tool than enforces a dust-energy balance. However, it appears that whilst this assumption is not formally true, in simulations MAGPHYS still appears to correctly calculate many galaxy properties (including the SFR, Smith & Hayward, 2018). This is perhaps a lucky coincidence, but is convenient for those trying to model a number of properties in sub-kpc regions, and does not invalidate this earlier work.

Given the differences seen in M33 when compared to the spiral galaxies it appears similar to, along with other galaxies in the Local Group that it shares similar properties with, it is clear that a single-wavelength or single property approach to infer the properties of a galaxy may not be appropriate. To truly gain an accurate picture of the galaxy in question, it is important to synthesise multiple independent measurements, and take a careful approach to our extragalactic studies.

5.1.2 A CHARACTERISTIC TRANSITION AT KILOPARSEC SCALES

A result that appears several times in this thesis is that there appears to be a characteristic scale below which the relationships we see on integrated galaxy scales become increasingly invalid. This is around 1 kpc, the scale at which a local dust-energy balance breaks down, and the scale at which we begin to depart from the canonical Kennicutt-Schmidt relation.

One possibility is that this scale simply arises due to it being the minimum scale over which we average out spatial and temporal variations of the material within that region; the scale at which this takes place must be affected by the relative lifetimes of star forming regions, or the timescales at which material is orbiting within that region, for example. In this case, systematic variations of this scale between different galaxies may give us an insight into the small-scale properties of the particular galaxy (even without necessarily high resolution measurements). For instance, although I have studied the average path length of all the photons in my radiative transfer work, differences between different wavelengths of photons may give us an insight into the variations in dust attenuation curves between different galaxies (Boquien, priv. comm.). Whether this scale is coincidental or not is currently unknown, but with large, high-resolution surveys of many galaxies we will be able to see whether this kiloparsec scale is indeed fundamental in our measurements of galactic properties.

5.2 FUTURE WORK

The work contained within this thesis presents a view of the star formation law that is significantly different to that shown by Kennicutt (1998a). Rather than the slope of the Kennicutt-Schmidt law, the interest should now lie in the *scatter* from this power-law; it is this scatter that highlights the diversity of the star forming regions within a galaxy. Individual regions must transition through the Kennicutt-Schmidt plane over their evolutionary lifetime – they first start gas-rich, before star formation switches on, use up that gas, and then star formation must cease. With cloud-scale observations of many nearby galaxies from large programmes such as PHANGS, it will be possible for the first time to truly chart the evolution of star forming regions in galaxies beyond our Milky Way, linking this with internal and

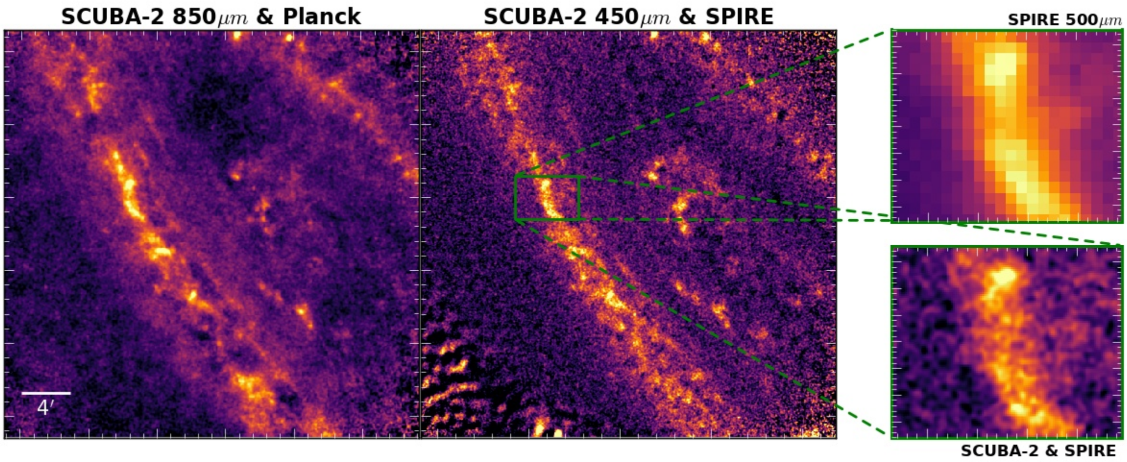

Figure 5.1: Pilot HASHTAG regions at 850 μm (left) and 450 μm (right). The smaller panels show *top*: the SPIRE 500 μm data only, and *bottom*: the data combined with the SCUBA-2 observations. Figure from Smith et al. (in prep.)

external processes. Ultimately, the evolution of a galaxy is driven by the evolution of its individual molecular clouds. Chapter 2 has shown that the scatter around the Kennicutt-Schmidt relation becomes greater at higher resolution, but I have not explored how the properties of a galaxy affect this. Using a large number of galaxies with consistently measured properties will allow a statistically rigorous study into how environment affects star formation in a much more detailed way than has been possible previously.

The Fourier combination script I have helped to develop as part of this thesis will be useful for a number of ground-based sub-millimetre telescopes. In particular, as part of the HARP and SCUBA-2 High Resolution Terahertz Andromeda Galaxy Survey (HASHTAG; Smith et al. in prep.), SCUBA-2 data will be combined in the same way as with M33, but for Andromeda (Fig. 5.1). Combining this new data with PPMAP (Marsh et al., 2017), an algorithm that allows for dust fitting at the best, rather than the worst, resolution data available, this will produce at 25 pc map of the cold dust of M31. This can then be used to study the radial variations in dust property, linking them to other properties of the galaxy (SFR, metallicity etc.). The high-resolution dust map will then be used to produce a GMC catalogue at higher resolution than presented in this thesis, and an estimated ∼2000 clouds will be detected. Combining this with high-resolution HI and CO maps, variation in the CO-conversion factor and a comprehensive search for CO-dark molecular gas will be carried out in unprecedented detail across the face of Andromeda's disc.

The combination script is not limited to SCUBA-2, however, and will also be useful with other telescopes for upcoming studies. Rigby et al. (in prep.) will combine their Galactic plane data from NIKA-2 (Catalano et al., 2018) with *Planck* data at 1 mm. This will allow for detailed SED modelling far into the Rayleigh-Jeans tail of the dust SED, where any sub-mm excess will be readily apparent. This technique will also be useful for the upcoming The Mexico-UK Sub-Millimetre Camera for AsTronomy (MUSCAT) and TolTEC on the Large Millimeter Telescope (LMT), which will both have 1 mm detectors. Whilst the loss of large spatial scales should not be as drastic as for SCUBA-2 or NIKA-2, some extended emission will be lost in reduction, which this algorithm will be able to replace.

The *Herschel* data reduction of the Magellanic Clouds also suffers from loss of large-scale information, due to their huge extent on the sky. Clark et al. (in prep.) will use the Fourier combination script to probe down to very low dust column densities. Combining this with a pixel stacking analysis based on HI column density bins, they will be able to probe dust properties (particularly dust-to-gas ratios) in very diffuse, low density environments.

The radiative transfer code used in this thesis has also seen major changes since my work with it has been completed. Rather than sampling photons from a discrete grid, they are now sampled from the underlying spectrum. This has the effect that now SKIRT can also include velocity information in its modelling, which will be useful for specifying geometries where kinematic information is available, for instance from MUSE IFU data. It can also now handle spatial variation in input material mixes – whilst in my work I use a constant dust grain mix throughout the entirety of M33, with this it is now possible to input calculated grain properties (from SED fitting) on a per-pixel basis. It should be possible to derive dust distributions from the attenuation of stellar spectra, but at high resolution work has shown it is vital to include the effects of geometry (Kreckel et al., 2013; Viaene et al., 2017b). By extending my SKIRT work to attempt to model MUSE spectra of galaxies (for instance, the $\sim$ 20 galaxies observed as part of PHANGS), it may be possible to derive arcsecond-scale dust maps for a number of nearby galaxies. Finally, SKIRT now allows for spheroidal dust grains, and allows for modelling dust polarization. This is in preparation for the proposed Space Infrared Telescope for Cosmology and Astrophysics (SPICA), which would have a polarimetric camera (B-BOP) aboard it. The polarization of dust grains gives us an independent view of the dust grain properties within galaxies, and also allows us to see more than we can just using the dust emission – Peest et al. (2017) have shown that spiral arms can be detected even in edge-on galaxies using their simulations.

5.3 CONCLUDING REMARKS

With the advent of new, high-resolution facilities, we are now at a point where we are able to map hundreds of nearby galaxies at the scales of individual star-forming regions. In order to develop our understanding of the interplay between the various constituents of a galaxy, it is also clear that a multi-wavelength approach is vital. The huge volumes of data that already exist, along with the enormous amount of data that will be delivered in coming years demand a data-based, statistical approach, with minimal human intervention. With the data already available, we are beginning to see that the relationships seen on integrated galaxy scales are driven by an average of the properties within each galaxy, and are not as constant as we once believed once resolved. It is, therefore, the deviations from these relationships that truly offer us a rigorous insight into galaxy evolution.

BIBLIOGRAPHY

Accurso G., et al., 2017, *MNRAS*, 470, 4750

Adler R. J., Casey B., Jacob O. C., 1995, American Journal of Physics, 63, 620

Alam S., et al., 2015, *ApJS*, 219, 12

Allamandola L. J., Tielens A. G. G. M., Barker J. R., 1985, *ApJ*, 290, L25

André P., et al., 2010, *A&A*, 518, L102

Aniano G., Draine B. T., Gordon K. D., Sandstrom K., 2011, *PASP*, 123, 1218

Astropy Collaboration et al., 2013, *A&A*, 558, A33

Astropy Collaboration et al., 2018, *AJ*, 156, 123

Baes M., Camps P., 2015, Astronomy and Computing, 12, 33

Baes M., Dejonghe H., 2001, *MNRAS*, 326, 722

Baes M., et al., 2003, *MNRAS*, 343, 1081

Baes M., et al., 2010, *A&A*, 518, L39

Bayet E., Gerin M., Phillips T. G., Contursi A., 2009, *MNRAS*, 399, 264

Bendo G. J., et al., 2015, *MNRAS*, 448, 135

Berry D. S., 2015, Astronomy and Computing, 10, 22

Bertin E., Arnouts S., 1996, A&AS, 117, 393

Bianchi S., 2008, *A&A*, 490, 461

Bianchi S., et al., 2018, *A&A*, 620, A112

Bigiel F., Leroy A., Walter F., Brinks E., de Blok W. J. G., Madore B., Thornley M. D., 2008, *AJ*, 136, 2846

Bigiel F., Bolatto A. D., Leroy A. K., Blitz L., Walter F., Rosolowsky E. W., Lopez L. A., Plambeck R. L., 2010, *ApJ*, 725, 1159

Bigiel F., Leroy A. K., Blitz L., Bolatto A. D., da Cunha E., Rosolowsky E., Sandstrom K., Usero A., 2015, *ApJ*, 815, 103

Blitz L., Rosolowsky E., 2006, *ApJ*, 650, 933

Blitz L., Fukui Y., Kawamura A., Leroy A., Mizuno N., Rosolowsky E., 2007, Protostars and Planets V, pp 81–96

Bohlin R. C., Savage B. D., Drake J. F., 1978, *ApJ*, 224, 132

Bolatto A. D., Wolfire M., Leroy A. K., 2013, Annual Review of Astronomy and Astrophysics, 51, 207

Boquien M., et al., 2011, *AJ*, 142, 111

Boquien M., et al., 2015, *A&A*, 578, A8

Boquien M., Burgarella D., Roehlly Y., Buat V., Ciesla L., Corre D., Inoue A. K., Salas H., 2019, *A&A*, 622, A103

Boselli A., Boissier S., Cortese L., Buat V., Hughes T. M., Gavazzi G., 2009, *ApJ*, 706, 1527

Bot C., Ysard N., Paradis D., Bernard J. P., Lagache G., Israel F. P., Wall W. F., 2010, *A&A*, 523, A20

Bothun G. D., 1992, *AJ*, 103, 104

Braine J., et al., 2010, *A&A*, 518, L69

Braine J., Shimajiri Y., André P., Bontemps S., Gao Y., Chen H., Kramer C., 2017, *A&A*, 597, A44

Bresolin F., 2011, *ApJ*, 730, 129

Bruzual G., Charlot S., 2003, *MNRAS*, 344, 1000

Buchbender C., et al., 2013, *A&A*, 549, A17

Calzetti D., 2001, *PASP*, 113, 1449

Calzetti D., Armus L., Bohlin R. C., Kinney A. L., Koornneef J., Storchi-Bergmann T., 2000, *ApJ*, 533, 682

Calzetti D., et al., 2005, *ApJ*, 633, 871

Calzetti D., et al., 2007, *ApJ*, 666, 870

Calzetti D., et al., 2010, *ApJ*, 714, 1256

Camps P., Baes M., 2015, Astronomy and Computing, 9, 20

Camps P., et al., 2015, *A&A*, 580, A87

Casey C. M., 2012, *MNRAS*, 425, 3094

Catalano A., et al., 2018, Journal of Low Temperature Physics, 193, 916

Chabrier G., 2003, *PASP*, 115, 763

Chandrasekhar S., 1960, Radiative transfer

Chapin E. L., Berry D. S., Gibb A. G., Jenness T., Scott D., Tilanus R. P. J., Economou F., Holland W. S., 2013, *MNRAS*, 430, 2545

Charlot S., Fall S. M., 2000, *ApJ*, 539, 718

Chastenet J., Bot C., Gordon K. D., Bocchio M., Roman-Duval J., Jones A. P., Ysard N., 2017, *A&A*, 601, A55

Chen H., Braine J., Gao Y., Koda J., Gu Q., 2017, *ApJ*, 836, 101

Chevallard J., Charlot S., 2016, *MNRAS*, 462, 1415

Cid Fernandes R., et al., 2013, *A&A*, 557, A86

Cignoni M., et al., 2018, *ApJ*, 856, 62

Clark C. J. R., Schofield S. P., Gomez H. L., Davies J. I., 2016, *MNRAS*, 459, 1646

Clark C. J. R., et al., 2019, *MNRAS*, p. 2174

Combes F., et al., 2012, *A&A*, 539, A67

Compiègne M., et al., 2011, *A&A*, 525, A103

Corbelli E., 2003, *MNRAS*, 342, 199

Corbelli E., Schneider S. E., 1997, *ApJ*, 479, 244

Corbelli E., Thilker D., Zibetti S., Giovanardi C., Salucci P., 2014, *A&A*, 572, A23

Corbelli E., Elmegreen B. G., Braine J., Thilker D., 2018, *A&A*, 617, A125

Cortese L., Boselli A., Franzetti P., Decarli R., Gavazzi G., Boissier S., Buat V., 2008, *MNRAS*, 386, 1157

Cox D. P., 2005, *ARAA*, 43, 337

Csengeri T., et al., 2016, *A&A*, 585, A104

Dalcanton J. J., et al., 2015, *ApJ*, 814, 3

Dale D. A., Helou G., 2002, *ApJ*, 576, 159

Dale D. A., Helou G., Contursi A., Silbermann N. A., Kolhatkar S., 2001, *ApJ*, 549, 215

Dale D. A., et al., 2009, *ApJ*, 703, 517

Davies J. I., et al., 2017, Publications of the Astronomical Society of the Pacific, 129, 044102

Davis T. A., Bureau M., Onishi K., Cappellari M., Iguchi S., Sarzi M., 2017, *MNRAS*, 468, 4675

Davis T. A., et al., 2018, *MNRAS*, 473, 3818

De Geyter G., Baes M., Fritz J., Camps P., 2013, *A&A*, 550, A74

De Geyter G., Baes M., Camps P., Fritz J., De Looze I., Hughes T. M., Viaene S., Gentile G., 2014, *MNRAS*, 441, 869

De Geyter G., et al., 2015, *MNRAS*, 451, 1728

De Looze I., Baes M., Fritz J., Verstappen J., 2012a, *MNRAS*, 419, 895

De Looze I., et al., 2012b, *MNRAS*, 427, 2797

De Looze I., et al., 2014, *A&A*, 571, A69

Del Popolo A., Le Delliou M., 2017, Galaxies, 5, 17

Dempsey J. T., et al., 2013, *MNRAS*, 430, 2534

Dobbs C. L., Pettitt A. R., Corbelli E., Pringle J. E., 2018, *MNRAS*, 478, 3793

Dopita M. A., Pereira M., Kewley L. J., Capaccioli M., 2002, *ApJS*, 143, 47

Draine B. T., 2006, *ApJ*, 636, 1114

Draine B. T., 2011, Physics of the Interstellar and Intergalactic Medium

Draine B. T., Li A., 2007, *ApJ*, 657, 810

Draine B. T., et al., 2007, *ApJ*, 663, 866

Dressler A., 1980, *ApJ*, 236, 351

Dreyer J. L. E., 1888, MmRAS, 49, 1

Druard C., et al., 2014, *A&A*, 567, A118

Dubois Y., Gavazzi R., Peirani S., Silk J., 2013, *MNRAS*, 433, 3297

Dunne L., Eales S., Edmunds M., Ivison R., Alexander P., Clements D. L., 2000, *MNRAS*, 315, 115

Eales S., et al., 2010, *PASP*, 122, 499

Eales S., et al., 2012, *ApJ*, 761, 168

Eales S. A., et al., 2018, *MNRAS*, 481, 1183

Eckart A., Downes D., Genzel R., Harris A. I., Jaffe D. T., Wild W., 1990, *ApJ*, 348, 434

Eden D. J., et al., 2017, *MNRAS*, 469, 2163

Elmegreen B. G., 1994, *ApJ*, 425, L73

Elmegreen B. G., Parravano A., 1994, *ApJ*, 435, L121

Engargiola G., Plambeck R. L., Rosolowsky E., Blitz L., 2003, *ApJS*, 149, 343

Engelbracht C. W., et al., 2007, *PASP*, 119, 994

Fabello S., Catinella B., Giovanelli R., Kauffmann G., Haynes M. P., Heckman T. M., Schiminovich D., 2011, *MNRAS*, 411, 993

Fazio G. G., et al., 2004, *ApJS*, 154, 10

Fitzpatrick E. L., Massa D., 2007, *ApJ*, 663, 320

Ford G. P., et al., 2013, *ApJ*, 769, 55

Galametz M., Madden S. C., Galliano F., Hony S., Bendo G. J., Sauvage M., 2011, *A&A*, 532, A56

Galliano F., Dwek E., Chanial P., 2008, *ApJ*, 672, 214

Galliano F., Galametz M., Jones A. P., 2018, Annual Review of Astronomy and Astrophysics, 56, 673

Gao Y., Solomon P. M., 2004a, *ApJS*, 152, 63

Gao Y., Solomon P. M., 2004b, *ApJ*, 606, 271

Gao Y., Zhang Z., Greve T., MALATANG Team 2017, in American Astronomical Society Meeting Abstracts. p. 324.01

García-Burillo S., Usero A., Alonso-Herrero A., Graciá-Carpio J., Pereira-Santaella M., Colina L., Planesas P., Arribas S., 2012, *A&A*, 539, A8

Gardan E., Braine J., Schuster K. F., Brouillet N., Sievers A., 2007, *A&A*, 473, 91

Gavazzi G., Boselli A., Donati A., Franzetti P., Scodeggio M., 2003, *A&A*, 400, 451

Gillett F. C., Forrest W. J., Merrill K. M., 1973, *ApJ*, 183, 87

Giovanelli R., et al., 2005, *AJ*, 130, 2598

Glover S. C. O., Clark P. C., 2012, *MNRAS*, 421, 116

Glover S. C. O., Clark P. C., 2016, *MNRAS*, 456, 3596

Goddard D., et al., 2017, *MNRAS*, 466, 4731

Gordon K. D., Hanson M. M., Clayton G. C., Rieke G. H., Misselt K. A., 1999, *ApJ*, 519, 165

Gordon K. D., Clayton G. C., Misselt K. A., Landolt A. U., Wolff M. J., 2003, *ApJ*, 594, 279

Gordon K. D., et al., 2007, *PASP*, 119, 1019

Gordon K. D., et al., 2016, *ApJ*, 826, 104

Graczyk D., et al., 2014, *ApJ*, 780, 59

Granato G. L., Lacey C. G., Silva L., Bressan A., Baugh C. M., Cole S., Frenk C. S., 2000, *ApJ*, 542, 710

Gratier P., et al., 2010, *A&A*, 522, A3

Gratier P., et al., 2012, *A&A*, 542, A108

Gratier P., et al., 2017, *A&A*, 600, A27

Griffin M. J., et al., 2010, *A&A*, 518, L3

Groves B., Dopita M. A., Sutherland R. S., Kewley L. J., Fischera J., Leitherer C., Brandl B., van Breugel W., 2008, *ApJS*, 176, 438

Hameed S., Devereux N., 2005, *AJ*, 129, 2597

Hao C.-N., Kennicutt R. C., Johnson B. D., Calzetti D., Dale D. A., Moustakas J., 2011, *ApJ*, 741, 124

Hartwick F. D. A., 1971, *ApJ*, 163, 431

Heitsch F., Burkert A., Hartmann L. W., Slyz A. D., Devriendt J. E. G., 2005, *ApJ*, 633, L113

Hermelo I., et al., 2016, *A&A*, 590, A56

Herschel W., 1785, Philosophical Transactions of the Royal Society of London Series I, 75, 213

Herschel J. F. W., 1864, Philosophical Transactions of the Royal Society of London Series I, 154, 1

Heyer M. H., Carpenter J. M., Snell R. L., 2001, *ApJ*, 551, 852

Heyer M. H., Corbelli E., Schneider S. E., Young J. S., 2004, *ApJ*, 602, 723

Heyer M., Krawczyk C., Duval J., Jackson J. M., 2009, *ApJ*, 699, 1092

Hildebrand R. H., 1983, *Quarterly Journal of the Royal Astronomical Society*, 24, 267

Hirashita H., Inoue A. K., Kamaya H., Shibai H., 2001, *A&A*, 366, 83

Ho L. C., Filippenko A. V., Sargent W. L. W., 1997, *ApJ*, 487, 579

Holland W. S., et al., 2013, *MNRAS*, 430, 2513

Hoopes C. G., Walterbos R. A. M., 2000, *ApJ*, 541, 597

Hubble E. P., 1925, The Observatory, 48, 139

Hubble E. P., 1926, *ApJ*, 64

Hughes A., et al., 2010, *MNRAS*, 406, 2065

Hunter J. D., 2007, Computing In Science & Engineering, 9, 90

Israel F. P., et al., 1993, *A&A*, 276, 25

James A., Dunne L., Eales S., Edmunds M. G., 2002, *MNRAS*, 335, 753

James P. A., et al., 2004, *A&A*, 414, 23

Jarrett T. H., et al., 2011, *ApJ*, 735, 112

Jones A. P., 2012, *A&A*, 542, A98

Jones A. P., Fanciullo L., Köhler M., Verstraete L., Guillet V., Bocchio M., Ysard N., 2013, *A&A*, 558, A62

Juvela M., Montillaud J., 2013, *A&A*, 557, A73

Kalberla P. M. W., Dedes L., 2008, *A&A*, 487, 951

Kam Z. S., Carignan C., Chemin L., Amram P., Epinat B., 2015, *MNRAS*, 449, 4048

Kashlinsky A., Jimenez R., 1997, *ApJ*, 474, L81

Kasparova A. V., Zasov A. V., 2008, Astronomy Letters, 34, 152

Kendall M. G., 1938, Biometrika, 30, 81

Kennicutt Jr. R. C., 1998a, *ARAA*, 36, 189

Kennicutt Jr. R. C., 1998b, *ApJ*, 498, 541

Kennicutt R. C., Evans N. J., 2012, *ARAA*, 50, 531

Kennicutt Jr. R. C., Lee J. C., Funes J. G., J. S., Sakai S., Akiyama S., 2008, *ApJS*, 178, 247

Kennicutt Jr. R. C., et al., 2009, *ApJ*, 703, 1672

Kewley L. J., Geller M. J., Jansen R. A., Dopita M. A., 2002, *AJ*, 124, 3135

Khoperskov S. A., Vasiliev E. O., 2017, *MNRAS*, 468, 920

Kirk J. M., et al., 2013, *MNRAS*, 432, 1424

Kirk J. M., et al., 2015, *ApJ*, 798, 58

Kirkpatrick A., et al., 2013, *ApJ*, 778, 51

Knapp G. R., Kerr F. J., Rose W. K., 1973, Astrophys. Lett., 14, 187

Köhler M., Jones A., Ysard N., 2014, *A&A*, 565, L9

Komugi S., Kohno K., Tosaki T., Nakanishi H., Onodera S., Egusa F., Sofue Y., 2007, *Pub. Astron. Soc. Japan*, 59, 55

Kormendy J., Kennicutt Jr. R. C., 2004, *ARAA*, 42, 603

Kramer C., et al., 2010, *A&A*, 518, L67

Kreckel K., et al., 2013, *ApJ*, 771, 62

Kreckel K., et al., 2018, *ApJ*, 863, L21

Kroupa P., 2001, *MNRAS*, 322, 231

Kruijssen J. M. D., Longmore S. N., 2014, *MNRAS*, 439, 3239

Kruijssen J. M. D., et al., 2019, *Nature*, 569, 519

Krumholz M. R., McKee C. F., 2005, *ApJ*, 630, 250

Krumholz M. R., Thompson T. A., 2007, *ApJ*, 669, 289

Krumholz M. R., McKee C. F., Tumlinson J., 2008, *ApJ*, 689, 865

Lada C. J., Lombardi M., Alves J. F., 2010, *ApJ*, 724, 687

Lada C. J., Forbrich J., Lombardi M., Alves J. F., 2012, *ApJ*, 745, 190

Larson R. B., 1981, *MNRAS*, 194, 809

Lee J. C., et al., 2011, *ApJS*, 192, 6

Leger A., Puget J. L., 1984, *A&A*, 137, L5

Leitherer C., et al., 1999, *ApJS*, 123, 3

Leroy A. K., Walter F., Brinks E., Bigiel F., de Blok W. J. G., Madore B., Thornley M. D., 2008, *AJ*, 136, 2782

Leroy A. K., et al., 2011, *ApJ*, 737, 12

Lewis A. R., et al., 2015, *ApJ*, 805, 183

Li A., Draine B. T., 2001, *ApJ*, 554, 778

Licquia T. C., Newman J. A., 2015, *ApJ*, 806, 96

Long K. S., Charles P. A., Dubus G., 2002, *ApJ*, 569, 204

Madau P., Dickinson M., 2014, Annual Review of Astronomy and Astrophysics, 52, 415

Madore B. F., Freedman W. L., 1991, *PASP*, 103, 933

Magdis G. E., et al., 2012, *ApJ*, 760, 6

Mainzer A., et al., 2011, *ApJ*, 731, 53

Marsh K. A., et al., 2017, *MNRAS*, 471, 2730

Martin D. C., et al., 2005, *ApJ*, 619, L1

Maschberger T., Kroupa P., 2009, *MNRAS*, 395, 931

McConnachie A. W., Irwin M. J., Ferguson A. M. N., Ibata R. A., Lewis G. F., Tanvir N., 2005, *MNRAS*, 356, 979

McConnachie A. W., Ferguson A. M. N., Irwin M. J., Dubinski J., Widrow L. M., Dotter A., Ibata R., Lewis G. F., 2010, *ApJ*, 723, 1038

Men'shchikov A., et al., 2010, *A&A*, 518, L103

Men'shchikov A., André P., Didelon P., Motte F., Hennemann M., Schneider N., 2012, *A&A*, 542, A81

Messier C., 1781, Technical report, Catalogue des Nébuleuses et des Amas d'Étoiles (Catalog of Nebulae and Star Clusters)

Meurer G. R., Heckman T. M., Calzetti D., 1999, *ApJ*, 521, 64

Mie G., 1908, Annalen der Physik, 330, 377

Misiriotis A., Popescu C. C., Tuffs R., Kylafis N. D., 2001, *A&A*, 372, 775

Miville-Deschênes M.-A., Murray N., Lee E. J., 2017, *ApJ*, 834, 57

Molinari S., et al., 2010, *A&A*, 518, L100

Morrissey P., et al., 2007, *ApJS*, 173, 682

Mosenkov A. V., et al., 2016, *A&A*, 592, A71

Mosenkov A. V., et al., 2018, *A&A*, 616, A120

Murgia M., Crapsi A., Moscadelli L., Gregorini L., 2002, *A&A*, 385, 412

Murphy E. J., et al., 2011, *ApJ*, 737, 67

Narayanan D., Krumholz M. R., Ostriker E. C., Hernquist L., 2012, *MNRAS*, 421, 3127

Natale G., Popescu C. C., Tuffs R. J., Debattista V. P., Fischera J., Grootes M. W., 2015, *MNRAS*, 449, 243

Nersesian A., et al., 2019, *A&A*, 624, A80

Nieva M. F., Przybilla N., 2012, *A&A*, 539, A143

Noll S., Burgarella D., Giovannoli E., Buat V., Marcillac D., Muñoz-Mateos J. C., 2009, *A&A*, 507, 1793

O'Halloran B., Satyapal S., Dudik R. P., 2006, *ApJ*, 641, 795

Onishi K., Iguchi S., Davis T. A., Bureau M., Cappellari M., Sarzi M., Blitz L., 2017, *MNRAS*, 468, 4663

Onodera S., et al., 2010, *ApJ*, 722, L127

Padmanabhan N., et al., 2008, *ApJ*, 674, 1217

Panuzzo P., Granato G. L., Buat V., Inoue A. K., Silva L., Iglesias-Páramo J., Bressan A., 2007, *MNRAS*, 375, 640

Paturel G., Theureau G., Bottinelli L., Gouguenheim L., Coudreau-Durand N., Hallet N., Petit C., 2003, *A&A*, 412, 57

Peest C., Camps P., Stalevski M., Baes M., Siebenmorgen R., 2017, *A&A*, 601, A92

Pietrzynski G., et al., 2019, arXiv e-prints, p. arXiv:1903.08096

Pilbratt G. L., et al., 2010, *A&A*, 518, L1

Planck Collaboration et al., 2011, *A&A*, 536, A19

Planck Collaboration et al., 2013, *A&A*, 557, A53

Planck Collaboration et al., 2014a, *A&A*, 571, A9

Planck Collaboration et al., 2014b, *A&A*, 571, A16

Planck Collaboration et al., 2015, *A&A*, 582, A28

Plucinsky P. P., et al., 2008, The Astrophysical Journal Supplement Series, 174, 366

Poglitsch A., et al., 2010, *A&A*, 518, L2

Popescu C. C., Tuffs R. J., 2002, *MNRAS*, 335, L41

Popescu C. C., Misiriotis A., Kylafis N. D., Tuffs R. J., Fischera J., 2000, *A&A*, 362, 138

Popescu C. C., Tuffs R. J., Dopita M. A., Fischera J., Kylafis N. D., Madore B. F., 2011, *A&A*, 527, A109

Popescu C. C., Yang R., Tuffs R. J., Natale G., Rushton M., Aharonian F., 2017, *MNRAS*, 470, 2539

Putman M. E., et al., 2009, *ApJ*, 703, 1486

Regan M. W., Vogel S. N., 1994, *ApJ*, 434, 536

Relaño M., Kennicutt Jr. R. C., 2009, *ApJ*, 699, 1125

Relaño M., et al., 2018, *A&A*, 613, A43

Rémy-Ruyer A., et al., 2013, *A&A*, 557, A95

Rémy-Ruyer A., et al., 2014, *A&A*, 563, A31

Rice W., Boulanger F., Viallefond F., Soifer B. T., Freedman W. L., 1990, *ApJ*, 358, 418

Rieke G. H., et al., 2004, *ApJS*, 154, 25

Rieke G. H., Alonso-Herrero A., Weiner B. J., Pérez-González P. G., Blaylock M., Donley J. L., Marcillac D., 2009, *ApJ*, 692, 556

Robitaille T., Bressert E., 2012, APLpy: Astronomical Plotting Library in Python, Astrophysics Source Code Library (ascl:1208.017)

Rohlfs K., Wilson T., 1996, Tools of Radio Astronomy. Astronomy and Astrophysics Library, Springer

Roman-Duval J., Jackson J. M., Heyer M., Rathborne J., Simon R., 2010, *ApJ*, 723, 492

Roman-Duval J., et al., 2014, *ApJ*, 797, 86

Roman-Duval J., Heyer M., Brunt C. M., Clark P., Klessen R., Shetty R., 2016, *ApJ*, 818, 144

Rosolowsky E., 2007, *ApJ*, 654, 240

Rosolowsky E., Simon J. D., 2008, *ApJ*, 675, 1213

Rosolowsky E., Keto E., Matsushita S., Willner S. P., 2007, *ApJ*, 661, 830

Rosolowsky E. W., Pineda J. E., Kauffmann J., Goodman A. A., 2008, *ApJ*, 679, 1338

Rosolowsky E., Pineda J. E., Gao Y., 2011, *MNRAS*, 415, 1977

Roussel H., et al., 2007, *ApJ*, 669, 959

Russell S. C., Dopita M. A., 1992, *ApJ*, 384, 508

Saftly W., Baes M., Camps P., 2014, *A&A*, 561, A77

Saintonge A., et al., 2011, *MNRAS*, 415, 32

Saintonge A., et al., 2017, *ApJS*, 233, 22

Salim S., Boquien M., Lee J. C., 2018, *ApJ*, 859, 11

Sandage A., Humphreys R. M., 1980, *ApJ*, 236, L1

Sanders D. B., Scoville N. Z., Solomon P. M., 1985, *ApJ*, 289, 373

Sandstrom K. M., et al., 2013, *ApJ*, 777, 5

Sanduleak N., 1969, *AJ*, 74, 47

Schaye J., Dalla Vecchia C., 2008, *MNRAS*, 383, 1210

Schiminovich D., et al., 2010, *MNRAS*, 408, 919

Schlafly E. F., Finkbeiner D. P., 2011, *ApJ*, 737, 103

Schmidt M., 1959, *ApJ*, 129, 243

Schruba A., Leroy A. K., Walter F., Sandstrom K., Rosolowsky E., 2010, *ApJ*, 722, 1699

Schruba A., et al., 2012, *AJ*, 143, 138

Schuster K.-F., et al., 2004, *A&A*, 423, 1171

Scoville N. Z., et al., 2000, *AJ*, 119, 991

Shetty R., Kelly B. C., Bigiel F., 2013, *MNRAS*, 430, 288

Shetty R., Kelly B. C., Rahman N., Bigiel F., Bolatto A. D., Clark P. C., Klessen R. S., Konstandin L. K., 2014, *MNRAS*, 437, L61

Shu F. H., Milione V., Gebel W., Yuan C., Goldsmith D. W., Roberts W. W., 1972, *ApJ*, 173, 557

Silva L., Granato G. L., Bressan A., Danese L., 1998, *ApJ*, 509, 103

Smith D. J. B., Hayward C. C., 2018, *MNRAS*, 476, 1705

Smith J. D. T., et al., 2007, *ApJ*, 656, 770

Smith M. W. L., et al., 2010, *A&A*, 518, L51

Smith M. W. L., et al., 2012, *ApJ*, 756, 40

Smith M. D., et al., 2019, *MNRAS*, 485, 4359

Solomon P. M., Sanders D. B., Scoville N. Z., 1979, in Burton W. B., ed., IAU Symposium Vol. 84, The Large-Scale Characteristics of the Galaxy. pp 35–52

Solomon P. M., Rivolo A. R., Barrett J., Yahil A., 1987, *ApJ*, 319, 730

Spitzer L., 1978, Physical processes in the interstellar medium. New York : Wiley, doi:10.1002/9783527617722

Stecher T. P., Donn B., 1965, *ApJ*, 142, 1681

Steinacker J., Baes M., Gordon K. D., 2013, *ARAA*, 51, 63

Strong A. W., Mattox J. R., 1996, *A&A*, 308, L21

Sun J., et al., 2018, *ApJ*, 860, 172

Tabatabaei F. S., et al., 2014, *A&A*, 561, A95

Tacconi L. J., et al., 2018, *ApJ*, 853, 179

Tavakoli M., 2012, arXiv e-prints, p. arXiv:1207.6150

Thilker D. A., et al., 2005, *ApJ*, 619, L67

Tojeiro R., Percival W. J., Heavens A. F., Jimenez R., 2011, *MNRAS*, 413, 434

Trewhella M., Davies J. I., Disney M. J., Jones H. G. W., 1997, *MNRAS*, 288, 397

Usero A., et al., 2015, *AJ*, 150, 115

Utomo D., Chiang I.-D., Leroy A. K., Sand strom K. M., Chastenet J., 2019, arXiv e-prints, p. arXiv:1902.08629

Verley S., Hunt L. K., Corbelli E., Giovanardi C., 2007, *A&A*, 476, 1161

Verley S., Corbelli E., Giovanardi C., Hunt L. K., 2009, *A&A*, 493, 453

Verley S., Corbelli E., Giovanardi C., Hunt L. K., 2010, *A&A*, 510, A64

Verstocken S., Van De Putte D., Camps P., Baes M., 2017, Astronomy and Computing, 20, 16

Viaene S., et al., 2014, *A&A*, 567, A71

Viaene S., et al., 2016, *A&A*, 586, A13

Viaene S., Sarzi M., Baes M., Fritz J., Puerari I., 2017a, *MNRAS*, 472, 1286

Viaene S., et al., 2017b, *A&A*, 599, A64

Walter F., Brinks E., de Blok W. J. G., Bigiel F., Kennicutt Robert C. J., Thornley M. D., Leroy A., 2008, *AJ*, 136, 2563

Whitworth A. P., et al., 2019, *MNRAS*, 489, 5436

Williams J. P., de Geus E. J., Blitz L., 1994, *ApJ*, 428, 693

Williams J. P., Blitz L., McKee C. F., 2000, in Mannings V., Boss A. P., Russell S. S., eds, Protostars and Planets IV. p. 97 (`arXiv:astro-ph/9902246`)

Williams B. F., et al., 2017, *ApJ*, 846, 145

Williams T. G., Gear W. K., Smith M. W. L., 2018, *MNRAS*, 479, 297

Williams T. G., Gear W. K., Smith M. W. L., 2019a, *MNRAS*, 483, 5135

Williams T. G., Baes M., De Looze I., Relaño M., Smith M. W. L., Verstocken S., Viaene S., 2019b, *MNRAS*, 487, 2753

Wilson C. D., Scoville N., 1990, *ApJ*, 363, 435

Witt A. N., Gordon K. D., 2000, *ApJ*, 528, 799

Wolfe S. A., Pisano D. J., Lockman F. J., McGaugh S. S., Shaya E. J., 2013, *Nature*, 497, 224

Wong T., Blitz L., 2002, *ApJ*, 569, 157

Wright E. L., et al., 2010, *AJ*, 140, 1868

Wu J., Evans II N. J., Shirley Y. L., Knez C., 2010, *ApJS*, 188, 313

Wyse R. F. G., 1986, *ApJ*, 311, L41

Xilouris E. M., Byun Y. I., Kylafis N. D., Paleologou E. V., Papamastorakis J., 1999, *A&A*, 344, 868

Xilouris E. M., et al., 2012, *A&A*, 543, A74

York D. G., et al., 2000, *AJ*, 120, 1579

Zhu Y.-N., Wu H., Li H.-N., Cao C., 2010, Research in Astronomy and Astrophysics, 10, 329

Zurita A., Bresolin F., 2012, *MNRAS*, 427, 1463

al-Sufi A. a.-R., 964, Book of Fixed Stars

da Cunha E., Charlot S., Elbaz D., 2008, *MNRAS*, 388, 1595 de Blok W. J. G., Walter F., Brinks E., Trachternach C., Oh S. H., Kennicutt R. C. J., 2008, *AJ*, 136, 2648

de Vaucouleurs G., 1959, *ApJ*, 130, 728

van Dishoeck E. F., Black J. H., 1988, *ApJ*, 334, 771

van der Walt S., Colbert S. C., Varoquaux G., 2011, CoRR, abs/1102.1523

Appendix A

Fitting With Uniform Weights

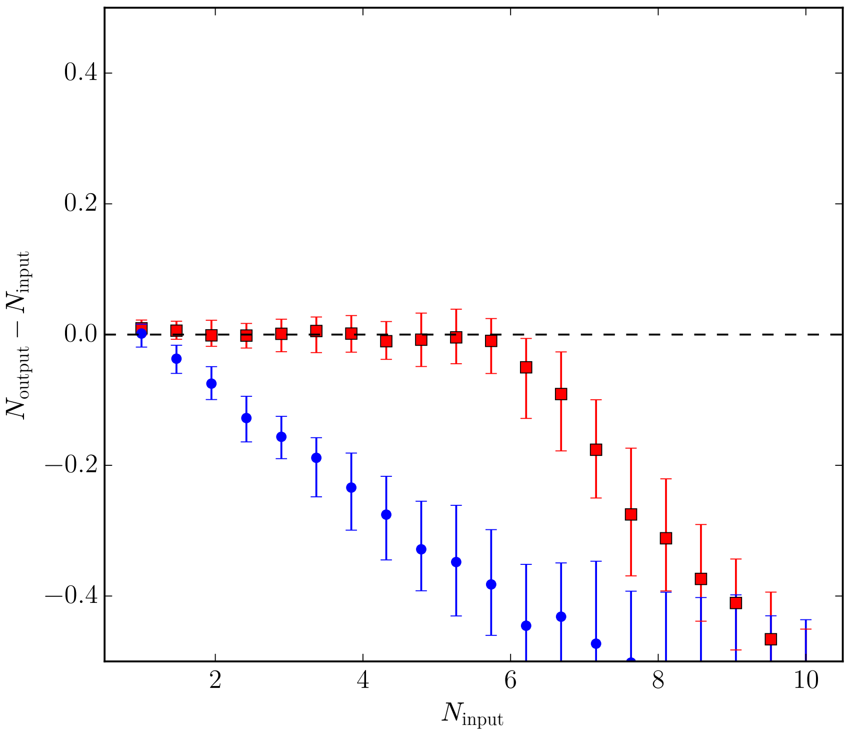

Figure A.1: Recovered N against input N for a variety of inputted slopes. The blue dots indicate points where I have assumed a constant percentage error in SFR and gas surface density, the red squares show the errors weighted based on the errors in the relevant maps. The dashed line shows where the recovered slope is equal to the input slope.

To avoid biasing the data set unnecessarily, I fit to all pixels regardless of S/N. As many of these points (particularly with the molecular gas) are low S/N, it is important to take into account the errors on these points, and I highlight this here.

I have performed a number of simulations where I sample 1000 points distributed normally over the dynamical range of the total gas density, and input a slope N that ranges from 1 to 10. The points are given scatter in both $\Sigma_{\rm SFR}$ and $\Sigma_{\rm gas}$ based on the approximate scatter in the data (here, I have assumed normal distributions in both $\Sigma_{\rm SFR}$ and $\Sigma_{\rm gas}$). I performed a fit in two different ways – firstly by weighting the errors assuming a constant percentage error on the data, and secondly by weighting by the RMS errors in the map. For each inputted N, I repeat this fit 100 times, and calculate the median recovered N, with the 16th and 84th percentiles forming the lower and upper errors. The results of these simulations can be seen in Fig A.1.

For any simulated N above a value of 1, it can be seen that the uniformly weighted error systematically underestimates the slope. When weighting based on the RMS errors of the map, I can reliably recover slopes up to an N of 6. This is due to the percentage errors being larger at lower S/N, and this variation at these low values dominating the fit, especially as the gradient of the slope increases. Since the distribution of $\Sigma_{\rm gas}$ in the real data is skewed to lower S/N rather than normally distributed, I would expect this effect to be even more pronounced in the real data. Realistically accounting for the errors in $\Sigma_{\rm SFR}$ and $\Sigma_{\rm gas}$ allows me to recover the underlying Schmidt index of the data across the entire range of N that I calculate in my work, and so I opt to use this method, rather than assuming a uniform weighting in either $\Sigma_{\rm SFR}$ or $\Sigma_{\rm gas}$.

APPENDIX B

SOURCE EXTRACTION COMPARISON

Here, we present a brief overview of the various source extraction algorithms used in our initial testing – FELLWALKER, SEXTRACTOR, and ASTRODENDRO. We have attempted to homogenise the extraction criteria to make testing these algorithms as fair as possible. In all cases, we detect objects only if they are 3σ above the background, with an area larger than the beam. For FELLWALKER and ASTRODENDRO, we also set a minimum significance for the structure to be 3σ (else the peaks will be merged into a single peak). For SEXTRACTOR, we turn off the deblending threshold. The results of these various algorithms are shown in Fig. B.1. There is good correspondence between the three algorithms, and each detect a similar number of sources (169 for FELLWALKER, 165 for ASTRODENDRO, and 188 for SEXTRACTOR). However, we can see that FELLWALKER essentially partitions all of the emission in the image, leading to clearly unreasonably large structures. ASTRODENDRO, however, finds more compact sources of emission. SEXTRACTOR can deblend some of the most crowded regions, resolving single sources in the other algorithms into several smaller sources, but produces an ellipse of emission, rather than an exact contour. Given that SEXTRACTOR can have overlapping ellipses (which is always the case in these crowded areas), whereas ASTRODENDRO separates sources by default, we have opted to use ASTRODENDRO in this work.

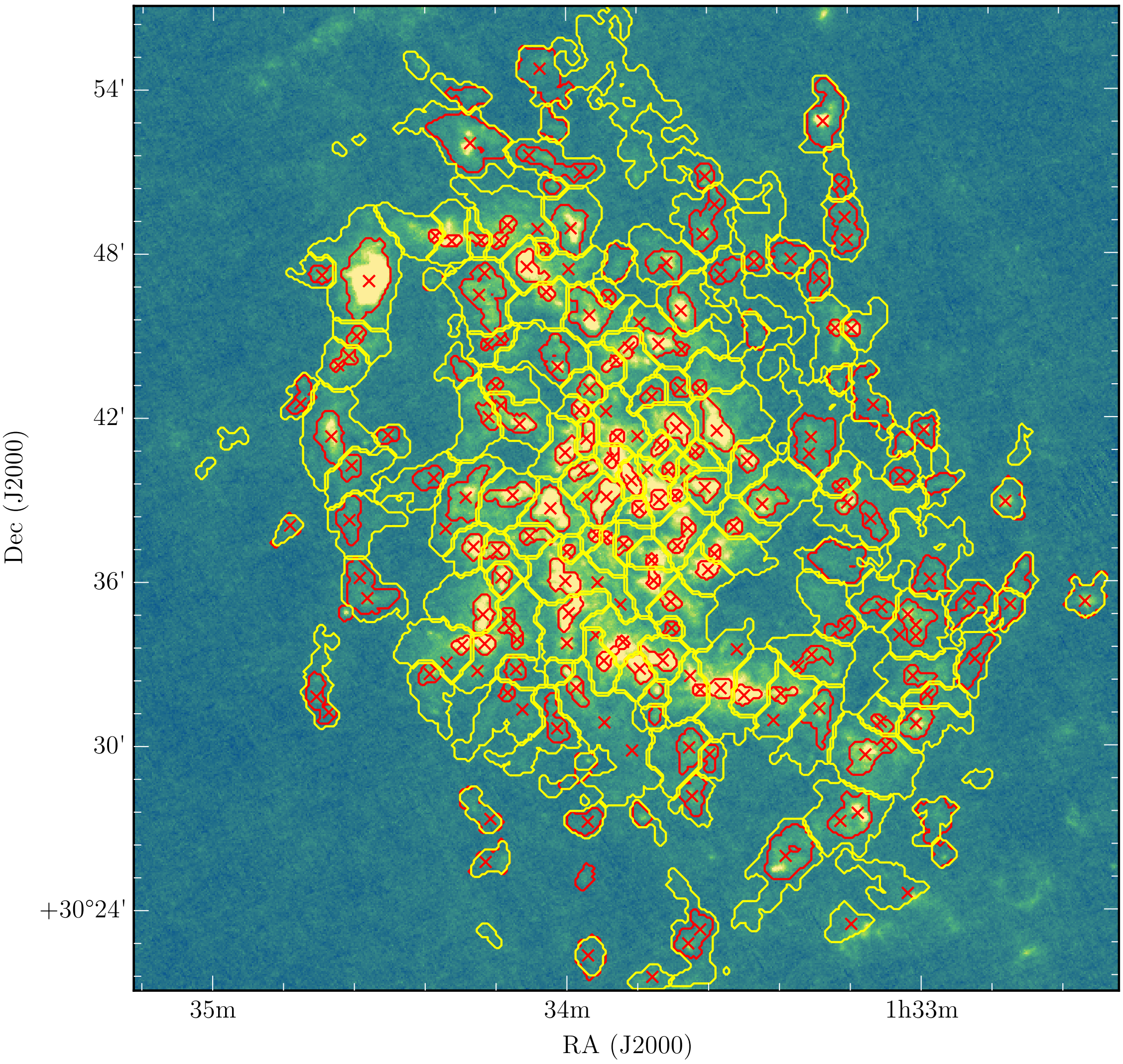

Figure B.1: Comparison of 3 extraction algorithms overlaid on the PACS 160μm map. Yellow contours indicate sources as detected by FELLWALKER, red contours by ASTRODENDRO and red crosses from SEXTRACTOR.

APPENDIX C
GMC LEAF NODE PARAMETERS

Table C.1: Leaf node parameters for the GMCs. Generally, errors given are 1σ errors. However, in the case of an 3σ upper limit, the flux is given as that upper limit.

GMC ID	R.A. (J2000)	Dec (J2000)	R (kpc)	FWHM (pc)	S_{100} (Jy)	S_{160} (Jy)	S_{250} (Jy)	S_{450} (Jy)	S_{850} (Jy)
0	1 33 56.0	30 22 22.4	6.9	152	0.43 ± 0.01	0.43 ± 0.02	0.55 ± 0.01	0.135 ± 0.009	0.036 ± 0.004
1	1 33 38.5	30 23 04.7	6.6	172	0.83 ± 0.03	1.24 ± 0.03	0.84 ± 0.01	0.151 ± 0.008	0.046 ± 0.002
2	1 33 56.9	30 25 14.2	5.8	87	0.06 ± 0.01	0.18 ± 0.01	0.15 ± 0.01	0.020 ± 0.002	0.005 ± 0.001
3	1 33 22.7	30 26 02.6	5.9	236	1.97 ± 0.04	2.83 ± 0.05	1.97 ± 0.02	0.495 ± 0.012	0.142 ± 0.004
4	1 34 12.8	30 25 50.0	5.8	155	0.37 ± 0.02	0.64 ± 0.02	0.54 ± 0.01	0.087 ± 0.009	0.032 ± 0.002
5	1 32 56.3	30 26 02.0	7.1	105	0.17 ± 0.01	0.21 ± 0.01	0.19 ± 0.01	0.021 ± 0.005	0.010 ± 0.002
6	1 32 57.5	30 27 22.9	6.6	178	0.34 ± 0.02	0.54 ± 0.02	0.38 ± 0.01	0.077 ± 0.009	0.028 ± 0.002
7	1 33 11.6	30 27 27.5	5.8	195	3.42 ± 0.04	3.40 ± 0.05	2.11 ± 0.02	0.444 ± 0.010	0.130 ± 0.003
8	1 33 56.8	30 27 17.2	4.9	134	0.25 ± 0.02	0.38 ± 0.02	0.28 ± 0.01	0.038 ± 0.003	< 0.004
9	1 34 14.5	30 27 39.2	5.2	176	0.47 ± 0.03	0.69 ± 0.02	0.52 ± 0.01	0.076 ± 0.007	0.009 ± 0.001
10	1 33 47.3	30 27 28.6	4.8	85	0.22 ± 0.01	0.22 ± 0.02	0.14 ± 0.01	< 0.012	0.004 ± 0.001
11	1 33 38.6	30 28 14.9	4.6	140	0.51 ± 0.02	0.68 ± 0.02	0.43 ± 0.01	0.096 ± 0.006	0.013 ± 0.001
12	1 33 57.5	30 29 12.3	4.2	144	0.18 ± 0.02	0.30 ± 0.02	0.22 ± 0.01	0.040 ± 0.005	0.010 ± 0.002
13	1 33 39.2	30 29 56.4	3.9	146	0.61 ± 0.03	0.96 ± 0.03	0.73 ± 0.01	0.152 ± 0.006	0.044 ± 0.001
14	1 33 09.0	30 29 42.3	5.3	180	2.07 ± 0.07	2.09 ± 0.06	1.34 ± 0.03	0.211 ± 0.012	0.050 ± 0.004
15	1 33 35.8	30 29 39.5	4.1	99	0.24 ± 0.02	0.25 ± 0.02	0.23 ± 0.01	0.039 ± 0.004	0.007 ± 0.001
16	1 33 17.2	30 31 13.0	4.4	177	0.61 ± 0.03	1.02 ± 0.02	0.72 ± 0.02	0.142 ± 0.007	0.029 ± 0.001
17	1 34 01.8	30 30 53.6	3.6	150	0.23 ± 0.01	0.44 ± 0.02	0.30 ± 0.01	0.041 ± 0.005	0.010 ± 0.001
18	1 33 00.7	30 30 49.4	5.5	139	1.49 ± 0.03	1.49 ± 0.04	0.90 ± 0.02	0.201 ± 0.008	0.043 ± 0.002
19	1 33 06.5	30 30 49.2	5.1	81	0.12 ± 0.02	0.16 ± 0.02	0.15 ± 0.01	0.051 ± 0.004	0.006 ± 0.001
20	1 33 45.0	30 31 09.9	3.4	64	0.10 ± 0.01	0.12 ± 0.02	0.10 ± 0.01	0.011 ± 0.003	0.003 ± 0.000
21	1 34 40.4	30 31 13.2	5.4	79	0.10 ± 0.01	0.18 ± 0.01	0.12 ± 0.01	0.015 ± 0.003	< 0.003
22	1 34 42.4	30 32 01.4	5.3	118	0.30 ± 0.02	0.35 ± 0.02	0.32 ± 0.01	0.046 ± 0.005	0.017 ± 0.001
23	1 33 58.2	30 32 04.1	3.1	103	0.41 ± 0.04	0.55 ± 0.04	0.42 ± 0.01	0.077 ± 0.007	0.011 ± 0.001
24	1 33 29.7	30 31 52.5	3.5	94	2.87 ± 0.08	2.43 ± 0.10	1.13 ± 0.05	0.176 ± 0.013	0.038 ± 0.003
25	1 32 58.7	30 31 52.1	5.4	76	0.10 ± 0.01	0.12 ± 0.02	0.13 ± 0.01	0.024 ± 0.003	0.004 ± 0.001
26	1 33 23.7	30 31 55.4	3.8	95	0.14 ± 0.03	0.25 ± 0.03	0.21 ± 0.02	0.056 ± 0.005	0.010 ± 0.001
27	1 34 10.0	30 31 58.9	3.5	70	0.14 ± 0.01	0.17 ± 0.01	0.12 ± 0.01	0.019 ± 0.004	0.005 ± 0.001

Table C.1: Leaf node parameters for the GMCs.

GMC ID	R.A. (J2000)	Dec (J2000)	R (kpc)	FWHM (pc)	S_{100} (Jy)	S_{160} (Jy)	S_{250} (Jy)	S_{450} (Jy)	S_{850} (Jy)
28	1 33 44.9	30 32 04.9	3.0	62	0.24 ± 0.02	0.25 ± 0.03	0.19 ± 0.01	0.018 ± 0.005	0.004 ± 0.001
29	1 33 33.9	30 32 07.7	3.3	97	2.13 ± 0.06	2.25 ± 0.08	1.24 ± 0.03	0.202 ± 0.007	0.040 ± 0.002
30	1 33 37.4	30 32 04.4	3.2	53	0.20 ± 0.03	0.23 ± 0.04	0.17 ± 0.02	0.029 ± 0.004	0.005 ± 0.001
31	1 32 51.0	30 33 02.6	5.7	160	0.26 ± 0.02	0.29 ± 0.02	0.37 ± 0.01	0.108 ± 0.007	0.020 ± 0.002
32	1 33 00.7	30 32 33.0	5.1	112	0.22 ± 0.01	0.34 ± 0.02	0.26 ± 0.01	0.033 ± 0.006	0.015 ± 0.001
33	1 34 23.2	30 32 39.5	3.9	93	0.17 ± 0.03	0.27 ± 0.02	0.21 ± 0.01	0.034 ± 0.004	0.010 ± 0.001
34	1 33 47.6	30 32 51.4	2.7	109	1.75 ± 0.08	1.74 ± 0.09	1.03 ± 0.03	0.168 ± 0.006	0.039 ± 0.002
35	1 34 08.6	30 32 50.7	3.1	100	0.23 ± 0.01	0.33 ± 0.03	0.27 ± 0.01	0.069 ± 0.006	0.008 ± 0.001
36	1 33 59.9	30 32 43.4	2.9	47	0.17 ± 0.01	0.16 ± 0.02	0.09 ± 0.01	< 0.008	0.003 ± 0.001
37	1 33 18.6	30 33 13.6	3.7	144	0.33 ± 0.02	0.46 ± 0.02	0.33 ± 0.02	0.061 ± 0.006	0.011 ± 0.002
38	1 33 53.3	30 33 12.5	2.6	90	0.86 ± 0.06	0.76 ± 0.08	0.43 ± 0.04	0.059 ± 0.008	0.013 ± 0.002
39	1 33 43.9	30 33 10.5	2.6	123	1.10 ± 0.06	1.19 ± 0.07	0.82 ± 0.03	0.136 ± 0.008	0.029 ± 0.002
40	1 34 17.7	30 33 43.2	3.3	75	0.90 ± 0.05	0.90 ± 0.06	0.56 ± 0.03	0.115 ± 0.006	0.021 ± 0.001
41	1 34 13.9	30 33 45.1	3.1	86	2.67 ± 0.07	2.53 ± 0.08	1.48 ± 0.03	0.284 ± 0.011	0.048 ± 0.002
42	1 34 09.2	30 34 21.1	2.6	130	0.24 ± 0.04	0.42 ± 0.04	0.29 ± 0.02	0.077 ± 0.007	< 0.006
43	1 33 50.5	30 33 47.6	2.3	52	0.19 ± 0.03	0.20 ± 0.03	0.15 ± 0.02	0.027 ± 0.004	0.004 ± 0.001
44	1 33 01.0	30 34 33.2	4.7	180	1.76 ± 0.03	2.12 ± 0.04	1.28 ± 0.02	0.222 ± 0.008	0.040 ± 0.002
45	1 33 42.2	30 34 18.3	2.2	63	0.10 ± 0.01	0.12 ± 0.01	0.11 ± 0.01	0.011 ± 0.003	< 0.002
46	1 33 13.3	30 34 20.5	3.8	114	0.19 ± 0.01	0.28 ± 0.02	0.21 ± 0.01	0.076 ± 0.006	< 0.005
47	1 34 14.2	30 34 51.3	2.7	123	1.83 ± 0.04	2.04 ± 0.06	1.31 ± 0.03	0.207 ± 0.010	0.041 ± 0.002
48	1 33 59.5	30 34 53.3	2.0	114	1.67 ± 0.09	1.80 ± 0.08	1.08 ± 0.04	0.219 ± 0.010	0.032 ± 0.002
49	1 32 44.2	30 35 31.5	5.9	199	1.08 ± 0.03	1.18 ± 0.02	0.96 ± 0.01	0.226 ± 0.009	0.053 ± 0.003
50	1 32 51.8	30 35 08.2	5.3	165	0.54 ± 0.02	0.60 ± 0.02	0.46 ± 0.01	0.091 ± 0.007	0.025 ± 0.001
51	1 34 37.4	30 34 53.9	4.4	62	0.29 ± 0.01	0.23 ± 0.01	0.12 ± 0.01	0.014 ± 0.003	0.003 ± 0.000
52	1 33 06.9	30 35 04.0	4.2	119	0.25 ± 0.01	0.34 ± 0.02	0.37 ± 0.01	0.058 ± 0.006	0.020 ± 0.001
53	1 32 31.8	30 35 21.8	6.9	173	1.58 ± 0.03	1.87 ± 0.02	1.28 ± 0.01	0.248 ± 0.009	0.053 ± 0.002
54	1 34 33.8	30 35 42.1	4.0	237	0.78 ± 0.03	1.64 ± 0.03	1.36 ± 0.01	0.302 ± 0.007	0.065 ± 0.002
55	1 33 42.3	30 35 18.5	1.8	83	0.37 ± 0.03	0.41 ± 0.03	0.26 ± 0.01	0.031 ± 0.006	0.007 ± 0.001
56	1 34 00.3	30 36 06.4	1.6	146	3.99 ± 0.11	3.43 ± 0.09	1.77 ± 0.03	0.296 ± 0.009	0.052 ± 0.001

Table C.1: Leaf node parameters for the GMCs.

GMC ID	R.A. (J2000)	Dec (J2000)	R (kpc)	FWHM (pc)	S_{100} (Jy)	S_{160} (Jy)	S_{250} (Jy)	S_{450} (Jy)	S_{850} (Jy)
57	1 32 58.2	30 36 11.6	4.7	169	0.37 ± 0.02	0.68 ± 0.02	0.43 ± 0.01	0.079 ± 0.006	0.008 ± 0.002
58	1 34 11.0	30 36 10.2	2.2	99	1.86 ± 0.04	1.77 ± 0.04	1.03 ± 0.02	0.152 ± 0.009	0.034 ± 0.002
59	1 33 45.2	30 36 06.3	1.5	66	0.34 ± 0.07	0.44 ± 0.05	0.27 ± 0.02	0.047 ± 0.005	0.008 ± 0.001
60	1 33 14.0	30 36 44.3	3.3	220	0.61 ± 0.03	0.83 ± 0.03	0.81 ± 0.01	0.179 ± 0.009	0.040 ± 0.002
61	1 33 36.0	30 36 28.0	1.8	88	1.19 ± 0.08	1.18 ± 0.07	0.60 ± 0.04	0.106 ± 0.007	0.025 ± 0.001
62	1 33 45.6	30 36 48.4	1.2	46	0.40 ± 0.06	0.32 ± 0.06	0.19 ± 0.02	0.019 ± 0.005	0.005 ± 0.001
63	1 34 15.8	30 37 19.0	2.3	97	1.62 ± 0.05	1.46 ± 0.06	0.74 ± 0.03	0.167 ± 0.006	0.024 ± 0.001
64	1 33 59.7	30 37 06.6	1.3	60	0.16 ± 0.02	0.18 ± 0.02	0.14 ± 0.01	0.027 ± 0.003	0.002 ± 0.000
65	1 33 34.8	30 37 04.2	1.7	54	0.48 ± 0.03	0.37 ± 0.03	0.22 ± 0.02	0.033 ± 0.004	0.006 ± 0.001
66	1 34 11.9	30 37 10.2	2.0	97	0.31 ± 0.04	0.53 ± 0.04	0.43 ± 0.02	0.084 ± 0.008	0.023 ± 0.001
67	1 33 50.3	30 37 23.4	0.9	70	0.57 ± 0.03	0.51 ± 0.03	0.34 ± 0.02	0.037 ± 0.004	0.006 ± 0.001
68	1 33 41.1	30 37 21.8	1.2	72	0.15 ± 0.01	0.21 ± 0.02	0.16 ± 0.02	0.014 ± 0.004	0.003 ± 0.001
69	1 34 47.1	30 37 58.7	4.8	121	0.32 ± 0.01	0.45 ± 0.02	0.31 ± 0.01	0.048 ± 0.004	0.006 ± 0.001
70	1 34 36.7	30 38 19.8	3.9	155	0.28 ± 0.02	0.51 ± 0.02	0.48 ± 0.01	0.076 ± 0.006	0.028 ± 0.002
71	1 34 05.3	30 37 42.1	1.4	107	0.30 ± 0.04	0.46 ± 0.05	0.32 ± 0.02	0.074 ± 0.008	0.009 ± 0.001
72	1 33 53.0	30 37 38.5	0.8	46	0.08 ± 0.01	0.12 ± 0.02	0.08 ± 0.01	0.013 ± 0.003	< 0.001
73	1 33 55.0	30 37 42.7	0.8	52	0.13 ± 0.02	0.18 ± 0.02	0.11 ± 0.01	< 0.009	0.003 ± 0.001
74	1 33 08.0	30 38 12.4	3.7	126	0.13 ± 0.02	0.35 ± 0.03	0.32 ± 0.01	0.077 ± 0.005	0.016 ± 0.001
75	1 33 39.4	30 37 59.4	1.2	71	0.54 ± 0.05	0.53 ± 0.04	0.33 ± 0.03	0.045 ± 0.005	0.010 ± 0.001
76	1 33 31.6	30 38 00.5	1.8	73	0.32 ± 0.02	0.44 ± 0.03	0.28 ± 0.02	0.024 ± 0.004	0.003 ± 0.001
77	1 34 02.7	30 38 42.1	1.1	166	7.36 ± 0.10	7.82 ± 0.10	4.28 ± 0.03	0.659 ± 0.012	0.139 ± 0.003
78	1 33 53.2	30 39 05.7	0.3	132	5.89 ± 0.13	5.15 ± 0.09	2.45 ± 0.03	0.425 ± 0.011	0.062 ± 0.002
79	1 34 16.9	30 39 09.4	2.2	199	1.45 ± 0.04	1.98 ± 0.06	1.50 ± 0.02	0.278 ± 0.011	0.062 ± 0.002
80	1 32 45.1	30 38 58.0	5.6	154	1.97 ± 0.02	1.70 ± 0.02	1.04 ± 0.01	0.229 ± 0.006	0.054 ± 0.002
81	1 33 47.6	30 38 41.8	0.5	65	0.60 ± 0.06	0.57 ± 0.07	0.29 ± 0.03	0.043 ± 0.005	0.009 ± 0.001
82	1 33 26.2	30 38 56.7	2.1	153	1.41 ± 0.04	1.66 ± 0.04	1.05 ± 0.02	0.205 ± 0.008	0.045 ± 0.002
83	1 33 12.3	30 38 53.3	3.3	92	0.82 ± 0.04	0.67 ± 0.03	0.39 ± 0.02	0.031 ± 0.006	0.011 ± 0.001
84	1 33 44.2	30 39 01.0	0.6	85	1.21 ± 0.07	1.17 ± 0.07	0.65 ± 0.03	0.091 ± 0.009	0.013 ± 0.001
85	1 34 09.1	30 39 11.4	1.6	140	2.14 ± 0.06	2.36 ± 0.06	1.39 ± 0.03	0.227 ± 0.009	0.042 ± 0.001

Table C.1: Leaf node parameters for the GMCs.

GMC ID	R.A. (J2000)	Dec (J2000)	R (kpc)	FWHM (pc)	S_{100} (Jy)	S_{160} (Jy)	S_{250} (Jy)	S_{450} (Jy)	S_{850} (Jy)
86	1 33 36.6	30 39 27.2	1.2	121	2.15 ± 0.07	2.23 ± 0.07	1.32 ± 0.03	0.260 ± 0.010	0.041 ± 0.003
87	1 33 41.5	30 39 10.5	0.8	46	0.16 ± 0.05	0.17 ± 0.04	0.13 ± 0.02	< 0.017	0.004 ± 0.001
88	1 33 49.0	30 39 45.6	0.2	98	1.72 ± 0.08	1.52 ± 0.08	0.85 ± 0.04	0.113 ± 0.007	0.021 ± 0.002
89	1 32 56.6	30 39 35.0	4.6	108	0.13 ± 0.01	0.30 ± 0.01	0.21 ± 0.01	0.033 ± 0.005	0.011 ± 0.001
90	1 33 13.3	30 39 30.4	3.2	66	0.25 ± 0.02	0.25 ± 0.03	0.17 ± 0.01	0.029 ± 0.004	< 0.004
91	1 34 23.3	30 39 48.9	2.8	120	0.18 ± 0.02	0.33 ± 0.02	0.30 ± 0.01	0.073 ± 0.006	0.014 ± 0.002
92	1 33 03.3	30 39 50.5	4.1	88	0.13 ± 0.01	0.29 ± 0.01	0.21 ± 0.01	0.039 ± 0.004	0.005 ± 0.001
93	1 34 36.5	30 40 14.3	3.9	108	0.15 ± 0.02	0.36 ± 0.02	0.37 ± 0.01	0.118 ± 0.005	0.018 ± 0.001
94	1 33 57.0	30 40 06.3	0.6	95	0.62 ± 0.03	0.77 ± 0.04	0.48 ± 0.02	0.067 ± 0.005	0.014 ± 0.001
95	1 33 42.6	30 40 02.4	0.7	63	0.08 ± 0.03	0.14 ± 0.02	0.12 ± 0.01	0.032 ± 0.005	0.004 ± 0.001
96	1 33 18.0	30 41 05.2	2.9	228	1.32 ± 0.03	2.23 ± 0.05	1.81 ± 0.02	0.372 ± 0.009	0.118 ± 0.002
97	1 33 29.3	30 40 27.2	1.9	93	3.33 ± 0.07	2.34 ± 0.06	1.11 ± 0.02	0.172 ± 0.007	0.028 ± 0.001
98	1 33 52.1	30 40 35.2	0.4	76	0.24 ± 0.05	0.29 ± 0.05	0.16 ± 0.02	0.043 ± 0.007	0.007 ± 0.002
99	1 34 39.9	30 41 19.9	4.2	167	2.73 ± 0.07	2.88 ± 0.07	1.92 ± 0.02	0.425 ± 0.009	0.097 ± 0.003
100	1 34 00.1	30 40 46.0	0.9	92	5.30 ± 0.07	4.10 ± 0.07	1.89 ± 0.04	0.269 ± 0.007	0.052 ± 0.001
101	1 33 38.0	30 40 47.7	1.2	59	0.12 ± 0.02	0.17 ± 0.01	0.13 ± 0.01	0.030 ± 0.004	0.004 ± 0.001
102	1 33 44.0	30 40 59.5	0.8	71	0.52 ± 0.03	0.48 ± 0.04	0.31 ± 0.03	0.061 ± 0.005	0.007 ± 0.001
103	1 33 02.6	30 41 02.4	4.2	101	0.18 ± 0.02	0.18 ± 0.01	0.18 ± 0.01	0.054 ± 0.005	0.010 ± 0.001
104	1 33 56.6	30 41 15.3	0.8	105	0.53 ± 0.06	0.68 ± 0.06	0.49 ± 0.02	0.065 ± 0.007	0.012 ± 0.001
105	1 33 34.4	30 41 33.7	1.6	156	13.27 ± 0.17	10.37 ± 0.09	4.52 ± 0.03	0.771 ± 0.010	0.141 ± 0.002
106	1 32 59.2	30 41 31.6	4.5	109	0.43 ± 0.01	0.53 ± 0.02	0.42 ± 0.01	0.091 ± 0.004	0.013 ± 0.001
107	1 33 41.2	30 41 37.0	1.1	109	1.24 ± 0.04	1.34 ± 0.06	0.77 ± 0.03	0.106 ± 0.007	0.017 ± 0.002
108	1 34 30.2	30 41 22.7	3.4	81	0.20 ± 0.01	0.32 ± 0.01	0.22 ± 0.01	< 0.011	0.004 ± 0.000
109	1 33 51.3	30 41 18.9	0.7	59	0.38 ± 0.05	0.39 ± 0.04	0.24 ± 0.02	0.038 ± 0.005	0.006 ± 0.001
110	1 34 08.8	30 41 59.2	1.8	165	1.40 ± 0.06	1.51 ± 0.06	0.89 ± 0.02	0.122 ± 0.009	0.022 ± 0.002
111	1 34 13.1	30 42 03.0	2.1	100	0.19 ± 0.02	0.35 ± 0.03	0.28 ± 0.01	0.053 ± 0.005	0.013 ± 0.001
112	1 33 08.5	30 42 39.1	3.8	221	0.58 ± 0.03	0.60 ± 0.03	0.75 ± 0.01	0.139 ± 0.007	0.037 ± 0.002
113	1 33 57.7	30 42 17.2	1.2	75	1.06 ± 0.04	0.99 ± 0.05	0.55 ± 0.02	0.081 ± 0.003	0.013 ± 0.001
114	1 34 44.8	30 42 47.6	4.8	131	0.24 ± 0.02	0.41 ± 0.02	0.30 ± 0.01	0.071 ± 0.005	0.011 ± 0.001

Table C.1: Leaf node parameters for the GMCs.

GMC ID	R.A. (J2000)	Dec (J2000)	R (kpc)	FWHM (pc)	S_{100} (Jy)	S_{160} (Jy)	S_{250} (Jy)	S_{450} (Jy)	S_{850} (Jy)
115	1 33 45.5	30 42 46.8	1.3	86	0.27 ± 0.03	0.33 ± 0.03	0.22 ± 0.01	0.012 ± 0.004	0.004 ± 0.000
116	1 33 55.9	30 43 01.5	1.4	113	0.44 ± 0.04	0.58 ± 0.03	0.49 ± 0.02	0.075 ± 0.007	0.019 ± 0.002
117	1 33 40.7	30 43 05.8	1.6	81	0.18 ± 0.02	0.34 ± 0.03	0.19 ± 0.01	0.036 ± 0.003	0.007 ± 0.001
118	1 33 37.2	30 43 05.6	1.8	62	0.21 ± 0.03	0.21 ± 0.02	0.16 ± 0.01	0.013 ± 0.004	0.007 ± 0.000
119	1 33 13.7	30 43 23.4	3.5	106	0.25 ± 0.03	0.19 ± 0.01	0.15 ± 0.00	0.035 ± 0.003	0.011 ± 0.001
120	1 34 12.0	30 43 11.9	2.3	60	0.08 ± 0.01	0.13 ± 0.01	0.11 ± 0.01	0.017 ± 0.004	0.005 ± 0.000
121	1 34 17.6	30 43 46.2	2.8	95	0.09 ± 0.01	0.20 ± 0.01	0.17 ± 0.01	0.039 ± 0.003	0.006 ± 0.001
122	1 34 01.6	30 44 08.9	2.0	160	1.39 ± 0.04	1.53 ± 0.05	0.92 ± 0.02	0.164 ± 0.008	0.043 ± 0.002
123	1 34 37.4	30 44 11.1	4.4	111	0.33 ± 0.03	0.39 ± 0.03	0.22 ± 0.02	0.060 ± 0.006	0.009 ± 0.002
124	1 33 52.0	30 44 00.2	1.7	70	0.31 ± 0.03	0.30 ± 0.04	0.19 ± 0.02	0.014 ± 0.004	0.007 ± 0.001
125	1 33 49.4	30 44 33.4	2.0	79	0.18 ± 0.04	0.30 ± 0.04	0.25 ± 0.02	0.052 ± 0.005	0.009 ± 0.001
126	1 33 43.8	30 44 42.6	2.1	155	3.53 ± 0.05	2.98 ± 0.05	1.41 ± 0.02	0.246 ± 0.010	0.039 ± 0.002
127	1 34 12.1	30 44 49.7	2.7	88	0.07 ± 0.01	0.22 ± 0.02	0.15 ± 0.01	0.031 ± 0.005	0.006 ± 0.001
128	1 33 27.9	30 45 10.1	3.0	127	0.09 ± 0.02	0.29 ± 0.01	0.26 ± 0.01	0.022 ± 0.004	0.010 ± 0.001
129	1 34 35.5	30 45 00.2	4.4	79	0.18 ± 0.01	0.27 ± 0.02	0.22 ± 0.02	0.050 ± 0.007	0.010 ± 0.001
130	1 33 56.0	30 45 46.9	2.5	190	3.81 ± 0.05	3.71 ± 0.06	2.04 ± 0.03	0.301 ± 0.009	0.065 ± 0.004
131	1 33 14.2	30 45 17.2	3.9	64	0.28 ± 0.02	0.30 ± 0.03	0.17 ± 0.02	0.027 ± 0.004	0.007 ± 0.001
132	1 33 11.4	30 45 15.1	4.0	67	1.35 ± 0.07	1.09 ± 0.06	0.58 ± 0.03	0.082 ± 0.006	0.014 ± 0.002
133	1 34 13.7	30 46 31.6	3.3	243	1.90 ± 0.08	2.62 ± 0.07	1.72 ± 0.03	0.341 ± 0.014	0.072 ± 0.004
134	1 33 40.4	30 45 55.4	2.7	142	2.24 ± 0.05	2.83 ± 0.04	1.93 ± 0.02	0.389 ± 0.007	0.079 ± 0.001
135	1 34 33.5	30 47 01.8	4.7	235	49.27 ± 0.17	38.43 ± 0.16	16.74 ± 0.05	2.754 ± 0.025	0.604 ± 0.006
136	1 33 52.8	30 46 23.4	2.7	63	0.11 ± 0.01	0.15 ± 0.01	0.13 ± 0.01	0.027 ± 0.003	0.007 ± 0.001
137	1 33 17.0	30 47 03.2	4.1	124	0.36 ± 0.01	0.54 ± 0.02	0.44 ± 0.01	0.068 ± 0.005	0.016 ± 0.001
138	1 34 03.3	30 46 36.6	3.0	70	0.11 ± 0.03	0.23 ± 0.04	0.20 ± 0.02	0.047 ± 0.004	0.011 ± 0.001
139	1 34 22.7	30 47 03.3	4.0	90	0.19 ± 0.01	0.19 ± 0.01	0.13 ± 0.00	0.014 ± 0.003	0.004 ± 0.001
140	1 34 41.5	30 47 14.7	5.3	92	0.22 ± 0.02	0.42 ± 0.03	0.27 ± 0.01	0.075 ± 0.005	0.013 ± 0.001
141	1 33 43.0	30 47 39.5	3.3	149	0.85 ± 0.03	1.23 ± 0.03	0.86 ± 0.02	0.227 ± 0.009	0.037 ± 0.002
142	1 33 32.8	30 47 22.0	3.5	126	0.23 ± 0.02	0.41 ± 0.02	0.35 ± 0.01	0.040 ± 0.006	0.010 ± 0.001
143	1 34 06.4	30 47 29.3	3.4	137	2.87 ± 0.08	2.63 ± 0.09	1.48 ± 0.04	0.243 ± 0.009	0.043 ± 0.002

Table C.1: Leaf node parameters for the GMCs.

GMC ID	R.A. (J2000)	Dec (J2000)	R (kpc)	FWHM (pc)	S_{100} (Jy)	S_{160} (Jy)	S_{250} (Jy)	S_{450} (Jy)	S_{850} (Jy)
144	1 33 51.2	30 47 39.0	3.2	148	0.32 ± 0.01	0.52 ± 0.02	0.41 ± 0.01	0.033 ± 0.006	0.017 ± 0.002
145	1 33 21.9	30 47 49.4	4.1	156	0.35 ± 0.02	0.84 ± 0.02	0.61 ± 0.01	0.123 ± 0.005	0.029 ± 0.002
146	1 33 28.0	30 47 42.0	3.8	78	0.23 ± 0.01	0.34 ± 0.03	0.24 ± 0.01	0.044 ± 0.005	0.007 ± 0.001
147	1 34 03.9	30 48 08.2	3.5	55	0.07 ± 0.02	0.09 ± 0.02	0.09 ± 0.01	0.019 ± 0.003	< 0.001
148	1 33 59.2	30 48 56.2	3.7	175	2.84 ± 0.05	3.25 ± 0.04	2.21 ± 0.02	0.489 ± 0.013	0.111 ± 0.004
149	1 33 12.5	30 48 56.6	5.0	188	0.88 ± 0.04	0.91 ± 0.03	0.71 ± 0.01	0.155 ± 0.008	0.035 ± 0.002
150	1 33 36.3	30 49 04.6	4.0	197	0.71 ± 0.03	1.25 ± 0.03	0.97 ± 0.01	0.219 ± 0.007	0.050 ± 0.002
151	1 34 11.3	30 48 29.3	3.9	66	0.11 ± 0.01	0.17 ± 0.03	0.14 ± 0.01	0.023 ± 0.005	0.004 ± 0.001
152	1 34 19.4	30 48 28.0	4.2	65	0.20 ± 0.03	0.29 ± 0.04	0.19 ± 0.02	0.038 ± 0.006	0.006 ± 0.001
153	1 34 14.7	30 48 31.5	4.1	66	0.20 ± 0.02	0.26 ± 0.03	0.17 ± 0.01	0.032 ± 0.005	0.005 ± 0.001
154	1 34 22.1	30 48 38.9	4.4	54	0.18 ± 0.04	0.25 ± 0.04	0.15 ± 0.02	0.032 ± 0.007	0.003 ± 0.001
155	1 34 09.8	30 49 03.5	4.1	72	0.10 ± 0.02	0.23 ± 0.03	0.25 ± 0.02	0.045 ± 0.004	0.012 ± 0.001
156	1 33 13.4	30 50 28.3	5.4	83	0.17 ± 0.01	0.18 ± 0.01	0.14 ± 0.01	0.034 ± 0.003	0.005 ± 0.001
157	1 34 02.3	30 50 26.7	4.4	65	0.11 ± 0.01	0.14 ± 0.02	0.10 ± 0.01	0.014 ± 0.002	0.004 ± 0.001
158	1 33 36.3	30 50 50.2	4.6	95	0.48 ± 0.02	0.46 ± 0.02	0.27 ± 0.01	0.034 ± 0.004	0.012 ± 0.001
159	1 34 02.2	30 51 18.0	4.7	207	0.60 ± 0.03	0.82 ± 0.03	0.63 ± 0.01	0.094 ± 0.007	0.019 ± 0.002
160	1 34 16.5	30 52 06.4	5.4	280	4.25 ± 0.06	4.91 ± 0.06	3.11 ± 0.02	0.600 ± 0.013	0.149 ± 0.004
161	1 33 16.1	30 52 55.3	6.1	189	8.67 ± 0.07	5.93 ± 0.04	2.92 ± 0.01	0.529 ± 0.010	0.133 ± 0.003
162	1 34 02.1	30 52 37.9	5.2	127	0.24 ± 0.01	0.27 ± 0.02	0.28 ± 0.00	0.036 ± 0.006	0.016 ± 0.001
163	1 34 16.1	30 53 43.3	6.0	133	0.22 ± 0.01	0.27 ± 0.01	0.27 ± 0.01	0.055 ± 0.005	0.008 ± 0.001
164	1 34 04.1	30 54 34.9	6.0	235	0.97 ± 0.03	1.05 ± 0.03	1.12 ± 0.01	0.229 ± 0.009	0.044 ± 0.003

APPENDIX D

GMC SED PARAMETERS

Table D.1: Calculated dust and gas properties for the GMCs. Generally, errors given are 1σ errors. However, in the case of an 3σ upper limit, the value given is that 3σ upper limit.

GMC ID	T (K)	$\log(\mathrm{M_{dust}}\ [\mathrm{M_\odot}])$	$\log(L_{\mathrm{TIR}}\ [L_\odot])$	L_{CO} (K km s^{-1})	Σ_{HI} (M$_\odot$ pc^{-2})
0	20.95 ± 0.54	3.76 ± 0.05	5.54 ± 0.02	$(1.95 \pm 0.15) \times 10^{-1}$	5.17 ± 0.18
1	21.04 ± 0.45	4.05 ± 0.04	5.83 ± 0.02	$(2.72 \pm 0.12) \times 10^{-1}$	2.73 ± 0.18
2	18.13 ± 0.42	3.43 ± 0.04	4.86 ± 0.03	$(9.47 \pm 1.60) \times 10^{-2}$	1.87 ± 0.21
3	20.98 ± 0.43	4.43 ± 0.04	6.21 ± 0.02	$(2.94 \pm 0.13) \times 10^{-1}$	3.62 ± 0.17
4	19.58 ± 0.41	3.92 ± 0.04	5.54 ± 0.02	$(1.25 \pm 0.10) \times 10^{-1}$	4.52 ± 0.34
5	21.14 ± 0.64	3.34 ± 0.05	5.14 ± 0.03	$(1.93 \pm 0.16) \times 10^{-1}$	2.16 ± 0.35
6	20.44 ± 0.50	3.74 ± 0.04	5.46 ± 0.02	$(2.74 \pm 0.85) \times 10^{-2}$	1.83 ± 0.10
7	24.54 ± 0.57	4.26 ± 0.04	6.41 ± 0.03	$(5.18 \pm 0.17) \times 10^{-1}$	2.97 ± 0.18
8	22.76 ± 0.61	3.38 ± 0.04	5.35 ± 0.03	$(4.03 \pm 1.26) \times 10^{-2}$	2.95 ± 0.16
9	21.97 ± 0.50	3.71 ± 0.04	5.61 ± 0.02	$< 4.11 \times 10^{-2}$	4.22 ± 0.21
10	25.55 ± 0.78	2.98 ± 0.05	5.23 ± 0.03	$(2.18 \pm 0.28) \times 10^{-1}$	< 0.60
11	22.20 ± 0.49	3.69 ± 0.04	5.60 ± 0.02	$(2.72 \pm 0.22) \times 10^{-1}$	1.20 ± 0.17
12	20.20 ± 0.61	3.51 ± 0.05	5.20 ± 0.03	$(9.63 \pm 1.75) \times 10^{-2}$	1.09 ± 0.21
13	20.24 ± 0.46	4.03 ± 0.04	5.73 ± 0.02	$(2.25 \pm 0.10) \times 10^{-1}$	3.18 ± 0.23
14	24.50 ± 0.61	4.04 ± 0.04	6.20 ± 0.03	$(3.34 \pm 0.33) \times 10^{-1}$	1.87 ± 0.26
15	22.22 ± 0.74	3.35 ± 0.06	5.27 ± 0.03	$(1.87 \pm 0.17) \times 10^{-1}$	1.82 ± 0.35
16	20.29 ± 0.43	4.02 ± 0.04	5.72 ± 0.02	$(1.93 \pm 0.12) \times 10^{-1}$	3.68 ± 0.21
17	20.26 ± 0.42	3.62 ± 0.04	5.31 ± 0.02	$(1.67 \pm 0.21) \times 10^{-1}$	1.38 ± 0.11
18	24.56 ± 0.60	3.89 ± 0.04	6.05 ± 0.03	$(2.01 \pm 0.21) \times 10^{-1}$	3.01 ± 0.42
19	19.93 ± 0.89	3.34 ± 0.08	5.00 ± 0.04	$(2.13 \pm 0.46) \times 10^{-1}$	< 1.42
20	22.57 ± 0.93	2.95 ± 0.07	4.90 ± 0.05	$(3.17 \pm 0.28) \times 10^{-1}$	1.51 ± 0.28
21	21.81 ± 0.68	3.08 ± 0.06	4.95 ± 0.03	$(9.01 \pm 2.85) \times 10^{-2}$	< 1.17
22	21.47 ± 0.58	3.54 ± 0.05	5.38 ± 0.03	$(2.48 \pm 0.19) \times 10^{-1}$	2.04 ± 0.19
23	21.93 ± 0.66	3.65 ± 0.05	5.54 ± 0.03	$(1.97 \pm 0.28) \times 10^{-1}$	1.82 ± 0.15
24	28.33 ± 0.85	3.84 ± 0.05	6.34 ± 0.03	$(1.57 \pm 0.14) \times 10^{0}$	< 3.19
25	20.59 ± 0.74	3.19 ± 0.06	4.92 ± 0.03	$(2.94 \pm 0.26) \times 10^{-1}$	< 1.09

Table D.1: Calculated dust and gas properties for the GMCs.

GMC ID	T (K)	log(M$_{\rm dust}$ [M$_\odot$])	log($L_{\rm TIR}$ [$L_\odot$])	$L_{\rm CO}$ (K km s^{-1})	$\Sigma_{\rm HI}$ (M$_\odot$ pc^{-2})
26	19.01 ± 0.86	3.57 ± 0.08	5.11 ± 0.04	$(6.97 \pm 0.93) \times 10^{-1}$	< 1.53
27	22.70 ± 0.79	3.07 ± 0.06	5.04 ± 0.04	$(2.63 \pm 0.37) \times 10^{-1}$	1.58 ± 0.48
28	24.69 ± 0.94	3.10 ± 0.06	5.27 ± 0.04	$(4.20 \pm 0.55) \times 10^{-1}$	2.38 ± 0.44
29	24.96 ± 0.63	4.01 ± 0.04	6.20 ± 0.03	$(8.75 \pm 0.89) \times 10^{-1}$	2.81 ± 0.42
30	23.39 ± 1.23	3.15 ± 0.08	5.19 ± 0.06	$(7.19 \pm 1.13) \times 10^{-1}$	< 2.89
31	19.30 ± 0.63	3.75 ± 0.06	5.33 ± 0.03	$(9.17 \pm 1.47) \times 10^{-2}$	2.61 ± 0.23
32	20.90 ± 0.54	3.50 ± 0.05	5.27 ± 0.03	$(1.80 \pm 0.19) \times 10^{-1}$	1.72 ± 0.53
33	20.79 ± 0.84	3.43 ± 0.06	5.18 ± 0.04	$(4.79 \pm 0.35) \times 10^{-1}$	2.58 ± 0.37
34	24.99 ± 0.71	3.92 ± 0.05	6.12 ± 0.03	$(8.52 \pm 0.32) \times 10^{-1}$	2.97 ± 0.26
35	20.64 ± 0.51	3.55 ± 0.05	5.29 ± 0.02	$(5.40 \pm 0.33) \times 10^{-1}$	2.62 ± 0.31
36	28.84 ± 1.51	2.58 ± 0.09	5.12 ± 0.05	$(2.08 \pm 0.48) \times 10^{-1}$	< 1.67
37	21.52 ± 0.56	3.58 ± 0.05	5.42 ± 0.03	$(1.23 \pm 0.33) \times 10^{-1}$	2.95 ± 0.34
38	27.23 ± 1.19	3.41 ± 0.06	5.81 ± 0.04	$(3.69 \pm 0.59) \times 10^{-1}$	< 2.62
39	23.45 ± 0.69	3.88 ± 0.05	5.92 ± 0.03	$(6.14 \pm 0.37) \times 10^{-1}$	1.23 ± 0.34
40	24.33 ± 0.80	3.69 ± 0.06	5.82 ± 0.03	$(4.91 \pm 0.32) \times 10^{-1}$	2.24 ± 0.40
41	25.41 ± 0.66	4.06 ± 0.04	6.30 ± 0.03	$(1.51 \pm 0.07) \times 10^{0}$	< 1.53
42	21.65 ± 0.83	3.50 ± 0.06	5.35 ± 0.04	$(2.96 \pm 0.29) \times 10^{-1}$	0.99 ± 0.20
43	24.06 ± 1.34	3.05 ± 0.08	5.16 ± 0.06	$< 4.82 \times 10^{-1}$	2.12 ± 0.69
44	23.31 ± 0.49	4.10 ± 0.04	6.13 ± 0.02	$(2.11 \pm 0.13) \times 10^{-1}$	2.97 ± 0.17
45	23.92 ± 0.97	2.84 ± 0.07	4.93 ± 0.04	$(2.29 \pm 0.25) \times 10^{-1}$	2.32 ± 0.23
46	21.08 ± 0.60	3.41 ± 0.06	5.20 ± 0.03	$(1.64 \pm 0.19) \times 10^{-1}$	< 1.51
47	23.76 ± 0.53	4.07 ± 0.04	6.15 ± 0.02	$(8.03 \pm 0.43) \times 10^{-1}$	2.98 ± 0.37
48	24.21 ± 0.70	3.98 ± 0.05	6.10 ± 0.03	$(4.30 \pm 0.34) \times 10^{-1}$	3.88 ± 0.44
49	22.43 ± 0.55	3.99 ± 0.04	5.93 ± 0.02	$(2.35 \pm 0.12) \times 10^{-1}$	2.17 ± 0.18
50	22.44 ± 0.59	3.67 ± 0.05	5.62 ± 0.03	$< 3.66 \times 10^{-2}$	4.21 ± 0.33

Table D.1: Calculated dust and gas properties for the GMCs.

GMC ID	T (K)	log(M$_{\rm dust}$ [M$_\odot$])	log($L_{\rm TIR}$ [$L_\odot$])	$L_{\rm CO}$ (K km s^{-1})	$\Sigma_{\rm HI}$ (M$_\odot$ pc^{-2})
51	28.97 ± 0.99	2.80 ± 0.05	5.35 ± 0.04	$(2.32 \pm 0.29) \times 10^{-1}$	< 1.47
52	19.79 ± 0.51	3.70 ± 0.05	5.34 ± 0.02	$(3.83 \pm 0.25) \times 10^{-1}$	< 1.06
53	22.71 ± 0.49	4.12 ± 0.04	6.09 ± 0.02	$(1.72 \pm 0.12) \times 10^{-1}$	5.06 ± 0.20
54	18.46 ± 0.36	4.43 ± 0.04	5.90 ± 0.02	$(3.31 \pm 0.11) \times 10^{-1}$	4.23 ± 0.14
55	24.88 ± 0.87	3.27 ± 0.06	5.46 ± 0.04	$< 18.63 \times 10^{-2}$	2.64 ± 0.22
56	27.34 ± 0.75	4.07 ± 0.04	6.48 ± 0.03	$(7.45 \pm 0.46) \times 10^{-1}$	1.92 ± 0.23
57	21.00 ± 0.48	3.74 ± 0.04	5.52 ± 0.02	$(7.75 \pm 1.24) \times 10^{-2}$	2.69 ± 0.29
58	25.65 ± 0.62	3.88 ± 0.04	6.14 ± 0.03	$(8.60 \pm 0.41) \times 10^{-1}$	1.93 ± 0.46
59	23.96 ± 1.18	3.36 ± 0.07	5.46 ± 0.06	$(9.48 \pm 0.85) \times 10^{-1}$	1.72 ± 0.39
60	20.07 ± 0.49	4.05 ± 0.05	5.72 ± 0.02	$(1.07 \pm 0.10) \times 10^{-1}$	3.48 ± 0.16
61	25.94 ± 0.91	3.66 ± 0.06	5.95 ± 0.04	$(9.09 \pm 0.56) \times 10^{-1}$	2.31 ± 0.44
62	29.58 ± 2.05	2.91 ± 0.09	5.51 ± 0.08	$(6.08 \pm 0.87) \times 10^{-1}$	< 2.77
63	26.67 ± 0.80	3.72 ± 0.05	6.08 ± 0.03	$(1.19 \pm 0.28) \times 10^{-1}$	2.73 ± 0.29
64	24.53 ± 0.98	2.95 ± 0.07	5.10 ± 0.04	$< 15.27 \times 10^{-2}$	3.42 ± 0.82
65	27.88 ± 1.15	3.10 ± 0.06	5.56 ± 0.04	$(5.26 \pm 0.93) \times 10^{-1}$	< 1.92
66	19.68 ± 0.71	3.82 ± 0.06	5.45 ± 0.04	$(9.62 \pm 0.66) \times 10^{-1}$	4.33 ± 0.36
67	27.03 ± 0.90	3.27 ± 0.05	5.65 ± 0.04	$(5.18 \pm 0.60) \times 10^{-1}$	< 1.18
68	23.87 ± 0.90	2.99 ± 0.07	5.07 ± 0.04	$(3.25 \pm 0.50) \times 10^{-1}$	1.27 ± 0.30
69	22.23 ± 0.48	3.50 ± 0.04	5.42 ± 0.02	$(1.46 \pm 0.19) \times 10^{-1}$	3.24 ± 0.27
70	18.97 ± 0.44	3.90 ± 0.04	5.44 ± 0.02	$(3.28 \pm 0.21) \times 10^{-1}$	1.78 ± 0.20
71	21.49 ± 0.77	3.57 ± 0.06	5.41 ± 0.04	$(3.70 \pm 0.33) \times 10^{-1}$	1.99 ± 0.43
72	25.14 ± 1.49	2.60 ± 0.10	4.81 ± 0.06	$(5.39 \pm 1.27) \times 10^{-1}$	< 1.02
73	26.85 ± 1.44	2.67 ± 0.08	5.04 ± 0.06	$(1.12 \pm 0.17) \times 10^{0}$	< 1.57
74	17.57 ± 0.54	3.86 ± 0.06	5.22 ± 0.03	$(3.61 \pm 0.17) \times 10^{-1}$	2.05 ± 0.26
75	25.86 ± 1.04	3.33 ± 0.06	5.61 ± 0.04	$(4.29 \pm 0.50) \times 10^{-1}$	< 1.49

Table D.1: Calculated dust and gas properties for the GMCs.

GMC ID	T (K)	$\log(\mathrm{M_{dust}}\ [\mathrm{M_\odot}])$	$\log(L_{\mathrm{TIR}}\ [L_\odot])$	L_{CO} (K km s^{-1})	Σ_{HI} ($\mathrm{M_\odot}$ pc^{-2})
76	25.54 ± 0.75	3.17 ± 0.05	5.42 ± 0.03	$(6.74 \pm 0.40) \times 10^{-1}$	1.05 ± 0.28
77	24.89 ± 0.55	4.55 ± 0.04	6.74 ± 0.02	$(1.12 \pm 0.03) \times 10^{0}$	4.87 ± 0.20
78	27.77 ± 0.73	4.20 ± 0.04	6.65 ± 0.03	$(1.02 \pm 0.04) \times 10^{0}$	3.73 ± 0.23
79	21.27 ± 0.45	4.27 ± 0.04	6.08 ± 0.02	$(3.52 \pm 0.18) \times 10^{-1}$	4.33 ± 0.15
80	26.08 ± 0.65	3.87 ± 0.04	6.17 ± 0.03	$(1.66 \pm 0.20) \times 10^{-1}$	1.47 ± 0.28
81	27.39 ± 1.29	3.25 ± 0.07	5.67 ± 0.05	$(4.98 \pm 0.90) \times 10^{-1}$	3.33 ± 0.68
82	23.04 ± 0.54	4.03 ± 0.04	6.03 ± 0.02	$(2.81 \pm 0.14) \times 10^{-1}$	2.14 ± 0.18
83	28.94 ± 0.96	3.27 ± 0.05	5.82 ± 0.04	$< 13.95 \times 10^{-2}$	1.47 ± 0.19
84	26.67 ± 0.85	3.62 ± 0.05	5.97 ± 0.04	$(4.77 \pm 0.44) \times 10^{-1}$	2.66 ± 0.34
85	24.28 ± 0.58	4.08 ± 0.04	6.21 ± 0.03	$(6.98 \pm 0.34) \times 10^{-1}$	1.83 ± 0.38
86	24.54 ± 0.63	4.05 ± 0.04	6.21 ± 0.03	$(1.25 \pm 0.05) \times 10^{0}$	3.37 ± 0.40
87	24.53 ± 1.96	2.95 ± 0.11	5.10 ± 0.09	$(1.80 \pm 0.35) \times 10^{0}$	1.03 ± 0.25
88	27.26 ± 0.86	3.72 ± 0.05	6.12 ± 0.04	$(8.33 \pm 0.60) \times 10^{-1}$	2.04 ± 0.41
89	19.09 ± 0.46	3.56 ± 0.05	5.12 ± 0.02	$(6.81 \pm 1.41) \times 10^{-2}$	2.31 ± 0.33
90	25.25 ± 1.02	3.06 ± 0.06	5.29 ± 0.04	$(4.77 \pm 0.94) \times 10^{-1}$	< 1.93
91	18.63 ± 0.51	3.74 ± 0.05	5.24 ± 0.03	$(1.93 \pm 0.17) \times 10^{-1}$	1.40 ± 0.24
92	19.84 ± 0.45	3.47 ± 0.04	5.11 ± 0.02	$(9.80 \pm 2.19) \times 10^{-2}$	0.66 ± 0.18
93	17.02 ± 0.52	3.97 ± 0.06	5.25 ± 0.03	$(7.69 \pm 0.67) \times 10^{-1}$	2.71 ± 0.32
94	23.57 ± 0.64	3.63 ± 0.04	5.69 ± 0.03	$(8.26 \pm 0.62) \times 10^{-1}$	2.73 ± 0.35
95	19.92 ± 1.19	3.23 ± 0.09	4.88 ± 0.06	$(4.12 \pm 0.44) \times 10^{-1}$	< 1.12
96	19.59 ± 0.37	4.47 ± 0.04	6.08 ± 0.02	$(2.87 \pm 0.08) \times 10^{-1}$	4.82 ± 0.12
97	30.75 ± 0.95	3.74 ± 0.04	6.43 ± 0.04	$(4.21 \pm 0.31) \times 10^{-1}$	< 1.34
98	23.28 ± 1.60	3.22 ± 0.10	5.25 ± 0.07	$(4.94 \pm 0.92) \times 10^{-1}$	1.69 ± 0.53
99	23.59 ± 0.57	4.26 ± 0.04	6.32 ± 0.03	$(8.14 \pm 0.43) \times 10^{-1}$	4.42 ± 0.17
100	29.64 ± 0.80	4.01 ± 0.04	6.62 ± 0.03	$(1.84 \pm 0.06) \times 10^{0}$	3.62 ± 0.32

Table D.1: Calculated dust and gas properties for the GMCs.

GMC ID	T (K)	$\log(\mathrm{M_{dust}}\ [\mathrm{M_\odot}])$	$\log(L_{\mathrm{TIR}}\ [L_\odot])$	L_{CO} (K km $\mathrm{s^{-1}}$)	Σ_{HI} ($\mathrm{M_\odot}$ $\mathrm{pc^{-2}}$)
101	21.33 ± 1.01	3.17 ± 0.08	4.99 ± 0.05	$(4.85 \pm 0.94) \times 10^{-1}$	1.75 ± 0.46
102	25.70 ± 0.98	3.32 ± 0.06	5.59 ± 0.04	$(5.23 \pm 0.65) \times 10^{-1}$	2.96 ± 0.43
103	20.51 ± 0.85	3.37 ± 0.07	5.10 ± 0.04	$(1.98 \pm 0.18) \times 10^{-1}$	1.28 ± 0.10
104	23.29 ± 0.83	3.62 ± 0.06	5.65 ± 0.04	$(6.48 \pm 1.03) \times 10^{-1}$	1.13 ± 0.21
105	29.54 ± 0.80	4.41 ± 0.04	7.01 ± 0.03	$(6.11 \pm 0.17) \times 10^{-1}$	2.92 ± 0.35
106	21.87 ± 0.47	3.66 ± 0.04	5.54 ± 0.02	$(1.23 \pm 0.15) \times 10^{-1}$	0.70 ± 0.18
107	25.20 ± 0.64	3.76 ± 0.04	5.97 ± 0.03	$(1.79 \pm 0.49) \times 10^{-1}$	4.95 ± 0.47
108	23.19 ± 0.51	3.17 ± 0.04	5.19 ± 0.03	$< 10.52 \times 10^{-2}$	2.91 ± 0.35
109	25.66 ± 1.19	3.21 ± 0.07	5.47 ± 0.05	$(3.48 \pm 0.66) \times 10^{-1}$	< 1.36
110	24.95 ± 0.67	3.84 ± 0.04	6.03 ± 0.03	$(4.33 \pm 0.22) \times 10^{-1}$	< 1.08
111	19.55 ± 0.59	3.64 ± 0.05	5.25 ± 0.03	$(3.78 \pm 0.30) \times 10^{-1}$	1.49 ± 0.26
112	20.90 ± 0.63	3.88 ± 0.06	5.65 ± 0.03	$(7.03 \pm 1.11) \times 10^{-2}$	1.40 ± 0.19
113	26.49 ± 0.73	3.57 ± 0.04	5.91 ± 0.03	$(7.32 \pm 0.53) \times 10^{-1}$	< 1.45
114	20.13 ± 0.56	3.65 ± 0.05	5.33 ± 0.03	$(2.15 \pm 0.18) \times 10^{-1}$	< 1.14
115	26.87 ± 1.02	2.99 ± 0.06	5.36 ± 0.05	$< 7.63 \times 10^{-2}$	< 1.10
116	21.27 ± 0.64	3.75 ± 0.05	5.56 ± 0.03	$(7.92 \pm 0.38) \times 10^{-1}$	1.00 ± 0.20
117	21.50 ± 0.67	3.36 ± 0.05	5.20 ± 0.03	$(2.39 \pm 0.25) \times 10^{-1}$	1.69 ± 0.22
118	24.73 ± 1.04	3.04 ± 0.07	5.21 ± 0.05	$(6.38 \pm 0.81) \times 10^{-1}$	< 1.64
119	22.36 ± 1.33	3.20 ± 0.09	5.13 ± 0.06	$(3.59 \pm 0.27) \times 10^{-1}$	< 0.68
120	20.46 ± 0.87	3.13 ± 0.07	4.85 ± 0.04	$(5.17 \pm 0.70) \times 10^{-1}$	< 1.44
121	18.59 ± 0.47	3.49 ± 0.05	4.98 ± 0.03	$(1.76 \pm 0.34) \times 10^{-1}$	2.49 ± 0.43
122	23.88 ± 0.58	3.93 ± 0.04	6.02 ± 0.03	$(4.79 \pm 0.18) \times 10^{-1}$	2.43 ± 0.19
123	23.45 ± 0.97	3.35 ± 0.07	5.39 ± 0.04	$(2.75 \pm 0.18) \times 10^{-1}$	< 2.59
124	28.05 ± 1.38	2.92 ± 0.07	5.39 ± 0.05	$(3.37 \pm 0.38) \times 10^{-1}$	3.04 ± 0.69
125	20.38 ± 0.92	3.51 ± 0.07	5.22 ± 0.05	$(4.89 \pm 0.47) \times 10^{-1}$	< 1.80

Table D.1: Calculated dust and gas properties for the GMCs.

GMC ID	T (K)	$\log(\mathrm{M}_{\mathrm{dust}}\ [\mathrm{M}_\odot])$	$\log(L_{\mathrm{TIR}}\ [L_\odot])$	L_{CO} (K km s^{-1})	Σ_{HI} ($\mathrm{M}_\odot$ pc^{-2})
126	28.10 ± 0.73	3.95 ± 0.04	6.43 ± 0.03	$(3.76 \pm 0.17) \times 10^{-1}$	< 0.87
127	18.27 ± 0.53	3.48 ± 0.06	4.93 ± 0.03	$(2.76 \pm 0.67) \times 10^{-1}$	1.27 ± 0.18
128	19.34 ± 0.50	3.54 ± 0.05	5.12 ± 0.03	$(1.26 \pm 0.19) \times 10^{-1}$	1.28 ± 0.18
129	20.26 ± 0.63	3.49 ± 0.06	5.18 ± 0.03	$(5.20 \pm 0.52) \times 10^{-1}$	4.01 ± 0.67
130	25.76 ± 0.59	4.18 ± 0.04	6.46 ± 0.03	$(2.91 \pm 0.15) \times 10^{-1}$	2.30 ± 0.22
131	25.02 ± 1.06	3.12 ± 0.07	5.32 ± 0.04	$(2.54 \pm 0.57) \times 10^{-1}$	3.02 ± 0.65
132	28.43 ± 0.99	3.51 ± 0.05	6.02 ± 0.04	$(3.35 \pm 0.52) \times 10^{-1}$	< 2.03
133	21.75 ± 0.51	4.32 ± 0.04	6.18 ± 0.02	$(3.44 \pm 0.15) \times 10^{-1}$	3.63 ± 0.15
134	22.21 ± 0.47	4.33 ± 0.04	6.25 ± 0.02	$(8.79 \pm 0.32) \times 10^{-1}$	2.88 ± 0.35
135	29.56 ± 0.79	4.98 ± 0.04	7.58 ± 0.03	$(1.50 \pm 0.01) \times 10^{0}$	4.00 ± 0.26
136	20.23 ± 0.88	3.25 ± 0.08	4.94 ± 0.04	$(4.79 \pm 0.64) \times 10^{-1}$	< 1.19
137	20.66 ± 0.43	3.74 ± 0.04	5.49 ± 0.02	$(1.46 \pm 0.17) \times 10^{-1}$	1.76 ± 0.20
138	18.79 ± 1.03	3.55 ± 0.09	5.07 ± 0.06	$(6.68 \pm 0.69) \times 10^{-1}$	1.36 ± 0.33
139	24.38 ± 0.69	3.01 ± 0.05	5.15 ± 0.03	$< 3.74 \times 10^{-2}$	1.57 ± 0.22
140	19.96 ± 0.66	3.64 ± 0.06	5.30 ± 0.03	$(3.72 \pm 0.23) \times 10^{-1}$	2.74 ± 0.75
141	21.00 ± 0.45	4.06 ± 0.04	5.84 ± 0.02	$(4.26 \pm 0.33) \times 10^{-1}$	2.80 ± 0.21
142	20.29 ± 0.49	3.63 ± 0.05	5.33 ± 0.03	$(3.03 \pm 0.22) \times 10^{-1}$	2.00 ± 0.23
143	26.22 ± 0.70	4.02 ± 0.04	6.33 ± 0.03	$(6.77 \pm 0.60) \times 10^{-1}$	2.71 ± 0.44
144	21.40 ± 0.43	3.62 ± 0.04	5.44 ± 0.02	$(1.65 \pm 0.15) \times 10^{-1}$	3.02 ± 0.13
145	18.37 ± 0.36	4.09 ± 0.04	5.56 ± 0.02	$< 4.76 \times 10^{-2}$	1.97 ± 0.08
146	21.54 ± 0.53	3.45 ± 0.04	5.29 ± 0.03	$(1.36 \pm 0.38) \times 10^{-1}$	2.60 ± 0.46
147	23.01 ± 1.35	2.77 ± 0.09	4.78 ± 0.07	$< 23.41 \times 10^{-2}$	< 1.16
148	22.89 ± 0.51	4.35 ± 0.04	6.34 ± 0.02	$(1.18 \pm 0.02) \times 10^{0}$	2.31 ± 0.13
149	22.84 ± 0.63	3.84 ± 0.05	5.82 ± 0.03	$(2.01 \pm 0.19) \times 10^{-1}$	3.33 ± 0.28
150	19.43 ± 0.40	4.21 ± 0.04	5.81 ± 0.02	$(2.24 \pm 0.15) \times 10^{-1}$	1.33 ± 0.18

Table D.1: Calculated dust and gas properties for the GMCs.

GMC ID	T (K)	log(M$_{\rm dust}$ [M$_\odot$])	log($L_{\rm TIR}$ [$L_\odot$])	$L_{\rm CO}$ (K km s^{-1})	$\Sigma_{\rm HI}$ (M$_\odot$ pc^{-2})
151	20.80 ± 0.80	3.21 ± 0.07	4.97 ± 0.04	$(7.30 \pm 0.83) \times 10^{-1}$	< 2.33
152	22.37 ± 1.03	3.29 ± 0.07	5.23 ± 0.05	$< 27.59 \times 10^{-2}$	< 1.36
153	22.95 ± 0.90	3.21 ± 0.06	5.20 ± 0.04	$(3.62 \pm 0.75) \times 10^{-1}$	< 2.15
154	24.10 ± 1.46	3.07 ± 0.08	5.18 ± 0.07	$(6.13 \pm 1.28) \times 10^{-1}$	< 2.26
155	17.92 ± 0.66	3.67 ± 0.07	5.07 ± 0.04	$(2.48 \pm 0.22) \times 10^{0}$	1.75 ± 0.50
156	22.72 ± 0.78	3.13 ± 0.06	5.10 ± 0.03	$(1.73 \pm 0.26) \times 10^{-1}$	< 1.22
157	23.15 ± 0.80	2.93 ± 0.06	4.95 ± 0.03	$< 19.48 \times 10^{-2}$	< 1.50
158	25.61 ± 0.77	3.30 ± 0.05	5.55 ± 0.03	$(6.66 \pm 1.73) \times 10^{-2}$	< 1.15
159	21.66 ± 0.50	3.84 ± 0.04	5.70 ± 0.02	$(1.26 \pm 0.16) \times 10^{-1}$	2.34 ± 0.14
160	23.20 ± 0.49	4.49 ± 0.04	6.51 ± 0.02	$(2.90 \pm 0.06) \times 10^{-1}$	3.33 ± 0.11
161	30.45 ± 0.86	4.17 ± 0.04	6.84 ± 0.03	$(2.05 \pm 0.11) \times 10^{-1}$	2.34 ± 0.28
162	21.36 ± 0.51	3.48 ± 0.05	5.30 ± 0.02	$(9.02 \pm 1.45) \times 10^{-2}$	1.72 ± 0.14
163	20.60 ± 0.57	3.52 ± 0.05	5.26 ± 0.03	$(8.50 \pm 0.99) \times 10^{-2}$	2.17 ± 0.15
164	21.56 ± 0.52	4.05 ± 0.04	5.89 ± 0.02	$(1.34 \pm 0.07) \times 10^{-1}$	3.14 ± 0.10

APPENDIX E

MODIFYING THE THEMIS MODEL

In order to better fit the THEMIS model to the data, I fit a dust emission model to the points longward of $3.4\,\mu$m using a similar method to that of Chastenet et al. (2017). The components of this fit are the small carbon grains (sCM20), large carbon grains (lCM20), and silicates, consisting of olivines and pyroxines, tied together as aSilM5. Due to a non-negligible contribution from stars at NIR wavelengths, I also include a blackbody at 5000 K, to approximate this contribution.

My initial fit kept the mass ratios of these various components fixed at the values calculated for the diffuse dust of the MW, and so there are only three free parameters in the model – the strength of the ISRF, a scaling factor for the stellar contribution and the overall dust mass. I generate a grid of ISRFs from $10^{-1} \leq U \leq 10^{3.5}$ (with 1 being the value for the local neighbourhood), equally spaced in steps of 0.01 in log space. The SEDs for this are generated using DUSTEM (Compiègne et al., 2011). I then fitted these three free parameters using an MCMC framework using EMCEE[1]. I use 500 walkers each taking 500 steps, using the first half of these steps as "burn-in", and the initial guesses for the ISRF is that of the MW, the stellar scaling factor the $3.6\,\mu$m point, and the dust mass by the $250\,\mu$m point. I account for correlated uncertainties between bands, and use the filter responses for each waveband to calculate the flux as seen by that particular instrument. The fit and residuals for this can be seen in Fig. E.1, and I find that the default THEMIS parameters consistently underestimate the bulk of the cold dust points.

Next, I performed a fit where I allowed the abundances of the amorphous hydrocarbons and silicates to vary (although I lock the abundances of the two silicate

---

[1] `http://dfm.io/emcee/current/`

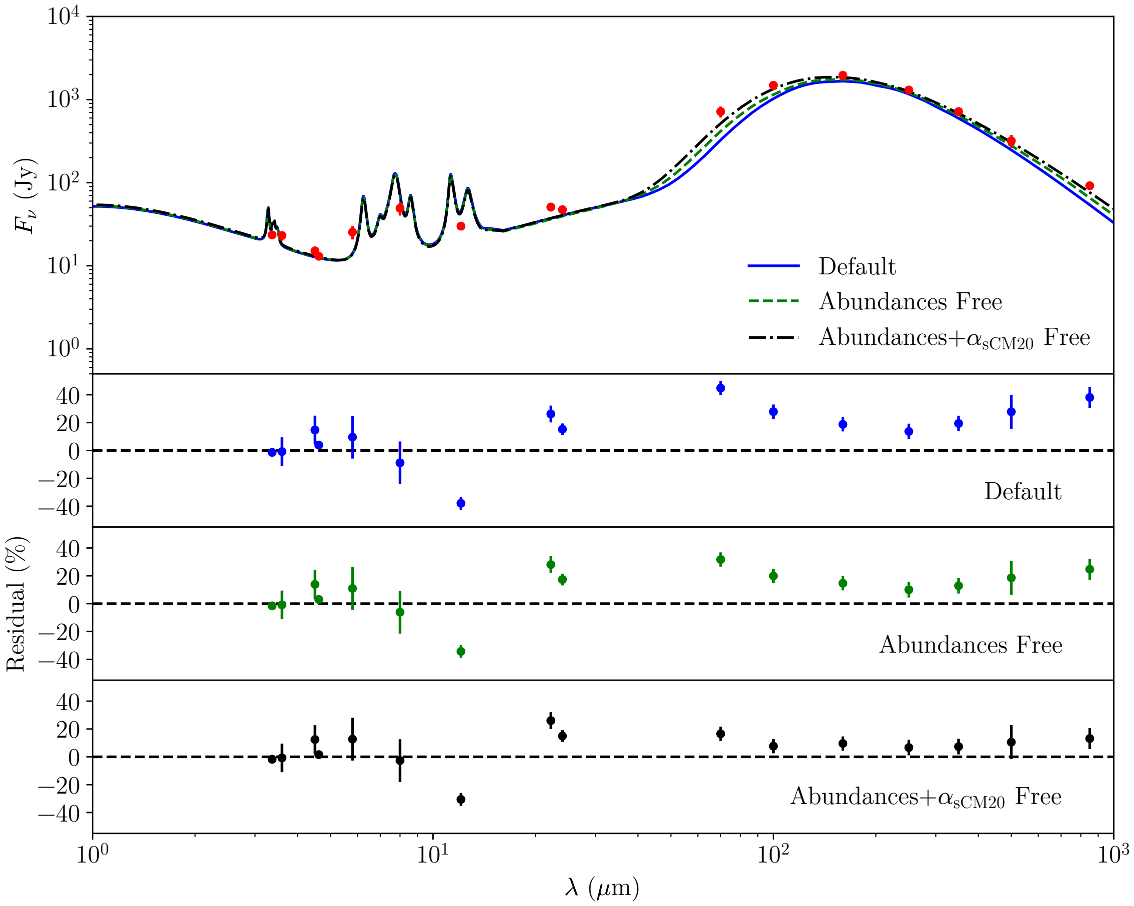

Figure E.1: *Top:* Various model THEMIS fits to the dust SED of M33. The solid blue line indicates the default THEMIS parameters, the dashed green line where I allow mass abundances to vary, and the black dot-dash line where I additionally vary the size distribution of small carbon grains. The residuals for each of these fits are given in the subsequent panels.

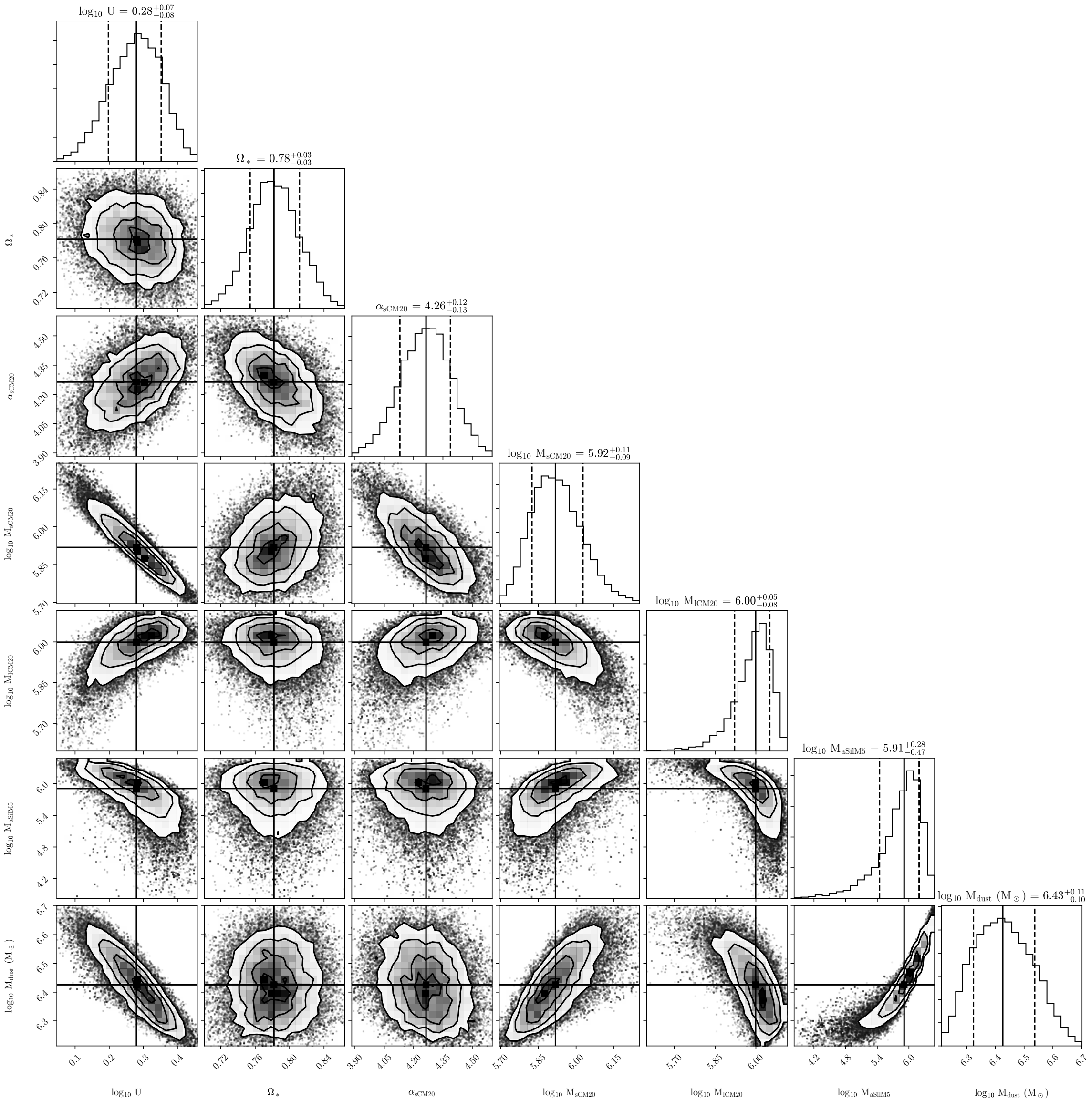

Figure E.2: Corner plot for the THEMIS dust fit with free dust grain abundances and small grain size distribution. From left to right, the panels show the ISRF strength U, the stellar scaling factor (with respect to the 3.6 μm flux), the small grain power-law slope, the mass for the small carbon grains, large carbon grains and silicates, and finally the total dust mass. The solid black line in each histogram shows the median value, with the dashed lines showing the 16th and 84th percentiles.

populations together). This increases the number of free parameters to 5, where compared to the total dust mass there is now the individual masses of the small and large carbon grains, and the silicates. This fit is also shown in Fig. E.1, and I find that while it performs slightly better than the default parameters, the fit is still poor across the FIR/sub-mm range.

Finally, I allowed variation in the small grain size distribution. The size distribution of small amorphous hydrocarbons is given by a power-law, partly defined by $\mathrm{d}n/\mathrm{d}a \propto a^{-\alpha_{\mathrm{sCM20}}}$, and I allow this value of α_{sCM20} to vary. For this, I calculated a grid of $2.6 \leq \alpha_{\mathrm{sCM20}} \leq 5.4$ (where 5 is the THEMIS default) in steps of 0.01, for each value of the ISRF strength defined earlier (leading to a total grid of some 100,000 combination of parameters). The inclusion of fitting α_{sCM20} brings the total number of free parameters to 6, and the best fit is shown, again, in Fig. E.1. I also show the corner plot of this fit in Fig. E.2. I find a median α_{sCM20} of around 4.3, somewhat lower than the THEMIS default of 5. In terms of the SED, this leads to a flatter slope at longer wavelengths. Physically, this corresponds to fewer very small carbon grains, as we might expect in a lower-metallicity environment such as M33. Much like the work of Chastenet et al. (2017) on the LMC and SMC, we find a much lower value for the silicate/carbon ratio of $\sim$0.3, compared to the MW value of $\sim$10. However, the ratio of small-to-large grains is very similar to the MW value of 0.4, with a value of 0.3.

Finally, I note that the fit does not perform so well in the 24-70 μm range. This can be improved by adding a second, warmer dust component (i.e. a higher ISRF strength). This produces a better fit in these wavelength ranges, but does not change the dust component masses, or α_{sCM20} significantly. As I am only performing this fit to calculate the dust grain properties, and leave SKIRT to model the ISRF, I only show the single-temperature component fit here.

Appendix F

Rotating and Projecting Images

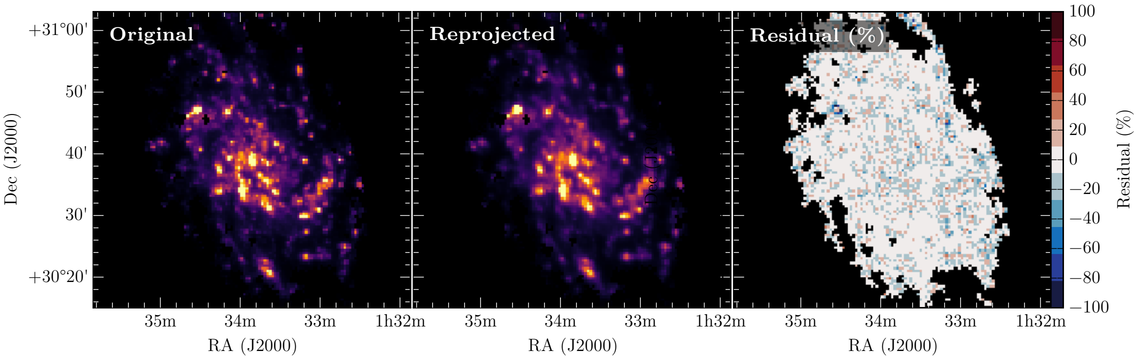

Figure F.1: The effect of deprojection and derotation on an input image. From left to right, I show the original GALEX FUV image, the image after derotation, deprojection, reprojection, and rotation, and the corresponding residuals of these two maps.

To add a 3D scale to the provided images, SKIRT deprojects and de-rotates the input image, given an inclination and position angle. This means that the image becomes "smeared" as it is transformed into the plane of the galaxy, and then back into the observer frame. To test the effect that this has on the images (particularly for the purposes of residuals), I de-rotated and deprojected M33 (using a PA of 22.5° and inclination of 56°), before rotating and projecting it back into its original frame. The result of this can be seen in Fig. F.1. The effects of this routine are minor and will not affect our residual plots in any significant way, so I opt to use the original images as-is.